University of Huddersfield Repository

Muhamedsalih, Yousif

Two-phase flow meter for determining water and solids volumetric flow rate in vertical and inclined solids-in-water flows

Original Citation

Muhamedsalih, Yousif (2014) Two-phase flow meter for determining water and solids volumetric flow rate in vertical and inclined solids-in-water flows. Doctoral thesis, University of Huddersfield.

This version is available at http://eprints.hud.ac.uk/23741/

http://eprints.hud.ac.uk/

TWO-PHASE FLOW METER FOR DETERMINING WATER AND SOLIDS VOLUMETRIC FLOW RATE IN VERTICAL AND INCLINED SOLIDS-IN-WATER FLOWS

YOUSIF MAKKI MUHAMEDSALIH

A thesis submitted to The University of Huddersfield

in partial fulfilment of the requirements for

the degree of Doctor of Philosophy

The University of Huddersfield

September 2014

Copyright statement

The following notes on copyright and the ownership of intellectual property rights must be included as written below:

i. The author of this thesis (including any appendices and/or schedules to this thesis) owns any copyright in it (the "Copyright") and s/he has given The University of Huddersfield the right to use such Copyright for any administrative, promotional, educational and/or teaching purposes.

ii. Copies of this thesis, either in full or in extracts, may be made only in accordance with the regulations of the University Library. Details of these regulations may be obtained from the Librarian. This page must form part of any such copies made.

iii. The ownership of any patents, designs, trademarks and any and all other intellectual property rights except for the Copyright (the "Intellectual Property Rights") and any reproductions of copyright works, for example graphs and tables ("Reproductions"), which may be described in this thesis, may not be owned by the author and may be owned by third parties. Such Intellectual Property Rights and Reproductions cannot and must not be made available for use without the prior written permission of the owner(s) of the relevant Intellectual Property Rights and/or Reproductions.

Declaration

No portion of the work referred to in this thesis has been submitted to support an application for another degree or qualification at this or any other university or other institute of learning.

Acknowledgment

All thanks and praises are due to God the Almighty for his blessing that made this work possible and for its completion.

I would like to express my sincere thanks to my supervisor Professor Gary Lucas for his continued guidance and encouragement throughout this project. His valuable suggestions during all the phases of this work were indispensable.

I would also like to thank all my colleagues in the systems engineering research group, especially: Dr Sulaiyam AL-Hinai, Dr Teerachai Leeuncgulsatien, Dr. Zhao Yuyang and Mr. Yiqing Meng.

I would also like to express my gratitude to University of Huddersfield for awarding me the fee waiver scholarship to continue my PhD.

Last, by no means least, my special thanks to Mum, Dad and brothers Sinan, Hussam and Haitham. Without your endless support and unlimited patience, I could have never completed this work.

Abstract

Multiphase flow can be defined as the simultaneous flow of a stream of two or more phases. Solids-in-water flow is a multiphase flows where solids and liquid are both present. Due to the density differences of the two phases, the results for such flow is often to have non-uniform profiles of the local volume fraction and local axial velocity for both phases in the flow cross-section. These non-uniform profiles are clearly noticeable in solids-in-water stratified flow with moving bed for inclined and horizontal pipelines. However in many industrial applications, such as oil and gas industry, food industry and mining industry, multiphase flows also exist and it is essentially important to determine the phase concentration and velocity distributions in through the pipe cross-section in order to be able to estimate the accurately the volumetric flow rate for each phase.

This thesis describe the development of a novel non-intrusive flow meter that can be used for measuring the local volume fraction distribution and local axial velocity distributions of the continuous and discontinuous phases in highly non-uniform multiphase flows for which the continuous phase is electrically conducting and the discontinuous phase is an insulator. The developed flow meter is based on combining two measurement techniques: the Impedance cross correlation ICC technique and the electromagnetic velocity profiler EVP technique.

Impedance cross correlation ICC is a non-invasive technique used to measure the local volume fraction distributions for both phases and the local velocity distribution for the dispersed phase over the pipe cross-section, whilst the electromagnetic velocity profiler EVP technique is used to

measure the local axial velocity profile of the continuous phase through the pipe cross-section. By using these profiles the volumetric flow rates of both phases can be calculated.

A number of experiments were carried out in solid-in-water flow in the University of Huddersfield solids-in-water flow loop which has an 80 mm ID and an approximately 3m long working section. ICC and EVP systems were mounted at 1.6 m from the working section inlet which was inclined at 0 and 30 degree to the vertical. The obtained result for the flow parameters including phase volume fraction and velocity profiles and volumetric flow rates, have been compared with reference measurements and error sources of difference with their reference measurements have been identified and investigated.

Table of Contents

Table of Figures

xvii

List of Tables

Nomenclature

<u>Acronyms</u>

AM   Area Methodology

ADC   Analogue-to-Digital Converter

CoA   Centre of Action

DAC   Digital-to-Analogue Converter

DAQ   Data Acquisition Board

DP   Differential Pressure

EMFM   ElectroMagnetic Flow Meter

EC   Electrical Conductance

ECT   Electrical Capacitance Tomography

EVP   Electromagnetic Velocity Profiler

FEA   Finite Element Analysis

LDA   Laser-Doppler Anemometer

LE   Latch Enabled

MFM   Multiphase flow meter

NI	National Instrument
ICC	Impedance Cross Correlation
ID	Internal Diameter
QVGA	Quarter Video Graphics Array
RAM	Random Access Memory
RF	radio frequency module

Symbols

ΔP	Differential pressure drop
Q	Volumetric flow rate
$\overline{Q}$	The mean volumetric flow rate
v	The axial flow velocity
A	Area cross-section.
Q_d	The dispersed phase volumetric flow rate
Q_w	The water phase volumetric flow rate

$\overline{\alpha}$	The mean volume fraction
α_d	The local volume fraction of the dispersed phase
α_w	The local volume fraction of the water phase
ρ_m	The mixture fluid flow density
ρ_w	The water density
ρ_s	The solids density
f_P	The pipe friction factor
θ	The angle of inclination from the vertical
τ	Solids time travel
τ_{samp}	The time interval between successive pairs of frames
$\phi(x,y)$	The electrical potential distribution
A_n	The area of nth pixel
U	Electrical potential difference
B	The density of magnetic flux
ψ	sensitivity parameter

j	electrical current density
V_{out}	The value of the output voltage from the inverting amplifier of the conductance circuit
$(V_{out})_w$	The value of the output voltage when the water is present
ϕ	Configurations (I,II,III or IV)
n	Rotational position (1 to 8)
$(Cx)_{\phi,n}$	The x – co-ordinate of the CoA for Configuration ϕ and rotational position n
$(Cy)_{\phi,n}$	The y – co-ordinate of the CoA for Configuration ϕ and rotational position n
$(\alpha_s)_{\phi,n}$	Local solids volume fraction for Configuration ϕ and rotational position n
$(v_s)_{\phi,n}$	Local solids volume fraction for Configuration ϕ and rotational position n
$\alpha_{s,ICC}$	The solids volume fraction distributions
$v_{s,ICC}$	The solids velocity distribution
$\alpha_{n,B}$	the mean solids volume fraction of area B_n

B_n	The area of the effective sensing region for Configuration IV
$\overline{\psi}_n$	The mean sensitivity of Configuration IV rotational position n
a_i	is the area of each sub-area/ pixel using AM method
$A_{8,1}$	The overlap area associated with the boundaries of the two rotational positions 8 and 1
A_1	The area only associated with the boundaries of rotational position 1
$A_{1,2}$	The overlap area associated with boundaries of the two rotational positions 1 and 2.
α_{LPn}	The solids volume fraction at LP_n points
$(\alpha_{s,AM})_i$	The local solids volume fraction obtained by AM (I = 1 to 32)
$(v_{s,AM})_i$	The local solids velocity obtained by AM (I = 1 to 32)
V_a^+	Excitation signal to array A
V_b^+	Excitation signal to array B
$V_{out,B}$	The output voltage from the inverting amplifier in channel B
$V_{out,A}$	The output voltage from the inverting amplifier in channel A
R_f	The electrical resistance of the fluid

R_2	The feedback resistance of the inverting amplifier between the excitation electrode(s) and the virtual earth electrode(s)
R_y	The electrical resistance of the fluid between the excitation electrode(s) and the grounded electrode(s).
R_x	The electrical resistance of the fluid between the virtual earth electrode(s) and the grounded electrodes
V_A	The output voltage from the conductance circuit, channel A
V_B	The output voltage from the conductance circuit, channel B
k	conductance circuit gain
σ_m	Mixture conductivity
K_B	The constant of the system
$R_{\phi,n}(\tau)$	Cross correlation function for Configuration ϕ and rotational position n
$\overline{\alpha}_{s,dp}$	Reference solids volume fraction
$Q_{s,ref}$	The reference solids volumetric flow rate
$Q_{w,ref}$	The reference water volumetric flow rate
$\dot{M}$	Mean mass flow rate

$\rho_{s,w}$ The mean density of the solids-in-water mixture

$U_{w,exc}$ The final excess volume of the water attached to the solids particle

$U_{s,corr}$ The final correct volume of the solids particles

$Q_{s,ICC}$ The volumetric flow rate of the solids phase obtained by the ICC device

$Q_{w,EVP}$ The volumetric flow rate of the water phase obtained by the EVP device

1. CHAPTER 1: Introduction

1.1 Introduction

The aim of this research is to develop a novel technique that can be used to measure the local axial velocity distributions and the local volume fraction distributions of the continuous and discontinuous phases in highly non-uniform multiphase flows (specifically flows which contain simultaneous streams of two phases). Here the continuous phase will be considered as electrically conducting and the discontinuous phase is an insulator. From these distributions the volumetric flow rates of both phases can be calculated.

Measurement of the different phase flow rates in multiphase flow is highly important in oil and gas recovery, chemical, mining, food processing and nuclear industries. Around the world, scientists with diverse backgrounds, as well as engineers from different specialities, have engaged with the problem of how to measure the different parameters of multiphase flow.

1.2 Multiphase Flow Properties

In order to understand the measurement challenges in multiphase flows, it is necessary to define the basic properties.

The properties of single-phase flows are relatively well understood and the volumetric flow rate can be defined as:

$$Q = \int_A v \, dA \qquad\qquad \text{Equation 1-1}$$

where v is the axial flow velocity and A is the area cross-section.

In multiphase flow, where many phases may be present, it is vital to precisely monitor the distributions of the time averaged local volume fraction α_j and the time averaged local velocity, v_j, of the jth phase to enable quantification of its flow rate Q_j.

For example, in two-phase flow where the water is the continuous phase and either solids or oil is the dispersed phase, the volumetric flow rate for both phases can be define as:

$$Q_d = \int_A \alpha_d v_d \, dA \qquad\qquad \text{Equation 1-2}$$

$$Q_w = \int_A \alpha_w v_w \, dA \qquad\qquad \text{Equation 1-3}$$

where α_d and α_w respectively represent the local volume fraction of the dispersed phase (solid or oil) and the continuous phase (water) , while v_d and v_w respectively represent the local axial velocity of the dispersed phase (solid or oil) and the continuous phase (water).

For two-phase flow the relation between α_d and α_w is:

$$\alpha_d + \alpha_w = 1 \qquad\qquad \text{Equation 1-4}$$

Thus, in two phase flow, it is necessary to find the local volume fraction distribution of only one phase in order to determine the other. Based on Equation 1-4, the volumetric flow rate for the continuous phase (water) can be written as:

$$Q_w = \int_A (1 - \alpha_d) v_w \, dA \qquad\qquad \text{Equation \quad 1-5}$$

Knowing these basic terms will help to understand the development of this thesis.

1.3 Multiphase Flow Regimes

1.3.1   Gas-in-Liquid Flow

The geometrical configurations taken by vertical upward gas-in-liquid flows in a pipe have been divided by, for example, Martyn [1] into four main regimes, see Figure 1.1. In the description below, the liquid flow rate is assumed to be constant:

- Bubble flow: In which liquid is the continuous phase and a dispersion of bubbles flows within this liquid continuum. Usually, the bubbles have non-uniform size and have complex motions.

- Slug flow: As the gas flow rate increases, the bubbles become large, referred to as Taylor bubbles [2], and start to have bullet-shapes and a diameter which is similar to the size of the pipe diameter. These large bubbles are often interspersed with a dispersion of smaller bubbles.

- Churn flow: As the gas flow rate becomes higher still, the Taylor bubbles break down and the flow starts to become chaotic.

- Annular flow: At even higher gas flow rates, the liquid flows as an annular film on the tube wall and the gas flows in the centre. Usually, some of the liquid phase is entrained as small droplets in the pipe core.

Because of the complexities of multiphase flow, a wide variety of flow regime classifications can be found in the literature [1, 3-10], in addition to those described above.

Increasing Gas flow ⟶

Bubble flow   Slug flow   Churn flow   Annular flow
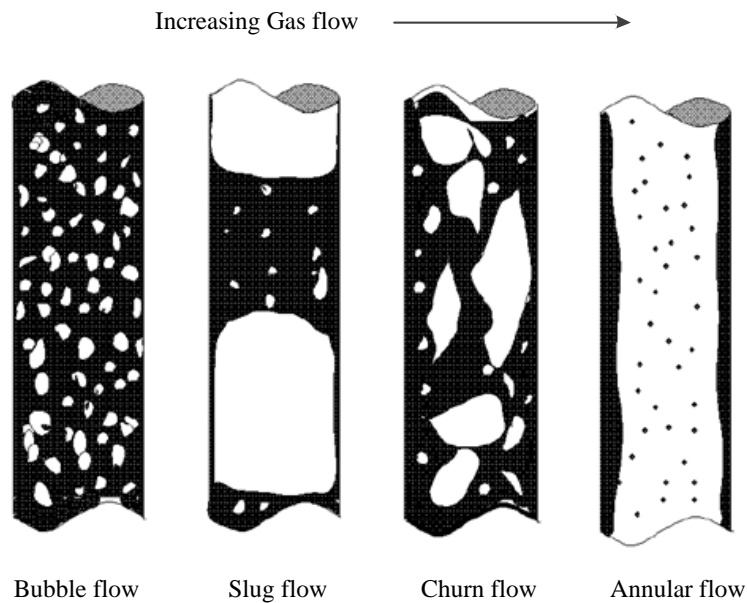
Figure 1.1 Flow regimes in vertical gas-liquid flows [1]

In the previous literature [1, 3-10] the flow patterns for vertical and horizontal multiphase flows are determined using different measurement techniques, some of which will be presented in more detail in Chapter Two. With vertical flow, the flow patterns when averaged over time are generally axisymmetric since the gravitational force acts parallel to the direction of the flow. However, in horizontal flow, in which the gravitational force is orthogonal to the flow direction, the flow patterns show asymmetric distributions including stratified or stratified wave flow, in which the more dense liquid phase tends to occupy the lower part of the horizontal pipe and the gas phase tends to occupy the upper part of the horizontal pipe.

1.3.2   Solids-in-Fluid Flows

The presence of a solids phase increases the complexity of the flow, Henthorn et. al., [11] used mica flakes, non-spherical sand and spherical glass beads having the same density and equivalent volumes as the solids in vertical solids-in-air flow. In this investigation the continuous phase was air and the dispersed phases were sand and glass. Henthorn et. al. found that the particle shape

and size could have a great effect on the flow regime. It was concluded that the greater drag forces on the less spherical particles significantly slowed the velocity of the solid particles.

In vertical solids-in-air flow, Lee and Durst [12] used spherical glass beads with four different diameters (0.1 mm, 0.2 mm, 0.4 mm and 0.8 mm) to examine the particles' motion in turbulent flow. The experimental results showed that the mean velocity profiles of the particles becomes close to being more constant across the pipe cross section as the particle diameter increases. Furthermore, the results showed a clearly recognizable particle-free region near the pipe wall which is increased as the particle diameter increased.

Alajbegovic et. al., [13] investigated solids-in-water vertical flow using solid spheres of ceramic and polystyrene using a Laser-Doppler Anemometer (LDA). In this investigation the continuous phase was water and the dispersed phases were ceramic and polystyrene. Both sets of spheres had diameters of 2.23 mm diameter, the ceramic spheres had a density of 2450 kgm^{-3} while the polystyrene spheres had a density of 32 kgm^{-3}. The velocity profiles for both sets of spheres showed a shallow peak at the centre of the pipe cross-section.

Alajbegovic et. al., [13] also presented the local volume fraction profiles for the ceramic beads for a number of flow conditions. The results showed that the local volume fraction profiles of the ceramic beads at low liquid flows were almost uniform across the pipe. However, the local volume fraction increased at the centre of the pipe as the fluid velocity increased. Alajbegovic et. al., presented results obtained by Sakaguchi et. al., [14] to support their findings that at higher liquid speed, the particles tend to move to the pipe centre. However this result depended on the size, shape, density and concentration of the solids and also the pipe diameter. Furthermore, both sets of authors agreed that there is a region free of particles close to the pipe wall. Bartosik and Shook [15] investigated solids-in-water vertical flow using sand particles as a dispersed phase

and water as continuous phase. They found that the concentration profiles for sand particles which were finer than those used by Alajbegovic et, al., were more uniform across the pipe cross-section. The global mean particle volume fractions used by Alajbegovic et. al., were less than 8% ,which is near to the mean solids volume fraction used in the experiments described in the current study(see Section 7.2.1).

In Horizontal/Inclined solids-in-liquid flow, the local velocity distribution and the local volume fraction distribution of each phase will depend on the density of the particles and the flow rate of the mixture. Due to gravitational forces, the more dense the particles the more likely they are to sink to the lower side of the pipe. Doron and Barnea [16] reviewed a number of studies to obtain a solids-liquid flow pattern map, see Figure 1.2. They grouped together flow patterns which have similar distributions and characteristic behaviours and derived three main flow patterns, see Figure 1.2:

a. Fully suspended flow: at high mixture flow rates, the solid particles tend to be suspended across the pipe section. The flow pattern may be subdivided into two sub-patterns:

(1) pseudohomogeneous suspension, when the solids are distributed nearly uniformly across the pipe cross-section. This pattern is happen when the mixture velocities are usually very high,

(2) heterogeneous suspension flow, this pattern occurs when the solids concentration gradient is in the direction perpendicular to the pipe axis, with a higher particle concentration travelling at the lower part of the pipe cross-section, see Figure 1.2a.

b. Stratified flow with moving bed: at lower mixture flow rates, the solids particles accumulate at the bottom of the pipe, forming a packed layer. The packed layer moves along the lower side of the pipe pushed by the liquid flow. The upper side of the pipe is occupied by a heterogeneous mixture which travels faster than the moving bed.

c. <u>Stratified flow with stationary bed</u>: in this case there will be three layers of particles inside the pipe cross section. A stationary bed at the bottom of pipe (this happens because the mixture flow rate is to too slow to move all the immersed particles), a separate moving layer on top of the stationary layer and above that a heterogeneous mixture which travels fastest.

Direction of flow

a. Heterogeneous suspension flow   Concentration Profile

Direction of flow

b. Flow with moving bed   Concentration Profile

Direction of flow

c. flow with a stationary bed   Concentration Profile
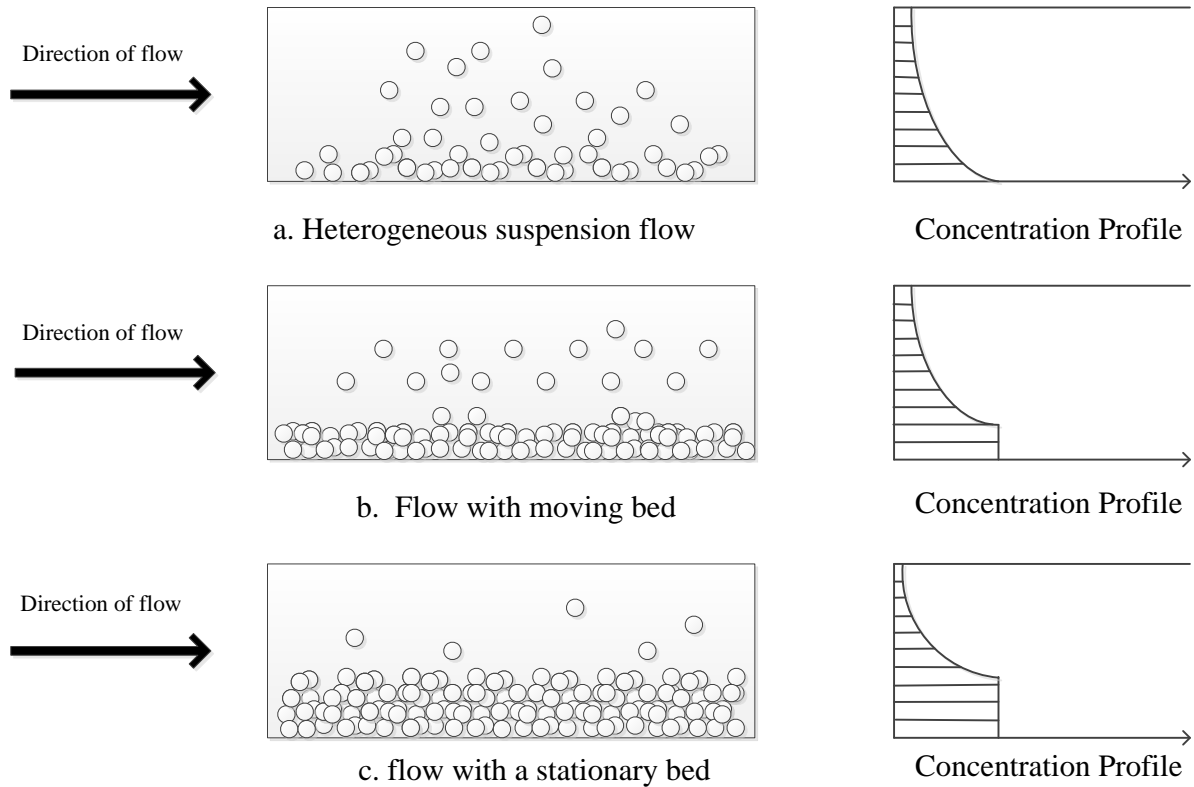
Figure 1.2 Schematic views of flow patterns and concentration distributions in a horizontal pipe

The study of **stratified solids-in-water flow in inclined pipes** is more complicated than for either horizontal or vertical flow. In inclined pipes, various flow patterns can be obtained depending on the particle and liquid densities, global mean in-situ volume fraction and the angle of inclination from the vertical [17]. Figure 1.3 shows a photograph of upward solids-in-water flow in a pipe inclined at 30° to the vertical. This photograph was taken using a high speed camera in the University of Huddersfield flow loop. Videos which were also obtained from the

high speed camera show that there is a continuous variation of the solids velocity from the upper to the lower sides of the inclined pipe. This variation produced three layers of solids travelling with different velocities and directions: (i) the bottom bed layer (maximum solids concentration) can experience reverse flow and travel downwards with a velocity u_a. (ii) the separated moving layer on top of the bottom bed travels up the pipe with a speed u_b, and (iii) the heterogeneous mixture above this travels with the greatest upword velocity, u_c. Additionally, the videos show a circulation phenomenon which helps the particles to travel upward in the overall flow direction.
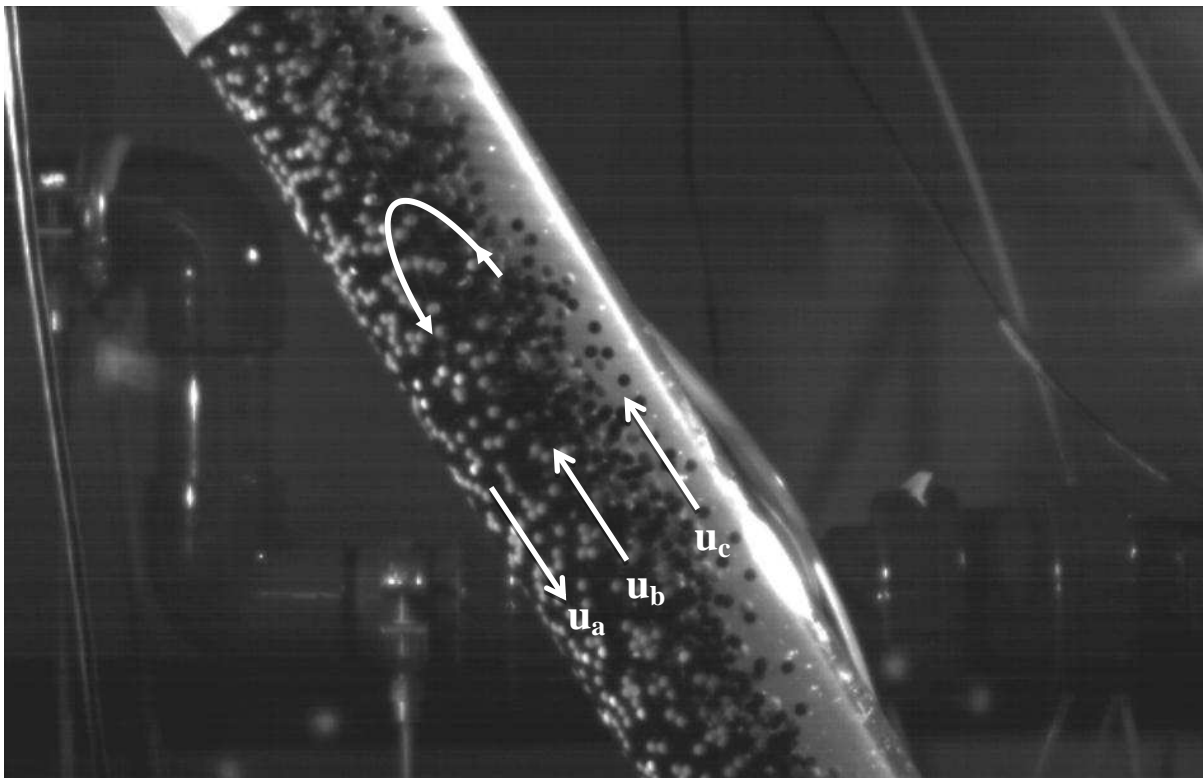
Figure 1.3 Photograph of upward solids-in-water flow in pipe inclined at 30° to the vertical

For highly non-uniform stratified flow, such as the inclined solids-in-water flow described above, it is very important to measure the local solids volume fraction distribution and the local

solids and water velocity distributions in order to determine the volumetric flow rates accurately

for both phases, the total volumetric flow rates Q_s and Q_w (for solids and water respectively)

associated with the profiles presented in Figure 2.4 and Figure 2.7 can be expressed as:

$$Q_s = \int (\alpha_s)_{x,y} (v_s)_{x,y} \, dxdy \hspace{3cm} \text{Equation 1-6}$$

$$Q_w = \int (1 - \alpha_s)_{x,y} (v_w)_{x,y} \, dxdy \hspace{2.5cm} \text{Equation 1-7}$$

Solids-in-liquid stratified flow is highly important in different industrial processes. Section 1.4

shows application examples of the solids-in-liquid flow in: the oil and gas industry, and the food

processing, mining and water treatment industries.

1.4 Multiphase Flow Applications in Industrial Processes

1.4.1 Oil and Gas Industry

Probably the largest area of interest in current multiphase flow measurement research is for oil

and gas production.

Presently, separation technology has a very important role in process industries where large and

expensive separators are used to split the mixture into its various phases which are then metered

individually. The installed cost of a separator will vary depending on the flow parameters (e.g

flow rate, temperature, pressure and the chemistry of the flow) and the location of the

installation; onshore, offshore or subsea. The typical cost of a separator varies between 1 to 5

US$ million [3]. Additionally, for offshore installations, the operational costs associated with a

test separator can reach as much as 350k US$ per year[3].

Due to the high cost of the separation processes, there remains in the energy sectors a need for

non-invasive and effective multiphase flow meters to replace conventional test separators for the

management of unprocessed different phases for long distance transportation.

The typical cost of multiphase flow meters (MFM) is generally less than that of conventional test separators, between 100k – 500k US$, although the cost of the MFM will depend on whether it is located topside or subsea, the size of the MFM and the measurement technique used.

It has been estimated that for a subsea development located 10 km from the host platform the use of MFMs reduces the cost of the test line by 62% and helps improve production management with a 6-9 % gain in the value of the oil recovered [18]. It was also estimated that the operational expenses for a MFM can be as high as 25% of its original cost for the first year and then reduce to 10k – 40k US$ per year for both offshore and topside applications [19].

Generally oil, gas, and water can be produced from the same well, although in deep and ultradeep water, the oil and gas production effectively involves many solid deposits such as hydrates, asphaltenes, emulsions and waxes [20-25]. These heavy solid deposits, in many instances, move from the well tubing to flow lines and to production separators, pumps, strainers and other fluid-handling equipment, creating further operational problems. As a result, for many cases, oil wells are completely shut down after being plugged by these heavy materials, which in turn causes great reduction in production volume and expensive operational problems, see Figure 1.4 and Figure 1.5. Different methods are currently in use for reducing the blocking problems e.g. by adding chemical solutions or controlling the pressure, temperature and concentration of the flow, yet these methods are dependent on knowing the concentration and velocity profiles for the different flowing phases [26].
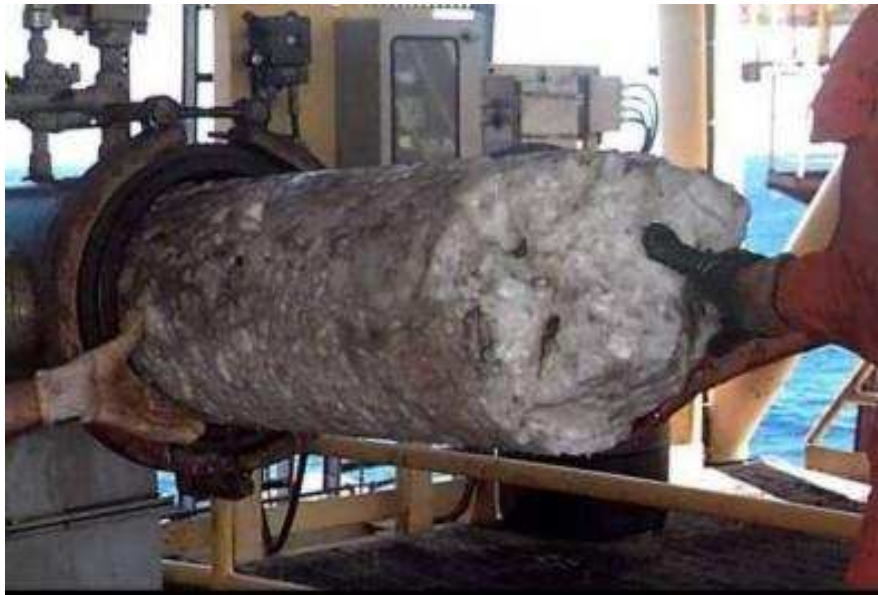
Figure 1.4 A large gas hydrate plug formed in a subsea hydrocarbon pipeline.[26]

Figure 1.5 Pipe blocked due to the paraffin and asphaltene buildup inside the walls of the pipes[27]

Additionally, during the oil drilling process, drilling mud is pumped into the oil well through the drill pipe. This fluid lubricates the cutting bit and helps to clean the well bore by carrying to the surface the drilling cuttings produced at the base of the well [28].

In some cases, there is a need for directional well drilling in order to reach to the geological target zone, see Figure 1.6. With directional well drilling, the higher cuttings concentration will lie at the lower side of the borehole which may partially block the fluid flow and hence lead to inadequate hole cleaning [17]. Thus a high pressure hydraulic pump is required for effectively cleaning the annular hole [20]. In order to select a suitable hydraulic system to control the volumetric cuttings flow rate, the mud and solids velocity and concentration distributions are required.
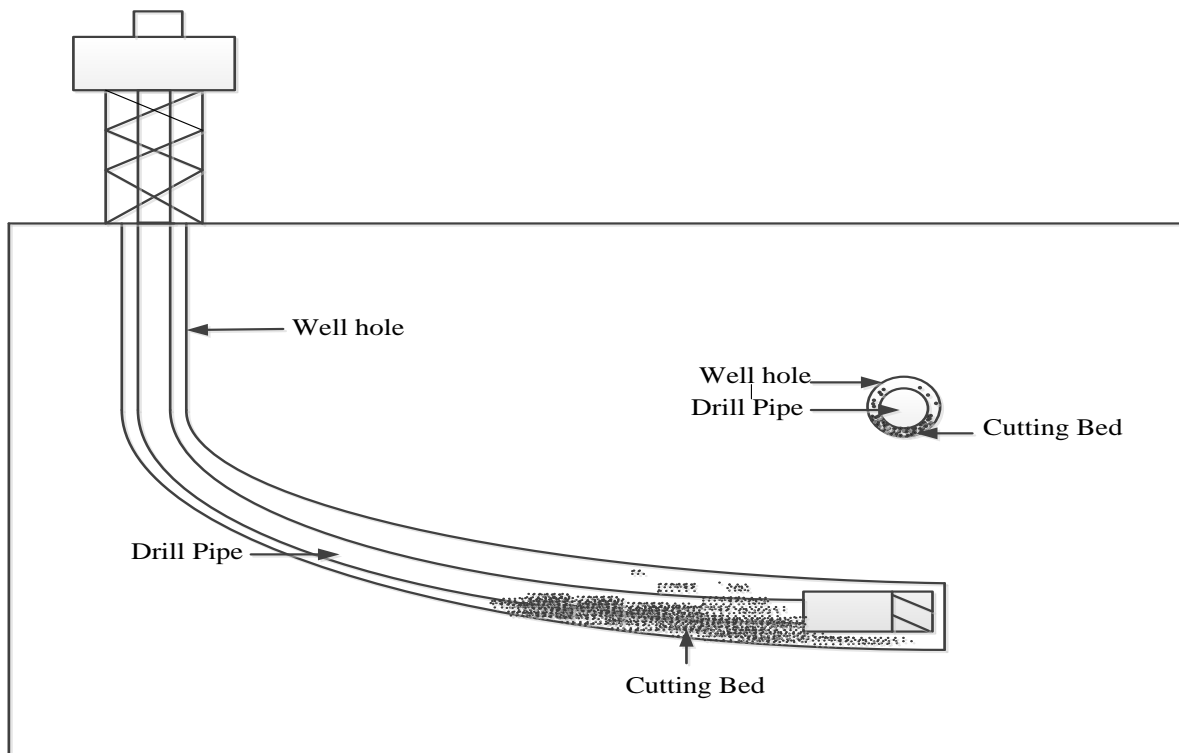
Figure 1.6 Schematic diagram of directional well drilling

1.4.2 Food Processing

Food transportation within a plant using pipes often includes solids-in-liquid multiphase mixture flows. Non-Newtonian fluids carrying solid particles of size between 3-20 mm diameter and volume fraction as high as 60% may occur within food transportation and processing [29].

12

Sterilising a solids-liquid mixture is one application of multiphase flow. The typical continuous sterilisation plants consist of three main sections: heating, holding and cooling. The flow mixture is pumped into the heating section at an appropriate rate to bring it to a suitable temperature, and maintain it at this temperature long enough to ensure the required sterility [30].

Temperature control in sterilisation plants (see Figure 1.7) is very important to prevent excessive nutrient degradation and quality loss of the product. Particle motion in a fluid is complex as the particles may rotate and move radially within the holding tube which will affect the convective heat transfer between the particles, the liquids and the containing tubes. The convective heat transfer coefficient will be a function of the relative velocity between the flowing solids and liquid phases, commonly known as the slip velocity [29-32]. The size of any steriliser process required for a given thermal duty will be determined by two factors: (i) the rate of heating of the particles, which will be controlled by a combination of the interfacial heat transfer and thermal conductivity of the particles and (ii) the velocities of the solids and liquids which will affect both solids-liquid heat transfer coefficient and the residence time of both phases.
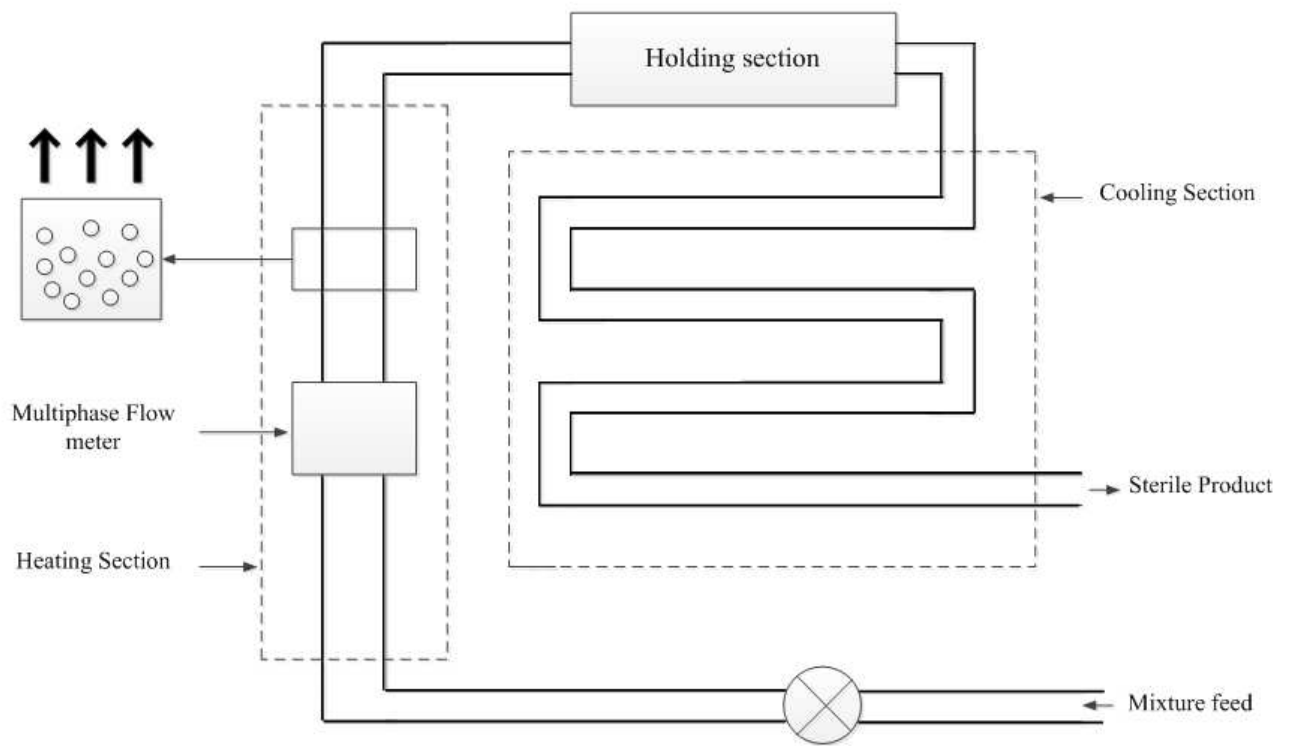
Figure 1.7 Schematic diagram of sterilisation plant

Based on the previous, it is very important to measure the velocity and volume fraction of both phases to control the heating process.

1.4.3 Mining Industry

In the mining industry, water is often used to carry important materials such as cement, coal, iron ore, cobalt, copper, manganese over long distances. Additionally, hydraulic transport is often used to carry the product to other sites either for further treatment or for shipping, see Figure 1.8.
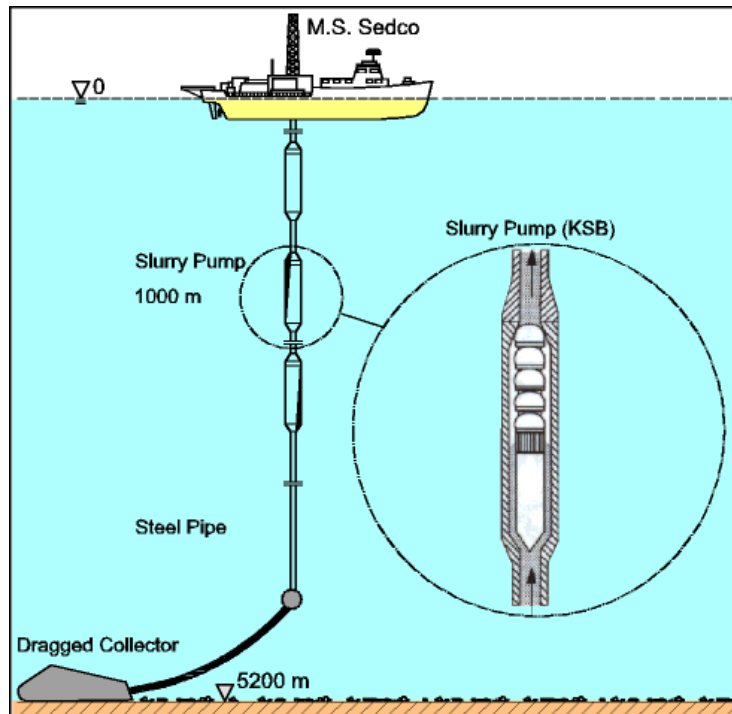
Figure 1.8 Deep sea mining system [33]

"Head loss" is considered one of the most important parameters especially in deep-ocean mining systems where it is plays an important role in the requirements of deep-sea mining hydraulic pumps and optimization of mining systems. Many factors such as fluid characteristics, space configuration of flexible hose and fluid−solid coupling affect the "head loss" [34].

Wang et. al. [34], studied the head loss of transport systems powered by a hydraulic pump. Based on the research results they concluded that to reduce the head losses and improve the efficiency of deep-ocean mining hydraulic pumps, sand volumetric concentrations C_v and mixture velocity v must be restricted to a suitable range (e.g. 10%−25% and 2.5−4 m/s respectively). Similar effects of the mineral content and the velocity of the internal fluid on the head losses were also reported by Wang et. al., [35]. Thus, measuring the volume fraction and velocity profiles for slurry in deep-sea mining is important in terms of increasing the efficiency of the hydraulic system.

15

1.4.4   Water Treatment

Water treatment (removing the solids from the solid-in-liquid flow) is one of the many applications involved in the water processing industry. Different treatments exist such as belt press separation and centrifugal filtering. Design of any separation system must consider all stages of pre-treatment, solids concentration, solids separation, and post-treatment. Pre-treatment is used when there is difficulty in filtering slurries and it involves changing the nature of the suspended solids by either chemical or physical means, or by adding a polymer to the suspension [36] where the polymer aggregates the suspended particles in the water. The quantity of polymer mass flow rate needed is related to the solids mass flow rate. Therefore, measuring the solids mass flow rate is very important to avoid unnecessary cost, which can reach millions of dollars, and to reduce the possibility of adding a polluting level of polymer to the water stream [37, 38].

1.5 Overall Research Aim

The overall aim of this research is to design and implement a novel non-intrusive two-phase flow meter which can be used in a non-uniform multiphase flow, e.g. solids-in-water flow, to measure the in-situ volume fraction distributions of both phases, the velocity profiles of both phases and the volumetric flow rates for both phases. Such a flow meter could potentially be used for the applications given in section 1.4. Ideally, this flow meter could be   i) low cost, ii) easy to use and iii) have no sophisticated algorithms needed to analyse the acquired data.

1.6 Objectives

The objectives for the current research are:

- Develop a flowmeter to measure the local solids and water volume fraction distributions, local solids and water velocity distributions and solids and water volumetric flow rates.

- Investigate suitable algorithms to analysie the data collected from the flow meter to obtain the distributions mentioned above.

- Integrate the flowmeter with a microcontroller unit to convert it to a standalone unit without a PC.

Chapter two gives details of previous measurement techniques for obtaining the global and local volume fraction and the global and local velocity of the dispersed continuous phases. Additionally, it is gives an overview of techniques currently used in commercial multiphase flow meters.

1.7 Contributions to Knowledge

The work contained in this thesis makes the following novel contributions to knowledge:

- Build and design the ICC device to measure the local solids fraction profiles, local solids velocity profiles and solids volumetric flow rate.

- Integrating the ICC device and EVP technique to give a two phase flowmeter for determining: (i) local solids and water volume fraction profiles, (ii) local solids and water velocity profiles and (iii) solids and liquid volumetric flow rates. It is believed that this last contribution represents a major step forward in two phase flow measurement for vertical and inclined (stratified) solids-in-water flows.

- The ICC/EVP system is considerably low cost, and have no sophisticated algorithms needed to analyse the acquired data. This latter feature enables the proposed system to avoid the error which could happen due to the reconstructed imaging process and hence increased the accuracy of the system.

- Development and demonstration of a new measurement methodology, Area Methodology, for analysing data collected from the ICC flow meter in vertical two phase flow at low dispersed phase volume fraction.

- Integration of the ICC device with a microcontroller, converting it to a stand-alone unit capable of measuring the solids volume fraction distributions through the pipe cross-section.

2. CHAPTER 2: Literature Review

2.1 Introduction

The need for a reliable method to accurately measure multiphase flow parameters has motivated research for about the last 25 years. Multiphase flows are defined as the simultaneous flow of two or more phases in direct contact in a given system. A solids-liquid flow is a multiphase flow where a solids phase, such as particulate sand, and a liquid phase, such as oil or water, are present. Multiphase flows can be any combination of flowing phases, e.g. gas-liquid, gas-solids, liquid-solids and gas-liquid-solids. Additionally, multiphase flows may also have more than one component of the same phase, e.g. liquid-liquid, such as oil and water [39].

Based on the declared needs of industry and the expertise, equipment and laboratory space available at the University of Huddersfield, the current investigation will be on the measurement of volume fraction and velocity distributions in two-phase solids-in-liquid flow.

The present literature review will concentrate on the techniques used in non-nuclear-based systems i.e. electrical, differential pressure and electromagnetic.

2.2 Multiphase Flow Measurement Methods

2.2.1 Differential Pressure Devices

Differential pressure (DP) devices have been widely used in multiphase flow metering and have been described by many authors [40-48]. DP devices include orifice plates, nozzles, V-cones and Venturi meters. Provided the instrument can be properly calibrated, with reproducible upstream flow conditions and steady flow, a good degree of accuracy can be obtained. It is simple in operation, easy to handle and of low cost.

A simple differential pressure measurement in a straight pipe is non-invasive and can provide a measurement of the mean fluid density ρ_m in vertical and inclined pipes in multiphase flow. Assuming that the lines connecting the tapping to the DP cell are water filled, the pressure drop ΔP across pressure tappings is given as [44, 45, 49-54]:

$$\Delta P = \rho_m gL\cos\theta + F - \rho_w gL\cos\theta \qquad \text{Equation 2-1}$$

$$\frac{\Delta P - F}{gL\cos\theta} + \rho_w = \rho_m \qquad \text{Equation 2-2}$$

where F is the frictional pressure loss between the pressure tappings, L is the separation of the pressure tappings, ρ_m is the mixture fluid flow density, ρ_w is the water density, g is the acceleration due to gravity and θ is the angle of inclination from the vertical. And so from Equation 2-1 the mixture fluid flow density ρ_m can be obtained from the pressure drop ΔP. The frictional pressure loss F is determined using the Darcy-Weisbach equation as [54]:

$$F = \frac{2\rho_w L\cos\theta \, f_P \, U_h^2}{D} \qquad \text{Equation 2-3}$$

where the pipe friction factor f_P depends solely on the pipe Reynolds Number ,U_h is the mean flow velocity and D is the working-section.

In the current investigation, the mixture fluid flow density ρ_m is used to obtain the reference solids volume fraction α_s for flows in vertical and inclined pipes as shown in Equation 2-4:

$$\rho_m = \alpha_s \rho_s + (1-\alpha_s)\rho_w \qquad \text{Equation 2-4}$$

where α_s is the mean solids volume fraction and ρ_s is the solid density. The detailed theory of DP technique is given in Section 6.3.2.

2.2.2 Electrical Conductance Techniques

The Electrical Conductance (EC) method has been developed to measure the dispersed phase volume fraction and dispersed phase velocity in two- or three-phase systems. The EC technique measures the electrical conductivity of a mixture, such as solids-in-water flow and oil-in-water flow, usually assuming that the solids (or oil) represent a non-conductive phase and the water present represents a continuous conductive phase. Based on the measurements of the fluid conductivity, the volume fractions for both phases and the velocity of the dispersed phase can be determined, see 2.2.2.2. These types of flow meters offer a high frequency response with a low initial cost.

The relationship between the dispersed phase volume fraction α_d and the fluid conductivity can be expressed according to Maxwell's relationship [55] as:

$$\frac{\sigma_m - \sigma_w}{\sigma_m + 2\sigma_w} = \alpha_d \frac{\sigma_d - \sigma_w}{\sigma_d + 2\sigma_w} \qquad\qquad \text{Equation 2-5}$$

where σ_m is the measured conductivity of the mixture, σ_w is the conductivity of water only and σ_d is the conductivity of the dispersed phase. Equation 2-2 assumes that the particles are uniformly sized spheres and are in an ordered arrangement at a low volume fraction so that the electrical field around each particle is unaffected by other particles present in the flow. In the current study non-conducting spherical plastic beads of 4 mm diameter were used as the dispersed phase. Thus σ_d in Maxwell's relationship is effectively zero and Equation 2-5 reduces to:

$$\sigma_m = \sigma_w \frac{2(1-\alpha_d)}{(2+\alpha_d)}$$

Equation 2-6

Equation 2-6 can be re-arranged in the term of the dispersed phase volume fraction as:

$$\alpha_d = \frac{2\sigma_w - 2\sigma_m}{2\sigma_w + \sigma_m}$$

Equation 2-7

Cory [56] reported a wide range of formulas used by different researchers to measure the dispersed phase volume fraction, these formulas varied according to the diameters and shapes of the particles forming the dispersed phase and volume fraction. However, Cory used the relation shown in Equation 2-7.

2.2.2.1 Global Volume Fraction Measurement

Various researchers [57-60] have shown that many different electrode arrangements can be used for successful solids/oil volume fraction global measurement, see Figure 2.1.

Figure 2.1 (a) represents a two phase flow meter with a single sensor comprising two ring electrodes separated by a fixed axial distance L. This type of flow meter is used to measure the global volume fraction only for the dispersed phase in continuous conductive phase. While Figure 2.1 (b) represents a two phase flow with two sensors and each sensor containing two electrodes. This type of flowmeter is used to measure the global volume fraction and the global velocity for the dispersed phase in continuous conductive phase.
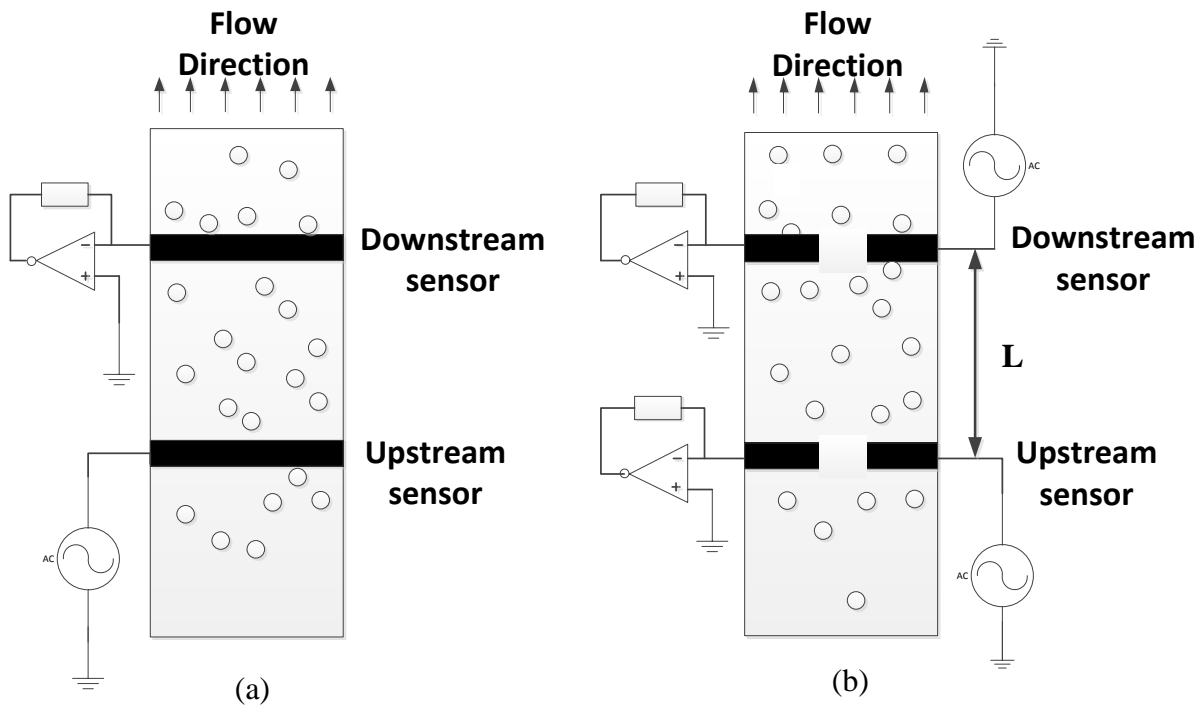
Figure 2.1 Different electrode arrangements in Electrical conductance probe

As shown in Figure 2.1 the flush mounted electrodes are fully in contact with the conductive continuous phase. The global measurements are correct only when the flow is fully developed and has uniform velocity profile and uniform volume fraction profile for both phases [57-60]. In order to measure the phase volumetric flow rates with higher accuracy in highly non-uniform flow in inclined two phase flow (refer to Figure 2.4 and Figure 2.7), the non-uniform volume fraction distributions for both phases and the non-uniform distributions velocity for both phases are required, see section 1.3.2.

2.2.2.2 Local Volume Fraction Measurement Using Conductance Techniques

Lucas and Cory [54] used a 6 electrode local probe to measure the solids velocity distribution and solids volume fraction distribution in vertical and inclined solids-in-water flows, see Figure 2.2. These distributions were obtained by traversing the local probe throughout the flow cross section. A homogenous mixture of solid beads, (mean solids diameter 4 mm and density 1340

kgm^{-3}), and water was pumped into 80 mm ID pipe line working section. The mean solids

volume fraction $\overline{\alpha}_s$ in these experiments reached 0.3.
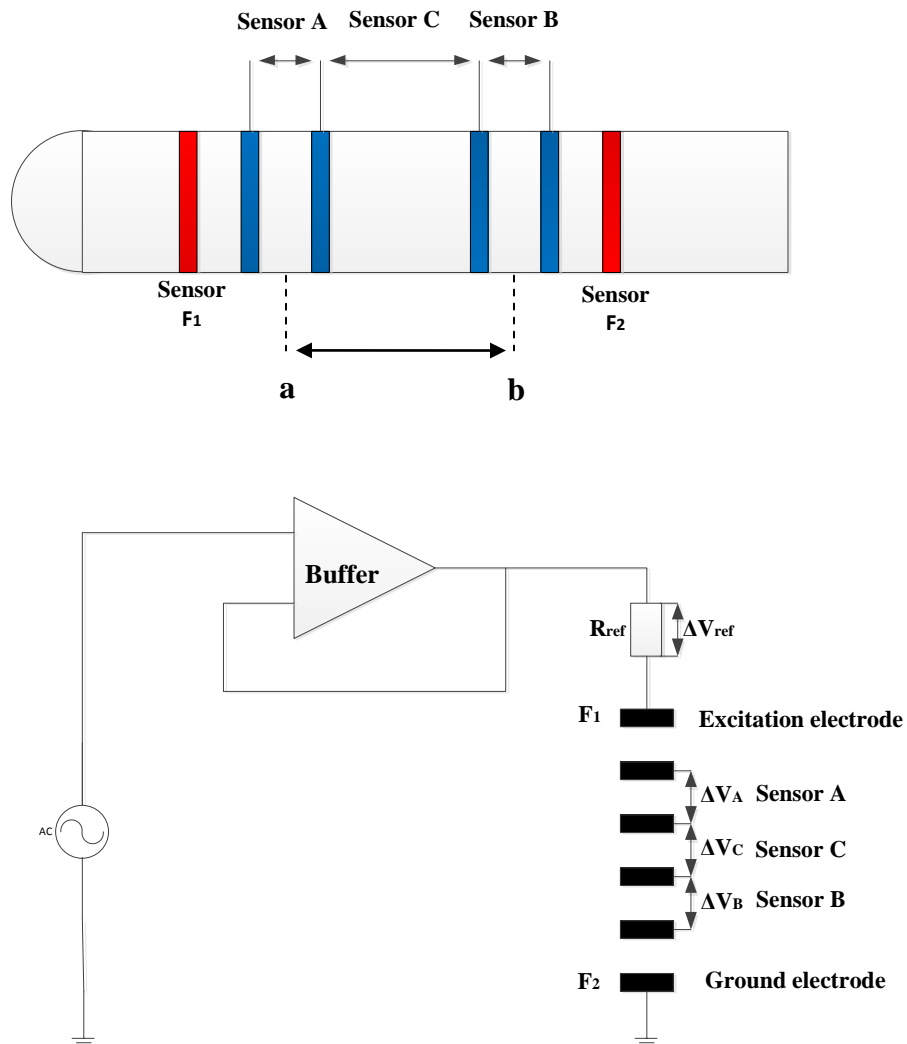
Figure 2.2 The 6-electrodes local probe

Sensor C in the 6 electrodes probe was used to measure the changing in the electrical conductivity of a mixture. Where the mixture conductivity σ_m is obtained using Equation 2-8:

$$\frac{\sigma_m}{\sigma_w} = \left(\frac{V_{ref}}{V_C}\right)_m \left(\frac{V_C}{V_{ref}}\right)_w \qquad \text{Equation 2-8}$$

Based on Maxwell's relationship, the local solids volume fraction distribution is obtained by substituting Equation 2-8 into Equation 2.7.

According to Cory, solids volume fraction α_s profiles in vertical flow show only small variations across the flow cross-section. While in pipes inclined at 30 degrees to the vertical α_s varied strongly from the lower side of pipe being much higher than on the upper side, see Figure 2.3 and Figure 2.4 .
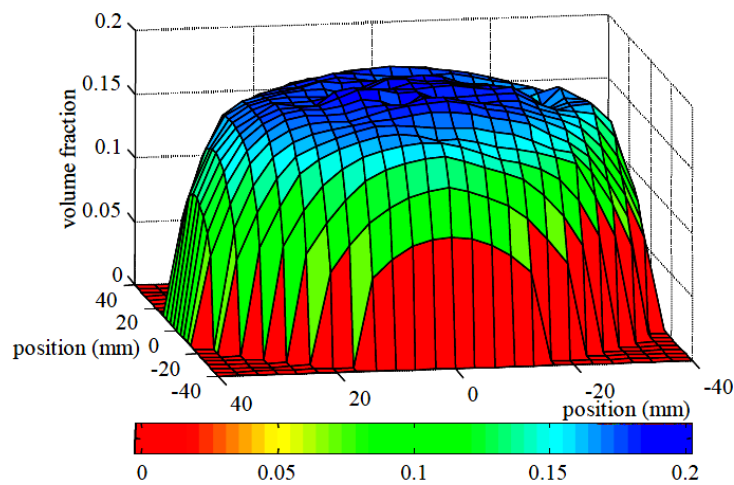
Figure 2.3 The solids volume fraction distribution in a vertical pipe measured by electrical conductance probe, solids –in-water flow [56], the coloured bar represents the magnitude of the solids volume fraction

25
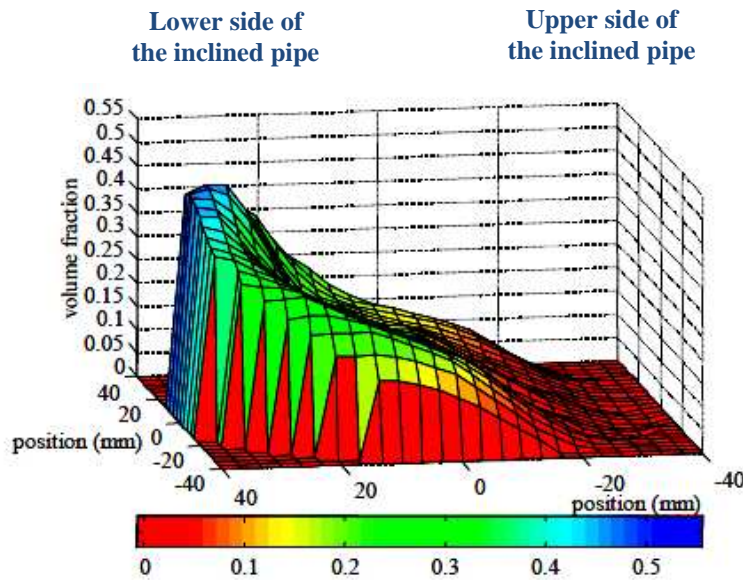
Figure 2.4 Solids volume fraction distribution in pipe inclined at 30 degree to the vertical measured by electrical conductance probe for solids –in- water flow [56], the coloured bar represents the magnitude of the solids volume fraction

These flow profiles show qualitative agreement with previous results reported [13, 61, 62].

Using the cross correlation technique, see section 2.2.2.3, sensor A and sensor B were used to measure the time travel τ of the solids passing two points (a and b) spaced along the direction of flow. The profiles of the solids velocity distribution obtained by Cory can be seen in Figure 2.6 and Figure 2.7.

2.2.2.3 Velocity Measurement Using Electrical Conductance Techniques

Cross correlation has been used for flow velocity measurement by a wide variety of researchers [54, 63-67]. The basic principle of cross correlation flow metering is to measure the time of travel of a disturbance passing two points spaced along the direction of flow. The output voltages from the upstream and downstream sensors represent the electrical conductivity of the fluid mixture flow inside the pipe. The electrical conductivity fluctuations are caused as the dispersed phase passes through the upstream sensor and then the downstream sensor as shown Figure 2.5.
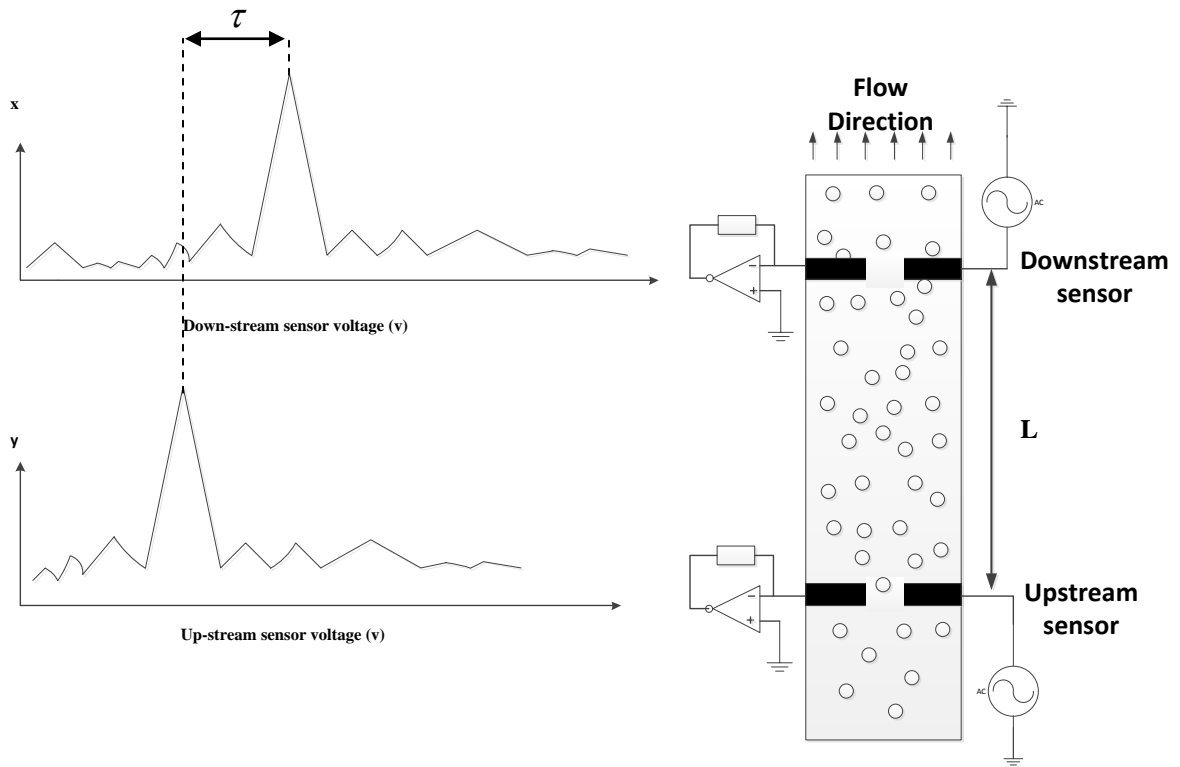
Figure 2.5 Electrical conductivity fluctuations in upstream and downstream sensors

The output voltages from the sensors changes according to these conductivity fluctuations. The time delay between these changes in output signal is approximately equal to the time taken for the particle to travel between the sensors. In order to calculate the time delay, the cross correlation function is calculated from a long record of data from the sensor using the following formula:

$$\hat{R}_{xy}(\tau) = \frac{1}{T} \int_0^T x(t)\,y(t+\tau)\,dt$$

Equation 2-9

Where T is the time period over which the signals $x(t)$ and $y(t)$ are sampled, and τ is the relevant time delay. Note that the cross correlation function has a maximum value at the time

delay τ such that $x(t)$ and $y(t+\tau)$ are well matched. Using τ, the velocity of the dispersed phase is calculated as:

$$v = \frac{L}{\tau}$$ Equation 2-10

Figure 2.6 and Figure 2.7 shows the solids velocity distributions obtained by Cory using the 6 electrode local probe [25], the results show that for vertical flow the solids velocity v_s has small variation across the central portion of the pipe cross section.
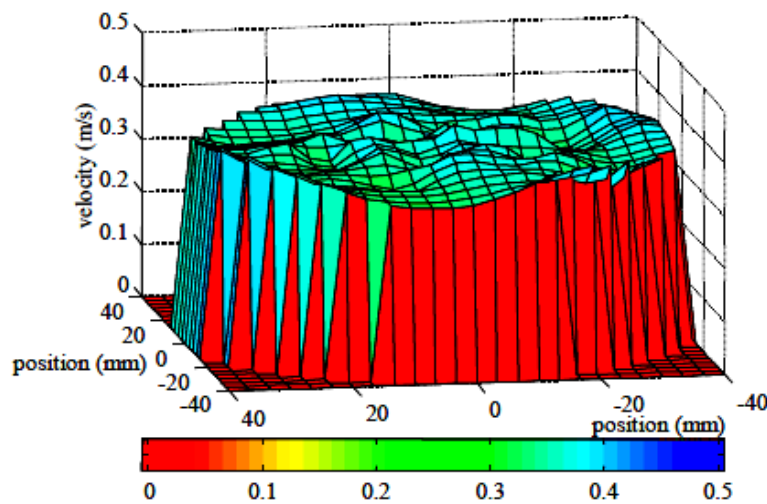
Figure 2.6 The solids velocity distribution in vertical pipes measured by cross-correlation for solids –in- water flow[56], the coloured bar represents the magnitude of solids velocity
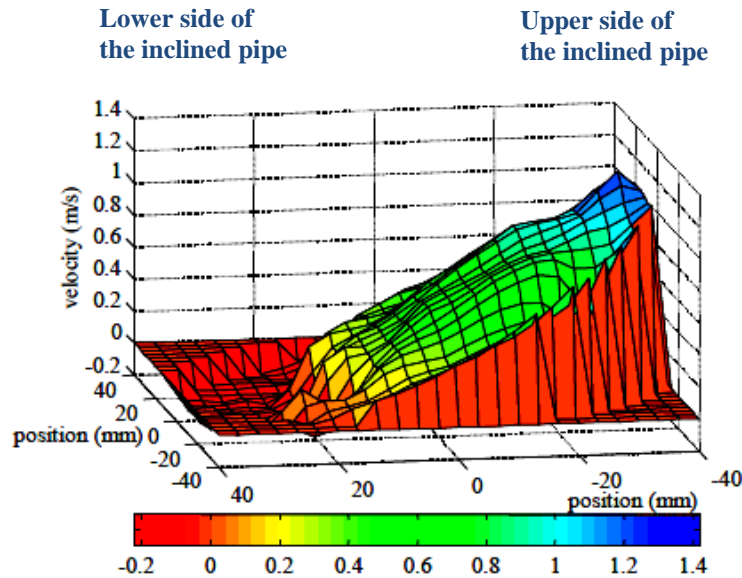
Figure 2.7 Solids velocity distribution in pipes inclined at 30 degree to the vertical measured by cross-correlation for solids-in-water flow [25], the coloured bar represents the magnitude of solids velocity

In inclined flow, the velocity at the lower side of the inclined pipe can be negative and a reverse flow can occur, see Figure 2.7. However moving towards the upper side of the pipe the velocity becomes positive. The results of Cory's experiments show a similar behaviour to the results obtained by visual observation and by a high speed camera. Additionally, these results shown qualitative agreement with results reported by [49-51].

2.3 Tomographic Imaging Techniques

Process Tomography is a non-invasive measurement technique used to provide the concentration, or density distribution and/or velocity distribution of at least one phase of a multiphase system. Tomography imaging techniques generally can be divided into two main systems [3]:

1. Nuclear-based imaging systems using either ionising radiation, such as gamma-rays and X-rays, or non- ionising imaging techniques such as nuclear magnetic resonance imaging.

2. Non-nuclear – based systems which use electrical (resistance or capacitance), optical, ultrasonic or microwave techniques.

This literature review of tomography techniques concentrates on the non-nuclear – based electrical techniques (resistance and capacitance) and the impedance cross correlation technique.

2.3.1 Electrical Resistance Tomography

Electrical Resistance Tomography (ERT) is a non-intrusive technique used to map the flow conductivity across the interior of a flow pipe. In ERT systems the electrodes are mounted around the pipe circumference and are in direct contact with the flow, refer to Figure 2.8. An electrical current is injected into the flow between pairs of electrodes and the resulting potential distribution is measured between other electrode pairs. The larger the number of sources and receivers the higher spatial resolution of the image produced.
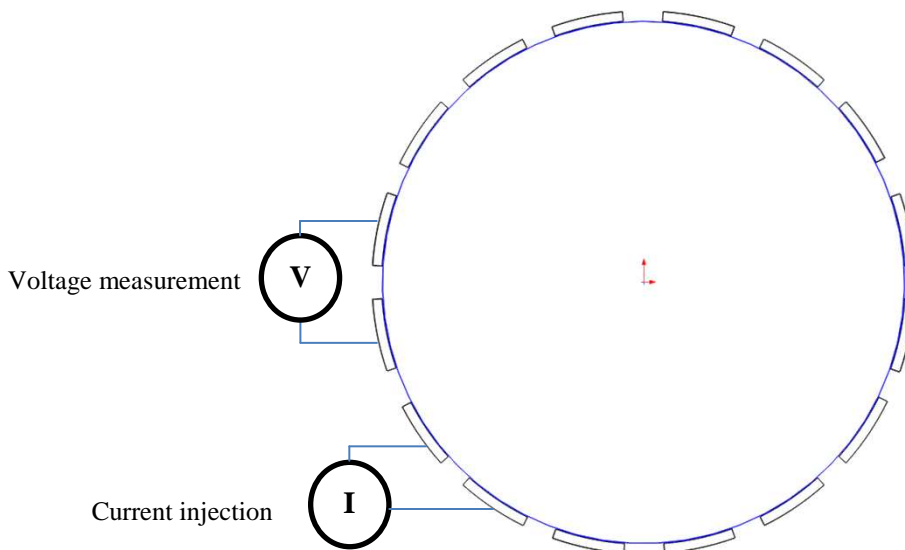
Figure 2.8 ERT 16-electrode system

The governing equation for the most of ERT systems can be expressed as [68]:

$$\nabla . [\sigma(x, y) \nabla \phi(x, y)] = 0 \qquad\qquad \text{Equation 2-11}$$

where $\sigma(x,y)$ is the conductivity distribution in the sensing field and $\phi(x,y)$ is the electrical potential distribution.

The number of voltage measurements depends on the number of electrodes mounted in the ERT array, for example, there are $M = n(n-1)/2$ independent pairs of voltage measurements for n electrode sensors. That means there are M equations in the form of Equation 2-8. which shown the relationship between the jth voltage measurement $\Delta\phi_j$ on the boundary for a small conductivity change $\Delta\sigma_i$ in the ith pixel as follows [68]:

$$\Delta\phi_j = \sum_{i=1}^{P} - S_{i,j}\Delta\sigma_i \qquad \text{Equation 2-12}$$

Here $S_{i,j}$ is a normalised sensitivity coefficient relating changes in the conductivity in the ith pixel to changes in the jth boundary voltage measurement ($j = 1,2,..M$) and P is the total number of pixel in the flow cross-section.

Equation 2-12 can be re-written in the form of a matrix as:

$$[\Delta\phi] = -[S][\Delta\sigma] \qquad \text{Equation 2-13}$$

where ϕ is a boundary potential difference matrix, S is the sensitivity matrix and σ is the conductivity matrix. The negative sign indicates that the boundary voltage measurements decrease as the conductivity increases. Equation 2-10 can be re-arranged to reconstruct the conductivity matrix σ [68]:

31

$$[\Delta\sigma] = -[S]^{-1}[\Delta\phi]$$

Equation 2-14

ERT has difficulties of soft-field phenomena and an ill-conditioned sensitivity matrix, it therefore requires a huge amount of computing power to accurately reconstruct the conductivity image using iterative algorithms [63–65].

From the conductivity distribution obtained by ERT, the local dispersed phase volume fraction α_d can be obtained using Maxwell's relationship, Equation 2-7.

Dual-plane ERT can be used also to determine the dispersed phase velocity by adding a second plane (plane a) with a known axial distance L from the first plane (plane b), see Figure 2.9. By using point-by-point cross correlation techniques, the dispersed phase velocity distribution can be obtained in multiphase flows in which the continuous phase is electrically conducting [9].
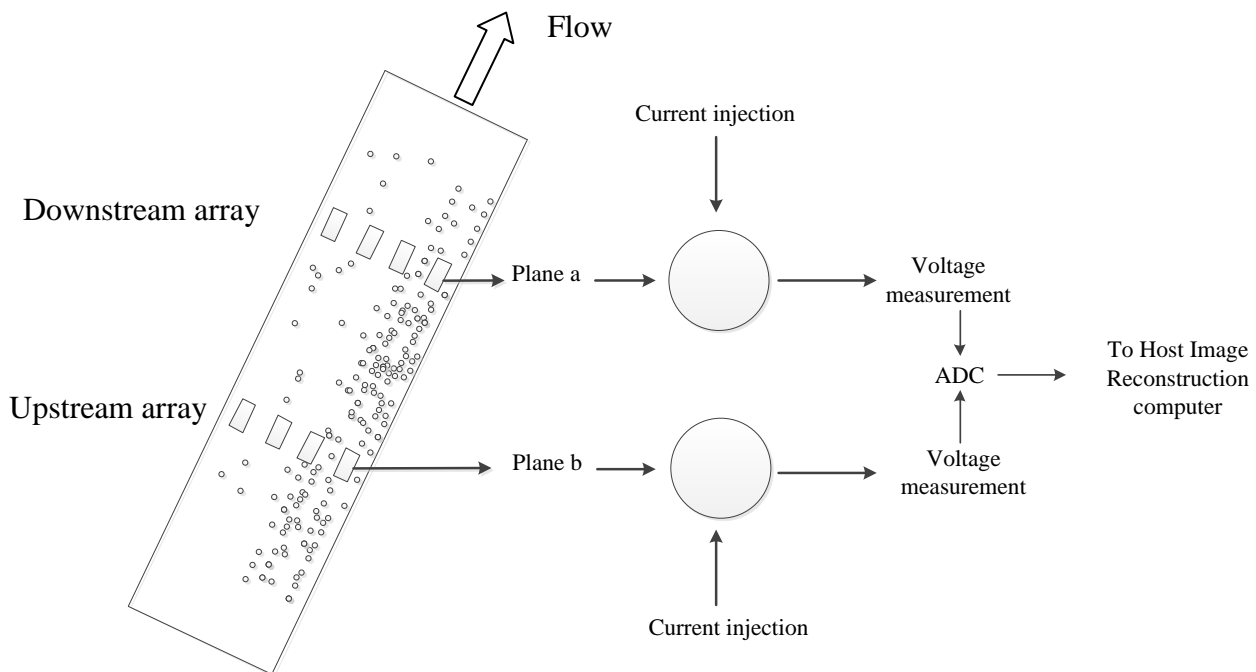
Figure 2.9 Dual- Plane Electrical Resistance Tomography

The continuous time domain correlation function in Equation 2-9 can be expressed in discrete form as:

$$\hat{R}_{xy,n}(p) = \frac{1}{N}\sum_{k=0}^{T-1} b_n(k)a_n(p+k)$$

Equation 2-15

where $\hat{R}_{xy,n}(p)$ is the cross correlation function for a frame delay p and pixel index n, T is the number of cross-sectional images for which $\hat{R}_{xy,n}(p)$ is calculated, $b_n(k)$ and $a_n(p+k)$ are the conductivity values obtained from upstream sensor b (associated with n^{th} pixel from image k) and downstream sensor a (associated with n^{th} pixel from image p+k) respectively.

The cross correlation peak $[\hat{R}_{xy,n}(p)]_{max}$ occurs at frame number $p_{n,max}$. Hence, the axial velocity for the dispersed phase in n^{th} region is given as:

$$(v_p)_n = \frac{L}{[P_{n,max}]\tau_{samp}}$$

Equation 2-16

where τ_{samp} is the time interval between successive pairs of frames.

The point-by-point cross correlation technique is based on the assumption that flow trajectories in planes a and b are parallel to each other and perpendicular to the sensor planes. However, this assumption ignores the fact that the flow trajectories of dispersed phase exhibit a complex three-dimensional behavior [9]. To over-come this problem , the signal from one pixel in plane b is somehow better correlated with the a signal from a non-axially corresponding pixel on the plane a [9]. The pixel from plane a is chosen from the axially corresponding pixel and its neighbours, This method of known as Best Pixel Correlation, Figure 2.10.
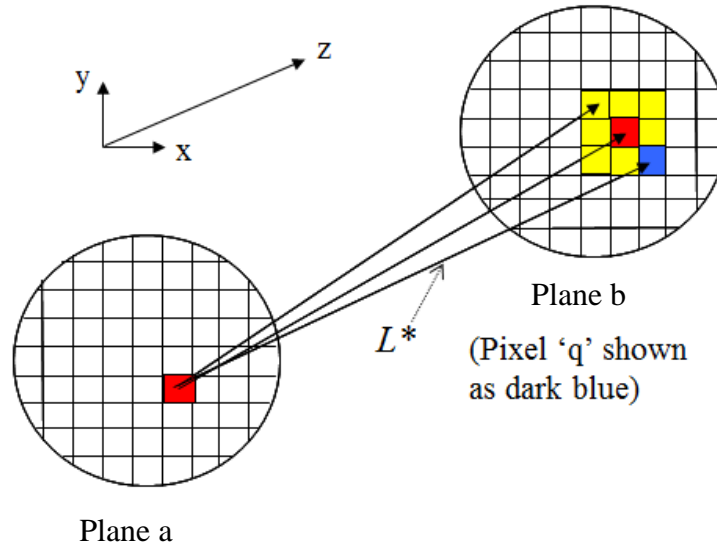
Figure 2.10 ERT Best Pixel Correlation to obtain axial flow velocity

The maximum value of the normalised cross correlation function $(\hat{R}_{ba,n,j})_{max}$ of $\hat{R}_{ba,n,j}$ is determined for all j (where values of j are in the range $n+1$, $n+2$, $n+3$,…, and represent pixels in the immediate vicinity of the nth pixel in plane b). The pixel in plane a for which $(\hat{R}_{xy,n,j})_{max}$ has the greatest value (pixel q) is assumed to be the location where dispersed particles from pixel n in plane b predominantly arrive at when reaching plane a [9].

The x and y coordinates of pixels n and q enable a unit vector in the direction of the local dispersed phase velocity at n to be determined. Thus, the magnitude of the local dispersed phase velocity $(v_p)_n$ at n is given by[9]:

$$(v_p)_n = \frac{L^*}{\tau_{p,q}}$$

Equation 2-17

where $\tau_{p,q}$ is the transit time of the flow signature passing the two sensing planes b and a. $\tau_{p,q}$ is calculated from the sampling time and the appropriate number of frames.

34

2.3.2   Electrical Capacitance Tomography

Electrical Capacitance Tomography (ECT) is also a non-intrusive technique used by many researchers [68-80] to measure the spatial distribution of a dielectric phase inside multiphase flow. This technique is based on measuring the capacitance between the sensing electrodes mounted around the pipe circumference and converting these measurements into an image of the permittivity distribution using a suitable algorithm. A typical ECT system contains three main units: a multi-electrode sensor, sensing electronic circuits to measure the capacitances for all possible electrode configurations, electrode switching circuit and a PC unit for hardware control and data processing, refer to Figure 2-11.
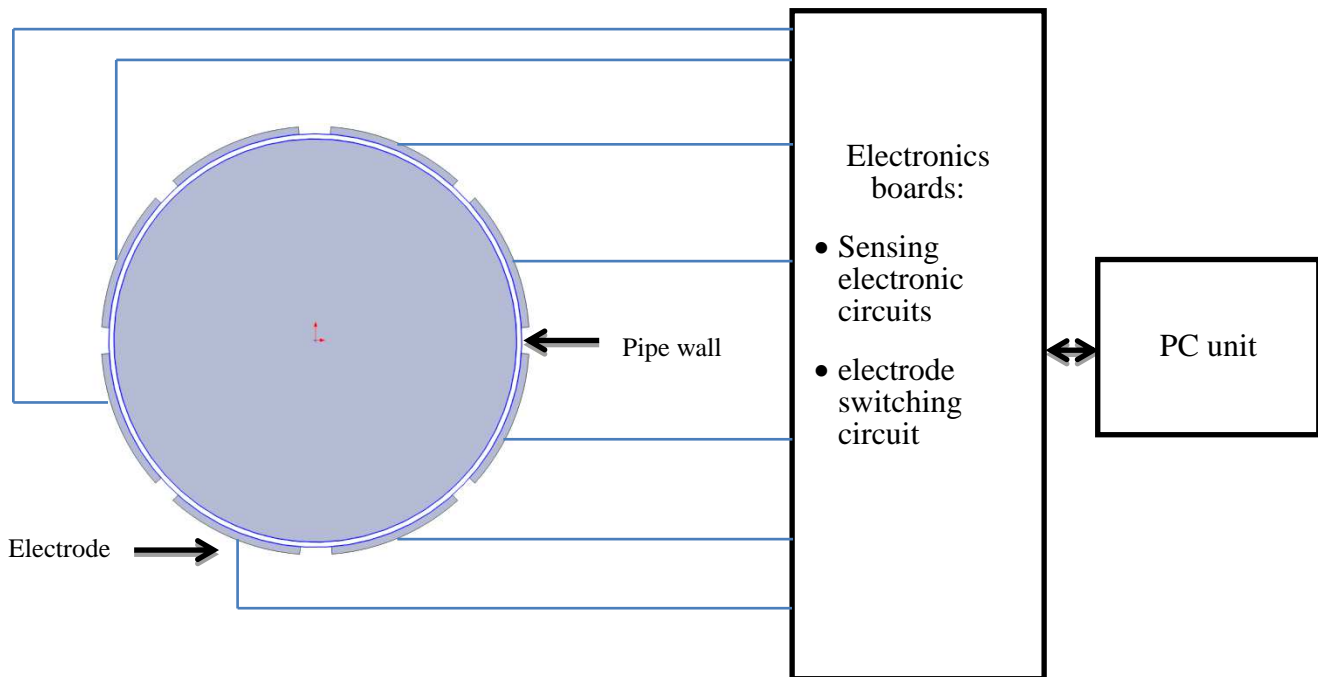
Figure 2.11 8-ECT electrode system

The governing equation for an ECT system can be expressed as [68]:

$$\nabla.[\varepsilon(x, y)\nabla\phi(x, y)] = 0 \qquad\qquad \text{Equation 2-18}$$

where $\varepsilon(x, y)$ is the permittivity distribution in the sensing field and $\phi(x, y)$ is the electrical potential distribution.

Similar to ERT, the number of capacitance measurements M depends on the number of electrodes mounted in the ECT array. The limitation of the number of capacitance measurements M often leads the sensitivity matrix to be ill-conditioned which generates measurement error and noise.

To reduce the above difficulties, a number of reconstruction algorithms have been developed. Yang and Peng [78] reviewed the most common reconstruction algorithms and categorized them into two groups: non-iterative (or single step) and iterative algorithms. They concluded that currently, most algorithms used in ECT systems are based on a simplified linear mathematical model. However, because ECT systems are essentially non-linear [78], future investigation is needed for nonlinear techniques for both forward problem modelling and image reconstruction.

ECT is used industrially to measure the concentration distribution of the dielectric materials (oils, plastics, minerals etc.) in multiphase flow systems [81]. The concentration distribution is measured and captured at high frame rates. The cost of ECT systems vary from £12,500 for a basic single plane version to as much as £65,000 for a high-speed two phase flow measurement system [81].

Since both ERT and ECT systems are governed by similar partial differential equations, the reconstruction algorithms for both tomographic techniques have many similar features. More details about reconstruction algorithms in ERT and ECT systems can be found in Dyakowski et al., [82] which presents a review of electrical tomography (ERT and ECT) systems for the investigation and monitoring of gas-in-liquid and solids-in-liquid flows.

This review includes explanations of the methods of measurements and reconstruction algorithms for both ERT and ECT systems.

2.3.3 Impedance Cross-Correlation Device

The Impedance Cross-Correlation (ICC) device is non-intrusive device developed by Lucas and Al-Hinai [49-51] to measure the local mixture conductivity in different regions of the flow cross-section. This ICC device consists of two arrays of electrodes separated by an axial distance of 50 mm. Each array contains eight electrodes. The ICC device is similar to ERT systems, however it has lower implementation cost and needs no sophisticated algorithms to analyse the acquired data.

Based on Maxwell's relationship (Equation 2-4), the ICC device uses variations in the local conductivity to estimate the local dispersed phase volume fraction distribution. Additionally, from the variations in the local conductivity of the mixture at two axially separated locations the ICC is able to measure the local velocity distribution of the dispersed phase using the cross correlation method. Using the distributions of the local dispersed phase volume fraction (α_d) and local axial velocity (v_d) , the dispersed phase volumetric flow rate can be estimated as shown by the following equation:

$$Q_d = \sum_{i=1}^{n} (\alpha_d)_n (v_d)_n A_n \qquad\qquad \text{Equation 2-19}$$

where A_n is the area of nth pixel.

ICC devices can be applied to measure the dispersed phase in flows such as gas-in-water, oil-in-water and solids-in-water.

Al-Hinai used an ICC device in solids-in-water flow using three inclinations; 0°, 15° and 30° to the vertical [49].The results for the solids volume fraction distributions and solids velocity distributions showed similar shape profiles as the results obtained by Cory [54, 56].

2.3.4   Summary of the Tomographic Techniques

The theory of tomographic techniques is based on measuring the distribution of a local physical property of flow and relating it to the dispersed phase volume fraction. The number of measurements depends on the number of the sensors mounted around the pipe, these measurements are taken around and across the pipe depending on the chosen electrode configurations. After measurements have been obtained, the local properties of the flow cross-section can be determined using a reconstruction algorithm, refer to Figure 2.12.

Multiple measurements

Reconstruction algorithm
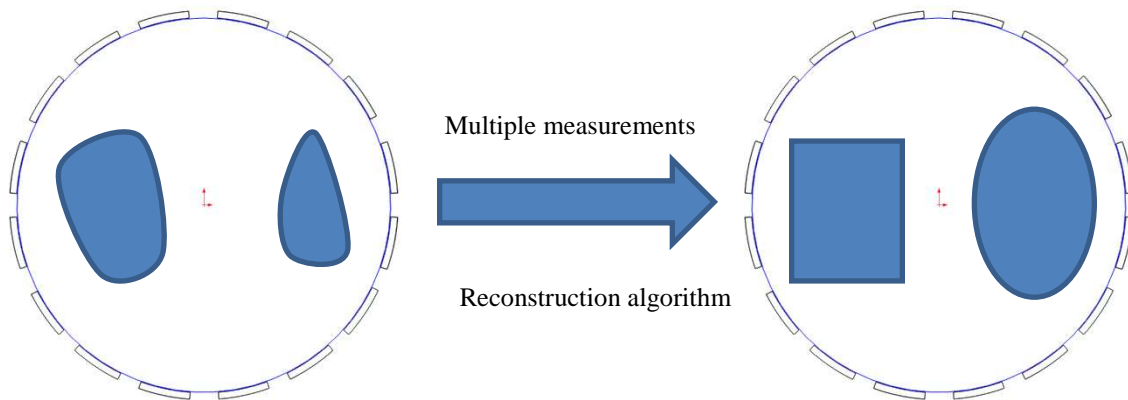
Figure 2.12 Principle of reconstruction in tomography technique

As shown in Figure 2.12, the reconstructed image does not necessarily represent the real distribution of the dispersed phase inside the pipe. The differences are due to the fundamental physics of the tomographic technique which depends on whether "hard-field" or "soft-field" tomography is used. In soft-field tomographic techniques, the sensing field distribution depends on the distribution of physical properties inside the medium and requires intensive computational

power for imaging reconstruction. However, the hard-field techniques, i.e gamma-ray measurements method, is considerably less complicated than the "soft-field" due to a line-of-sight between the emitter of the energy waves and the sensors[87].

In general, electrical process tomography such as ECT and ERT systems use the "soft-field" measurement technique, and thus requires intensive and expensive computational power to reconstruct the image.

2.4 Electromagnetic Flow Meter in Multiphase Flow

The Electromagnetic Flow Meter (EMFM) has been used successfully for over 40 years to measure the velocity of an electrically conducting fluid in single phase flow. The electromagnetic flow meter is based upon Faraday's Law, which states that the voltage induced across any conductor as it moves at right angles through a magnetic field is proportional to the velocity of that conductor. For axisymmetric flow, the electrical potential difference U between electrode A and electrode B (refer to Figure 2.13) can be written as the following equation [39]:

$$U = \bar{v} B D \hspace{5cm} \text{Equation 2-20}$$

where $\bar{v}$ is the mean velocity of the conductor fluid, B is the density of magnetic flux and D is the internal pipe diameter.
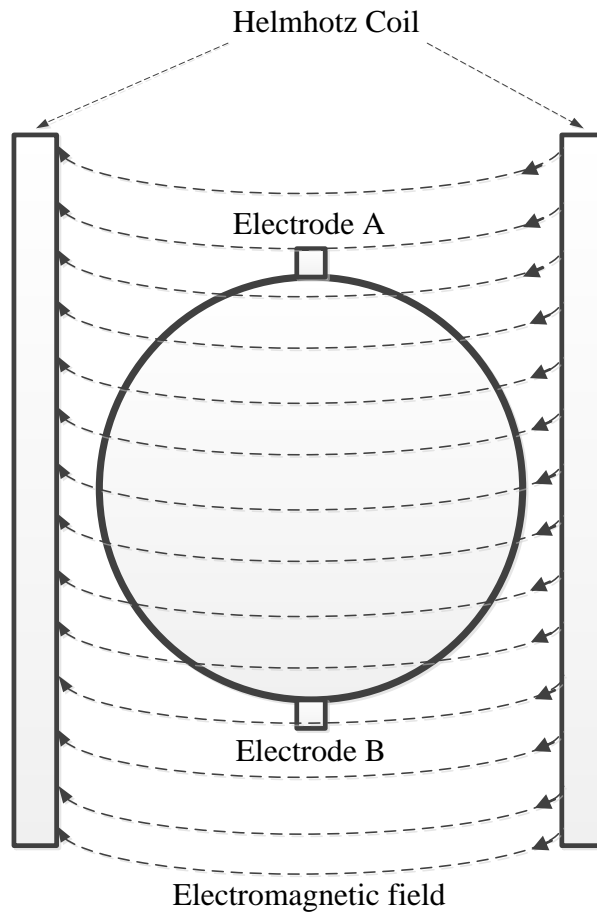
Figure 2.13 Schematic diagram for electromagnetic flowmeter, dashed lines represent the magnetic field direction

The liquid volumetric flow rate Q_l in a single phase flow can be calculated as:

$$Q_l = \bar{v}\frac{\pi D^2}{4}$$

Equation 2-21

By combining Equation 2-20 and Equation 2-21, the relation between the liquid volumetric flow rate Q_l and the measured electrical potential difference U can be written as:

$$Q_l = U\frac{\pi D}{4B}$$

Equation 2-22

The accuracy of the measured volumetric flow rate depends on the axial symmetry of the fluid velocity profile. Thus, the accuracy of the volumetric flow rate given by Equation 2-21 can be reduced in the case of non- axisymmetric velocity profiles. Due to this limitation, the majority of manufacturers' guidelines recommend that the MFMF be installed with a straight run in of upstream pipe of adequate length, (e.g. at least five pipe diameters away from any flow disturbance such as a bend), to achieve fully developed velocity profiles [83].

Some thirty years ago, Bernier and Brennen [84] investigated the use of electromagnetic flow meters in two-phase flows. They concluded that a homogeneous two-phase flow e.g. bubbly flow would give rise to a potential difference ΔU_{TP} as :

$$\Delta U_{TP} = \frac{\Delta U_{sp}}{(1-\alpha)} \qquad\qquad \text{Equation 2-23}$$

where ΔU_{sp} is the potential difference that would be if the liquid flowed on its own and α is the new void fraction of the second, non-conducting phase. Based on Equation 2-23, the potential difference ΔU_{TP} can be defined according to the fluid volumetric flow rate Q_l as:

$$\Delta U_{TP} = \frac{4BQ_l}{\pi D(1-\alpha)} \qquad\qquad \text{Equation 2-24}$$

Measurement of ΔU_{TP} allows the liquid flow rate to be found (assuming $\overline{\alpha}$ is known) but it does not provide the local axial velocity distribution. EMFMs using the above measurement principle are correct only when the flow is fully developed and has uniform velocity profile and uniform volume fraction [85-87]. Therefore, this measurement technique will not be sufficient for highly non-uniform volume fraction for both phases and highly non-uniform velocity for continuous phase as occur in inclined two phase flow (refer to Figure 2.4 and Figure 2.7).

To avoid these limitations, many researchers have tried to developed a multi-electrode electromagnetic flow meter to obtained more accurate mean velocity measurements [83, 87-96]. These devices obtain the continuous phase velocity profiles through the pipe cross-section using suitable signal processing of the electrical potential difference distribution on the non-conducting boundary. Horner [89, 90] designed a 16 electrode electromagnetic flow meter device to measure the fluid velocity over the pipe cross-section. He concluded that conventional two-electrode EMFM devices perform accurately with axially symmetric flow but produced unacceptable error if there are severe flow distortions, e.g. downstream of bends and valves as reported by Wang et al., [65]. Horner also states that the error in velocity measurements is reduced and the accuracy of measurements increased by increasing the number of electrodes and using two perpendicular magnetic fields.

Leeungculsatien et al., [87, 95, 97] investigated water velocity profiles in water flow and solids-in-water two-phase flows using an Electromagnetic Velocity Profiler (EVP). The EVP consisted of a non-conducting pipe wall with an array of eight electrodes fitted flush with the inner pipe wall and which are spaced equally around the 80 mm ID pipe (refer Figure 6.9).

EVP is based on existing electromagnetic flow meter theory and is used to obtain the local axial water velocity distribution in the flow cross-section.

2.5 Review of Commercial Multiphase Metering Systems

Research projects in the early 1980's resulted in the first commercial Multiphase flow meters focused on applications for the oil and gas industry [3]. The metering of multiphase flows depends on successfully combining two or more measurement technologies and techniques such as electromagnetic, DP and Cross-correlation to obtain flow velocities. The typical accuracy of the current in-line flow meters for multiphase flow measurements are around ±10% for each

individual phase. Different measurements techniques were used in MFMs to measure the parameters of the multiphase flow and the phase characteristics [98].

This section presents a review of some commercial multiphase flow meters used or tested in gas and/or oil production. In the following review, it's worth defining the terms used to avoid confusion and ambiguity:

- Absolute error: result of a measurement minus a true value of the measurand.

- Relative error: absolute error of measurement divided by a true value of the measurand.

- Water cut: is the ratio of the water produced compared to the total volume of the liquids produced.

- water in liquid ratio (WLR): is the water volumes flow rate relative to the total liquid volume flow rate.

2.5.1   Roxar Multiphase Meter, MPFM 2600:

In February 2009, Roxar launched its third generation multiphase flow meter based on its new ZectorTM technology [99]. The MPFM2600 is based on a combination of systems such as the venturi meter to measure the total volumetric flow rate, density measurements (gamma system required when the gas volume fraction is above 90%) and capacitance sensor technology to measure the mean volume fraction in the flow cross-section and local volume fraction. In addition, the mean axial velocity of the dispersed phase is obtained using a cross-correlation technique. The operating range of the MPFM2600 is between 0-100 % water in liquid ratio (WLR) and 0-100% gas volume fraction (GVF). Typical system uncertainties (the dispersion of the readings) for the multiphase mode are given as [99]

- Liquid rate: +/-3.5 % relative error.

- Water cut (the ratio of water produced compared to the total volumetric flow of liquids produced): +/-2.5 % absolute error.

- Gas rate: +/- 6 % relative error.

2.5.2   Framo Multiphase Flow Meter

Framo Engineering AS in Norway developed a multiphase flow meter based on a multiple-energy level gamma fraction meter and a venturi momentum meter to determine the oil, water and gas fractions and their different flow rates [100]. The device has a flow mixer to provide a homogeneous flow to the metering section, thus making it independent of the type of flow regime. According to multi-meter tests which took place at Norsk Hydro's Porsgrunn research facility, the meter performed well over a wide operating envelope, including gas volume fractions up to 98%, the top of the testing range, and up to 100% water cut.

2.5.3   Schlumberger VX Technology

Schlumberger VX multiphase flow meters are designed to measure oil, gas, and water flow rates without prior separation. The instrument is based on nuclear detector technology where gamma ray energy is used to obtain the mean volume fractions of the dispersed phase across the cross-section of a venturi throat, while the total volumetric flow through the venturi is found using a differential pressure transmitter [101].

2.5.4   Summary of commercial multiphase flow meters

The amount of published information on the performance of the various multiphase flow meters is very limited and comparison is far from being an easy task. Usually this is due to the devices being protected by commercial secrecy and patents. However, it has been found that commercial multiphase metering systems tend to use a gamma ray densitometry technique to determine the volume fractions of the dispersed phase across the cross-section of the flow meter. However, due to concerns about the health of personnel and the high cost of such systems, multiphase flow

meter research continues to try to develop non-radioactive flow measurement techniques such as the electrical tomographic techniques.

2.6 Research Methodology to be adapted in the present Investigation

- A review of existing techniques for measuring multiphase flows has been presented, including the DP cell technique, intrusive measuring techniques and tomographic techniques.

- The DP cell technique is used to measure the mean volume fraction for the dispersed phase. It has been widely used in multiphase flow metering and it shows good accuracy. Thus, in the current investigation it was decided to use the DP cell as a global measurement technique to obtain the reference mean solids volume fraction.

- A review of solids/oil local volume fraction profiles and local solids velocity profiles has been presented. These profiles were obtained using intrusive measuring techniques. In the current investigation, the presented profiles will be used to evaluate measured solids-in-water flow parameters.

- Most current techniques such as electrical tomography only provide information on the local volume fraction and local axial velocity of the dispersed phase. Tomographic techniques such as ERT and ECT systems use complicated imaging reconstruction algorithms and require intensive and expensive computational power to process the measured signal and reconstruct the images.

- The EMFM review shows that conventional EMFM only provides the mean velocity of the conducting fluid in the flow cross-section. This measurement can produce a significant error in the continuous phase volumetric flow rate in multiphase flow especially if the volumetric flow rate of a particular phase has to be obtained by integrating the product local phase volume fraction and the local phase velocity in the flow cross-section.

45

- The ICC device is used to obtain the local volume fraction profiles of both the dispersed and continuous phases and local axial velocity profiles of the dispersed phase. By integrating these profiles, the volumetric flow rate for the dispersed phase is estimated.

- The ICC device is similar to ERT systems, however it is less expensive than ERT and ECT systems and needs no sophisticated algorithms to analyse the acquired data. This latter feature enables the ICC device to avoid the error which could happen due to the reconstructed imaging process and hence increased the accuracy of the system[49-51].

Based on the above, for the current investigation, the ICC device will be used to obtain the local axial velocity distribution of the solids and the local volume fraction distribution of both phases in the flow cross-section and this is where the research work in this thesis is concentrated. Detailed theory will be explained in Chapters three and four.

- The EVP is a new technique used to obtain the local axial velocity distribution of the electrically conducting continuous phase.

2.7 Summary

In the current investigation, the local volume fraction distribution and local velocity distribution of the dispersed phase obtained using the ICC device will be combined with the measured continuous phase velocity distribution obtained by the EVP device to obtain the volumetric flow rate for both phases. The detailed operation procedure of the EVP for obtaining the local water velocity is described later in Section 6.4.1, additionally, the detailed theory for combing ICC and EVP will be explained in Section 6.4.2.

2.8 Thesis Overview

This section provides brief a description of the contents for each chapter in this thesis.

Chapter 3   This chapter describes the measurements methodologies used in the current investigation. The methods are "Centre of Action" (CoA) and "Area Methodology" (AM). Additionally, this chapter also describes the use of a commercial finite element analysis (FEA) software package, COMSOL Multiphysics, which was used to perform simulations of the Impedance Cross Correlation device to determine the influence of its physical geometry on its real world behaviour.

Chapter 4   This chapter describes the design and implementation of the Impedance Cross Correlation (ICC) device which can be used in solids-water pipe flows to measure the in-situ volume fraction distributions of both phases and the local solids velocity distribution. The local solids velocity in the interrogated region is obtained by cross-correlation between the two electrode arrays. Additionally, the local in-situ solids volume fraction is obtained from the mean mixture conductivity in the region under interrogation.

Chapter 5   This chapter describes the microcontroller design and programming routines which enable the ICC device to be used as a standalone unit without a PC. This chapter also describes the setup of PC based software for operating the ICC device in order to measure the solids velocity profiles.

Chapter 6   This chapter presents the experimental apparatus used in the investigations, including the multiphase flow loop facility, the reference measurement instruments used in this study: the pressure gradient method and its calibration and the gravimetric flow measurement system and their calibration. The Electromagnetic Velocity Profiler EVP flow meter is described together with an explanation of the integration of the ICC device and EVP flow meter. Finally, this chapter presents the flow conditions which were used in the experiments.

Chapter 7   This chapter presents the experimental results and discusses the solids-in-water flow parameters for vertical and inclined solids-in-water flows.

Chapter 8   This chapter presents the conclusions of the thesis and suggests further work with recommendations and suggestions for a more advanced version of this technique.

3. CHAPTER 3: ICC Measurement Methodology

3.1 Introduction

This chapter describes the Measurement Methodology which is used by the Impedance Cross correlation (ICC) device to investigate the solids parameters in vertical and inclined solids-in-water flows. The ICC is used to measure the in-situ volume fraction distributions of both phases and the local solids velocity distribution in solids-water pipe flows. The ICC device comprises two arrays of electrodes, separated by an axial distance of 50 mm. Each array contains eight electrodes equally spaced over the internal circumference of the inner flow tube. The Measurement Methodology is divided into two main techniques known as: Centre of Action (CoA) and Area Methodology (AM). Both techniques are based on calculating the electrical current flow in the region bounded by electrodes in the ICC instrument, which in turn enables the spatial distributions of sensitivity to changes of conductivity in the flow cross section to be determined for different electrode configurations.

- **The Centre of Action (CoA)** technique is used to measure the solids parameters in stratified solids-in-water flows encountered in horizontal and inclined pipes. Using the sensitivity distribution profile for each electrode configuration, the boundaries of the effective sensing region for a given electrode configuration can be determined. Note that the boundary of the effective sensing region for a given electrode configuration is arbitrarily defined as the line along which the sensitivity to change in conductivity is 10% of the maximum sensitivity for that configuration. Each effective sensing region has a "Centre of Action" which can be taken as an indicator of how far the sensing field extends into the fluid. In this technique, the measured solids parameters were assigned to the corresponding CoA positions. The detailed explanation for CoA technique is shown in section 3.4.1.

49

- **The Area Methodology (AM)** technique is used to measure the solids parameters in vertical solids-in-water flows. The AM technique divides the pipe cross-section into pre-defined sub-areas. The boundary outline of each sub-area for a given electrode configuration depends on the sensitivity distribution for the electrode configuration. This technique also depends on a sensitivity parameter ψ obtained from the sensitivity distribution, the detailed explanation for the AM technique is given in section 3.4.3.

This chapter also describes the use of a commercial Finite Element Analysis (FEA) software package, COMSOL Multiphysics, to simulate the electrical current flow in the ICC instrument. This study provides an overview of the modelling process by discussing the model geometry, material properties, boundary conditions and the simulation outcomes. Although the ICC has two arrays of electrodes, it is necessary to use only one array of electrodes to simulate the electrical current flow for a particular electrode configuration.

This chapter is divided into four sections:

Section 3.2 describes the COMSOL simulations of the ICC instrument defining the model geometry and the physical boundary conditions for the model and model meshing.

Section 3.3 describes the sensitivity distributions of the results for different electrode configurations.

Section 3.4 describes the Centre of Action (CoA) and Area Methodology (AM) techniques for measurements made using the ICC device.

Section 3.5 presents the summary for chapter three.

3.2 COMSOL Software Package

COMSOL Multiphysics software is a powerful Finite Element (FEM) and Partial Differential Equation (PDE) solution engine which is widely used in fluid dynamics, electromagnetics, heat transfer. It also includes AC/DC and RF modules[102]. The ICC simulation can be divided into three steps: defining the model geometry, defining the physical boundary conditions for the model and defining model meshing for the simulation

3.2.1   Defining the Model Geometry

COMSOL Version 3.5a was used in the present investigation. The AC/DC module was chosen from the main COMSOL platform. The model was built using the 3D space dimension capability as shown in Figure 3.1
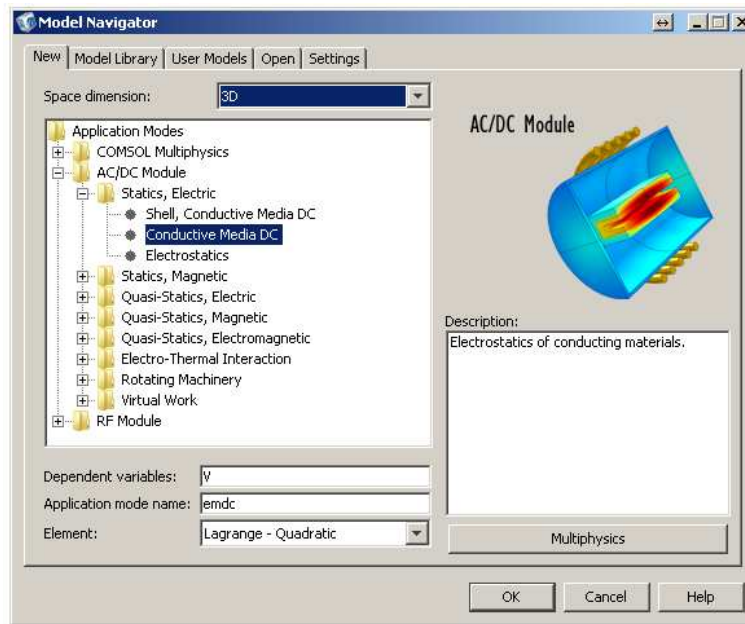
Figure 3.1 COMSOL platform showing 3D capability of the AC/DC Module

This modelling was based on the geometry of a pre-existing ICC geometry. The ICC device consists of two arrays of eight electrodes separated by an axial distance of 50 mm. In each array

the electrodes are mounted equidistantly around the internal circumference of the 80 mm internal diameter pipe carrying the flow. Each electrode had dimensions of 10 mm long in the circumstantial direction x 5 mm high in the axial flow direction x 1.5 mm thick (refer to Section 4.2). Since Array A and Array B have identical electrode arrangements, it was decided to use just one array to simulate the electrical current flow inside the pipe.

The following steps were used to model an eight electrodes array:

>> A work plane was generated by opening the **Work-Plane Settings** dialog box from the **Draw** menu and then clicking the **Quick** tab to create a work plane (Gemo2) in the XY plane. A 2D model was sketched in Gemo2.

To model the eight electrodes, eight isosceles triangles were drawn with the same point for their apexes as shown in Figure 3.2. Two circles (80 mm and 82 mm diameter) with the apex of the triangles as their centre were drawn to represent the electrode thicknesses. The triangles were equally spaced around the circles with the angle at the apex of each isosceles triangle being 30.65º.
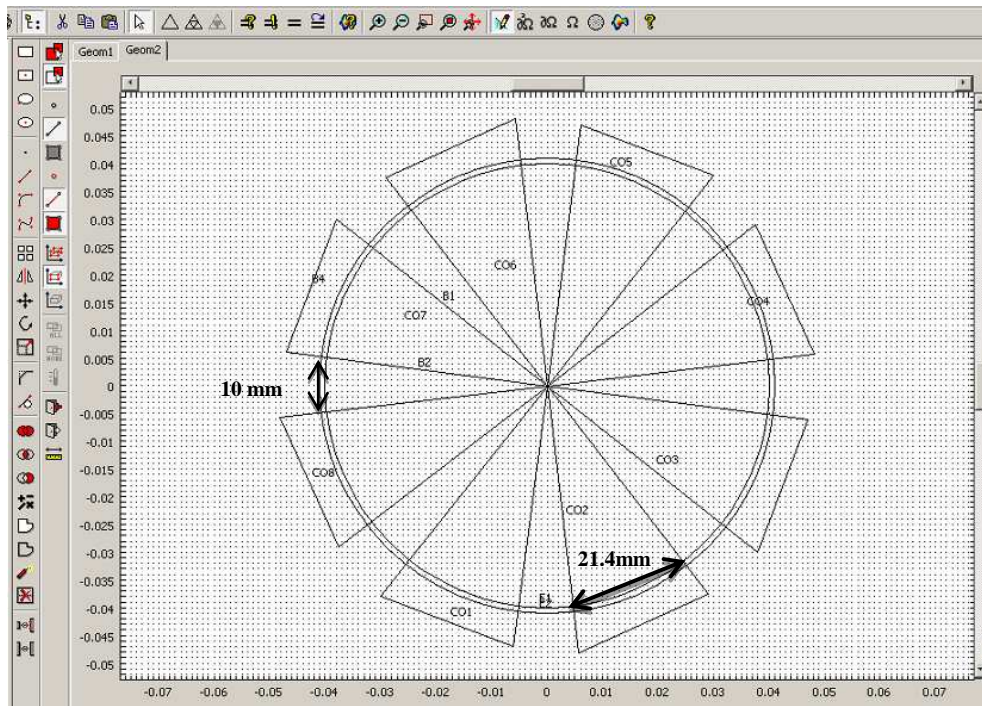
Figure 3.2 the 2D geometry used to model the eight electrodes

>> The "Difference" icon was used to delete all common areas between the triangles and the two circles. Thus eights electrodes where created with a thickness equal to the difference in radii of the two circles (1.5 mm) and length 10 mm: note that the real surface area of the ICC electrode is 10 mm circumferentially and 5 mm longitudinally (z direction), see Section 4.2.

The 80 mm circle represents the boundary of water media (e.g. the pipe wall). The 2D model was extended by 5 mm in the z direction using:

>> Opening the **Extrude** dialog box from the **Draw** menu and inserting the distance of 5 mm into the " Extrusion" parameter.

The final geometrical model in Gemo1 is in 3 dimensions as shown in Figure 3.3.

53
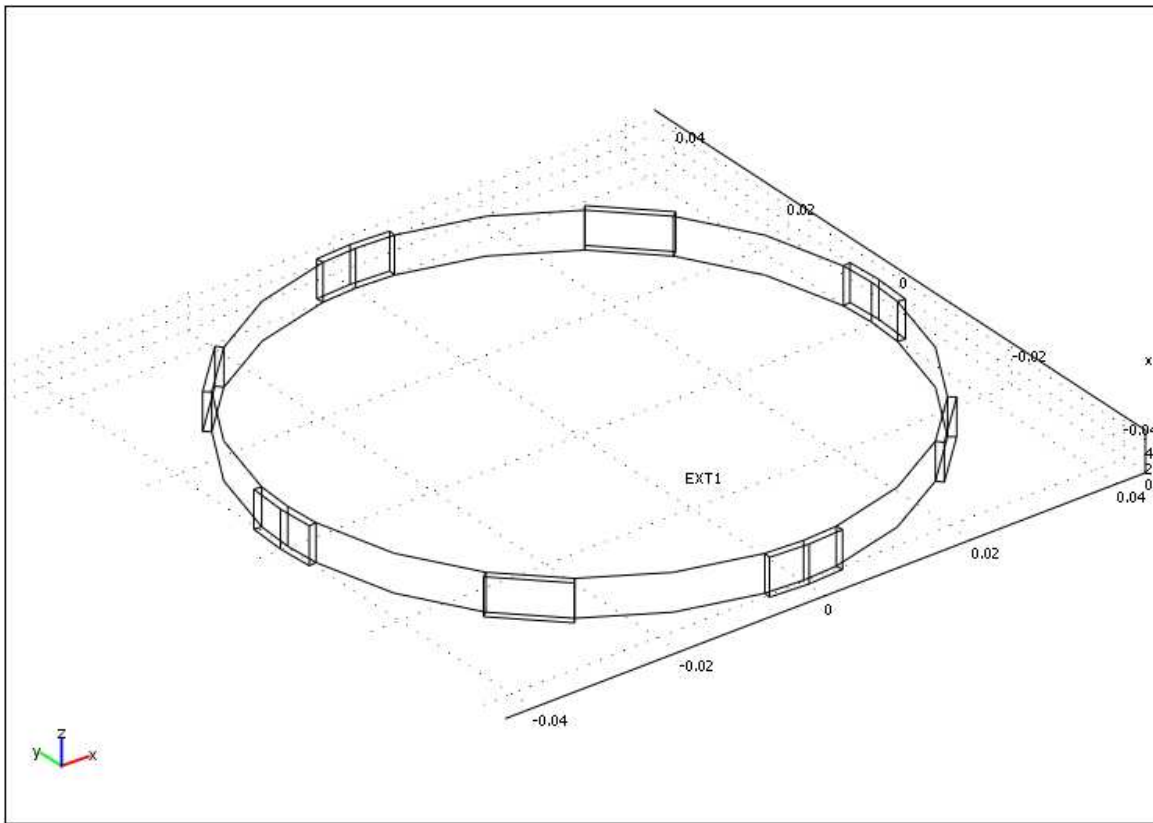
Figure 3.3 Array geometry of eight electrodes of dimensions: 10x 5x1.5 mm arranged equidistantly around an 80 mm diameter pipe

3.2.2 Defining the Physical Boundary Conditions For The Model

Before beginning the simulation, the boundary conditions and local sub-domain conditions need to be defined for the eight electrode array shown in Figure 3.3. For example, the electrical conductivity used for the stainless-steel was 4.032 S/m. The conductivity of the water inside the flow pipe was set at 0.016 S/m (160 S/cm) which is the conductivity of the tap water used in the experiments described later in this thesis.

Since there are no current sources in the flow cross section, the distribution of electrical potential ψ in the flow cross section is found by solving the following equation [49]:

$$\nabla.(\sigma\nabla\psi)=0 \hspace{6cm} \text{Equation 3-1}$$

where σ is the local electrical conductivity.

The local electrical current density j is given by:

$$j=-\sigma\nabla\psi \hspace{6cm} \text{Equation 3-2}$$

The electrical potential ψ and electrical current density j need to be determined in order to find the sensitivity distribution profile for each electrode configuration see section 3.3.

Section 3.3 details the boundary conditions set for the eight electrodes. The boundary conditions were inserted using the **Boundary setting** dialog box from the **Physics** menu.

3.2.3   The Model Mesh and Simulation

In finite element modelling, the meshing process divides the active area/volume of the model into a number of sufficiently small elements that a converged approximation solution can be achieved. The size and the numbers of elements will vary according to the complexity of the model geometry, the computing power available, the time allowable for the computation process, the required accuracy of the outcome and the investigation methodology.

A mesh convergence technique is used to ensure that i) the solution obtained in the study is as close as possible to reality and ii) there is a balance between accuracy and computing resources.

The model was tested by increasing the number of mesh elements n and measuring the current density at the face of one test electrode. The shape of the mesh element is chosen to be prism with triangular base. This type of layer has an advantage when resolving the boundary layer efficiently.

Figure 3.4 shows the variation in current density at the face of the test electrode for different mesh element densities.
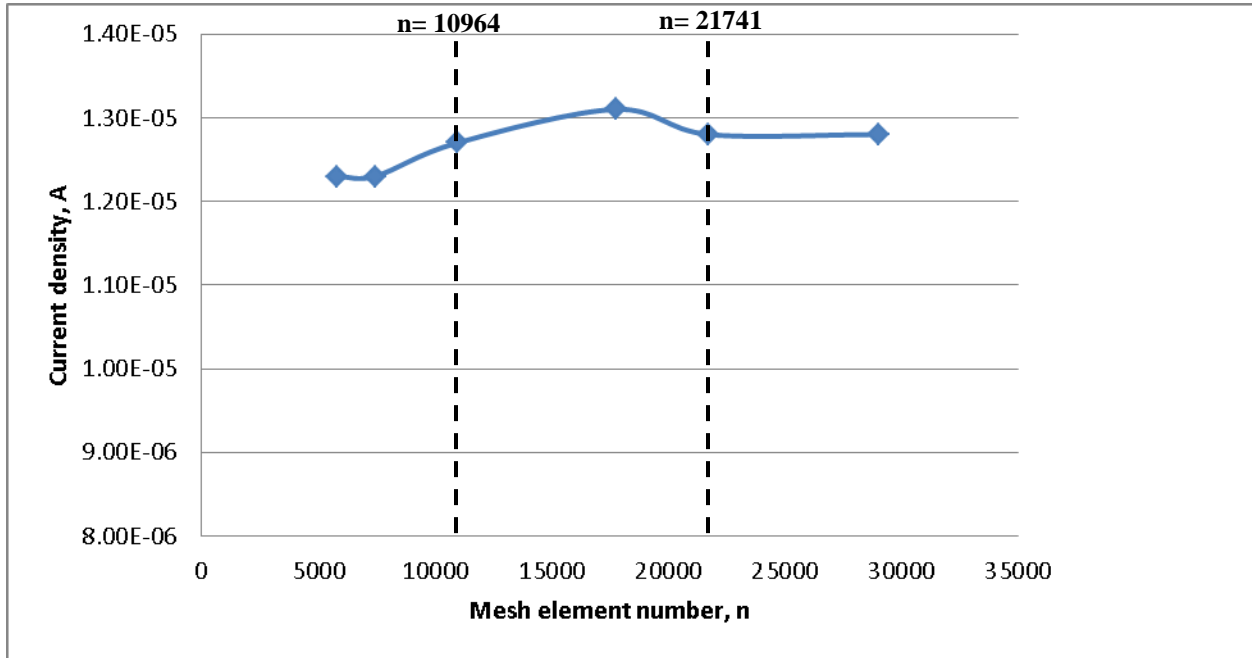
Figure 3.4 A plot of current density A versus mesh element number n

As shown in Figure 3.4, there was no great change in current density results as the number of mesh elements increased beyond approximately 10964 elements. Due to the limitations of the computing power, the solution process sometimes failed when 29039 elements were used but always failed for 30821 mesh elements.

Based on the mesh convergence test result in Figure 3.4, the mesh geometry for the present model was decided to be 21741 'fine' mesh elements as shown in Figure 3.5.
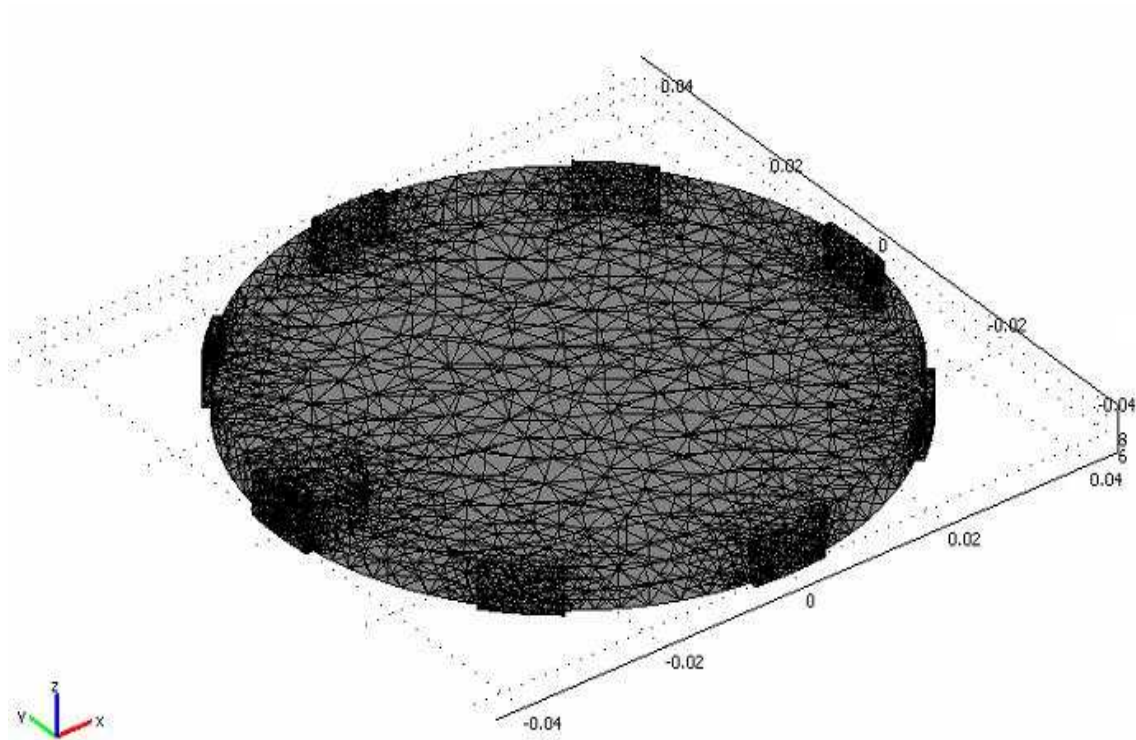
Figure 3.5 The finite element mesh for the eight electrode model

The geometrical model shown in Figure 3.5 was solved using the "**Solve problem"** icon from the **Solve** menu and took approximately 5 minutes execution time for each model investigation to reach to a solution. The solution was run using desktop PC with the Intel® Core™2 processor and installed RAM memory 4 GB.

3.3 Sensitivity Distribution - Investigation and Analysis

In the present study of solids-in-water flow, water is considered as the continuous conducting phase while the solids are considered as the dispersed phase with zero electrical conductivity. Different electrode configurations were simulated however, when the ICC device is used to sense regions inside the pipe, three electrode configurations were chosen based on how far the sensing field extends into the pipe cross section.

In each configuration one electrode or two adjacent electrodes are excited, all the other electrodes are earthed. Although all of the other electrodes were at earth potential, some were simulating as "virtual earth" electrodes whilst other were simulating "true earth" electrode (see the section below).

Each of the three configurations is rotated in eight steps of 45° to make measurements over the entire cross-section area of the pipe.

The three electrode configurations were:

- **Configuration I** (see Table 3-1)**:** in this configuration, only one electrode is excited with the next electrode selected as a virtual earth (ve) measurement electrode. The remaining six electrodes are earthed (E). For example, in rotational position-1, electrode 1 is the excitation electrode and electrode 2 is the measurement electrode (ve), with electrodes 3, 4, 5, 6, 7 and 8 connected to ground (E). Seven similar arrangements are possible by simple rotation of the arrangement, see Table 3-1.

- **Configuration II** (see Table 3-2): in this configuration, only one electrode is excited and the nearest electrode on either side are used for virtual earth measurements (ve). The remaining five electrodes are earthed (E). For example, in rotational position-1, electrode 1 is the excitation electrode, electrodes 2 and 8 are the measurement electrodes and electrodes 3, 4, 5, 6 and 7 are connected to ground. Again seven similar arrangements are possible by simple rotation of the first arrangement, see Table 3-2.

- **Configuration III** (see Table 3-3): in this configuration, two adjacent electrodes are excited and the two adjacent electrodes are used for virtual earth measurements (ve). The remaining four electrodes are earthed (E). For example, in rotational position-1 electrodes 1 and 2 are the excited, electrodes 3 and 8 are the measurement electrodes and electrodes 4, 5, 6 and 7

58

earthed (E). Again seven similar arrangements are possible by simple rotation of the first arrangement, see Table 3-3.

Table 3-1 Electrodes states for Configuration I

Configuration I			
Rotational position (n)	**Excitation (V^+)**	**Virtual earth (ve)**	**Ground (E)**
n=1	Electrode 1	Electrode 2	Electrode 3,4,5,6,7 and 8
n=2	Electrode 2	Electrode 3	Electrodes 1,4,5,6,7 and 8
n=3	Electrode 3	Electrode 4	Electrodes 1,2,5,6,7 and 8
n=4	Electrode 4	Electrode 5	Electrodes 1,2,3,6,7 and 8
n=5	Electrode 5	Electrode 6	Electrodes 1,2,3,4,7 and 8
n=6	Electrode 6	Electrode 7	Electrodes 1,2,3,4,5 and 8
n=7	Electrode 7	Electrode 8	Electrodes 1,2,3,4,5 and 6
n=8	Electrode 8	Electrode 1	Electrodes 2,3,4,5,6 and 7

Table 3-2 Electrodes states for Configuration II

Configuration II			
Rotational position (n)	**Excitation (V^+)**	**Virtual earth (ve)**	**Ground (E)**
n=1	Electrode 1	Electrodes 2 and 8	Electrodes 3,4,5,6 and 7
n=2	Electrode 2	Electrodes 3 and 1	Electrodes 4,5,6,7 and 8

n=3	Electrode 3	Electrodes 4 and 2	Electrodes 1,5,6,7 and 8
n=4	Electrode 4	Electrodes 5 and 3	Electrodes 1,2,6,7 and 8
n=5	Electrode 5	Electrodes 6 and 4	Electrodes 1,2,3,7 and 8
n=6	Electrode 6	Electrodes 7 and 5	Electrodes 1,2,3,4 and 8
n=7	Electrode 7	Electrodes 8 and 6	Electrodes 1,2,3,4 and 5
n=8	Electrode 8	Electrodes 1 and 7	Electrodes 2,3,4,5 and 6

Table 3-3 Electrodes states for Configuration III

Configuration III			
Rotational position (n)	**Excitation (V^+)**	**Virtual earth (ve)**	**Ground (E)**
n=1	Electrodes 1 and 2	Electrodes 3 and 8	Electrode 4,5,6 and 7
n=2	Electrodes 2 and 3	Electrodes 4 and 1	Electrodes 5,6,7 and 8
n=3	Electrodes 3 and 4	Electrodes 5 and 2	Electrodes 1,6,7 and 8
n=4	Electrodes 4 and 5	Electrodes 6 and 3	Electrodes 1,2 ,7 and 8
n=5	Electrodes 5 and 6	Electrodes 7 and 4	Electrodes 1,2,3 and 8
n=6	Electrodes 6 and 7	Electrodes 8 and 5	Electrodes 1,2,3 and 4
n=7	Electrodes 7 and 8	Electrodes 1 and 6	Electrodes 2,3,4 and 5
n=8	Electrodes 8 and 1	Electrodes 2 and 7	Electrodes 3,4,5 and 6

The geometrical model shown in Figure 3.6 was used to calculate the sensitivity distribution for each configuration and rotational position. For a given plane the sensitivity of the sensing field of a given electrode configuration was calculated at 12 discrete positions (or elements denoted H1 to 12) in the flow cross section (see Figure 3.6).
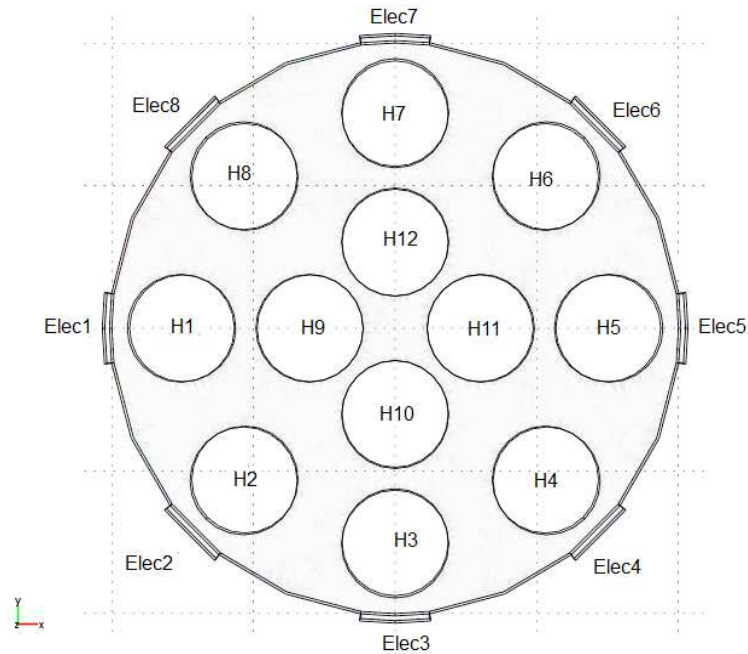
Figure 3.6 the 12 numerous positions (or elements) in the flow cross-section

In these simulations, the flow cross-section was assumed to be filled with water (the conducting medium) of conductivity equal to 0.016 S/m and material of zero conductivity with a 15 mm diameter was inserted, **in turn**, at positions H1 to H12 to simulate the presence of a non-conducting particle of the dispersed phase.

The sensitivity parameter S_i at each position was calculated as follows

$$(S_i) = (V_{out})_w - (V_{out})_i \qquad \text{Equation 3-3}$$

61

where $(V_{out})_w$ is the value of the output voltage (from a simulation of the conductance measurement circuit see Figure 3.7) when only water is present, and $(V_{out})_i$ is the value of the output voltage when a non-conducting particle is present at the ith location given above.
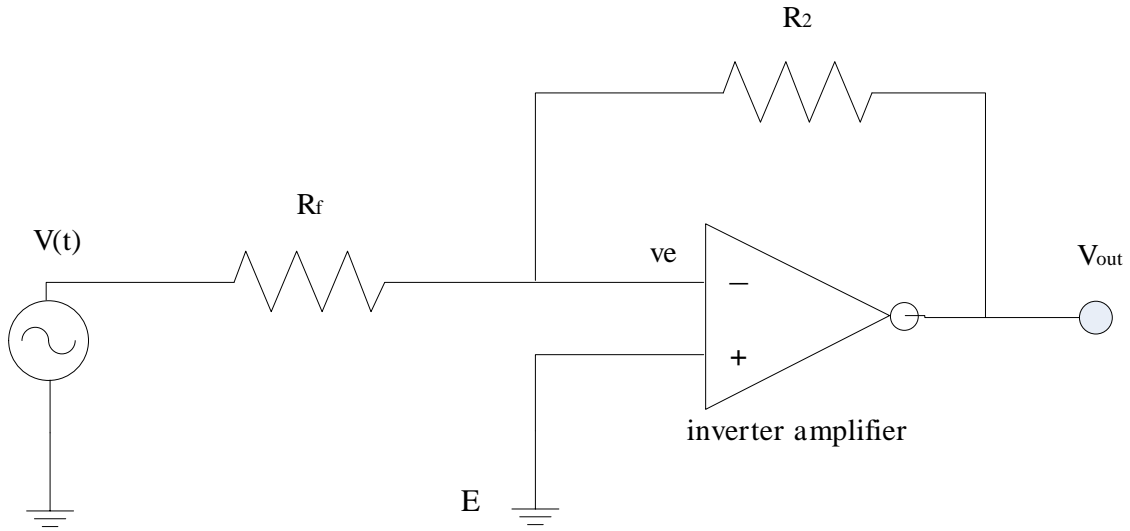
Figure 3.7 Simulation of the conductance measurement circuit

The output voltage V_{out} from the simulated conductance measurement circuit is found using

$$\frac{V_{out}}{V(t)} = -\frac{R_2}{R_f}$$ Equation 3-4

where R_f is the fluid resistance between the excitation electrodes and the virtual earth electrodes and R_2 is the feedback resistance for the inverting amplifier and $V(t)$ represents the amplitude of the simulated excitation signal.

Introducing the non-conducting particle into the simulated sensing field results in a change in the current density, see Figure 3.8. Introducing the non-conducting particle increases the fluid

resistance and hence the output voltage V_{out} from the simulated conductance measurement circuit will decrease. From this, the fluid resistance R_f can be calculated using the equation:

$$R_f = \frac{V(t)}{I}$$ Equation 3-5

where I is the total, or integrated, current density over the virtual earth measuring electrodes(denoted as ve in Figure 3.8).

I is calculated as:

$$I = \int i \, dxdy$$ Equation 3-6

where i is the current density at the virtual earth electrode surface.

a) Simulated current density when the nylon rod is inserted into position H2

b) Simulated current density for the water only
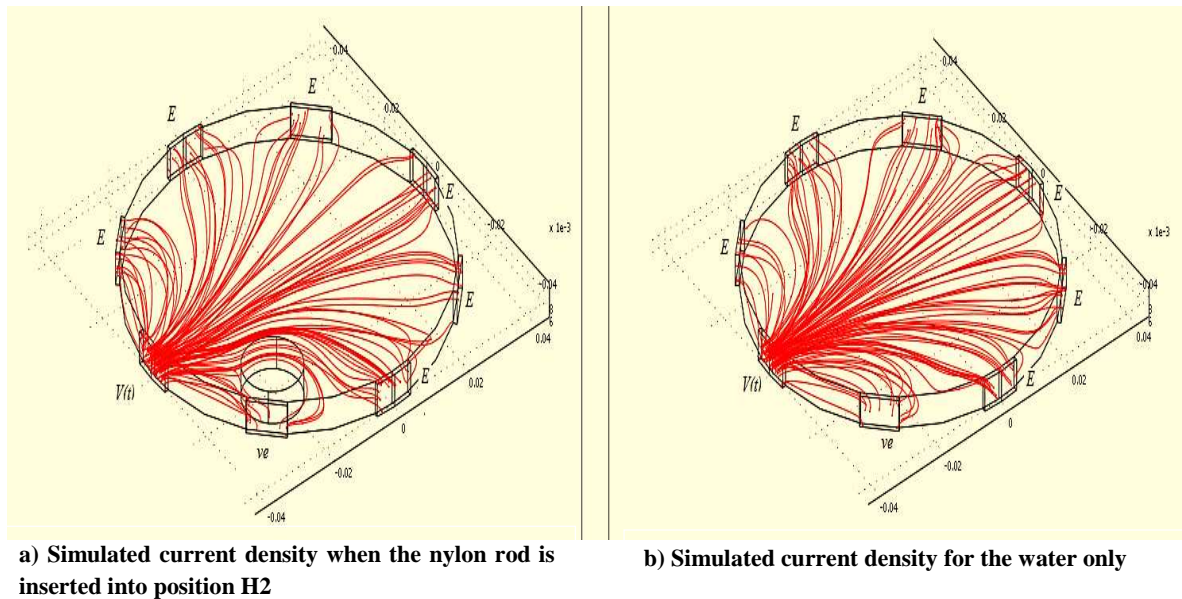
Figure 3.8 Simulated current flow between the electrodes, (the electrode 1 is excitation electrode V(t) and electrode 2 is the measurement electrode (ve), and electrodes 3,4,5,6,7 and 8 are connected to ground (E).

Because of the circular symmetry of the electrode arrangement it was necessary to test only one rotational position to determine the sensitivity distribution for any of the given Configurations (ϕ = I, II or III).

63

Sections 3.3.1 to 3.3.3 show the sensitivity distribution results for the three configurations described in Table 3-1, Table 3-2 and Table 3-3.

3.3.1   Sensitivity Distribution Result for Configuration I

The resolution of the sensitivity distribution depends on the number of measurement points at which the sensitivity parameters are calculated. The following sensitivity distributions were obtained using 12 measurement points. These 12 measurements points were enough to obtain the needed sensitivity distributions for the centre of action measurement method.

The sensitivity parameters (S_1 to S_{12}) which were obtained by Equation 3-3 were each assigned to the central coordinate for the relevant hole position shown in Figure 3.6. For each Configuration (ϕ = I, II or III) and n rotational position, the 12 sensitivity parameters were interpolated into 80x80 elements (side of 1 mm) in order to obtain the sensitivity distributions through the pipe cross section, see the MATLAB program in Appendix B.

The interpolation method which was used in this study was MATLAB 4 griddata method V4 [103]. The V4 interpolation algorithm is based on the Green function of the biharmonic operator [104]. The advantage of this method is that it is easily applied to interpolation problems in three or more dimensions and also it helped to extend the interpolation of the 12 sensitivity parameter data to the pipe wall [104].

Figure 3.9 represents the sensitivity distribution for Configuration I at rotational position 1. In this figure, the x axis and y axis represent the coordinates of the sensitivity parameters while the colour bar represents the sensitivity value.
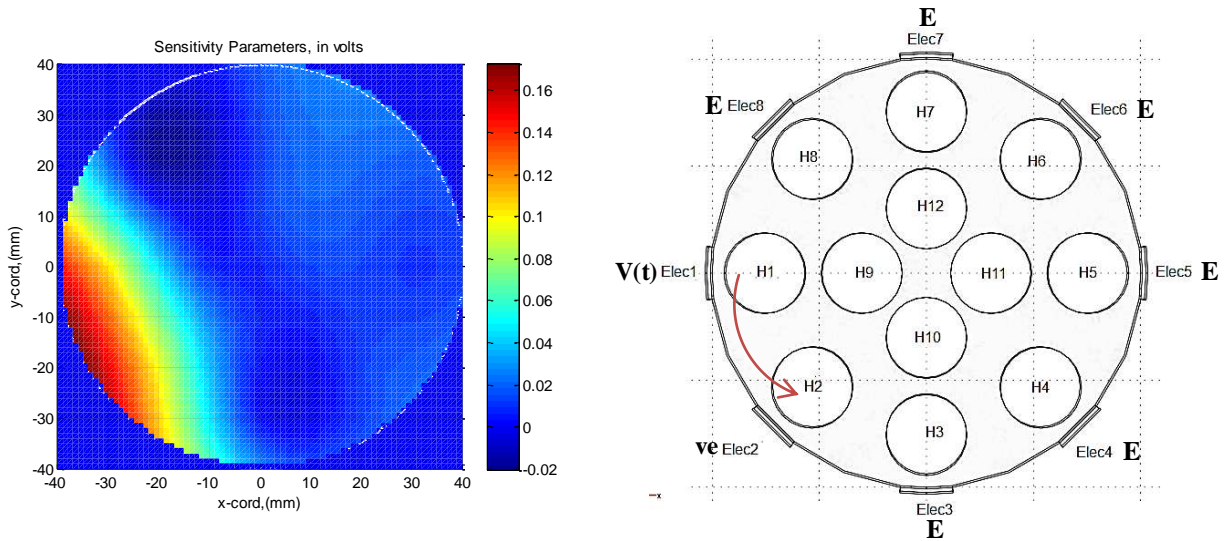
Figure 3.9 Configuration I sensitivity distribution for rotational position 1

(Electrode 1 is excited electrode V(t), electrode 2 is measurement electrode (ve), and electrodes 3,4,5,6,7 and 8 are earthed (E)) (The right hand part of figure is simply for reference showing the positions H1 to H12)

As shown in Figure 3.9, the highest sensitivity for Configuration I and rotational position 1 occurs at positions H1 and H2. However, the sensitivity parameter rapidly reduces with distance from H1 and H2 to a minimum value and will give little or no indication of the presence of non-conducting material at positions H3 to H12. This happened because H1 and H2 were the closest positions to the electrode 1 (V (t)) and electrode 2 (ve).

3.3.2   Sensitivity Distribution Result for Configuration II

Figure 3.10 represents the sensitivity distribution for Configuration II at rotational position 1. As shown in Figure 3.10, the highest sensitivity for Configuration II (rotational position 1) occurred at position H1. At this position, the non-conducting material was close to the excitation electrode (electrode1). However, the sensitivity parameter reduced towards the measurement electrodes (electrodes 2 and 8) and reached a minimum value adjacent to the earth electrodes.

65
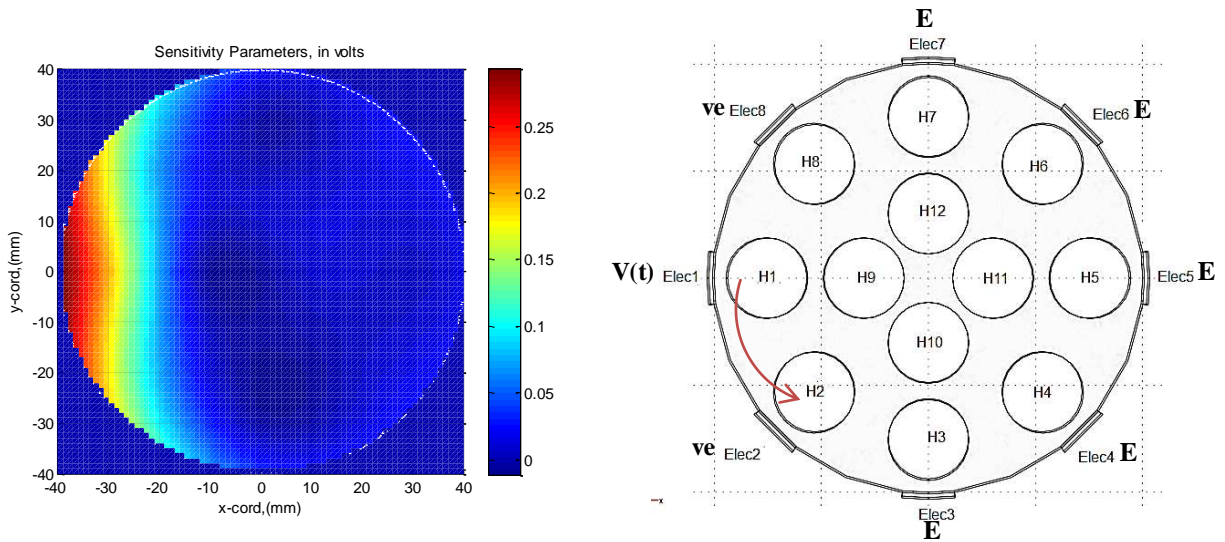
Figure 3.10 Configuration II sensitivity distribution for rotational position-1

(Electrode 1 is excitation electrode V(t), and electrodes 2 and 8 are measurement electrodes (ve) and electrodes 3,4,5,6 and 7 are earthed (E)) (The right hand part of figure is simply for reference showing the positions H1 to H12)

3.3.3 Sensitivity Distribution Result for Configuration III

Figure 3.11 represents the sensitivity distribution for Configuration III at rotational position 1. It was again found that the sensitivity is highest close to the excitation and virtual earth electrodes and lowest close to the earthed electrodes. Figure 3.11 suggests Configuration III has an effective sensing region which is larger than for Configurations I and II. However, even Configuration III gives little information about the region at the centre of the pipe.
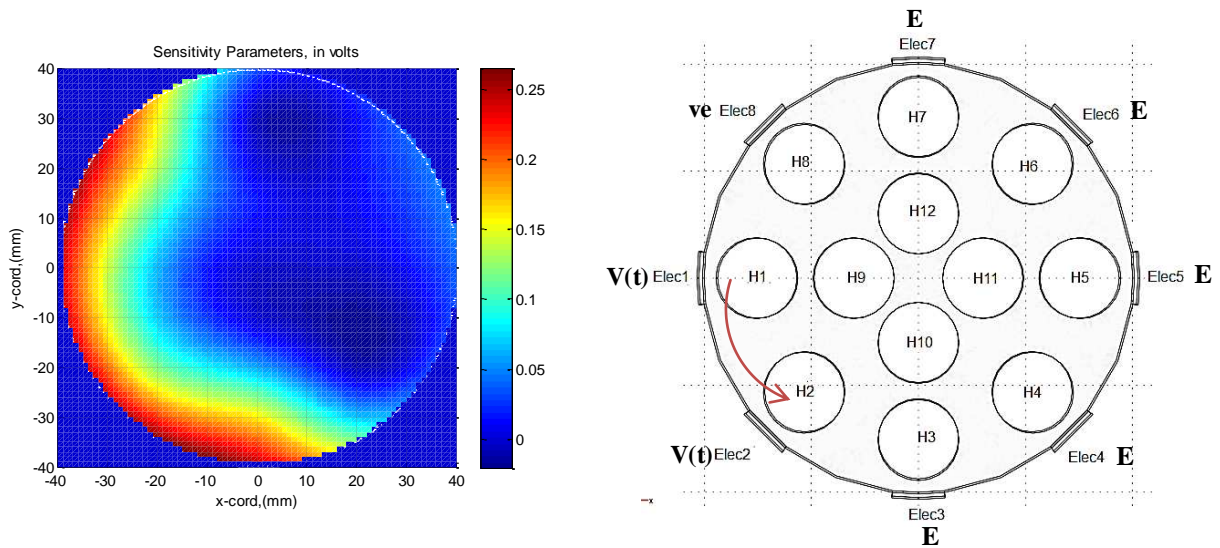
Figure 3.11 Configuration III sensitivity distribution for rotational position-1

(Electrodes 1 and 2 are excitation electrodes V(t), and electrodes 3 and 8 are measurement electrodes (ve) and electrodes 4,5,6 and 7 are earthed (E)) (The right hand part of figure is simply for reference showing the positions H1 to H12)

Section 3.4 discusses the two measurement methodologies used to analyse the measured data. Both depend on the sensitivity distributions shown in Figure 3.9, Figure 3.10 and Figure 3.11.

3.4 Measurement Methodology

3.4.1   Centre of Action (CoA): Calculation and Analysis

A boundary of the effective sensing region in each Configuration ($\phi = \mathrm{I, II\, or\, III}$) and the nth rotational position ($n = 1\, to\, 8$) can be arbitrarily defined as 10% of the maximum sensitivity distribution (see Al-Hinai 2010) [49]. Each effective sensing region may also be assumed to have a "Centre of Action" which can be taken as an indicator of how far the sensing field extends into the fluid. For example, if the COA is close to the pipe wall, this means that the effective sensing region will not be sensitive to the presence of non-conducting particles in the centre of the pipe. Conversely, for an effective sensing region that extends well into the pipe, the CoA will be nearer to the centre of the pipe. In a two-dimensional system, the CoA coordinates can be defined using Equation 3-7 and Equation 3-8.

67

The co-ordinate accuracy for the Centre of Action (CoA) depends on the resolution of the sensitivity distributions in Figures 3-9, 3-10 and 3-11. Therefore For the ϕth electrode Configuration ($\phi = I, II$ or III) and the nth rotational position ($n = 1$ to 8), the sensitivity distribution in Figures 3-9, 3-10 and 3-11 were gridded into 80x80 elements with (side of 1 mm).

The x co-ordinate for the Centre of Action (CoA) for the effective sensing region can be defined as:

$$(Cx)_{\phi,n} = \frac{\sum_{i=1}^{N} x_i a_i s_i}{\sum_{i=1}^{N} a_i s_i} \qquad \text{Equation 3-7}$$

where: $(Cx)_{\phi,n}$ is the $x -$ co-ordinate of the CoA for Configuration ϕ and rotational position n, x_i is the distance in the x direction to the ith element in the sensitivity distribution profile, a_i is the area of the ith element, s_i is the sensitivity parameter for the ith element for Configuration ϕ and rotational position n and N is the total number of elements (of side 1mm) in the flow cross-section. Similarly the y co-ordinate of the Centre of Action for Configuration ϕ and rotational position n may be calculated from:

$$(Cy)_{\phi,n} = \frac{\sum_{i=1}^{N} y_i a_i s_i}{\sum_{i=1}^{N} a_i s_i} \qquad \text{Equation 3-8}$$

where $(Cy)_{\phi,n}$ is the $y -$ co-ordinate of the CoA for Configuration ϕ and rotational position n and y_i is the distance to the ith element in sensitivity distribution profile.

The equations defining the CoA are identical in form to the equations defining the centre of mass in a two-dimensional system, with the product for a_i and s_i element replacing the mass m_i for that element.

By repeating the same steps for ϕ^{th} electrode Configuration ($\phi = I, II \text{ or } III$) and the nth rotational position ($n = 1 \text{ to } 8$), the coordinates of 24 different CoAs were calculated, see Figure 3.12. The x and y coordinates of the CoA is also shown in Appendix A Table 9.1.
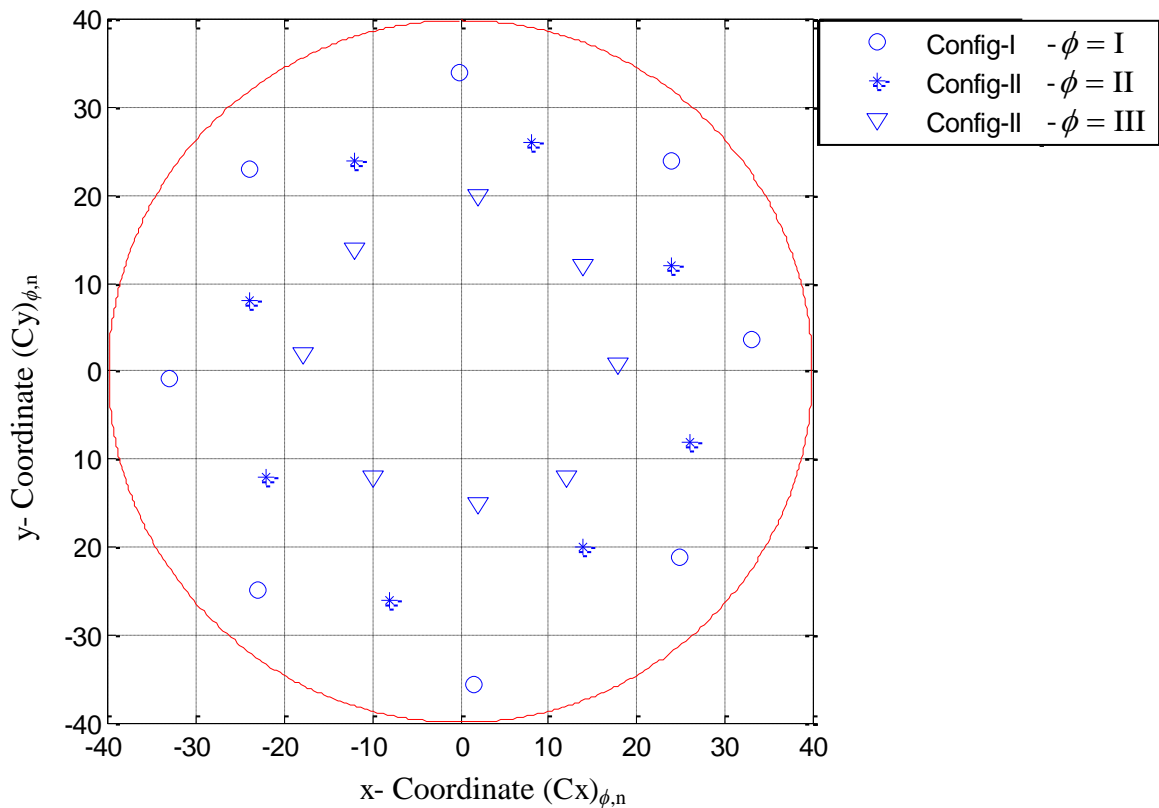
Figure 3.12 Location of CoA for Config-I, II and III for each of the eight possible electrode rotational positions

The measured local solids volume fraction $(\alpha_s)_{\phi,n}$ and the local solids velocity $(v_s)_{\phi,n}$, see Sections 4.3.1 and 4.3.2, were assigned to their corresponding centre of action. In order to find the solids volume fraction distributions $\alpha_{s,ICC}$ and the solids velocity distribution $v_{s,ICC}$, the 24

measurement values were interpolated through the pipe cross section using MATLAB 4griddata method V4.

3.4.2 Limitation of CoA Method for Low Volume Fraction in Vertical Solids-In-Water Flow

The CoA method was previously applied successfully by Al-Hinai [50] to measure volume fraction in vertical and inclined flow with a mean solids volume fraction $\overline{\alpha}_s$ between 0.15 to 0.3. In the present investigation, the author also used the CoA technique to measure the solids volume fraction in vertical flow with mean solids volume fraction $\overline{\alpha}_s$ less than 0.08. It is shown in chapter 7 that there is a significant error in the measured mean solids volume fraction $\overline{\alpha}_s$ using the CoA method for vertical flow for $\overline{\alpha}_s < 0.08$. Based on the fact that in vertical flows at low mean solids volume fractions the dispersed phase local volume fraction distribution tends to have a power law shape with the greatest solids volume fraction at the centre of the pipe flow [13], an obvious reason for this significant measurement error is the lack of precision in measuring the local solids volume fraction at the centre of the pipe due to the poor presentation of the "sensing field" into the flow cross section, even when Configuration II and Configuration III were used. It is important to find a new technique that can measure the solids volume fraction near to the pipe centre. Section 3.4.3 describes a new methodology developed by the author to measure the solids volume fraction in a greater proportion of the pipe cross section.

In inclined flow, where the stratification of the phases take place, the CoA technique tends to give more accurate results than vertical flow even when solids volume fraction is low. The reason behind this is that since the solids more dense than water, the majority of the solids sink to the bottom of the pipe. And this basically means that the majority of the solids volume fraction will lay inside the sensing field of Configuration I. Therefore, use of Configuration I will be adequate to measure the solids volume fraction inside the pipe cross section.

3.4.3   Area Methodology (AM) Technique

A new investigation was carried out using new and different electrode configurations in order to obtain an effective sensing region near to the pipe centre. A higher resolution for the sensitivity parameter is needed for the AM technique; therefore a new COMSOL simulation was used to assess the sensitivity parameters for a small non-conducting particle of the dispersed phase. Using the same simulation steps as described in sections 3.2 and 3.3, the flow cross-section was assumed to be filled with water (the conducting medium) and material of zero conductivity with a 10 mm diameter inserted, **in turn**, into 41 positions (denoted E1 to E41), see Figure 3.13.
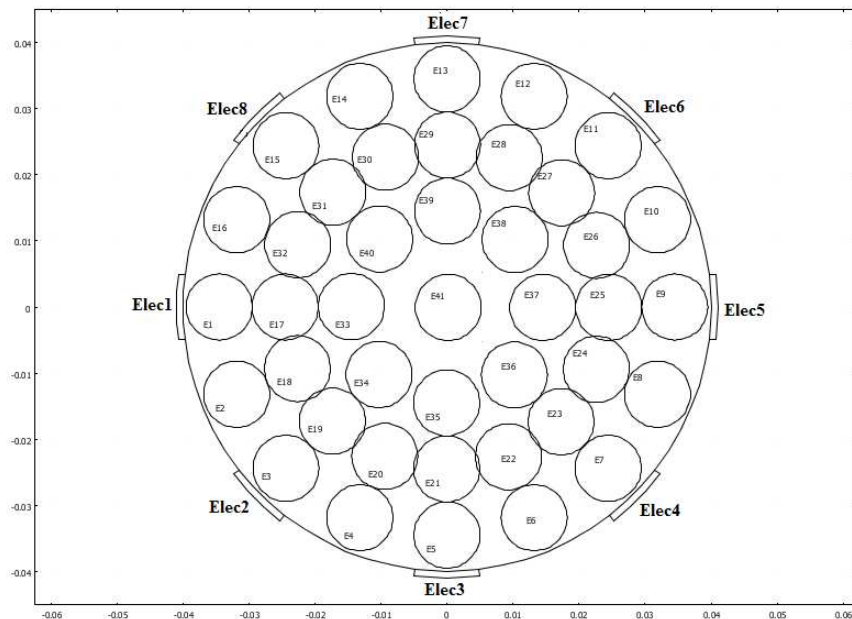
Figure 3.13 The 41 positions (or elements) in the flow cross-section

The AM technique is used to divide the pipe cross-section into defined sub-areas. Each sub-area has a local solids volume fraction which is obtained either by direct measurement or by mathematical calculation as will be shown later in section 3.4.3.2. Additionally each sub-area has a local solids velocity which is measured by the cross correlation technique.

71

The boundary outline of these sub-areas is defined based on the sensitivity distributions of Configuration I and Configuration IV (where Configuration IV is a new configuration which is used to obtain an effective sensing region near to the centre of the pipe, see Section 3.4.3.1). This technique is also depends on a sensitivity parameter ψ obtained from the sensitivity distribution for Configuration IV.

3.4.3.1 Sensitivity Distribution Result for Configuration IV

In Configuration IV there is one excitation electrode and one virtual earth (ve) electrode however the virtual earth (ve) is not the adjacent electrode to the excitation electrode but the next one along, see Figure 3.14. Thus if the excitation electrode is electrode 1 the virtual earth is electrode 3. As previously the remaining electrodes, 2, 4, 5, 6, 7 and 8 are earthed (E). Obviously there are seven similar possible arrangements obtained by simply rotating the configuration in steps of 45 degrees around the pipe, see Table 3-4. The sensitivity distribution for Configuration IV is shown in Figure 3.14

Table 3-4 Electrode states for Configuration IV

Configuration IV			
Rotational position (n)	**Excitation (V^+)**	**Virtual earth (ve)**	**Ground (E)**
n=1	Electrode 1	Electrode 3	Electrode 2,4,5,6,7 and 8
n=2	Electrode 2	Electrode 4	Electrodes 1,3,5,6,7 and 8
n=3	Electrode 3	Electrode 5	Electrodes 1,2,4,6,7 and 8
n=4	Electrode 4	Electrode 6	Electrodes 1,2,3,5,7 and 8
n=5	Electrode 5	Electrode 7	Electrodes 1,2,3,4,6 and 8

n=6	Electrode 6	Electrode 8	Electrodes 1,2,3,4,5 and 7
n=7	Electrode 7	Electrode 1	Electrodes 8,2,3,4,5 and 6
n=8	Electrode 8	Electrode 2	Electrodes 1,3,4,5,6 and 7
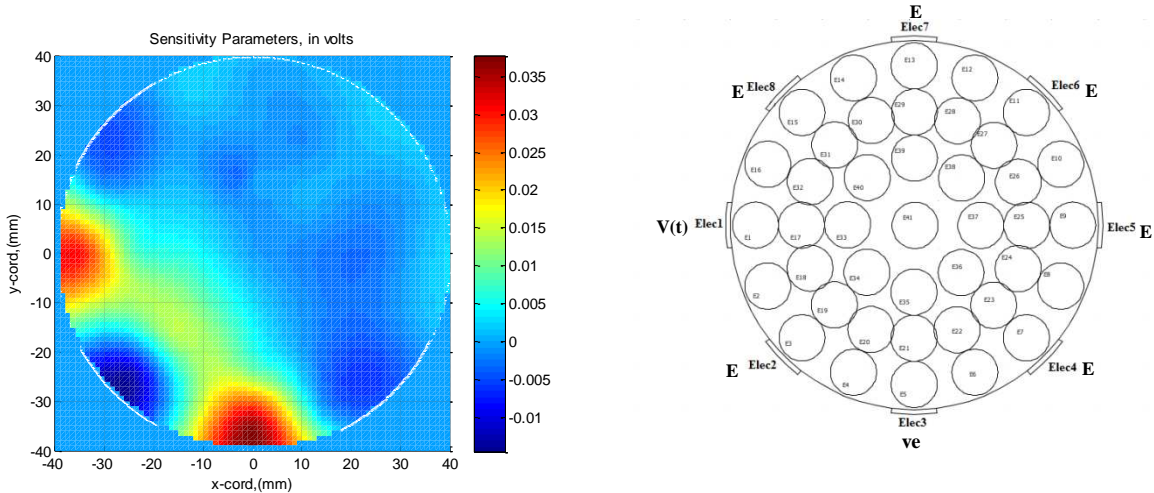
Figure 3.14 Configuration IV sensitivity distribution for rotational positions-1 (41 position present)

(Electrode 1 is excitation electrode V(t), electrode 3 is the measurement electrode (ve), and electrodes 2,4,5,6,7 and 8 are earthed (E))

Figure 3.14 shows that the maximum sensitivity for Configuration IV is primarily around the excitation and measuring electrodes (1 and 3 respectively). The sensitivity parameter is reduced to one half of the maximum value in the arc between electrodes 1 and 3 as shown in Figure 3.14 , and reaches a minimum value at the ground electrodes, including electrode 2.

A boundary of the effective sensing region for Configuration IV and the nth rotational position ($n = 1$ to 8) can again be arbitrarily defined as 10% of the maximum sensitivity distribution shown in Figure 3.14, therefore, it was assumed that the measured solids volume fraction using Configuration IV and rotational position n (n=1 to 8) represents the mean solids volume fraction $\alpha_{n,B}$ in the hatched region in Figure3.15b.
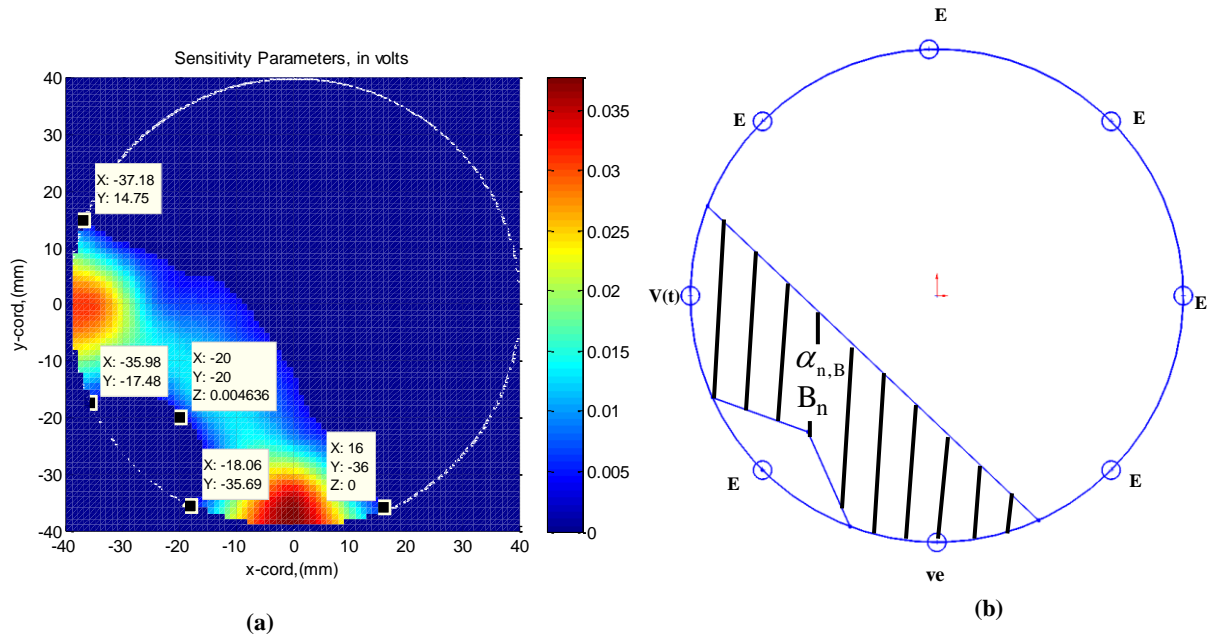
Figure 3.15 the effective sensing region for Configuration IV, rotation position n

The mean solids volume fraction $\alpha_{n,B}$ in the hatched region can be expressed as [56]:

$$\alpha_{n,B} = \frac{1}{B_n} \int_{B_n} \alpha_i \ dB_n \qquad \text{Equation 3-9}$$

where B_n is the area of the hatch region and α_i is the solids volume fraction for the sub-area i.

Where area B_n is divided into sub-areas i, as will be explained later in section 3.4.3.2.

Since there was a variation in the sensitivity parameters between electrodes 1 and 3, it was assumed that the sensitivity parameter ψ needs to be added into Equation 3-9. Where ψ_i and area magnitude of sub-area i can be considered as a weighting factor to the measured solids volume fraction.

Based on this assumption, Equation 3-9 can yield to:

$$\alpha_{n,B} = \frac{1}{\overline{\psi}_n B_n} \int_{B_n} \overline{\psi}_i \alpha_i \ dB_n \qquad \text{Equation 3-10}$$

where $\overline{\psi}_n$ is the mean sensitivity of Configuration IV rotational position n, $\overline{\psi}_i$ is the mean sensitivity parameter for each of the sub-areas i. Note that the subscript i will re-define later based on the type of Configuration I or IV and rotational position n.

The discrete formula of Equation 3-10 is:

$$\alpha_{n,B}\,\overline{\psi}_n\,B_n = \sum_{i=1}^{7}\overline{\psi}_i\,a_i\,\alpha_i \qquad\qquad \text{Equation 3-11}$$

where a_i is the area of each sub-area/ pixel. The sub-area a_i will re-define and re-samples later based on the type of Configuration I or IV and rotational position n.

Next Section 3.4.3.2 will illustrate the steps of dividing region B_n into 7 sub-areas and the measurements procedure of the solids volume fractions and solids velocity.

3.4.3.2 AM Measurement Procedure

The pipe cross-section is divided into sub-areas (or pixels) dependent upon the boundaries of the "effective sensing regions" for Configurations I and IV. The AM measurement procedure can be explained by three stages:

- Stage1: defines the boundaries of the sub-areas near the pipe wall and their correlated local solids volume fraction. This was done by using the "effective sensing regions" of Configuration I rotational position n.

- Stage2: defines the boundaries of the sub-areas deeper in the pipe centre and estimates the local solids volume fraction correlated to these sub-areas. This was done by overlapping the "effective sensing regions" for Configurations I and IV. The local solids volume fraction in the deeper sub-areas was calculated using a mathematical calculation shown in Equation 3-16.

- Stage3: carries out an investigation to measure the solids volume fraction near the pipe centre.

The following stages demonstrate the procedure:

1. Stage 1:

This stage shows the steps of defining the boundaries of the sub-areas near the pipe wall and their correlated solids volume fraction.

Figure 3.16 represents the sensitivity distribution for Configuration I at rotational position 1. The sensitivity distribution was obtained using the "41 position" shown in Figure 3.13.
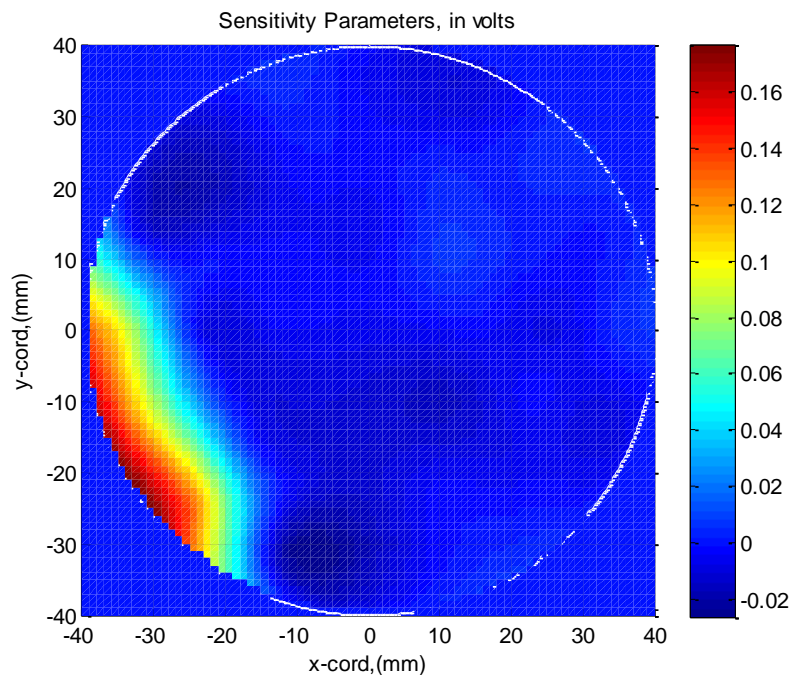
Figure 3.16 the sensitivity distribution for Configuration I using forty-one elements of 10 mm diameter.

The boundary of the "effective sensing region" of Configuration I was defined using the sensitivity distribution shown in Figure 3.16. Configuration I was used to measure the solids volume fraction near the pipe wall. In order to define the sub-areas beside the pipe wall, the boundaries of Configuration I, for rotational positions 1, 2 and 8, were overlapped as shown in Figure 3.17. Combining these three regions produced three areas of overlap denoted as $A_{8,1}$, A_1 and $A_{1,2}$ where:

- $A_{8,1}$ represents the overlap area associated with the boundaries of the two rotational positions 8 and 1.

- A_1 represents the area only associated with the boundaries of rotational position 1

- $A_{1,2}$ represents the overlap area associated with boundaries of the two rotational positions 1 and 2.
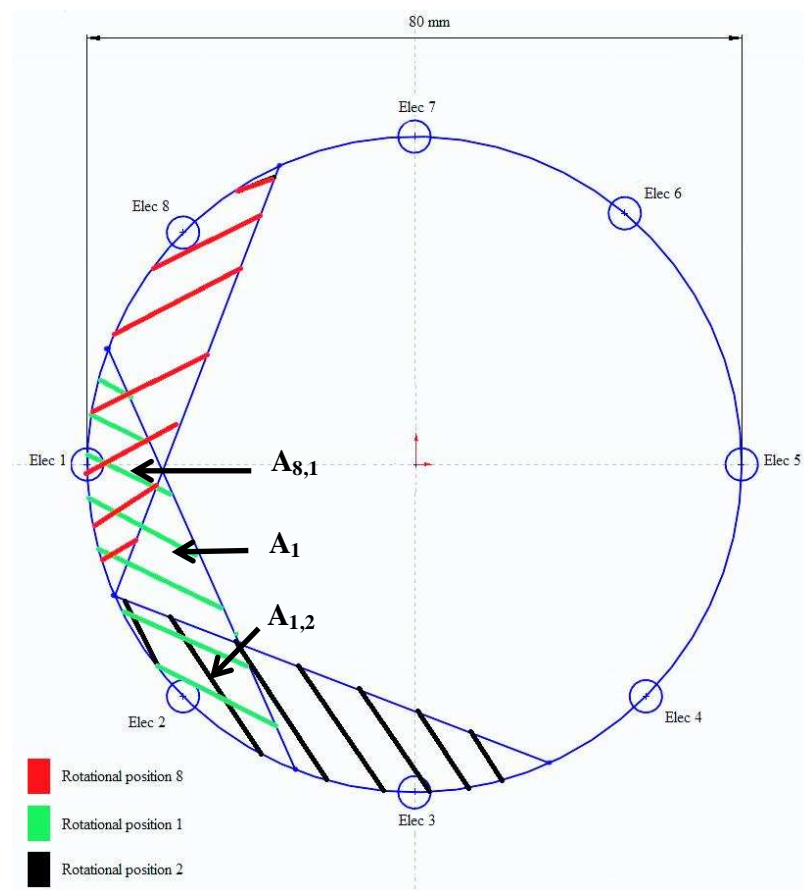
Figure 3.17 the area boundaries for Configuration_I (Rational positions 1,2 and 8)

The coordinates of the CoA for Configuration I rotational position 1 lies within area A_1, thus the solids volume fraction α_1 in area A_1 can be assumed to be the same as the measured volume

fraction of Configuration I rotational position 1. The solids volume fraction in areas $A_{8,1}$ and $A_{1,2}$ may be defined as:

$$\alpha_{1,8} = \frac{\alpha_1 + \alpha_8}{2}$$
Equation 3-12

$$\alpha_{1,2} = \frac{\alpha_1 + \alpha_2}{2}$$
Equation 3-13

where α_8 and α_2 represent the measured solids volume fraction of Configuration I at rotational position 8 and rotational position 2 respectively. Rotating in steps of 45° covers the remaining seven positions, see Figure 3.18. The subscripts in Equation 3-12 and Equation 3-13 will change according to each rotational position.
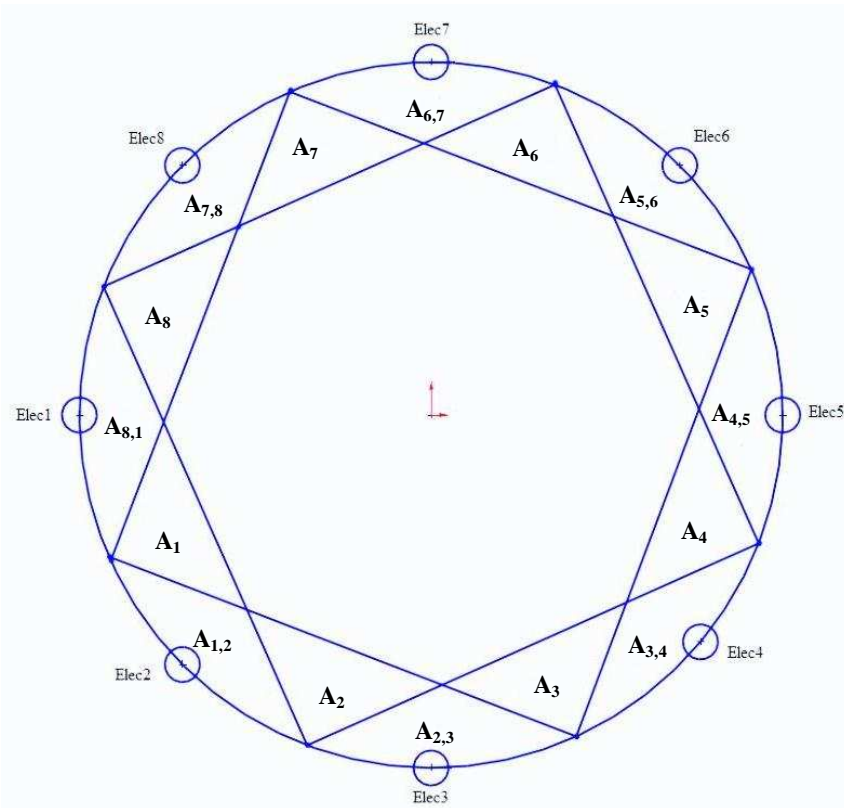
A_1	α_1
A_2	α_2
A_3	α_3
A_4	α_4
A_5	α_5
A_6	α_6
A_7	α_7
A_8	α_8
$A_{8,1}$	$\alpha_{8,1}$
$A_{1,2}$	$\alpha_{1,2}$
$A_{2,3}$	$\alpha_{2,3}$
$A_{3,4}$	$\alpha_{3,4}$
$A_{4,5}$	$\alpha_{4,5}$
$A_{5,6}$	$\alpha_{5,6}$
$A_{6,7}$	$\alpha_{6,7}$
$A_{7,8}$	$\alpha_{7,8}$

Figure 3.18 Total boundaries of the Configuration I, rotational positions n=1 to 8

Figure 3.18 shows the 16 sub-areas near to the pipe wall. Where each of these sub-areas has a local solids volume fraction and a local solids velocity (the AM measurements for the local solids velocity will be explained later in section 3.4.3.3).

2. Stage 2:

This stage shows the steps to define the deeper sub-areas into the pipe centre and the calculations of their related solids volume fraction.

The boundary outline for Configuration IV in Figure 3.19 b is now used in conjunction with the boundary outlines for Configuration I in Figure 3.19a. Accordingly, new sub-areas are produced and denoted as '*B*', see Figure 3.20.

79

(a)

(b)
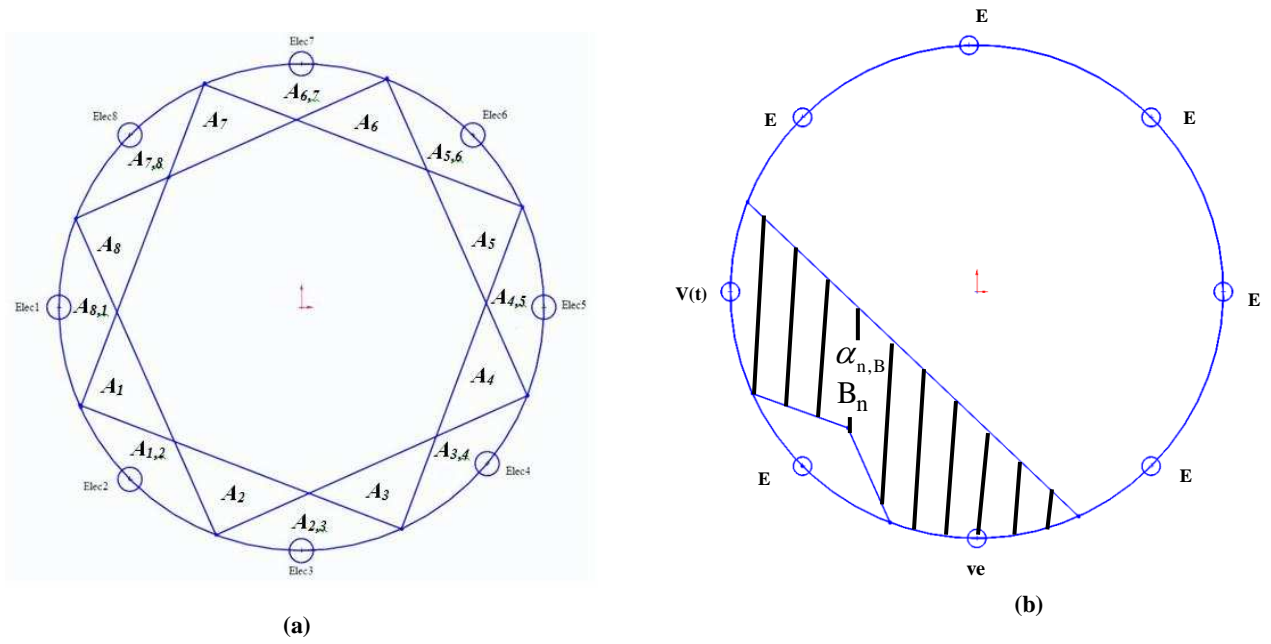
Figure 3.19 a)The boundary of the effective sensing region using Configuration I, rotational position n=1 to 8 ,b) The boundary of the effective sensing region using Configuration IV, rotational position n=1
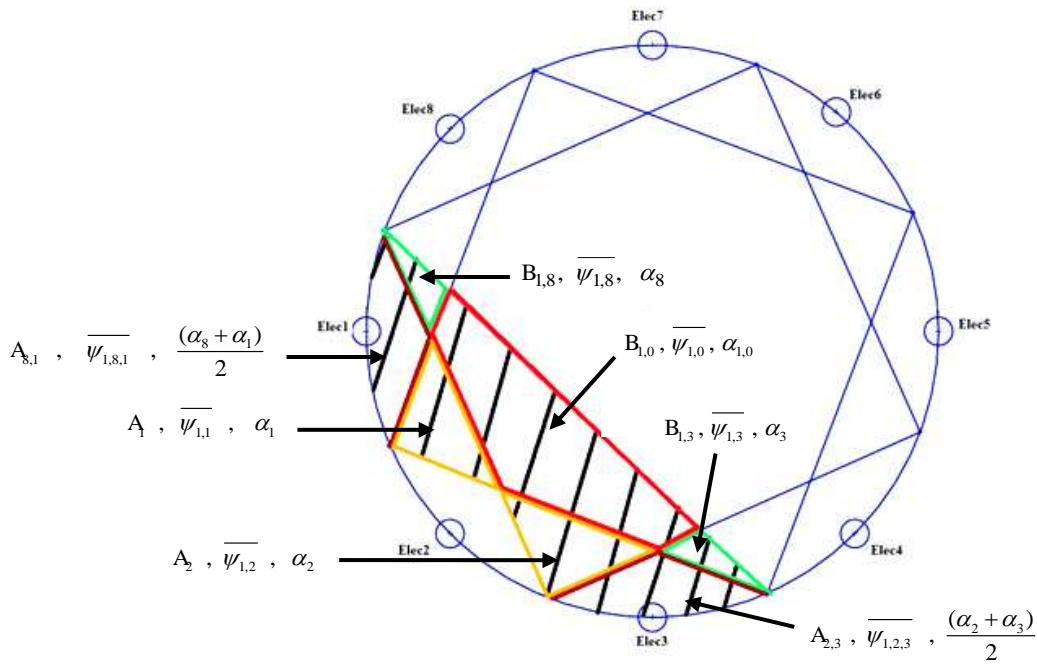
Figure 3.20 Areas under Configuration I , n=1 to 8 and Configuration IV , n=1

From Figure 3.20 the hatched line represents the effective sensing region of Configuration IV at rotational position 1. The sensitivity parameter $\overline{\psi}$ in each sub-area was calculated using MATLAB software and Excel Microsoft as will be shown later in this section. The new terms in Figure 3.20 are defined as:

- $B_{1,8}$ is the area of overlapping of Configuration IV, rotational position 1 and Configuration I, rotational position 8. This area has a solids volume fraction equal to α_8 from Configuration I rotational position 8, see Figure 3.18 . Additionally, this area has a mean sensitivity parameter denoted as $\overline{\psi_{1,8}}$.

- $B_{1,3}$ is the overlapped area of Configuration IV , rotational position 1 and Configuration I, rotational position 3. This area has a solids volume fraction equal to α_3 from Configuration I rotational position 3, see Figure 3.18 . Additionally, this area has a mean sensitivity parameter denoted as $\overline{\psi_{1,3}}$.

- $B_{1,0}$ is the associated with Configuration IV , rotational position 1 only and dose not overlap any of the areas associated with Configuration I. This area has a solids volume fraction denoted as $\alpha_{1,0}$ and a mean sensitivity parameter denoted as $\overline{\psi_{1,0}}$.

- B_1 is the whole area covered by effective sensing region of Configuration IV, rotational position 1 (the entire hatched area in Figure 3.20 and Figure 3.19).

- $\overline{\psi_1}$ is the mean sensitivity parameters for effective sensing region of Configuration IV, rotational position 1

- $\alpha_{1,B}$ is the measured value for the mean solids volume fraction in area B_1 using Configuration IV at rotational position 1.

- $\overline{\psi_{1,8,1}}$ is the mean sensitivity parameter in area $A_{8,1}$. The subscript 1,8,1 refers to the region of Configuration IV (rotational position 1), region of Configuration I (rotational position 8) and region of Configuration I (rotational position 1) respectively.

- $\overline{\psi_{1,2,3}}$ is the mean sensitivity parameter in area $A_{2,3}$. The subscript 1,2,3 refers to the region of Configuration IV (rotational position 1), region of Configuration I (rotational position 2) and region of Configuration I (rotational position 3) respectively.

- $\overline{\psi_{1,1}}$ is the mean sensitivity parameter in area $A_{1.}$ The subscript 1,1 refers to the region of Configuration IV (rotational position 1) and region of Configuration I (rotational position 1) respectively.

- $\overline{\psi_{1,2}}$ is the mean sensitivity parameter in area $A_{2.}$ The subscript 1,2 refers to the region of Configuration IV (rotational position 1) and region of Configuration I (rotational position 1) respectively.

- $\overline{\psi_{1,3}}$ is the mean sensitivity parameter in area $A_{3.}$ The subscript 1,3 refers to the region of Configuration IV (rotational position 1) and region of Configuration I (rotational position 3) respectively.

In order to calculate the mean sensitivity parameter $\overline{\psi}$ in each sub-area, a MATLAB program was used to define the boundary of the effective sensing region for configuration IV rotational position 1, see Figure 3.21. The results of the sensitivity parameters were saved in an 80x80 matrix named as sensitivity_matrix and transferred into an Excel sheet. Hence, each sub-area was excluded and the mean sensitivity parameter $\overline{\psi}$ was calculated by taking the average of the sensitivity parameter for the N (side of 1 mm) pixels, see Table 3-5.
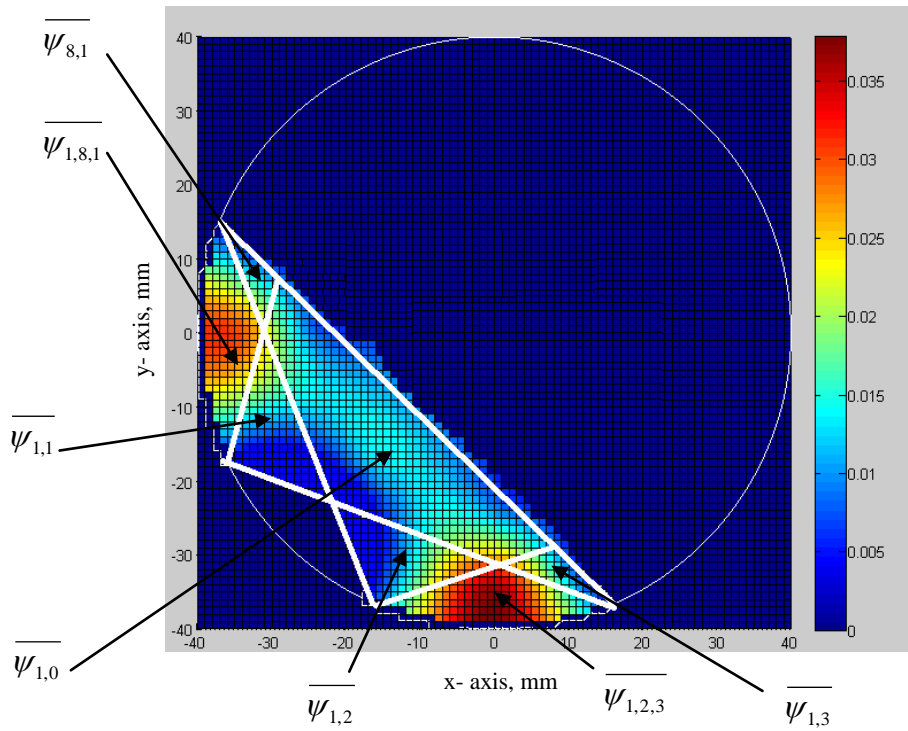
Figure 3.21 the sensitivity distribution for Configuration IV rotational position 1

Here, it is important to emphasise that it is the solids volume fraction $\alpha_{1,0}$ in pixel $B_{1,0}$, refer Figure 3.20, that needs to be determine.

Using Equation 3-11, the results of the solids volume fraction for both Configurations I and IV were combined together into a single generalised relationship as shown by Equation 3-14.

$$B_n \overline{\psi_n} \alpha_{n,B} = B_{n,n-1} \overline{\psi_{n,n-1}} \alpha_{n-1} + \frac{A_{n-1,n} \overline{\psi_{n,n-1,n}} (\alpha_{n-1} + \alpha_n)}{2} + A_n \overline{\psi_{n,n}} \alpha_n + A_{n+1} \overline{\psi_{n,n+1}} \alpha_{n+1} +$$

$$\frac{A_{n+1,n+2} \overline{\psi_{n,n+1,n+2}} (\alpha_{n+1} + \alpha_{n+2})}{2} + B_{n,n+2} \overline{\psi_{n,n+2}} \alpha_{n+2} + B_{n,0} \overline{\psi_{n,0}} \alpha_{n,0}$$

For $n = 1$ if $n - 1 = 0$ then $n - 1 = 8$ Equation 3-14

For $n = 7$ if $n + 2 = 9$ then $n + 2 = 1$

For $n = 8$ if $\begin{cases} n + 1 = 9 & \text{then } n + 1 = 1 \\ n + 2 = 10 & \text{then } n + 2 = 2 \end{cases}$

83

Equation 3-14 can be written in terms of rotational position n=1 for Configuration IV as follows:-

$$B_1 \overline{\psi_1} \alpha_{1,B} = B_{1,8} \overline{\psi_{1,8}} \alpha_8 + \frac{A_{8,1} \overline{\psi_{1,8,1}} (\alpha_8 + \alpha_1)}{2} + A_1 \overline{\psi_{1,1}} \alpha_1 + A_2 \overline{\psi_{1,2}} \alpha_2 + \frac{A_{2,3} \overline{\psi_{1,2,3}} (\alpha_2 + \alpha_3)}{2} + B_{1,3} \overline{\psi_{1,3}} \alpha_3 + B_{1,0} \overline{\psi_{1,0}} \alpha_{1,0}$$

Equation 3-15

Equation 3-15 can re-arranged in the term of $\alpha_{1,0}$ as:

$$\alpha_{1,0} = \frac{B_1 \overline{\psi_1} \alpha_{1,B} - \left[\begin{array}{c} B_{1,8} \overline{\psi_{1,8}} \alpha_8 + \dfrac{A_{1,8} \overline{\psi_{1,8,1}} (\alpha_8 + \alpha_1)}{2} + A_1 \overline{\psi_{1,1}} \alpha_1 + A_2 \overline{\psi_{1,2}} \alpha_2 + \\ \dfrac{A_{2,3} \overline{\psi_{1,2,3}} (\alpha_2 + \alpha_3)}{2} + B_{1,3} \overline{\psi_{1,3}} \alpha_3 \end{array} \right]}{B_{1,0} \overline{\psi_{1,0}}}$$

Equation 3-16

The remaining local solids volume fractions ($\alpha_{2,0}$ to $\alpha_{8,0}$) can simply be calculated by rotating Configuration IV in step of 45° and using Equation 3-16 for each rotation, see Figure 3.22.

n=1   n=2   n=3   n=4

n=5   n=6   n=7   n=8

Ele7

Ele8

Ele6

$\alpha_{6,0}$

$\alpha_{7,0}$

$\alpha_{5,0}$

Ele1

$\alpha_{81,0}$

$\alpha_{4,0}$

Ele5

$\alpha_{3,0}$

Ele2

$\alpha_{1,0}$

$\alpha_{2,0}$

Ele4

Ele3
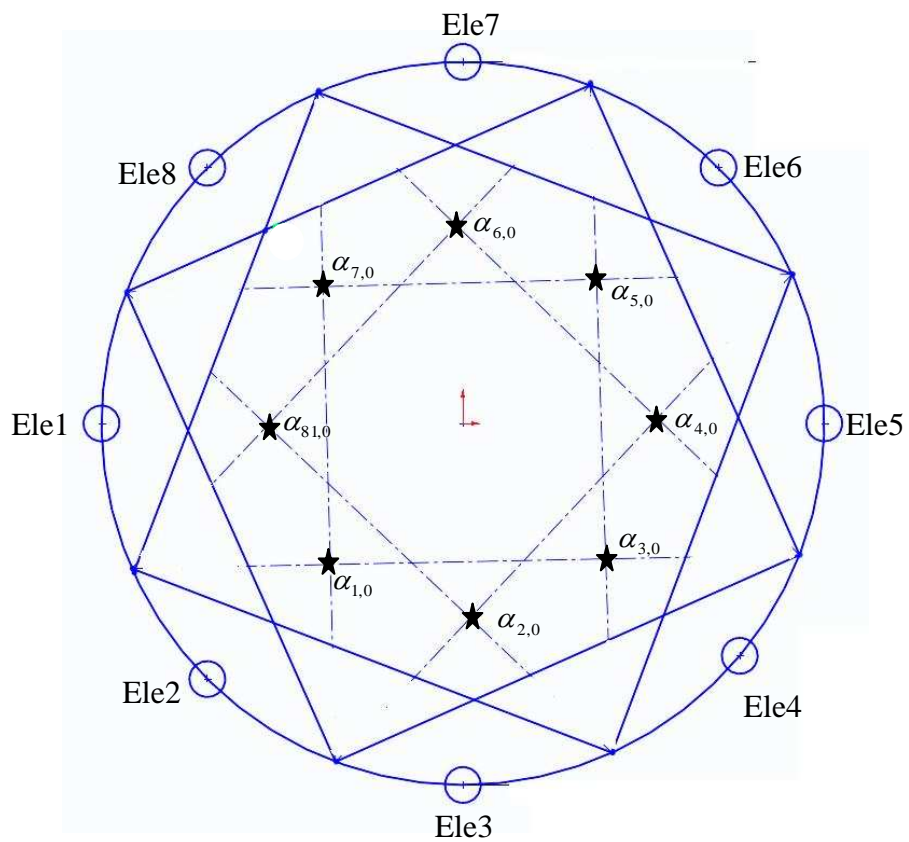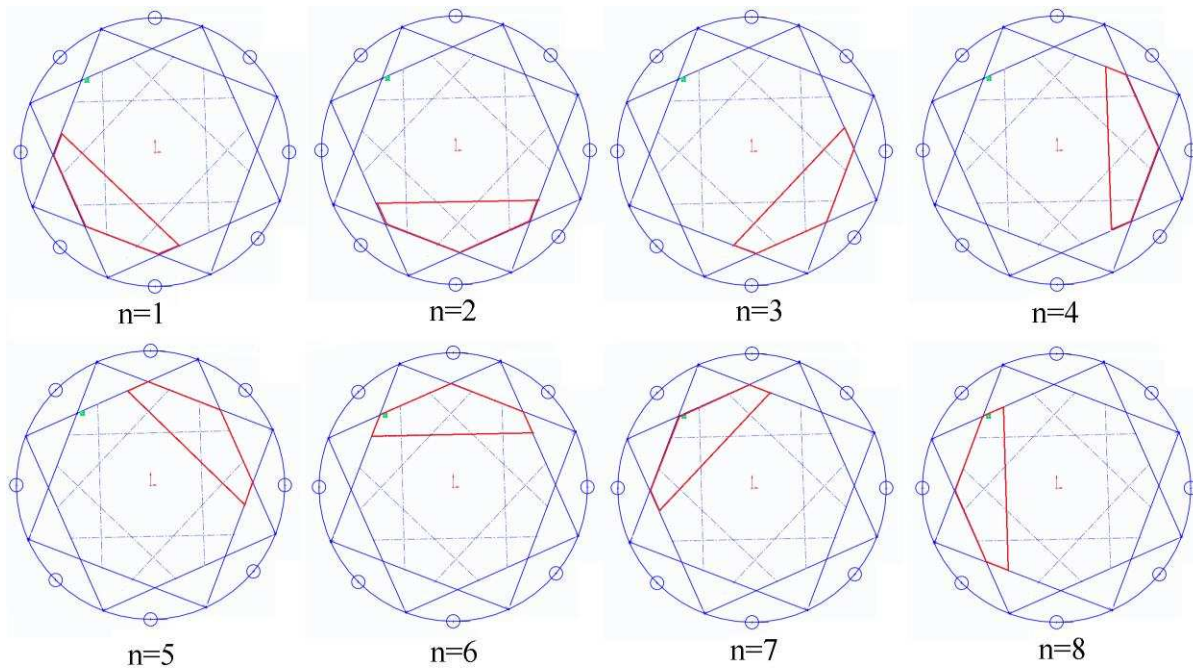
Figure 3.22 the boundary layer for Configuration IV, rotational position n (n= 1 to 8)

85

The measured solids volume fraction (α_1 to α_8) and calculated solids volume fraction ($\alpha_{1,0}$ to $\alpha_{8,0}$) are assumed to be located at the related Centres of Action CoA for Configuration I and Configuration IV respectively. The x and y coordinates for each CoA was obtained by applying Equations 3-7 and 3-8 (see section 3.4.1) to the sensitivity distributions of Configuration I (see Figure 3.16) and Configuration IV (see Figure 3.21). While $\alpha_{1,2}$ to $\alpha_{8,1}$ were located of the centroids of sub-areas $A_{1,2}$ to $A_{8,1}$, see Figure 3.23. The x and y coordinates of the sub-areas centroid ($A_{1,2}$ to $A_{8,1}$) was determined using solid-work software.
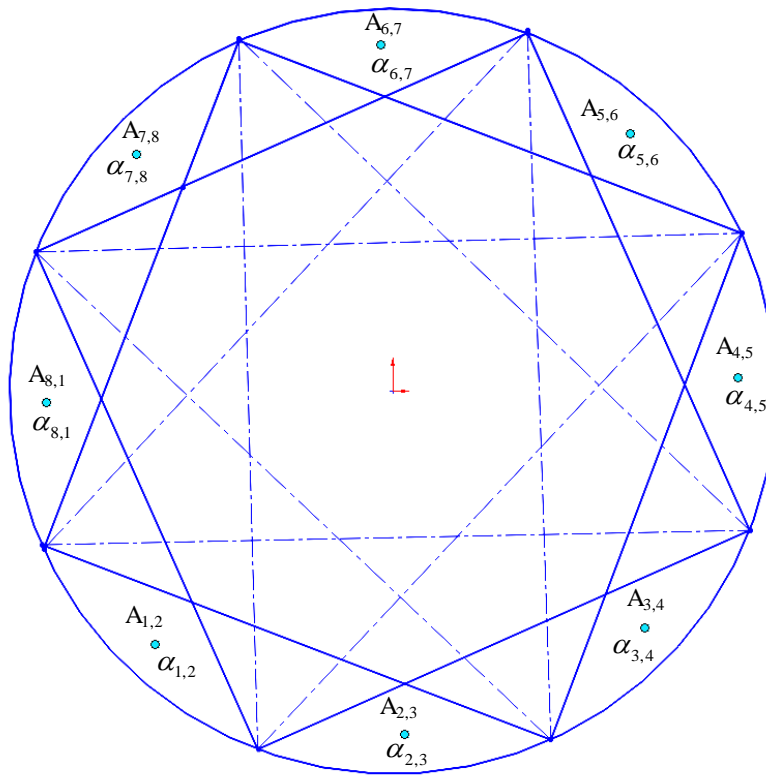
Figure 3.23 the centroid positions for the sub-areas $A_{1,2}$ to $A_{8,1}$

The x and y coordinates associated with α_1 to α_8 (areas A_1 to A_8), $\alpha_{1,0}$ to $\alpha_{8,0}$ (areas $A_{1,0}$ to $A_{8,0}$) and $\alpha_{1,2}$ to $\alpha_{8,1}$ (areas $A_{1,2}$ to $A_{8,1}$) are shown in Figure 3.26.

The values of the parameters which are shown in Equation 3-12 can be seen in Table 3-5

<div align="center">Table 3-5 the parameters values which are shown in Equation 3-11</div>

Equation 3-11 parameters	Values
A_1 and A_8	141.2 mm^2
$A_{8,1}$ and $A_{2,3}$	165.5 mm^2
$B_{1,8}$ and $B_{1,3}$	39 mm^2
$B_{1,0}$	474.2 mm^2
B_1	1165.4 mm^2
$\overline{\psi_1}$	0.0159 V
$\overline{\psi_{1,8,1}}$	0.026 V
$\overline{\psi_{1,2,3}}$	0.024 V
$\overline{\psi_{1,1}}$	0.0168 V
$\overline{\psi_{1,2}}$	0.0145 V
$\overline{\psi_{1,3}}$	0.013 V
$\overline{\psi_{1,8}}$	0.015 V
$\overline{\psi_{1,0}}$	0.012 V

3. Stage 3

Stage 3 was intended to investigate new configurations to find the local solids volume fraction distribution near the pipe centre with high sensitivity. These configurations failed to achieve the desired result because the measurement electrodes cannot detect the non-conductive elements at the middle of the pipe. Thus, in order to determine the solids' parameters at the pipe centre, a linear relationship was assumed between the measured solids parameters in stages 1 and 2 and selected points near the pipe centre (LP_n, n=1 to 8). A linear relationship was assumed between the local solids volume fraction in $A_{n-1,n}$ and $B_{n,0}$ and LP_{n+1} (n=1 to 8), see Figure 3.24.
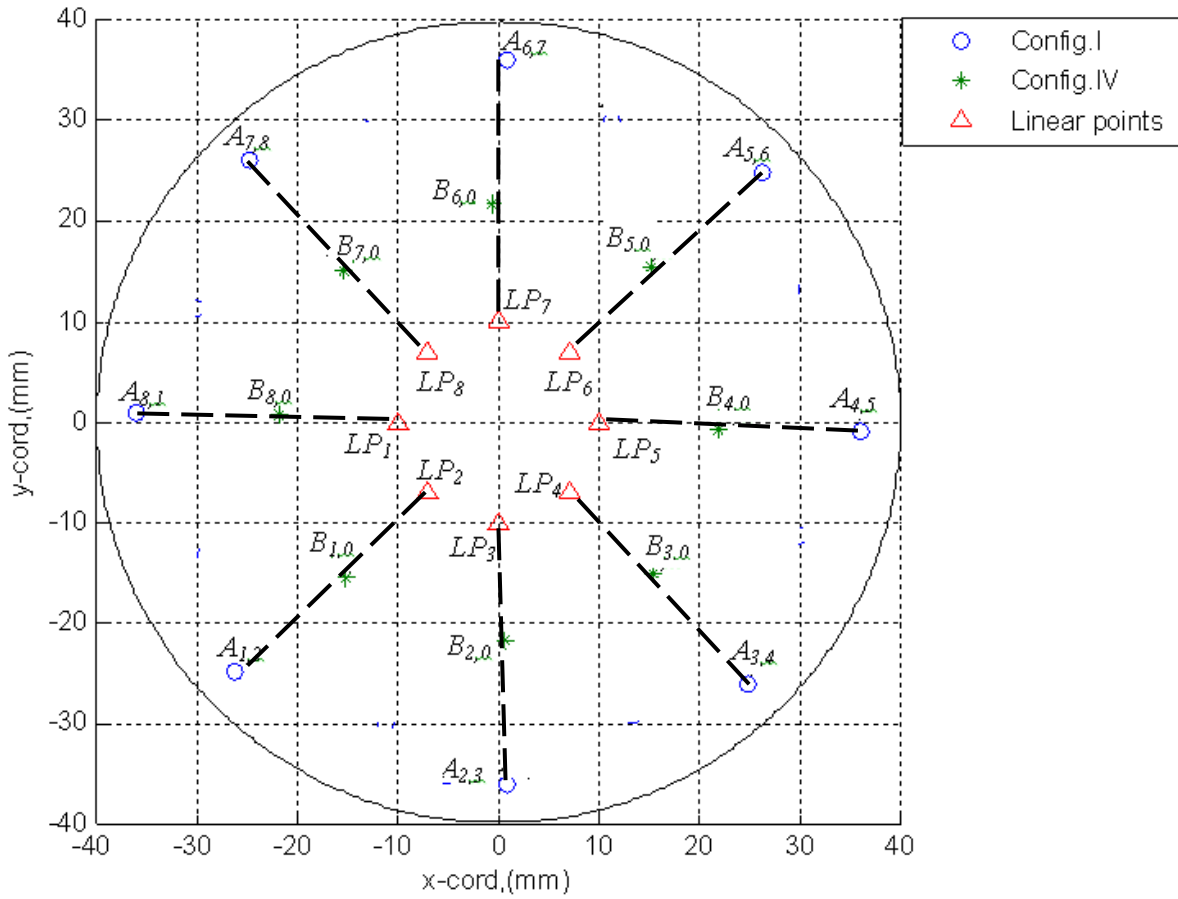
Figure 3.24 the linear relationship line between $A_{n-1,n}$ and B_n and LP_{n+1}

For vertical flow previous literature [15,16] shows that the solids volume fraction profile varies from being a "power law" shape for $\overline{\alpha} > 0.08$ to a flat shape for $\overline{\alpha} > 0.15$. For $\overline{\alpha} < 0.15$ the local solids volume fraction increases approximately linearly from near the pipe wall to mid-way to the pipe center, see Figure 3.25. For $\overline{\alpha} > 0.15$ the local solids volume fraction will have a relatively constant value throughout the pipe cross section.
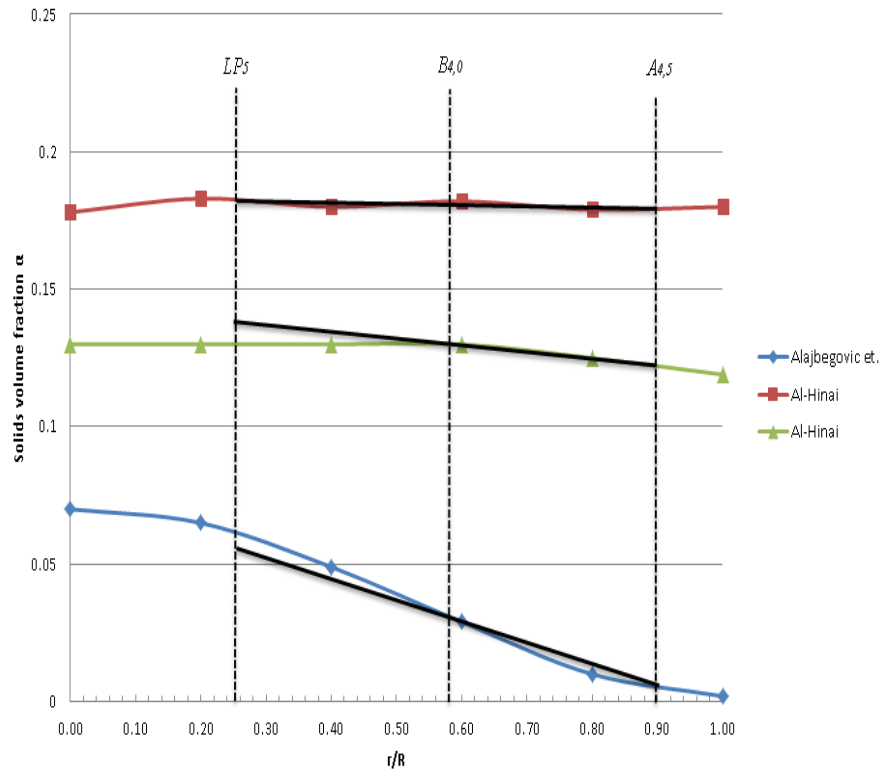
Figure 3.25 the solids volume fraction profiles obtained by Alajbegovic[15] and Al-Hinai [49]

As shown in Figure 3.25, assuming a linear relationship (black line) between the solids volume fractions at $A_{4,5}$ and $B_{4,0}$ will still give reasonable values for the solids volume fraction at point LP_5. Therefore, it was assumed that the local solids volume fraction α_{LP5} at LP_5 is given by:

$$\alpha_{LP5} = mx + b$$

Equation 3-17

where the magnitude of the slop m and the intercept b are depends on the values of the solids volume fractions at $A_{4,5}$ and $B_{4,0}$.

At 0° inclination, the solids flow profile is an axisymmetric profile. Therefore, the linear assumption between the solids volume fraction at $A_{n,n+1}$, $B_{n,0}$ and LP_n can be still applied in order

89

to measure the α_{LPn}. The magnitude of the slope m and the intercept b of the linearity are depends on the values of the solids volume fractions at $A_{n,n+1}$ and $B_{n,0}$, see Figure 3.24.

AM technique gives 32 solids volume fraction $(\alpha_{s,AM})_i$ (i=1 to 32) measurements inside the pipe cross-section, the x and y coordinates of these 32 points can be seen in Appendix A Table 9.2.
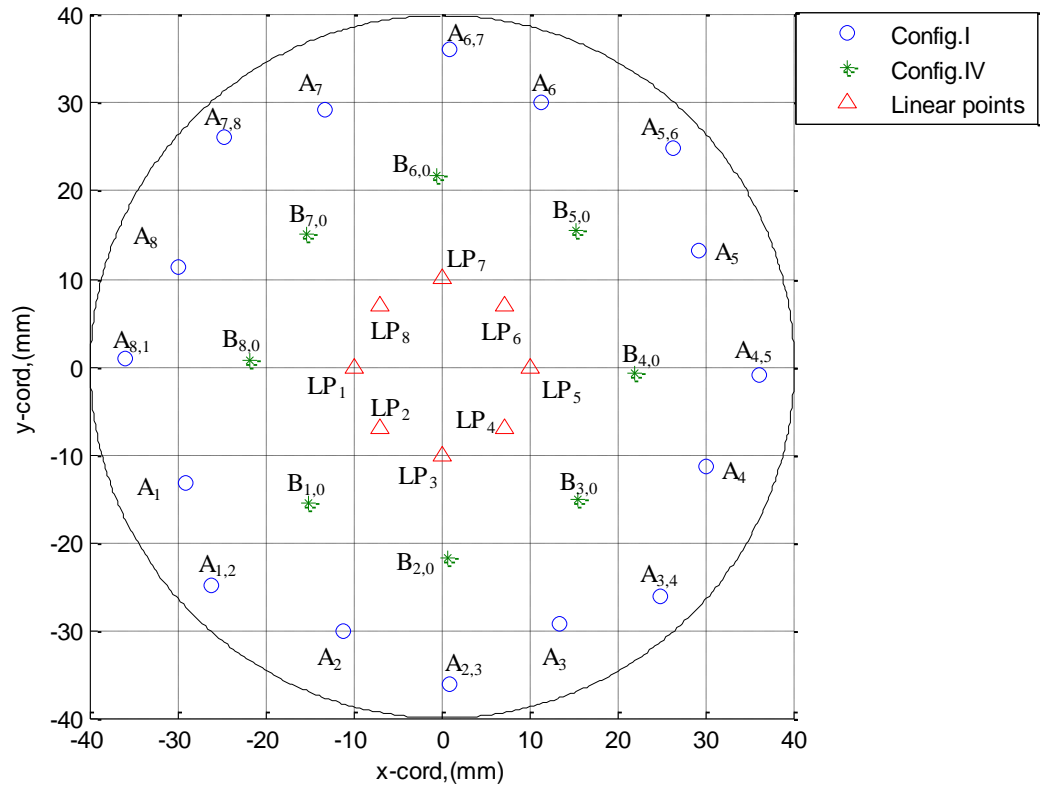
Figure 3.26 x and y coordinates of 32 measurements points

The area methodology technique was used effectively to measure the solids parameters in vertical solids-in-water flow, see Chapter 7 (Sections 7.2 and 7.3). However in solids-in-water flow inclined at 30º to vertical, the AM technique shows non-realistic values of solids volume fraction, the reason being that the AM can be only applied to the axisymmetric flows. The full explanation for the AM limitation is given in Section3.4.4.

90

3.4.3.3 Solids Velocity Measurement Using Area Methodology

The Area Methodology technique was used with the cross correlation technique in order to determine the solids velocity distribution in solids-in-water vertical flow. The measured solids velocity was assigned to the CoAs of Configurations I and IV rotational position n(n=1 to 8). This represents the solids velocity in areas A_1, A_2,..., A_8 and $B_{1,0}$, $B_{2,0}$,...., $B_{8,0}$.

The solids velocity in areas $A_{8,1}$ may be defined as:

$$v_{8,1} = \frac{v_8 + v_1}{2}$$

Equation 3-18

where v_8 and v_1 represent the solids velocities measured by cross correlation techniques, see section 4.3.2, for areas A_8 and A_1 respectively. Following the same steps, the velocities in areas $A_{1,2}$, $A_{1,2}$,...., $A_{7,6}$ were defined.

The previous literature review [15,49,56] shows that in vertical solids-in-water flows the solids velocity profiles have flat shapes. That means the solids velocity always has approximately the same values across the pipe cross section. Therefore the assumption of the linear relationship between the solids volume fraction at points $A_{n,n+1}$, $B_{n,0}$ and LP_n is still valid for the solids velocity measurement. Rotating in steps of 45°, the total solids velocities v_{LPn} (n=1 to 8) were calculated.

In order to obtain the solids velocity distribution $v_{s,ICC}$ and the solids volume fraction distribution $\alpha_{s,ICC}$, the 32 measurement points of the solids velocity $(v_{s,AM})_i$ and the solids volume fraction $(\alpha_{s,AM})_i$ (i=1 to 32) were interpolated through the pipe cross section using MATLAB 4griddata method V4.

3.4.4 Limitation of AM Technique

In solids-in-water flow inclined at 30° to the vertical, the solids volume fraction α_s varies as a function of y-coordinate, where α_s is much greater at the lower side of the pipe than the upper side. For the 30º inclined flow the AM managed to obtain a solids distribution inside the pipe, though it didn't produce realistic distributions. This failure could be due to the large variation in solids volume fraction between the lower and upper sides of the pipe. The validity of relationship in Equation 3-9 is highly dependent upon an axisymmetric solids concentration distribution in the flow cross section. Additionally, Equation 3-11 is also highly dependent on the mean sensitivity parameter $\overline{\psi}$. Any small error in $\overline{\psi}$ will effect α_s especially if α_s is relatively high, e.g. if it reaches 65-70 % at lower side of the pipe.

For the current study, the solids-in-water flow parameters were investigated for inclinations of 0°, and 30° degrees from the vertical. Based on the previous CoA and AM investigation, it was decided to use CoA methodology in inclined flow, while AM methodology was used in vertical flow.

3.5 Summary

- The COMSOL software was used to to simulate the sensitivity changes with dispersed phase for different Configurations $\phi = $ I, II, III and IV , see Section 3.2.

- An element with zero conductivity was used to simulate a dispersed phase. The sensitivity parameter was calculated using Equation 3-2 .

- The sensitivity distributions of Configurations $\phi = $ I, II, III and IV were rotated in steps of 45° in order to cover the total pipe cross-section.

- The boundary of the effective sensing region in each Configuration ($\phi = $ I, II, III and IV) and the nth rotational position ($n = 1\,to\,8$) can be defined as 10% of the maximum sensitivity distribution, Section 3.3.

- The x and y co-ordinates for the CoAs are calculated using Equation 3-7 and Equation 3-8, see Section 3.4.1. The measured solids parameters are assumed to be assigned to the x and y co-ordinates of the CoA.

- CoA technique provides 24 measurement points for each solids volume fraction and solids velocity inside the pipe. The 24 measured parameters were interpolated later through the pipe cross section to obtain the solids volume fraction distribution and the solids velocity distribution.

- CoA has a limited capability to measure low solids volume fraction in vertical flow see Section 3.4.3, though it worked effectively in inclined flow, section 3.4.1.

- Due to the CoA limitation in vertical flow, a new technique (Area methodology) was proposed by the author in order to measure the low solids volume fraction in solids-in-water vertical flow.

- The AM technique was based on dividing the pipe cross section into sub-areas. Where each of these sub-areas has a particular solids volume fraction and solids velocity obtained by direct measurement or mathematical calculations, see section 3.4.3.

- The AM has in total 32 measurement points inside the pipe cross section. The 32 measured parameters were interpolated later through the pipe cross section to obtain the solids volume fraction distribution and the solids velocity distribution.

- AM technique has a limited capability to measure solids volume fraction in inclined flow see Section 3.4.3, though it worked effectively in vertical flow, see Section 3.4.3.

93

- For the current study, it was decided to use CoA methodology in inclined flow and AM methodology in vertical flow.

4. CHAPTER 4: Implementation of the Impedance Cross Correlation Flow Meter

4.1 Introduction

This chapter describes the design and implementation of an Impedance Cross Correlation (ICC) flow meter which can be used in solids-water pipe flows to measure the in-situ volume fraction distributions of both phases and the local solids velocity distribution. The ICC flow meter comprises two arrays of electrodes, each array can be arranged in different configurations as described in Section 3.3. Changing the electrode configuration changes the electric field, and hence the region in the flow cross-section that is interrogated. The local solids velocity in the interrogated region is obtained by cross-correlating between the two electrode arrays. The local in-situ solids volume fraction is obtained from the mean mixture conductivity in the region under interrogation. A number of "interrogated regions" are used to obtain the solids velocity profile and the in-situ solids volume fraction profile in the flow cross-section. This process is carried out for each flow condition to be investigated. The in-situ water volume fraction, α_w is readily obtained from the measured in-situ solids volume fraction, α_s, by simple subtraction ($\alpha_w = 1 - \alpha_s$).

4.2 ICC Design and Construction

The ICC device is used to determine the distribution of the local solids velocity v_s the distributions of the local solids volume fraction α_s and hence the distribution of the local water volume fraction α_w. The ICC device consists of two arrays of eight electrodes separated by an axial distance of 50 mm. In each array the electrodes are mounted equidistantly around the

internal circumference of the pipe carrying the flow, see Figure 4.1. Every electrode in each array can be selected to be either "excitation", "measurement" or "earth".
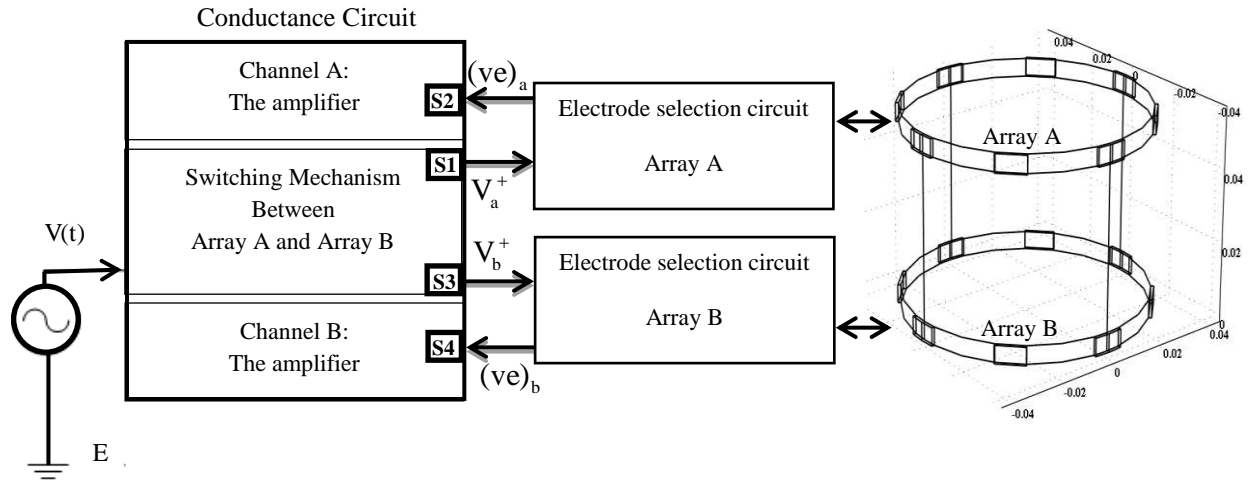
Figure 4.1 Schematic diagram for the ICC flow meter

The ICC device has similar features to dual-plane electrical resistance tomography (ERT) systems because both techniques consist of two electrode arrays mounted around the pipe. However in contrast to ERT systems, the ICC device has low implementation costs and needs no sophisticated algorithms to analyse the acquired data. In the present study of solids-in-water flow, water is the continuous conductive phase while the solids are considered to be the dispersed phase with zero electrical conductivity. For the ICC device to produce sensing regions inside the pipe, the states of each array are changed according to four predefined configurations, see Section 3.2 , These configurations can each be rotated (in steps of 45°) to one of eight positions (n=1 to 8) to allow measurement over the cross-sectional area of the pipe. In Figure 4.1, the excitation (V^+) electrodes in array A and B are connected to S1 and S3 respectively and the ve electrodes in array A and B are connected to points S2 and S4 respectively. The earth (E)

96

electrodes are grounded. The chosen configuration of electrodes was obtained using the electrode selection circuit described in Section 4.2.3, and shown schematically in Figure 4.1.

4.2.1 The ICC Body Design

The body of the ICC consisted of two parts: a stainless steel casing and an inner flow tube, see Figure 4.2. The stainless steel casing was to protect the inner structure and electrode connections and to electrically shield the electrodes from external sources of electrical noise. The flow tube is a tube machined from Polyether Ether Ketone (PEEK) material, which is non-conducting. The flow tube has an 80 mm internal diameter matching the pipe carrying the solids-in-water flow and is 310 mm long.

Two arrays of electrodes measured the fluid velocity using a cross correlation technique. The value of the axial array separation L of the two arrays in the present investigation was 50 mm. The selection of the optimum axial separation L between the two electrode arrays was based on a survey of previous work carried out by Deng et al., [105]. According to this study, for an 80 mm diameter pipe the optimum distance L between the two electrodes arrays for the purpose of determining the flow velocity by cross-correlation should be 50 mm centre to centre, a result which was obtained by experimentally varying the distance between two electrode arrays incrementally and observing which separation gave the best results, see also S.Al-Hinai [49].
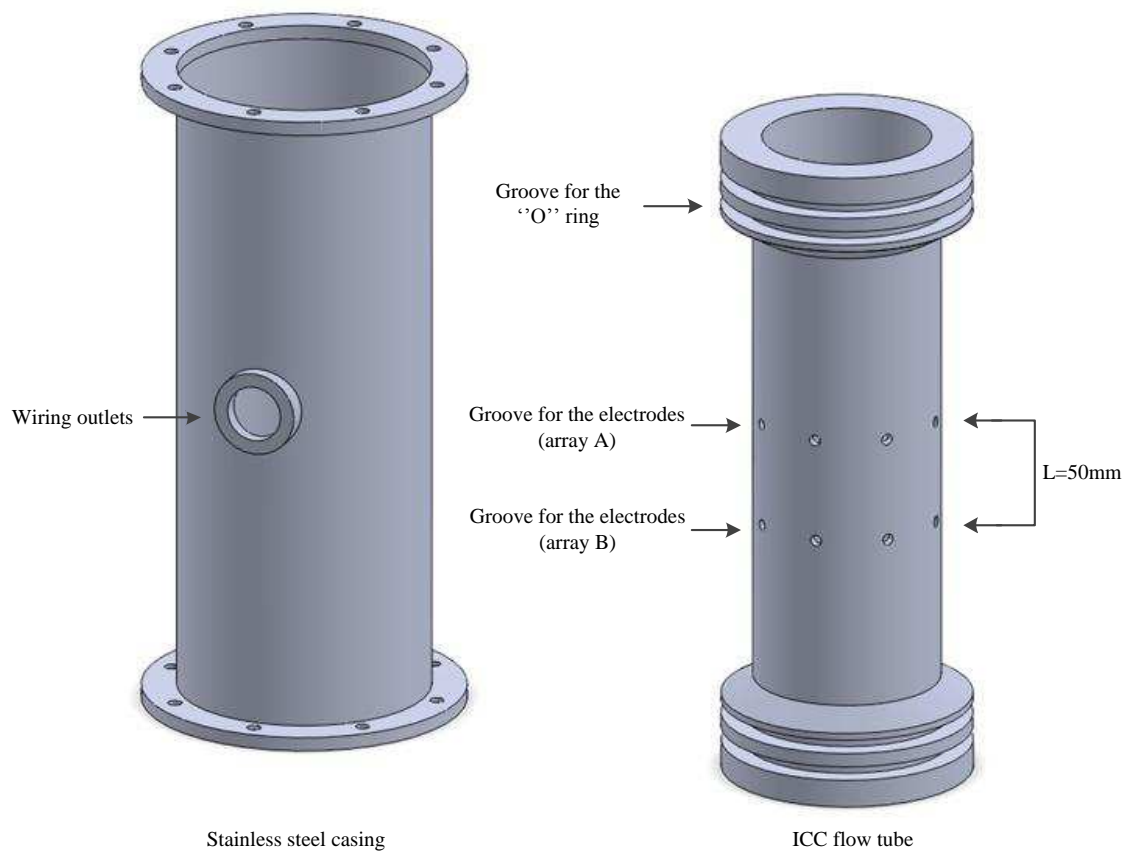
Figure 4.2 ICC stainless steel casing and inner flow tube

Each array contained eight electrodes equally spaced over the internal circumference of the inner flow tube. Each electrode had dimensions of 10 mm long x 5 mm wide x 1.5 mm thick, see Figure 4.3. While the electrodes were close enough to give an adequately detailed picture of the flow in the pipe, the electrode arrangement prevented interference between the electrode connections in the space among the ICC flow tube and stainless steel casing.
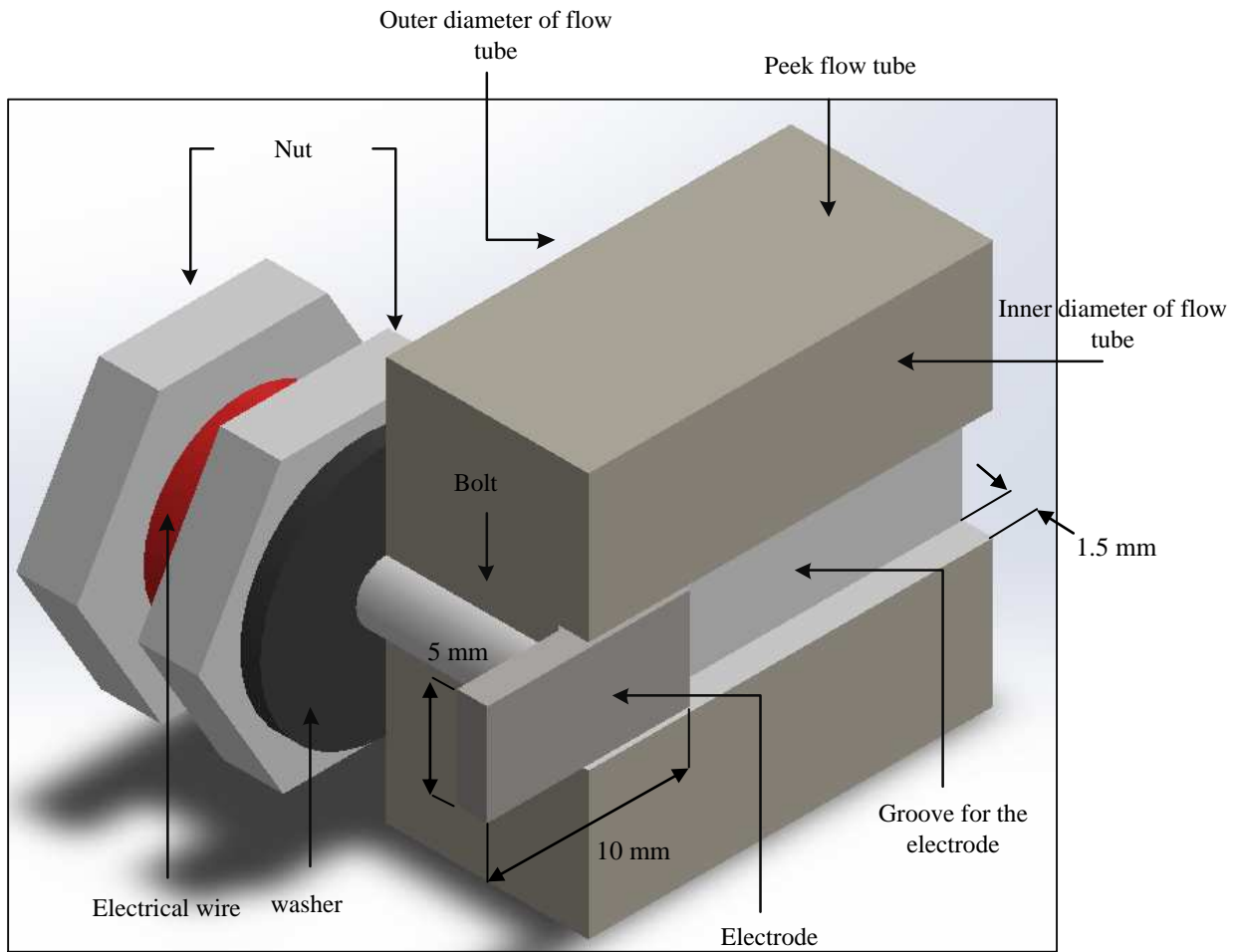
Figure 4.3 Electrode assembly inside the inner flow tube

As shown in Figure 4.3, a hole was drilled through the tube wall and a rectangular groove 1.5 mm deep and 5 mm wide was cut in the inner face of the flow tube to take the stainless steel electrodes. Each electrode has a long threaded pin on its back that passed through the wall of the tube. Each electrode was mechanically fixed firmly into its position using a washer and nut. The copper wires carrying the excitation and measurement signals were attached to the pin and gripped using a second nut.
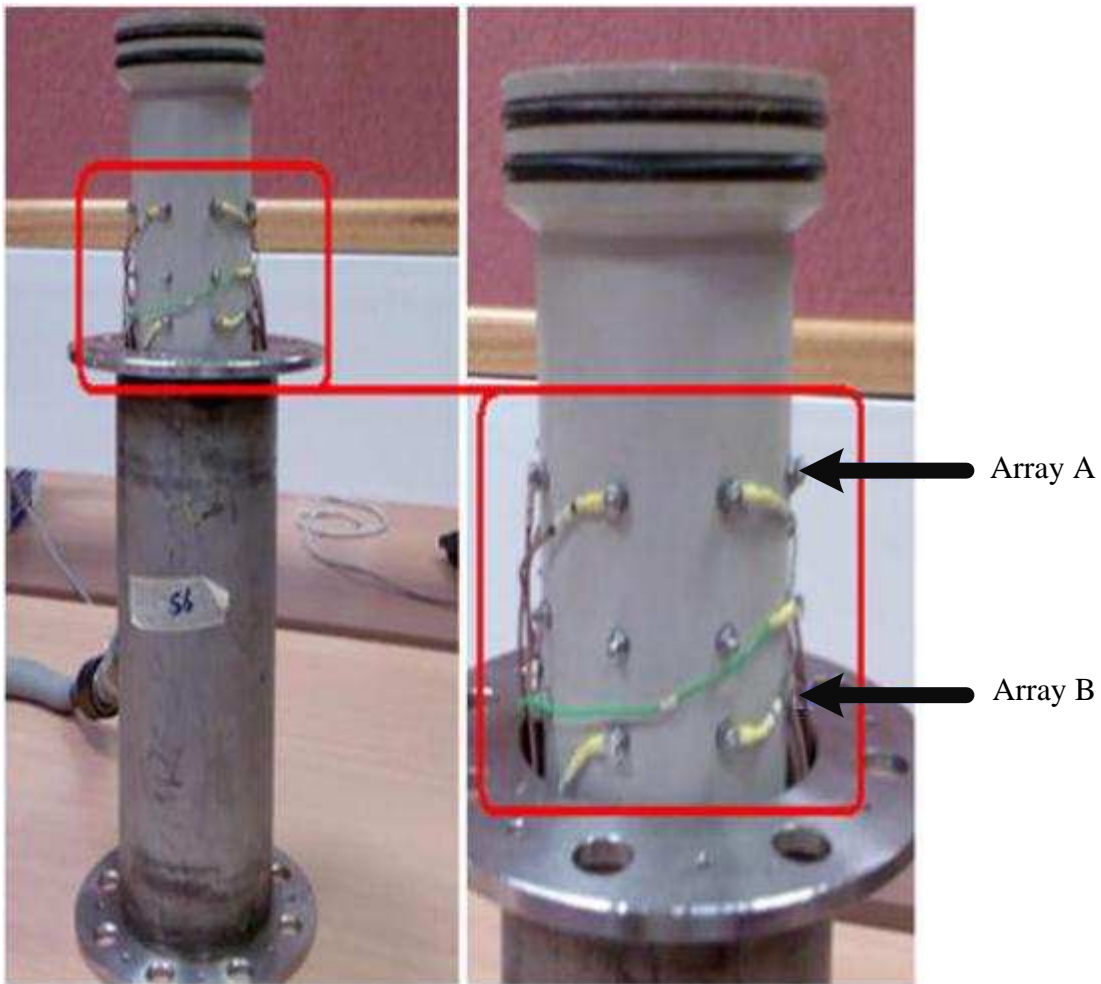
Figure 4.4 Photo of Impedance Cross – Correlation device

Figure 4.4 shows a photo of the body of the ICC device, note that the flow tube has four electrode arrays in preparation for possible future investigations. In the present investigation only arrays A and B were used.

4.2.2 Conductance Circuit Design

A circuit was designed and built to measure the conductance of the multiphase mixture between the V^+ and ve electrodes, sequentially for each of the eight rotational positions and, for each configuration. The schematic diagram, Figure 4.5, shows the main stages of the circuit for measuring the conductance of the multiphase mixture at each of the two electrode arrays. It is made up of two main stages. As the channels, for both arrays A and B, are the same it is only necessary to describe one channel.
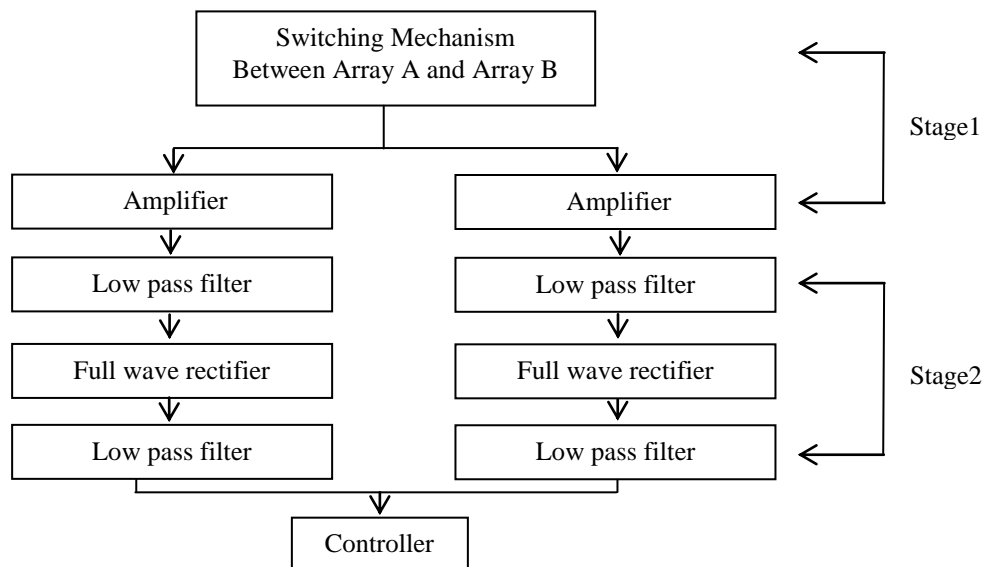
Figure 4.5 Schematic diagram of the conductance measurement circuit

1. Stage1:

Since the ICC has two arrays (A and B), it was necessary to ensure that there was no cross-talk between Channel A and Channel B. A switching mechanism was built to ensure that the V^+ electrodes in array A (connected to point S1, see Figure 4-1) and the V^+ electrode in array B (connected to point S3, see Figure 4-1) were connected alternately to the excitation source V(t). This meant that both arrays were never active at the same time, see Figure 4.6, (i.e. when array A is active, array B is not), and so cross-talk between the two arrays was prevented.
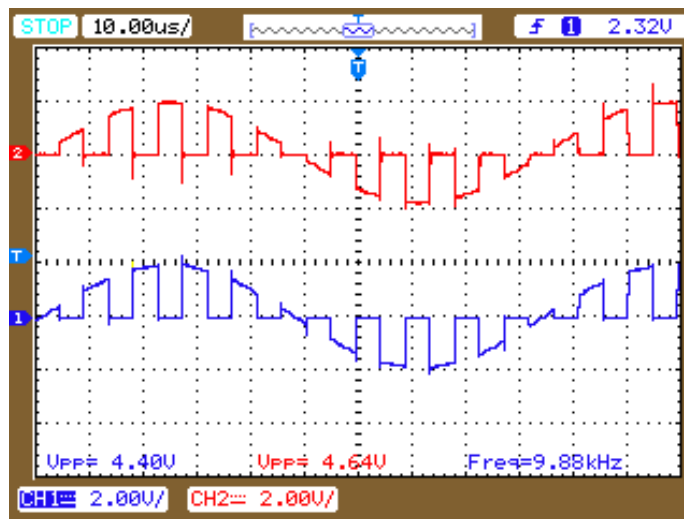
Figure 4.6 The excitation signals in array A (red signal denotes V_a^+) and array B (blue signal denotes V_b^+)

The switching mechanism, see Figure 4.7, consisted of an XR-2206 function generator (working in a similar manner to a 555 timer) and two MAX 303 high speed analogue switches. The XR-2206 fed the two MAX 303 analogue switches with a 100 kHz switching frequency which represents the two states: low (0) and high (1), and which switched the 10 kHz excitation source V(t) alternately between array A and array B as shown in Figure 4.6.

Figure 4.7 shows the MAX 303 analogue switches in the normally open configuration i.e. where the output from XR-2206 was at the low state (0).
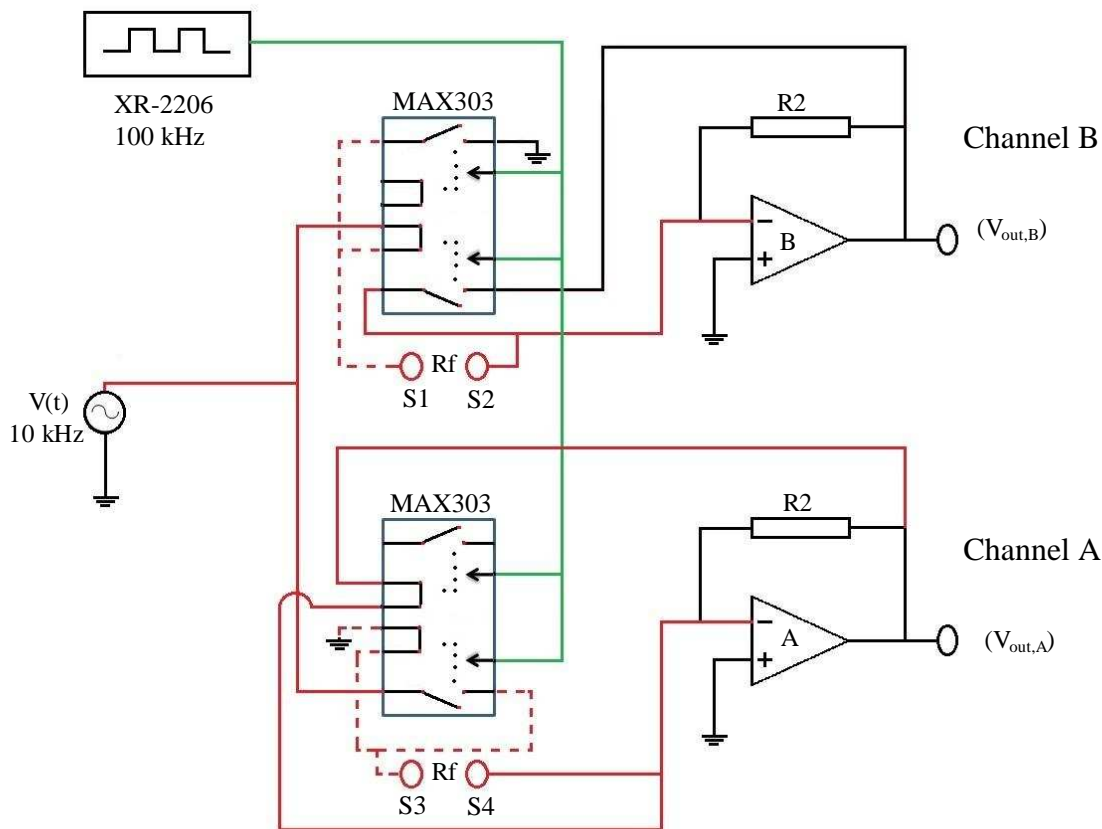
Figure 4.7 Switching mechanism with low state (0)

As shown in Figure 4.7, at low state, S1 is connected to the excitation signal $V(t)$ while S2 is connected to the negative input of the channel B inverting amplifier. Depending upon the electrode configuration selected, one or more electrodes in Channel B will also be connected to point S1 as described in Section 4.2.3. At the low state, the output voltage ($V_{out,B}$) of the inverting amplifier in channel B will be representative of the fluid mixture conductivity between the excitation and virtual earth electrodes in channel B. Also during the low state, point S3 is earthed while point S4 is connected to the negative input of the inverting amplifier for channel A and

also is short circuited to the output of this inverting amplifier. This design methodology also helps to reduce interference between array A and array B.

When switched to the high (1) state, the configuration of the MAX 303 analogue switches acts as shown in Figure 4.8.
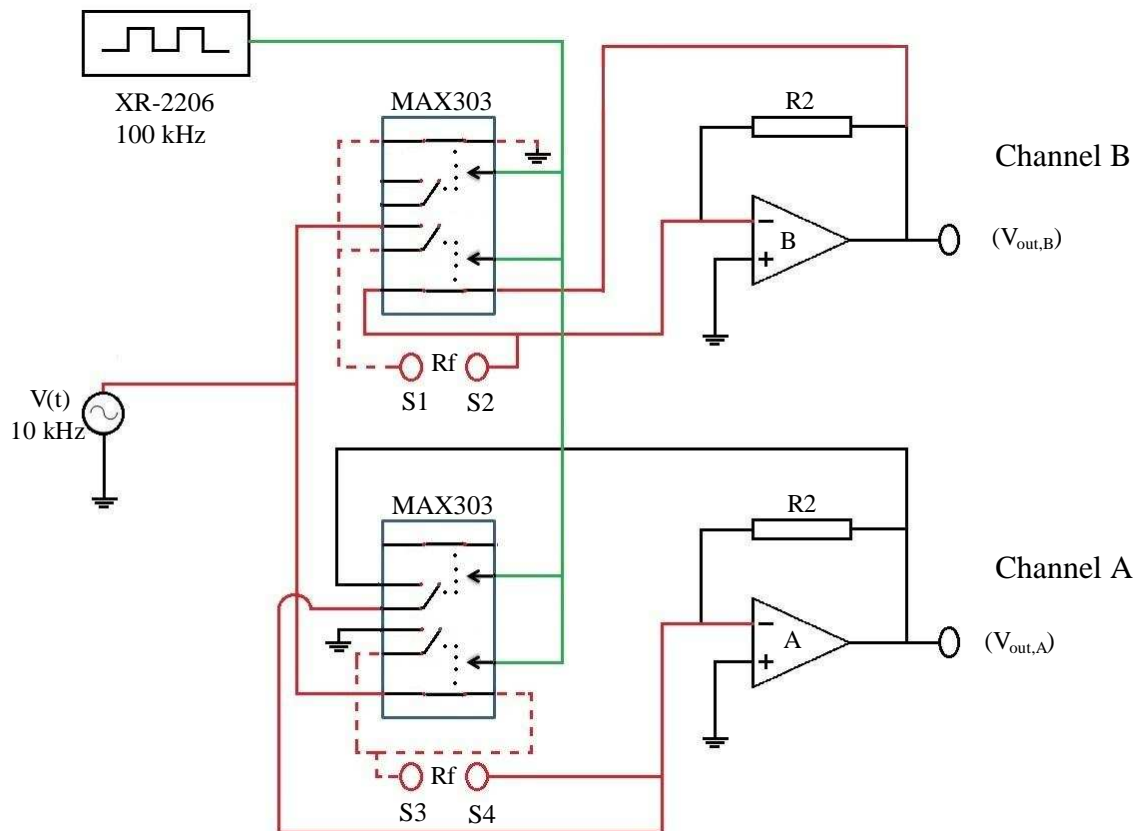
Figure 4.8 Switching mechanism with high state (1)

In the high state (1) in array A, S3 is connected to the excitation signal $V(t)$ and S4 is connected to the negative input of the channel A inverting amplifier. Additionally, the output ($V_{out,A}$) of the inverting amplifier in channel A will be activated since the output from the channel A amplifier is no longer short circuited to the inverting input. Meanwhile, S1 is earthed and S2 is connected

104

to the negative input of the inverting amplifier for channel B and also to the output of this inverting amplifier. The conductance circuit in Figure 4.7 and Figure 4.8 can be simulated as shown in Figure 4-9. Figure 4-9 represents the conductance circuit simulation for channel B only. Note that Channel A has a similar simulation as Channel B.
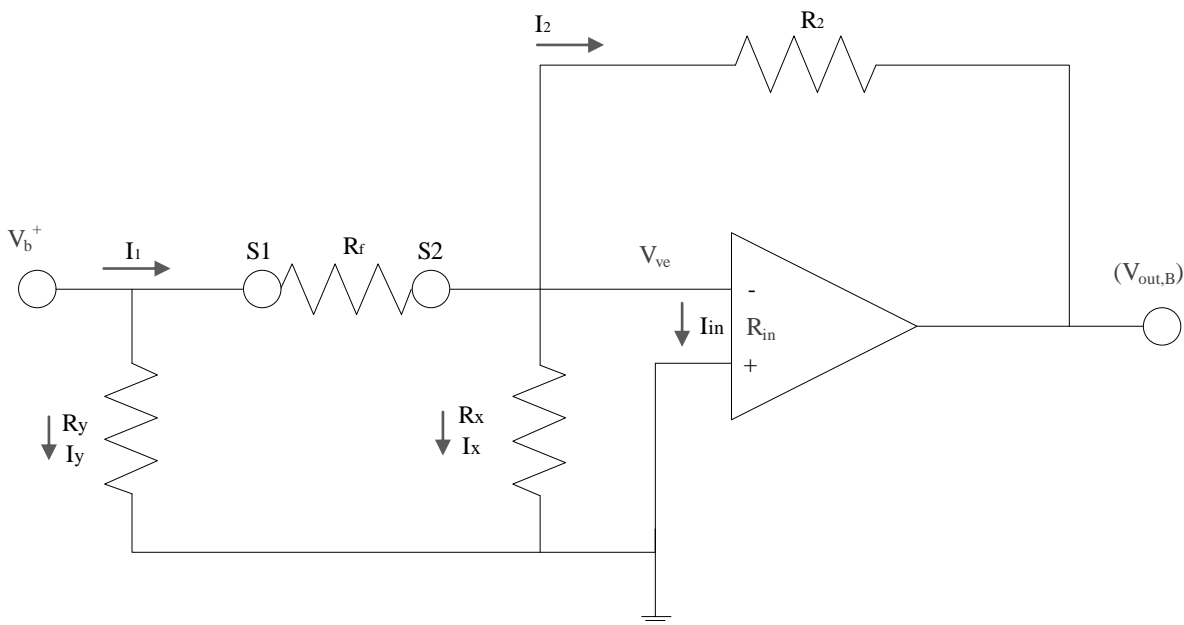
Figure 4.9 simulated conductance circuit for channel B

Figure 4-9 shows the conductance circuit used to measure the change in conductivity of the flow inside the tube, where R_f is the electrical resistance of the fluid between the excitation electrode(s) and the virtual earth electrode(s) and R_2 is the feedback resistance of the inverting amplifier.

R_y is the electrical resistance of the fluid between the excitation electrode(s) and the grounded electrode(s), while R_x is the electrical resistance of the fluid between the virtual earth electrode(s) and the grounded electrodes.

Since R_y has no effect on the operation of the amplifier, the current equation of the conductance circuit can be written as:

105

$$I_1 = I_2 + I_x + I_{in}$$
<div align="right">Equation 4-1</div>

where: I_2 is the feedback current, I_1 is the current between the V(t) and V_{ve}, I_x is the current between the ve and ground and I_{in} is the internal amplifier current. The V_{ve} voltage can be written as:

$$V_{ve} = -\frac{V_{out,B}}{A}$$
<div align="right">Equation 4-2</div>

where: A is the open loop amplifier gain.

Equation 4-1 can re-write in term of the voltages and resistances as follows:

$$\frac{V_b^+ - V_{ve}}{R_f} = \frac{V_{ve} - V_{out,B}}{R_2} + \frac{V_{ve}}{R_{in}} + \frac{V_{ve}}{R_x}$$
<div align="right">Equation 4-3</div>

Substituting Equation 4-2 into Equation 4-3:

$$\frac{V_b^+ - (-V_{out,B}/A)}{R_f} = \frac{(-V_{out,B}/A) - V_{out,B}}{R_2} + \frac{(-V_{out,B}/A)}{R_{in}} + \frac{(-V_{out,B}/A)}{R_x}$$
<div align="right">Equation 4-4</div>

Equation 4-4 can be simplified as:

$$V_{out,B}[\frac{1}{R_2} + \frac{1}{AR_2} + \frac{1}{AR_f} + \frac{1}{AR_{in}} + \frac{1}{AR_x}] = \frac{-(V_b^+)}{R_f}$$
<div align="right">Equation 4-5</div>

The relation between $V_{out,B}$ and V^+ can be obtained by re-arranging Equation 4-5:

$$\frac{V_{out,B}}{V_b^+} = -\frac{R_2}{R_f} \left\{ \frac{1}{1 + \frac{1}{A}\left(1 + \frac{R_2}{R_f} + R_2\left(\frac{1}{R_{in}} + \frac{1}{R_x}\right)\right)} \right\}$$

Equation 4-6

When the open loop gain A is very high, (which is the case for the LF356 amplifier used in the present study) Equation 4-6 can be simplified to:

$$\frac{V_{out,B}}{V_b^+} = -\frac{R_2}{R_f}$$

Equation 4-7

And so the fluid resistance R_x in Figure 4.9 can be ignored. Note that Equation 4-7 is the same equation used in the COMSOL simulation to calculate the sensitivity parameter, see section 3.2.

2. Stage2:

Figure 4-10 shows stage 2 of the conductance measurement circuits. Since Stage 2 in channel A and Channel B are the same it is only necessary to describe one.
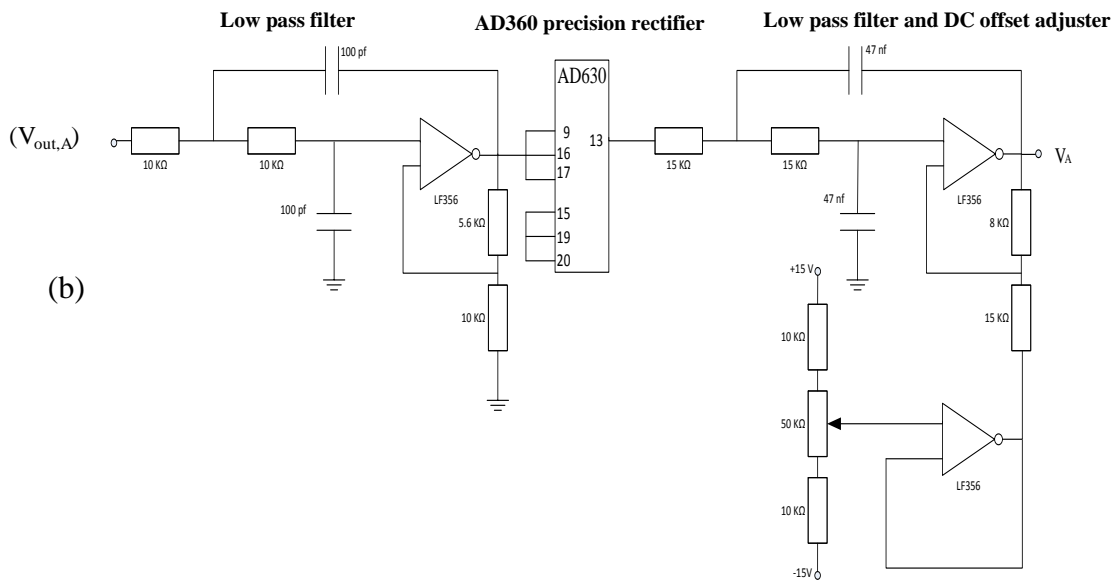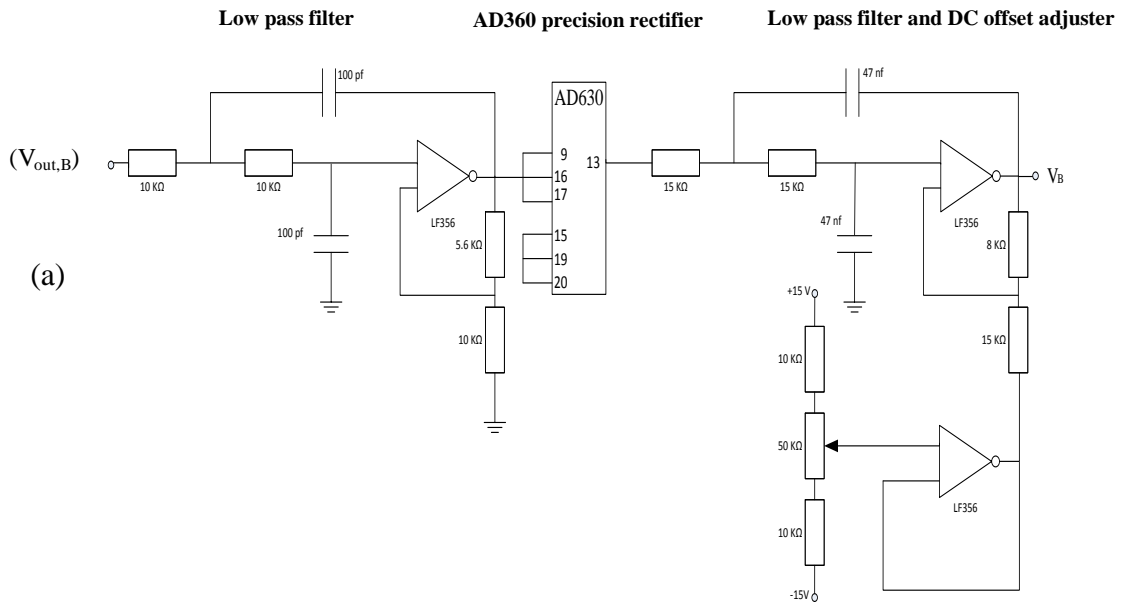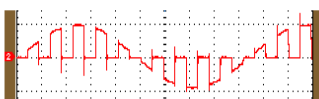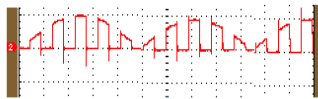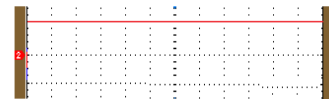
Figure 4.10 Stage 2 of the conductance circuit (a) and (b) for both channels B and A respectively, (c) is the output signal from low pass filter, (d) is the output signal from the AD630 precision rectifier and (e) is the output signal from the low pass filter and DC offset adjuster

In Channel B, the output signal $V_{out,B}$ from the inverting amplifier passed through a low pass Butterworth filter with a cut-off frequency of 150 kHz to remove any high frequency noise which produced by the high speed switching between the two arrays A and B, Figure 4-10c . An AD630 integrated circuit was used as a precision rectifier, see Figure 4.10.

The main purpose of the AD630 was to perform full wave rectification on the $V_{out,B}$ voltage signal, refer Figure 4.10d. This signal was then fed into a low pass Butterworth filter with cut-off frequency of 200 Hz to give a DC output voltage V_B, refer Figure 4.10e. A DC offset adjuster was used during the setting-up procedure to adjust the output signal V_B to zero when air only was present in the pipe and hence the mixture conductivity (σ_m) was effectively zero.

The output signal from Channel B can be written as:

$$V_B = k\,V_{out,B}$$
<div align="right">Equation 4-8</div>

Where k represent the circuit gain.

The same circuit design was applied to channel A, where V_A represents the output signal from Channel A.

In this study, the solids volume fraction was obtained using the output single V_B from Channel B, while the solids velocity was determined using the cross correlation technique between the output signals V_A and V_B , see Section 4.3 .

4.2.3   Electrode Switching Circuit

Since the ICC flow meter has two electrode arrays, two electrode selection circuits were designed to control the state of each electrode inside each array, see Figure 4.1. The electrode selection circuits were designed to be able to select any electrodes from a given array (A or B)

and connect them to the excitation V^+ (potential points S1 and S3 in Channel A and B respectively), virtual earth measurement ve (points S2 and S4 in Channel A and B respectively) or to earth E potential.

Each electrode selection circuit has three 74AC573 latch chips denoted as Latch1 to Latch3 in array B and Latch4 to Latch6 in array A. Each one of these chips is fed with eight defined signals and one latch signal. The latch output response to the received signal depends upon the state of the Latch Enabled (LE) input. Additionally, each electrode selection circuit has 24 DG-403 high speed analogue switches to control the eight electrodes in each array.

Note that, if the ith electrode in array B is set to a given potential (V^+, ve or E) then the corresponding electrode in array A is also set to the same potential.

Fourteen digital outputs (D/I1 to D/I14) from a VM1 Microcontroller were used to control the two electrode selection circuits, see section 5.3.1. Digital outputs D/I1 to D/I8 were used to set the defined signals to all the six latches input (Dm_j)th (m=1 to 8, j =1 to 6 where j represents the Latch label and m is the electrode number), see Figure 4.11. As an example, in the electrode selection circuit of array B, the digital signal from D/I1 is connected to D1_1 in Latch1, D1_2 in Latch2 and D1_3 in Latch3. Meanwhile, the same digital signal from D/I1 is also connected to D1_4 in Latch4, D1_5 in Latch5 and D1_6 in Latch6 in the electrode selection circuit of array A, see Figure 4.11. The latch outputs $(Q_{m\_j})^{th}$ (m=1 to 8, j = 1 to 6) in response to the received signal depended upon the state of the Latch Enabled input (LE1 to LE6) where LE1 to LE6 are controlled by D/I9 to D/I14 respectively.

Array A

Array A

D-Type Latch4
Q1-1 Q2-1 Q3-1 Q4-1 Q5-1 Q6-1 Q7-1 Q8-1
H
D1-1 D2-1 D3-1 D4-1 D5-1 D6-1 D7-1 D8-1 LE-4

D-Type Latch5
Q1-2 Q2-2 Q3-2 Q4-2 Q5-2 Q6-2 Q7-2 Q8-2
L
D1-2 D2-2 D3-2 D4-2 D5-2 D6-2 D7-2 D8-2 LE-5

D-Type Latch6
Q1-3 Q2-3 Q3-3 Q4-3 Q5-3 Q6-3 Q7-3 Q8-3
L
D1-3 D2-3 D3-3 D4-3 D5-3 D6-3 D7-3 D8-3 LE-6

D/I1 D/I2 D/I3 D/I4 D/I5 D/I6 D/I7 D/I8
Digital Output
from VM1
D/I9 D/I10 D/I11 D/I12 D/I13 D/I14

Array B

Array B

D-Type Latch1
Q1-1 Q2-1 Q3-1 Q4-1 Q5-1 Q6-1 Q7-1 Q8-1
H
D1-1 D2-1 D3-1 D4-1 D5-1 D6-1 D7-1 D8-1 LE-1

D-Type Latch2
Q1-2 Q2-2 Q3-2 Q4-2 Q5-2 Q6-2 Q7-2 Q8-2
L
D1-2 D2-2 D3-2 D4-2 D5-2 D6-2 D7-2 D8-2 LE-2

D-Type Latch3
Q1-3 Q2-3 Q3-3 Q4-3 Q5-3 Q6-3 Q7-3 Q8-3
L
D1-3 D2-3 D3-3 D4-3 D5-3 D6-3 D7-3 D8-3 LE-3

D/I1 D/I2 D/I3 D/I4 D/I5 D/I6 D/I7 D/I8
Digital Output
from VM1
D/I9 D/I10 D/I11 D/I12 D/I13 D/I14

Figure 4.11 schematic diagram for the 6 D type Latch connected to fourteen Digital outputs (D/I1 to D/I14) from VM1 microcontroller

111

The latch setup mechanism can be summarised as shown in Figure 4.12 below:
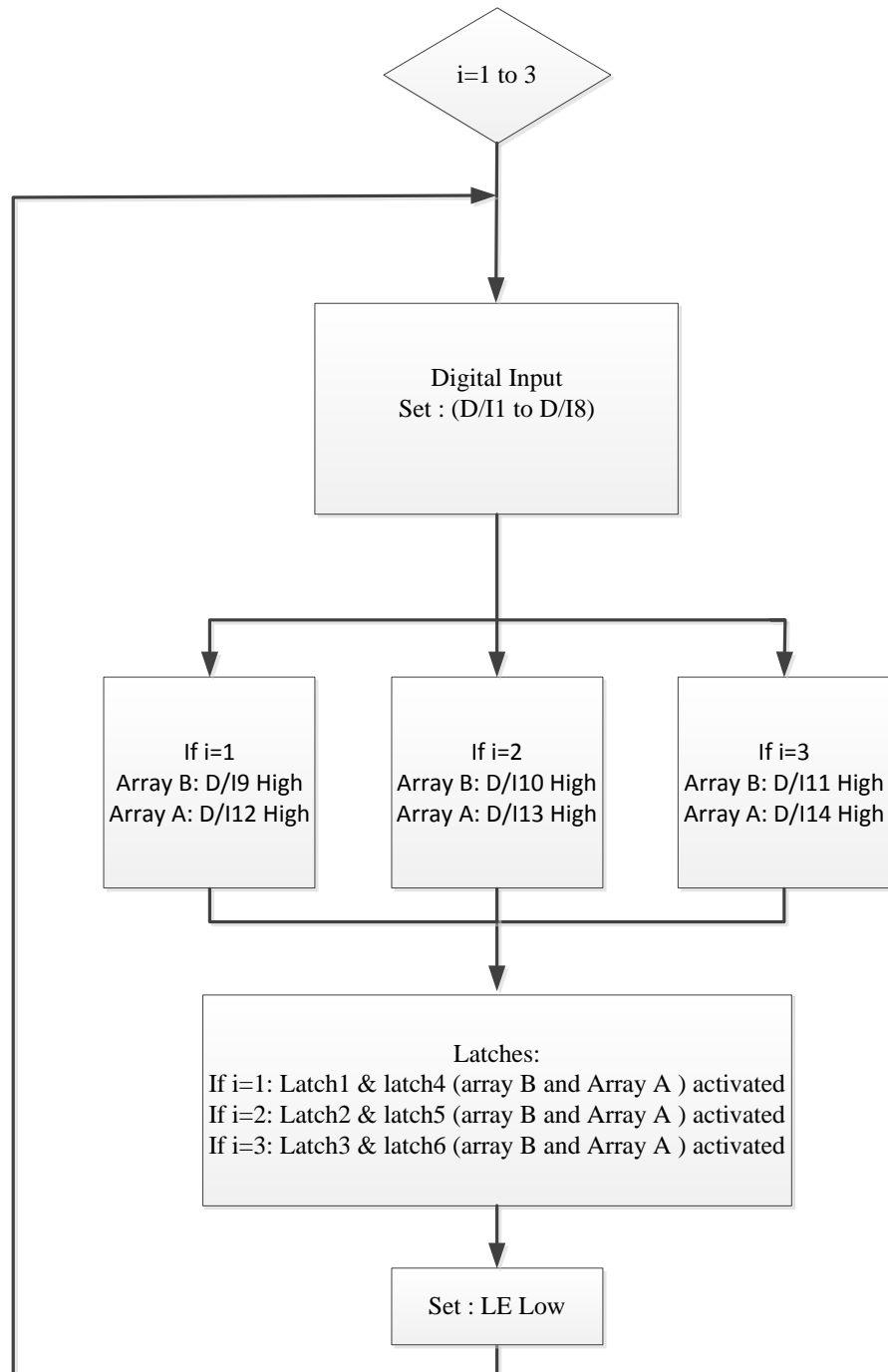
Figure 4.12 The latch setup mechanism for arrays A and B

112

Each electrode array (A or B) in the ICC meter has an input from each of the three latches. The selection of the electrode configurations is operated by the DG-403 analogue switches (see Figure 4.13). The output of this circuit is connected to the S1 (V^+) and S2 (ve) in the conductance circuit (see Figure 4.1). As mentioned earlier, there are three states to be chosen in order to define the electrode status. Table 4-1and Table 4-2 show the truth tables of the selection of the three states for arrays B and A respectively.

Table 4-1: Truth table for m^{th} electrode in array B

Electrode status	Q_{m_1}	Q_{m_2}	Q_{m_3}
Excitation electrode (V^+)	H	L	L
Virtual earth measurement electrode (ve)	L	L	L
Earth (E)	L	H	L

Table 4-2 Truth table for m^{th} electrode in array A

Electrode status	Q_{m_4}	Q_{m_5}	Q_{m_6}
Excitation electrode (V^+)	H	L	L
Virtual earth measurement electrode (ve)	L	L	L
Earth (E)	L	H	L

where: H is state High (1), L is state Low (0) and m is the electrode number (m=1 to 8).

Based on the truth table, the electrode m in each array can be connected to one of three potentials (V^+, ve and E). The schematic diagram in Figure 4.13 is used to explain the operating principles of the electrode selection circuit when connecting electrode 1 to the excitation signal V^+ of channel B (i.e. to point S1 of the channel B).
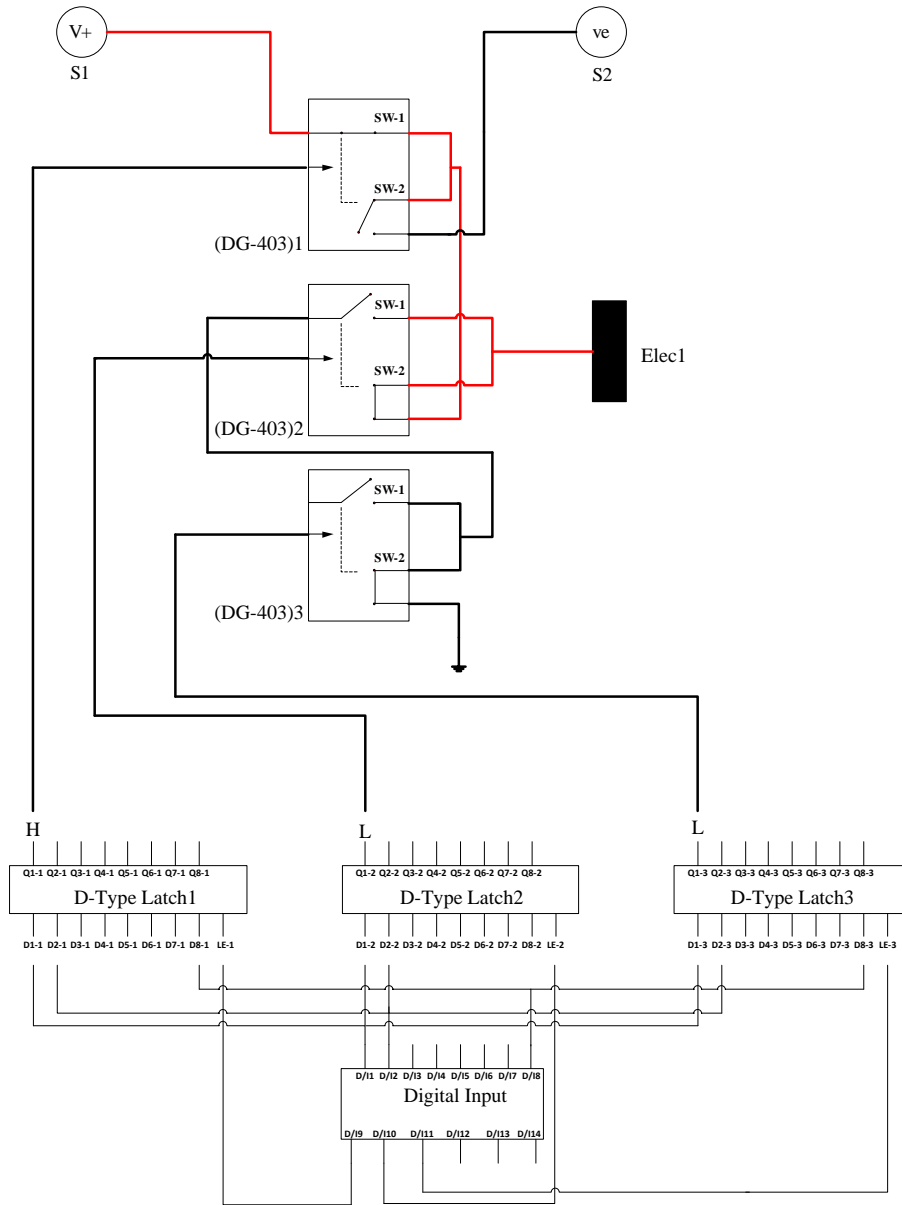
Figure 4.13 Electrode 1 connected to Excitation signal V^+, Array B

Taking electrode 1 in array B as an example:

114

- **Connected to excitation voltage (V^+):**

According to Table 4-1, to connect electrode 1 to excitation V^+, Q_{1_1} in Latch1 is set to High and Q_{1_2} in Latch2 and Q_{1_3} in Latch3 are set to Low, see Figure 4.13. This arrangement closes the high speed analogue switch $(DG-403)_1$ leading to the SW-1 terminal and opens SW-2. Since Q_{1_2} in Latch2 and Q_{1_3} in Latch3 are set Low, the analogue switches $(DG-403)_2$ and $(DG-403)_3$ remain at normally open configuration (SW-1 open and SW-2 close). This configuration of switches sets electrode 1 to excitation.

- **Connected to virtual earth measurement (ve)**

To connect electrode 1 to the virtual earth measurement (ve), Q_{1_1} in Latch1, Q_{1_2} in Latch2 and Q_{1_3} in Latch3 are set Low, see Figure 4.14. This arrangement allows the analogue switches $(DG-403)_1$, $(DG-403)_2$ and $(DG-403)_3$ to stay at normally open configuration (SW-1 open and SW-2 closed). This configuration of switches sets electrode 1 for virtual earth measurement (ve).
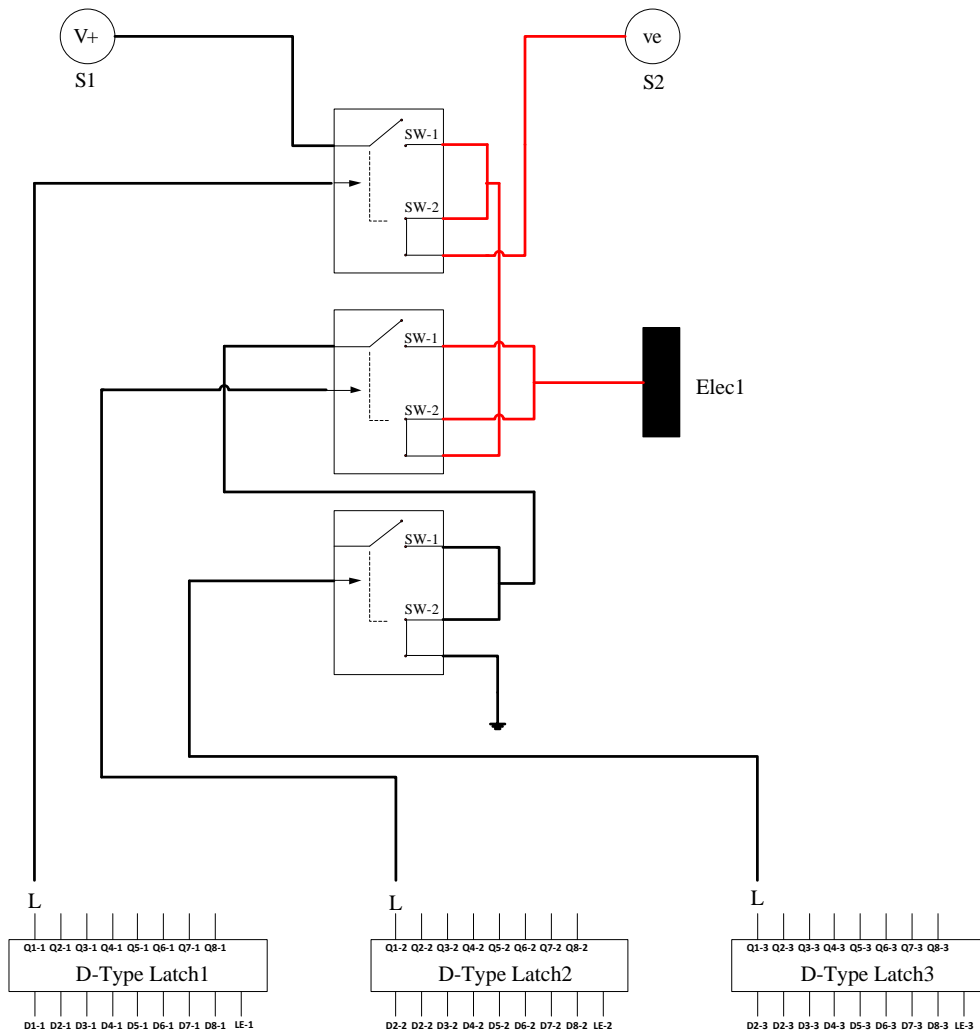
Figure 4.14 Electrode 1 connected to virtual earth measurement (ve), array B

- **Connected to earth (E):**

To connect electrode 1 to earth (E), Q_{1_2} in Latch2 is set High while Q_{1_1} in Latch1 and Q_{1_3} in Latch3 are set Low, see Figure 4.15. With this arrangement, the high analogue switch $(DG-403)_2$ is activated causing the SW-1 terminal to be closed and SW-2 to be opened. Since Q_{1_1} in Latch1 and Q_{1_3} in Latch3 are set Low, the analogue switches $(DG-403)_1$ and $(DG-403)_3$ remain at

116

normally open configuration (SW-1 open and SW-2 closed). This grounds electrode 1, see Figure 4.15.
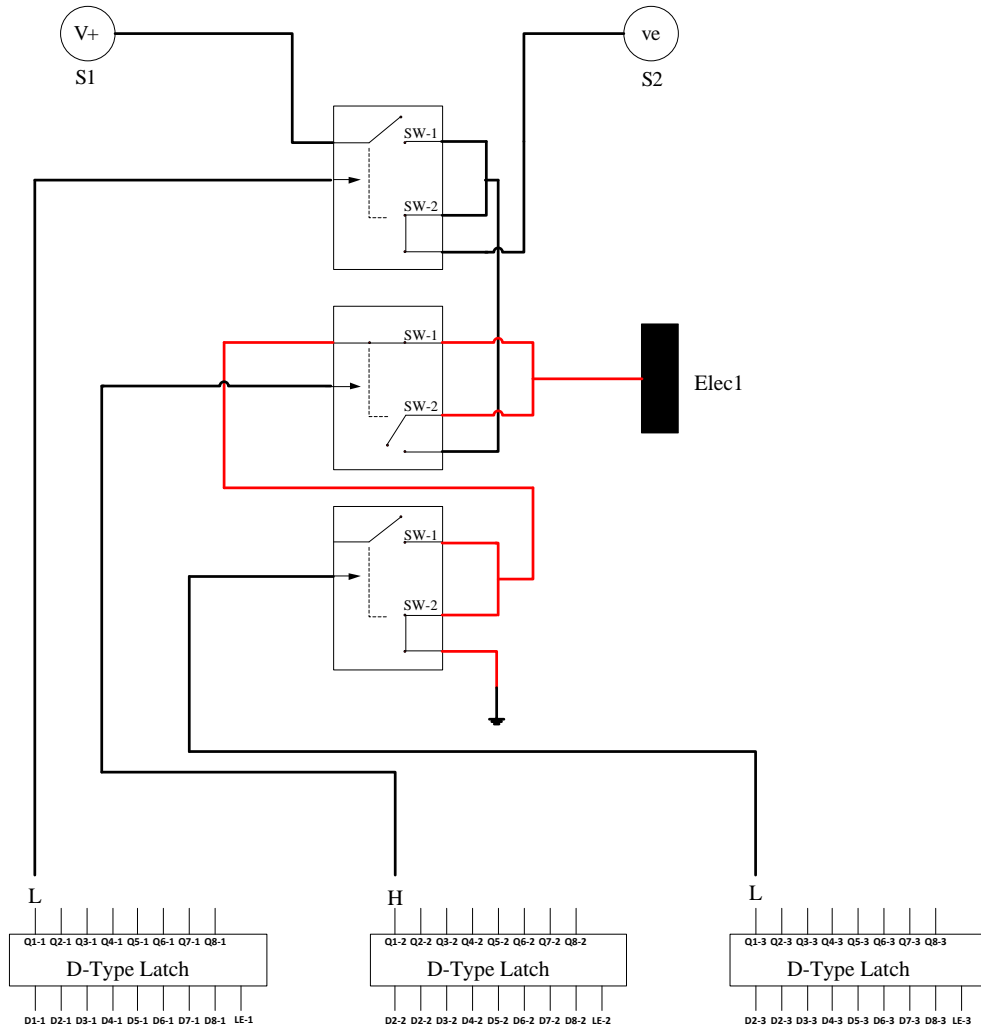
Figure 4.15 Electrode 1 connected to ground (E) , array B

An array of LEDs was used in the circuit to indicate the status of the electrodes. Each column of LEDs represented the three states (excitation, virtual earth measurement and earth) of each electrode, see Figure 4.16. Since there are two electrode arrays, two identical LED circuits were used.
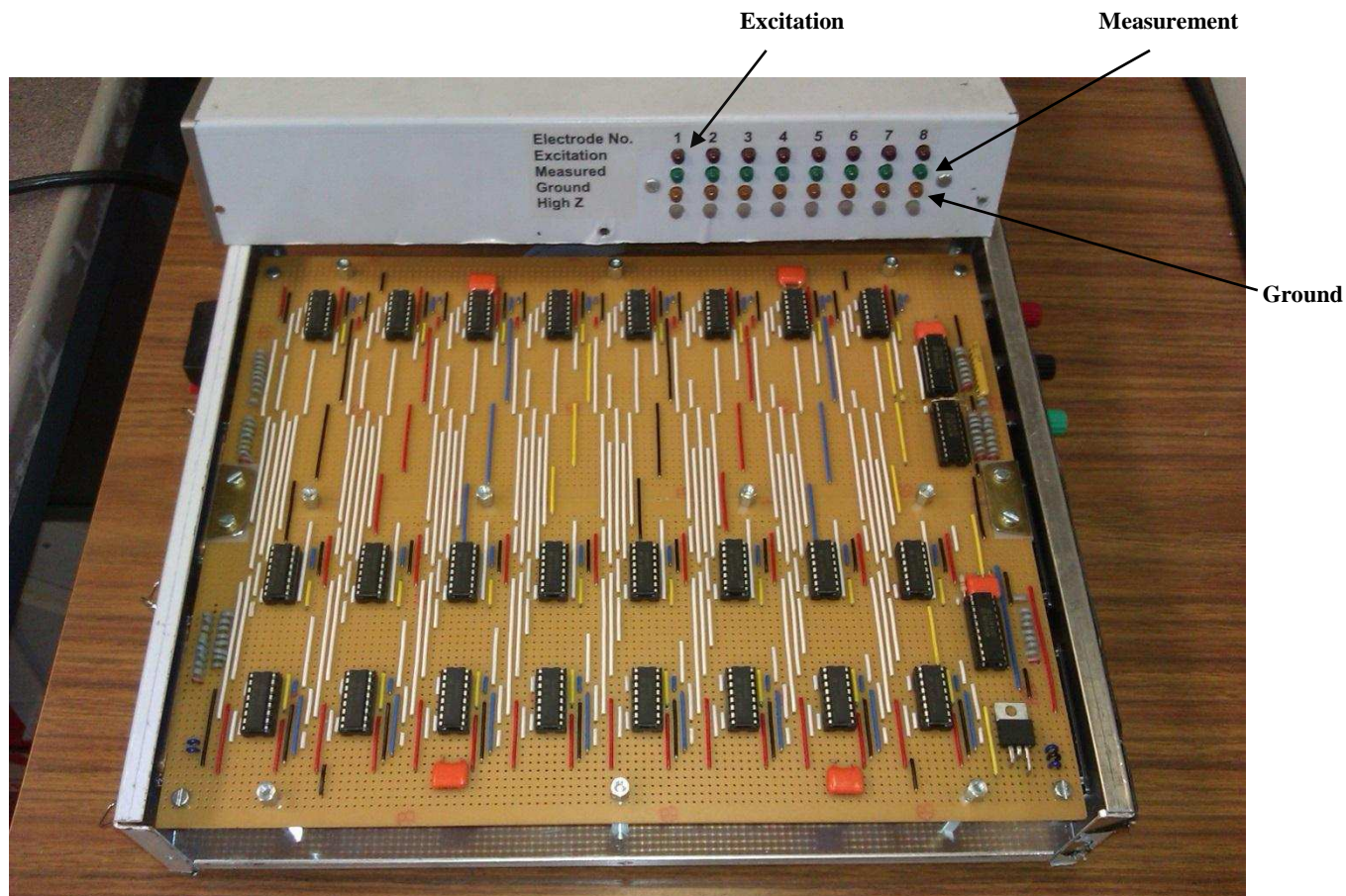
Figure 4.16 the electrode selection circuit

The electrode selection circuits were integrated with a microcontroller (VM1) in order to set the electrodes states according to different configurations as described in Section3.3 and Section 4.2.3. The full integration method and program are explained in Chapter Five.

4.3 Theory of Measurement

4.3.1   Volume Fraction Measurement

The local solids volume fraction α_s measured by the ICC device is given by Maxwell's relationship, see Section 2.2.2

$$\alpha_s = \frac{2\sigma_w - 2\sigma_m}{2\sigma_w + \sigma_m}$$

Equation 4-9

Substituting Equation 4-8 into Equation 4-7 yields the output voltage V_B in the conductance circuit:

$$V_B = -k\frac{R_2}{R_f}V_b^+$$

Equation 4-10

The relationship between the electrical resistance of the fluid R_f and the fluid conductivity, σ can be defined as:

$$\sigma = \frac{1}{gR_f}$$

Equation 4-11

where g is the cell constant. Therefore, the output voltage V_B in Equation 4-10 can be re-written in terms of the fluid conductivity σ using :

$$V_B = -k\,R_2\,V_b^+\,g\sigma$$

Equation 4-12

$$V_B = K_B\sigma$$

Equation 4-13

Where K_B represents the constant of the system

In practical operation, for a given Configuration ϕ and a given rotational position n, a conductance measurement circuit is used to measure the local solids volume fraction $(\alpha_s)_{\phi,n}$ using:

$$(\alpha_s)_{\phi,n} = \frac{2(\sigma_w)_{\phi,n} - 2(\sigma_m)_{\phi,n}}{2(\sigma_w)_{\phi,n} + (\sigma_m)_{\phi,n}} \qquad \text{Equation 4-14}$$

Where: $(\sigma_w)_{\phi,n}$ is the electrical conductivity of the water for a given Configuration ϕ and a given rotational position n. The local volume fraction $(\alpha_w)_{\phi,n}$ of the water at the relevant CoA is then given by $(\alpha_w)_{\phi,n} = 1 - (\alpha_s)_{\phi,n}$.

$(\sigma_w)_{\phi,n}$ and $(\sigma_m)_{\phi,n}$ can be defined in terms of output voltages for Configuration ϕ and a given rotational position n:

$$(V_{B,w})_{\phi,n} = (K_B)_{\phi,n}(\sigma_w)_{\phi,n} \qquad \text{Equation 4-15}$$

$$(V_{B,m})_{\phi,n} = (K_B)_{\phi,n}(\sigma_m)_{\phi,n} \qquad \text{Equation 4-16}$$

where $(V_{B,w})_{\phi,n}$ is the output voltage from channel B when water is the only fluid present in the tube and $(V_{B,w})_{\phi,n}$ is the output voltage from channel B when the mixture of solids and water fluid is present in the tube. The method of measurement assumes that the system constant $(K_B)_{\phi,n}$ doesn't change with time or for different water conductivities. Therefore, dynamic tests were carried out to check the invariability of the system constant $(K_B)_{\phi,n}$, see Section 4.4.

Substituting Equation 4-15 and Equation 4-16 into Equation 4-14 gives:

$$(\alpha_s)_{\phi,n} = \frac{2(V_{B,w})_{\phi,n} - 2(V_{B,m})_{\phi,n}}{2(V_{B,w})_{\phi,n} + (V_{B,m})_{\phi,n}}$$

Equation 4-17

In the present study, Equation 4-17 was used to calculate the local solids volume fraction $(\alpha_s)_{\phi,n}$

for a given Configuration ϕ and a given rotational position n.

4.3.2   Solids Velocity Measurement

A cross correlation technique was used to determine the dispersed phase velocity in solids-in-

water flow. For a given configuration and rotational position, The DC output voltages $(V_A(t))_{\phi,n}$

and $(V_B(t))_{\phi,n}$ were cross correlated to provide information on the local solids velocity of a two

phase flow at the particular region of the flow cross-section 'interrogated' at planes A and B.

The cross correlation function for the dispersed phase in each interrogated region can be written

as:

$$R_{\phi,n}(\tau) = \frac{1}{T} \int_0^T (V_A(t))_{\phi,n} \, ((V_B)(t+\tau))_{\phi,n} \, dt$$

Equation 4-18

Where ϕ is the configuration type, n is the rotation number, $(V_A(t))_{\phi,n}$ is the output voltage from

channel A at time t, $((V_B)(t+\tau))_{\phi,n}$ is the output voltage from channel B at time $(t+\tau)$, τ is the

delay time and T is the total time period for which data is acquired.

As the delay time τ varies from 0 to the total time period T, the value of cross correlation

function $R_{\phi,n}(\tau)$ will change, attaining a maximum value when τ is equal to τ_p the mean time

for the perturbations in the measured conductance of the flow to travel from array A to array B.

Thus, τ_p can be found by determining the value of τ at which $R_{\phi,n}(\tau)$ is a maximum. The local

velocity $(v_s)_{\phi,n}$ in each interrogated region is given by:

$$(v_s)_{\phi,n} = \frac{L}{(\tau_p)_{\phi,n}}$$

where ϕ is the configuration, n is the rotational position and L is the axial distance between arrays A and B.

4.4 Dynamic Testing of The ICC System

Dynamic tests were performed to check the operation of the ICC device and to assess the linearity of the conductance circuit output voltages to different water conductivities.

4.4.1 The Calibration of the Conductance Circuit

The variation of the conductance circuit output voltages with water conductivity was examined by using distilled water with known amounts of sodium chloride (NaCl) added. The ICC device was filled with low conductivity distilled water (of measured conductivity 2 µS/cm). The conductivity was increased by gradually adding small amounts of NaCl (nearly 22 mg each time) to water. At each step the water conductivity was measured using a conductivity meter and plotted against the output voltage V_B of array B for the three Configurations ($\phi =$ I, II and III) and eight rotational positions (n= 1 to 8), see Figure 4.17, Figure 4.18 and Figure 4.19.
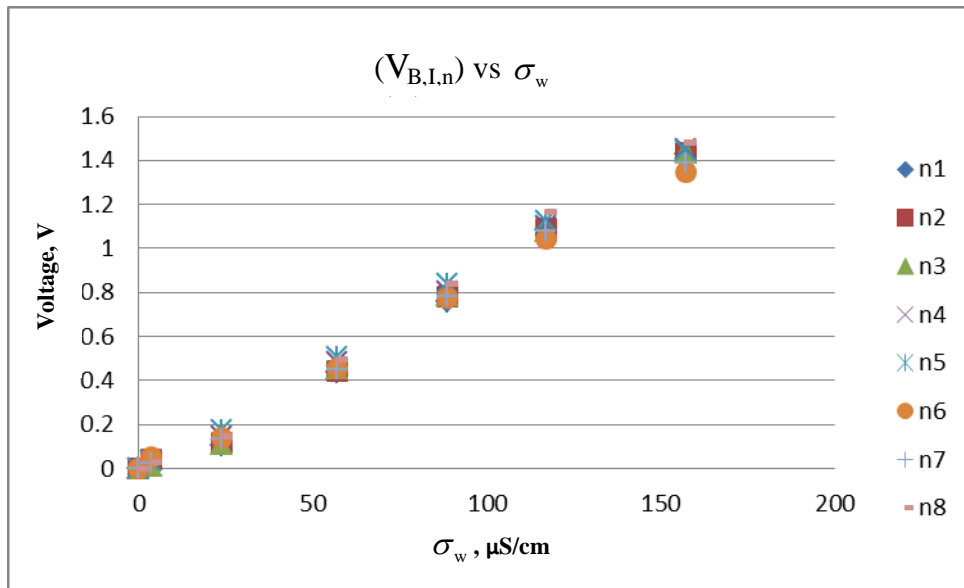
Figure 4.17 Calibration curve for water conductivity and output voltage of array B for Configuration I and rotational positions n=1 to 8
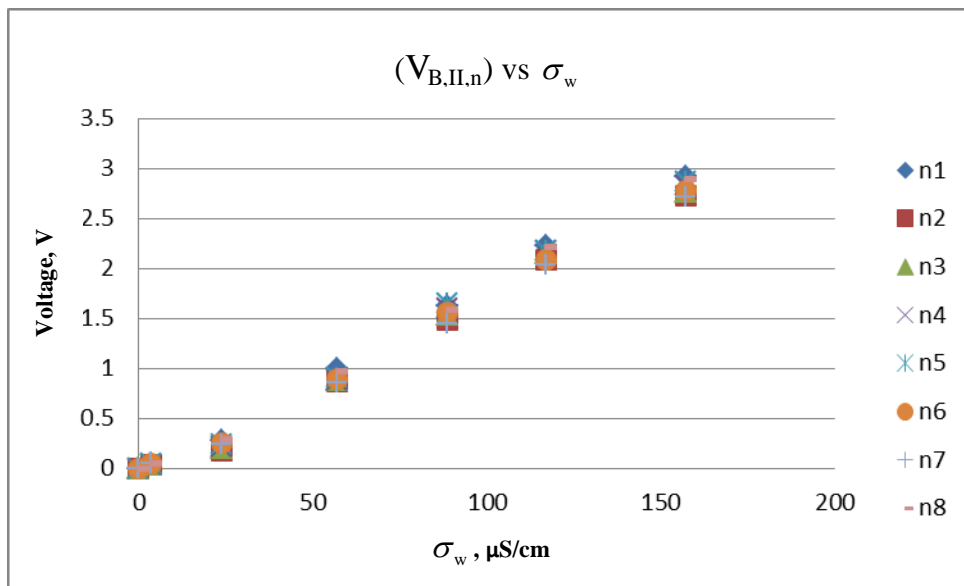
Figure 4.18 Calibration curve for water conductivity and output voltage of array B for Configuration II and rotational positions n=1 to 8

123
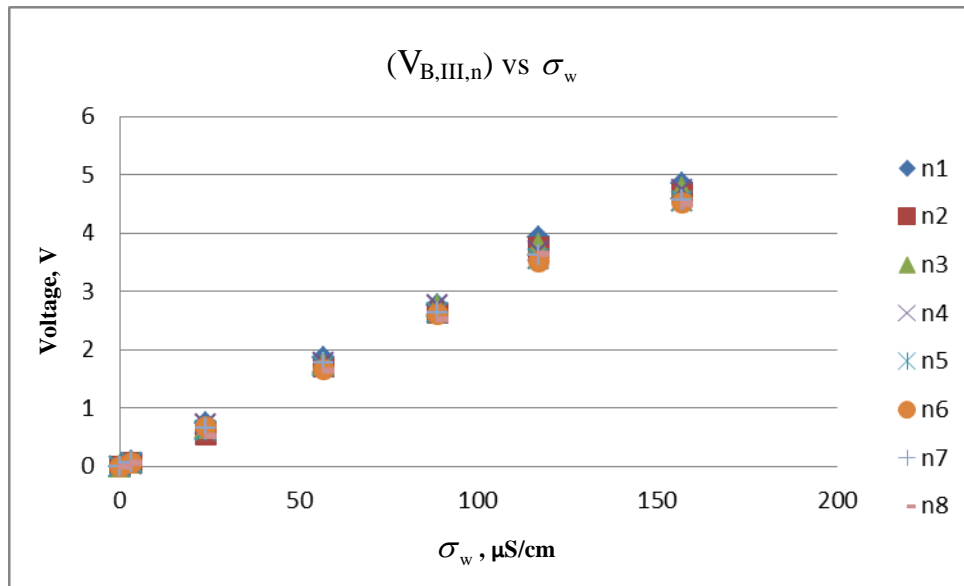
Figure 4.19 Calibration curve for water conductivity and output voltage of array B for Configuration III and rotational positions n=1 to 8

Figures 4.16, 4.17 and 4.18 show a linear relationship between water conductivity σ_w and the output voltage V_B of the conductance circuit. Where $(K_B)_{\phi,n}$ represents the slop between the output voltage and the water conductivity, σ_w. This linearity confirms that the value of the system constant $(K_B)_{\phi,n}$ in Equation 4-15 and Equation 4-16 remains constant for different water conductivities. This confirmation is essentially important to prove that our assumption of invariability of the system constant $(K_B)_{\phi,n}$ is valid for the solids volume fraction derivation, refer to Equation 4-12 to Equation 4-15.

4.5 Summary

- A non-intrusive ICC instrument which can be used to determine the distribution of the local solids velocity (v_s), the distributions of the local solids volume fraction (α_s) and the local

water volume fraction (α_w where $\alpha_w = 1 - \alpha_s$) in solids-in-water flow has been designed and built.

- The ICC device consists of a non-conducting flow tube with an internal diameter of 80 mm. The flow tube was constructed from Polyether Ether Ketone (PEEK). Rectangular grooves were cut in the internal face of the flow tube to take stainless steel electrodes see Section 4.2.1.

- The ICC device used in this study has two arrays of electrodes, separated by an axial distance of 50 mm. Each array contains eight electrodes mounted over the internal circumference of the tube carrying the flow. The electrodes were mechanically fixed firmly into their positions using a washer and nut.

- The ICC device has two electrode selection circuits which were designed to allow selection of any electrodes from a given array (A or B) and connect them to excitation (V^+), measurement (ve) or earth (E) in the corresponding channel (A or B) of the conductance measurement circuit. refer to Section 4.2.3. Based on the truth Tables 1 and 2, the electrode m in each array can be connected to one of three potentials (V^+, ve and E).

- The electrode selection circuits were controlled using fourteen digital inputs applied from a VM1 microcontroller, refer to Chapter Five.

- The ICC device has a conductance circuit to measure the conductance of the multiphase mixture between the V^+ and ve electrodes, sequentially for each of the eight rotational positions, for a given configuration.

- The conductance tests included testing the output voltages of the conductance circuit for different water conductivities. This was a test to determine whether the voltage output was linear with changes in conductivity due to the presence of a dispersed solid phase in the fluid flow.

- For a given configuration and rotational position, the local solids volume fraction α_s measured

  by the ICC device is given by Maxwell's relationship, refer Equation 4-9.

5. CHAPTER 5: Impedance Cross Correlation Flow Meter Measurements Using A PC and Stand-Alone Microcontroller

5.1 Introduction

Chapter 4 described the design and manufacture of the ICC flow meter and the measurement procedures. The ICC system requires processing units to control the electrode selection circuit using the digital outputs D/I 1 to D/I 14 (refer to Figure 4.11), and to record and analyse the output signals V_A and V_B in order to determine volume fraction and velocity for the dispersed phase.

This chapter introduces two systems which combine to make the processing unit. The first system is a stand-alone online processing unit (VM-1 microcontroller [106]) which does not require connection to a computer, and the second system which is an online/offline processing unit and which requires integration of the VM-1 microcontroller with a National Instruments data acquisition card and PC running LABVIEW software.

The stand-alone unit VM-1 can dynamically process and analyse the measurements made to obtain the solids volume fraction. The VM-1 consists of a controller board, an analogue module and a display module. All the electrode "state selection" and measuring analysis routines are programmed into the controller board using the VENOM programming language (downloaded from the website www.microrobotic.co.uk) see Section 5.3.3. The microcontroller chooses the configuration and rotates it to each of the eight rotational positions for arrays A and B, and measures the required voltages. After capturing the data, the microcontroller performs the necessary analysis to obtain the solids volume fraction. The results are presented on the LED Quarter Video Graphics Array QVGA display module whose dimensions are 320×240 pixels

[106]. A user can interact with the ICC device and send commands using a touch screen on the QVGA display module.

To measure the solids' velocity with a high degree of accuracy, the data needs to be collected at a high sampling rate (see Section 5.4). Due to the low sampling rate of the VM-1 unit, a PC based measurement system was used to collect the measured data from arrays A and B at 2000 samples/second and perform all of the necessary analysis to obtain the solids velocity distributions. Using such PC based measurement the results can be processed either online or offline.

5.2 VM-1 Microcontroller

The VM-1 is a credit-card-sized embedded controller intended for intelligent instruments [106] and using Venom-SC programming language protocols it can accommodate Analogue and Digital I/O, graphical user interfaces (GUI), data and text files and many other functions.
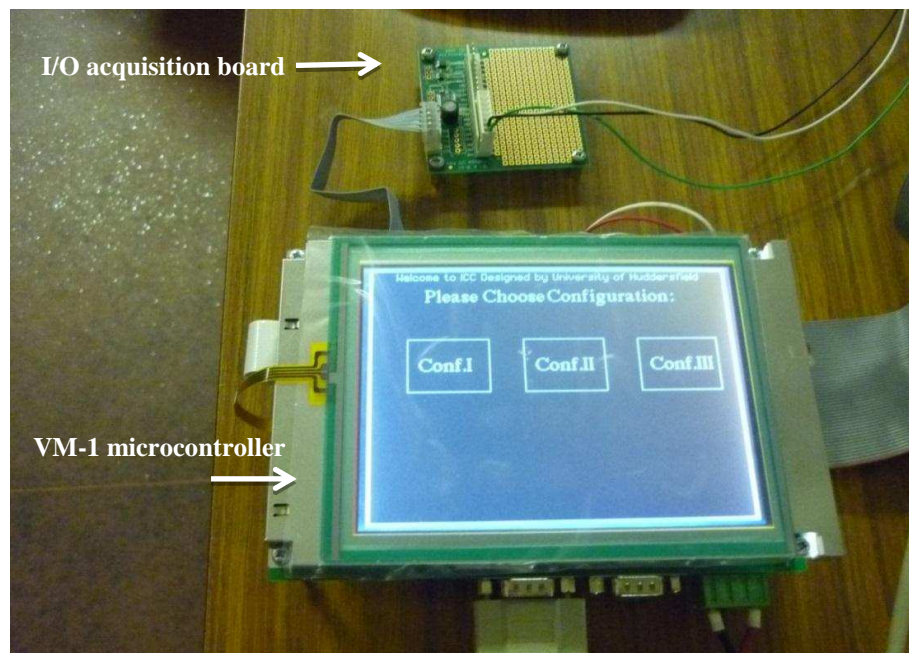
Figure 5.1 VM-1 Microcontroller and I/O acquisition board

The VM-1 microcontroller unit consists of an application board, which provides access to RS232 serial ports, graphic display interfaces, a I^2C bus and terminals for mounting the VM-1 microcontroller, see Figure 5.2. The RS232 serial port1 is used for downloading instructions onto the VM-1 microcontroller. The allows the data acquisition unit to communicate with the VM-1 microcontroller. To display the obtained results, the graphic display interfaces the VM-1 microcontroller with the Quarter Video Graphics Array (QVGA) display. The CPU resources for VM-1 include:

• 16-bit Hitachi H8S processor running at 16MHz.

• 512K RAM – battery backed.

• 512K Flash (supplied separately) for Venom-SC and user application.

The I/O Resources for VM-1 have:

• 10 x Pulse I/O Channels (6 PWM, 4 Pulse counting),

• 2 x Quadrature shaft encoder inputs,

• 8 x 10-bit Analogue inputs.

• 2 x 8-bit Analogue outputs, and

• 42 x Digital I/O.

The I/O capabilities of the VM-1 were used to control the electrode selection circuits by sending 14 Digital outputs to latches of array A and array B, (refer to Section 5.3.1).

The following section describes the procedure of integration and programming structure using the VM-1.

5.3 ICC Integration with VM-1

5.3.1   VM-1 and electrode selection circuit

Section 4.2.3 shows the design of the electrode selection circuit. Based on this design, these circuits need 14 digital inputs to set the two electrode arrays into a defined configuration. The VM-1 microcontroller was used to control the electrode selection circuit by providing the 14 digital outputs are denoted: A, B, C, D, E, F, G, H, I, J, K, L, O, and P. The VM-1 changes the status of the digital inputs (A to H) according to the Truth Table 4-1, and then activates the latches (Latch1 to Latch6) using the six remaining digital lines (I, J, K, L, O, and P). The digital outputs I and J are used to excite the Latch Enabled (LE) inputs of Latch1 and Latch 4 respectively, the digital outputs K and L are used to excite the Latch Enabled (LE) inputs of Latch 2 and Latch 5 respectively, and the digital outputs O and P are used to excite the Latch Enabled (LE) inputs of Latch 3 and Latch 6 respectively.

For the purpose of programming, the status of the electrodes, which can be confirmed by the LED arrays, were defined by a one digit number as follows:

1 - denotes connected to excitation signal (V^+),

2 - denotes connected to virtual earth measurement (ve), and

3 - denotes connected to earth (E).

Taking as an example that the desired electrode configuration is Configuration I and rotational position n=1 (refer to Section 3.3.1), the status of the eight electrodes (ELE_ST) will be (1, 2, 3, 3, 3, 3, 3, 3), i.e. electrodes 1 in both array A and B are set as excitation electrode, while electrodes 2 will be the measurement electrode and electrodes 3 to 8 will be connected to earth.
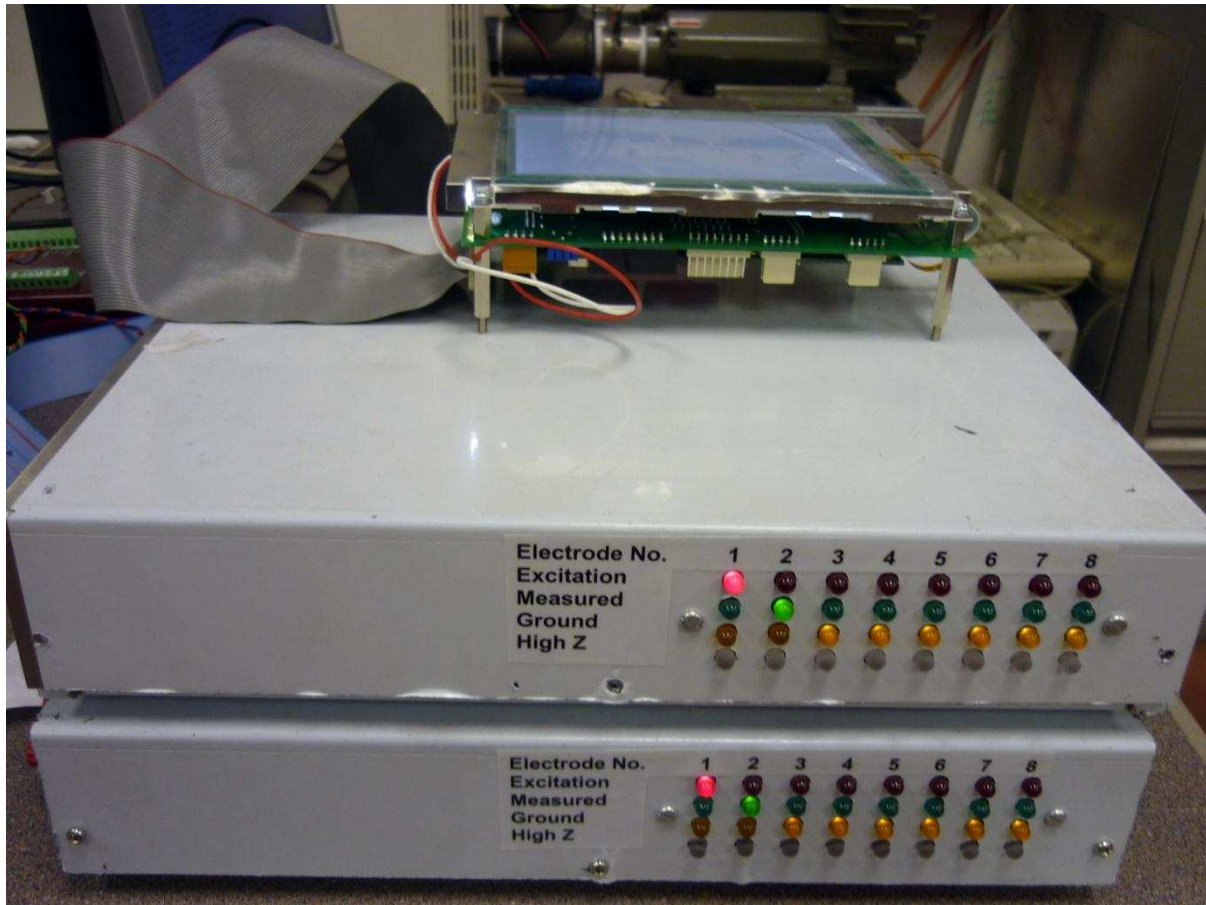
Figure 5.2 Electrodes selection circuits integrated with VM-1 microcontroller

To set up the six latches, three arrays were created and denoted as:

- Latch1: this array was used to set Latch 1 in array A and Latch 4 in array B,

- Latch2: this array was used to set Latch 2 in array A and Latch 5 in array B, and

- Latch3: this array was used to set Latch 3 in array A and Latch 6 in array B.

Based on the Truth Tables in Section 4.2.3, the three arrays were set either high (1) or low (0) as demonstrated in the following commands:

```
TO LATCH_STEUP

[

wait50

IF ELE_ST. element(M) = 1 then [lath1. element (M) := 1 ]

IF ELE_ST. element(M) = 1 then [lath2. element (M) := 0 ]

IF ELE_ST. element(M) = 1 then [lath3. element (M) := 0 ]

wait50

IF ELE_ST. element(M) = 2 then [lath1. element (M) := 0 ]

IF ELE_ST. element(M) = 2 then [lath2. element (M) := 0 ]

IF ELE_ST. element(M) = 2 then [lath3. element (M) := 0 ]

wait50

IF ELE_ST. element(M) = 3 then [lath1. element (M) := 0 ]

IF ELE_ST. element(M) = 3 then [lath2. element (M) := 1 ]

IF ELE_ST. element(M) = 3 then [lath3. element (M) := 0 ]

]

End

;Where m = 1 to 8
```

Figure 5.3 VM1 commands to set arrays states for the three latches

Table 5-1 shows the latches set up according to electrode Configuration I, rotational position n=1

Table 5-1 Latches set up for Configuration I, rotational position 1 in array A and array B

Electrode	Electrode status	Latch1	Latch2	Latch3	Digital Output
1	$1 = (V^+)$	1	0	0	A
2	$2 = (ve)$	0	0	0	B
3	$3 = (E)$	0	1	0	C
4	$3 = (E)$	0	1	0	D
5	$3 = (E)$	0	1	0	E
6	$3 = (E)$	0	1	0	F
7	$3 = (E)$	0	1	0	G
8	$3 = (E)$	0	1	0	H

The digital outputs (A, B, C, D, E, F, G and H) to the electrode selection circuits were changed three times, see Table 5-1. For each electrode arrangement, data from array A and array B was collected and analysed, refer to Sections 5.3.2 and 5.3.3.

5.3.2   Data acquisition unit

To obtain accurate readings, a 12-bit analogue I/O acquisition board was integrated with the VM-1 microcontroller. The I/O acquisition board has a standard micro-robotics I2C bus connector - note that this bus is a communication line between the data acquisition unit and the VM-1 microcontroller on the application board. The 12-bit acquisition board comprises:

- 8 channels of 12-bit analogue input, and

- 2 channels of 12-bit digital I/O port.

The 12-bit AC/DC will measure single polarity signals in the range 0 V to the 5 V (the reference voltage). Two channels of the 12-bit analogue input are connected to channels A and B in the conductance circuit to obtain the measured output signals V_A and V_B (refer to Section 4.2.2) respectively.

5.3.3   Programming structure

Venom was the 'object oriented' translation of the language that ran on the Micro-Robotics Scorpion Control Computer[106]. Venom-SC was developed for writing small-to-medium sized control applications on the VM-1 microcontroller and provides high processing speed whilst maintaining small code size and flexibility as an interpreter. 'SC' stands for 'Semi-Compiled' which means that the code is partly compiled, but not all the way down to built-in machine code.

The Venom-SC language has multitasking built-in which gives all tasks equal priority to run simultaneously, being interchanged by the task manager with little external control. This feature makes the system efficient and easy to manage[106].

5.3.3.1 Procedure for Operating the ICC Device with a Stand-alone VM-1 Microcontroller

The VM-1 microcontroller was used to select the desired electrode states based on pre-defined configurations. Using the I/O board, the data from channel B were collected to measure the solids volume fraction for all eight rotational positions and display the results on the LCD graphics panel, see Figure 5.4.

The programing flow chart for the ICC device and VM-1 microcontroller is shown in Figure 5.5. In order to measure the solids volume fraction α_s, the reference measurements of the output

voltage $(V_{B,w})_{\phi,n}$ from channel B, when water only is present in the pipe, need to be collected, refer to Section 4.3.1.
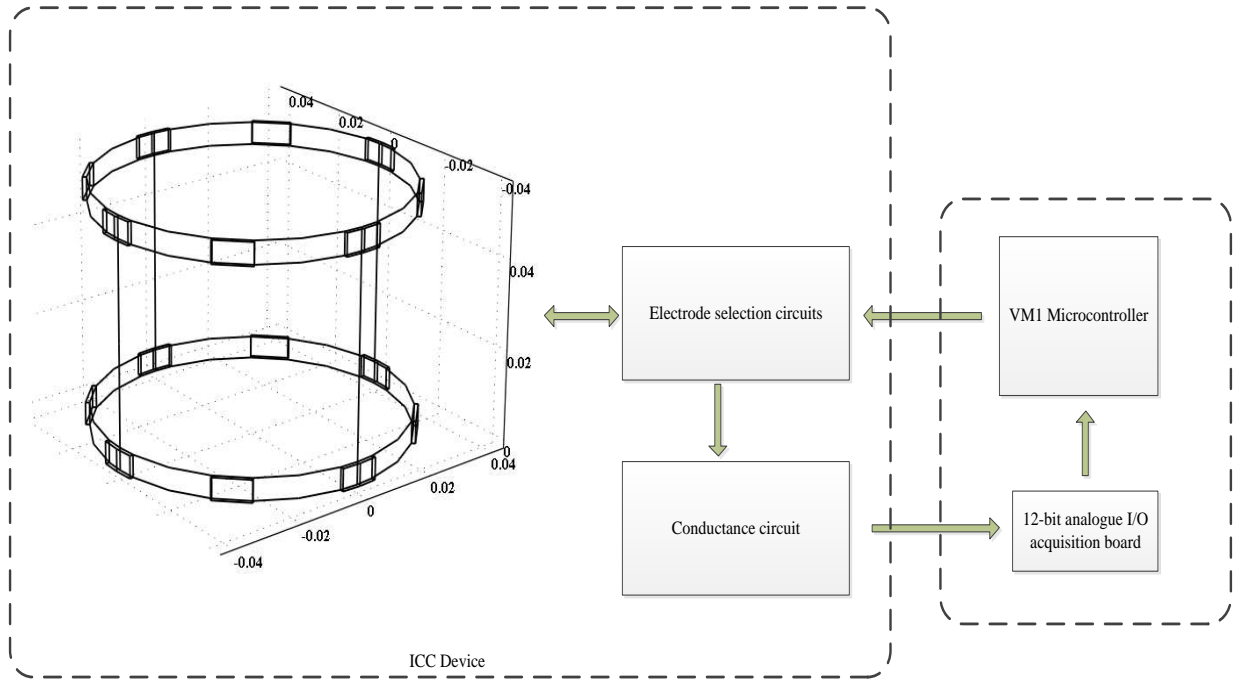
Figure 5.4 ICC device integrated with VM-1 microcontroller

The program starts by calibrating the ICC device with tap water only in the tube. By pressing the virtual key 'Start' on the touchscreen, the mean value $(\overline{V_{B,w}})_{\phi,n}$ of 5000 measurements was collected at 500 samples per second for all Configurations ϕ and rotational positions n as follows:

$$(\overline{V_{B,w}})_{\phi,n} = \frac{\sum\limits_{i=1}^{5000}(V_{B,w})_{\phi,n}}{5000}$$

Equation 5-1

where 5000 is the number of samples.

Before the ICC device starts running, the number of cycles C, over which it is required to find the mean mixture output voltage $(V_{B,m})_{\phi,n}$ for each Configuration ϕ and rotational position n, is input to the microcontroller. Additionally, the program allows the user to choose the desired configuration and the desired distributions (solids volume fraction distributions or voltage distributions). By pressing the virtual key 'Start' on the touchscreen, the ICC device starts running and the mean values $(\overline{V_{B,m}})_{\phi,n}$ is collected for the selected Configurations ϕ (where ϕ =I, II or III) and rotational position (n= 1 to 8); where $(\overline{V_{B,m}})_{\phi,n}$ is defined by:

$$(\overline{V_{B,m}})_{\phi,n} = \frac{\sum\limits_{i=1}^{C*5000}(V_{B,m})_{\phi,n}}{C*5000}$$

Equation 5-2

Where C is the numbers of cycles.

For each selected Configurations ϕ (where ϕ =I, II or III) and rotational position n, the solids volume fraction $(\alpha_s)_{\phi,n}$ was calculated as follows:

$$(\alpha_s)_{\phi,n} = \frac{2(\overline{V_{B,w}})_{\phi,n} - 2(\overline{V_{B,m}})_{\phi,n}}{2(\overline{V_{B,w}})_{\phi,n} + (\overline{V_{B,m}})_{\phi,n}}$$

Equation 5-3

The results $(\alpha_s)_{\phi,n}$ are displayed on the touch screen for each C.

```
                    ┌─────────────────────────────┐
                    │          Start              │
                    │   Define configurations     │
                    └─────────────────────────────┘
                                  │
                                  ▼
┌──────────────────────────────────────────────────────────────────────────┐
│                         Water Calibration                                  │
│              ADC measures the $(\overline{V_{B,w}})_{\phi,n}$   as          │
│  Configuration I          Configuration II          Configuration III      │
│                                                                            │
│  Save data of all n in array   Save data of all n in array  Save data of all n in array │
│         V_water1                    V_water2                    V_water3    │
│                                                                            │
│                          where n=1 to 8                                    │
└──────────────────────────────────────────────────────────────────────────┘
                                  │
                                  ▼
                    ┌─────────────────────────────┐
                    │  Input water conductivity    │
                    └─────────────────────────────┘
                                  │
                                  ▼
                    ┌─────────────────────────────┐
                    │  Input number of cycles: C   │
                    └─────────────────────────────┘
                                  │
                                  ▼
              ┌─────────────────────────────────────────┐
              │           Choose function:              │
              │                                         │
              │  Solids volume fraction   Or   Voltages │
              │      distributions                      │
              │                            distributions│
              └─────────────────────────────────────────┘
                                  │
                                  ▼
┌──────────────────────────────────────────────────────────────────────────┐
│                      Choose Configuration:                                 │
│                                                                            │
│   Configuration I        Configuration II        Configuration III         │
└──────────────────────────────────────────────────────────────────────────┘
                                  │
                                  ▼
┌──────────────────────────────────────────────────────────────────────────┐
│         ┌──────────────────────────────────────────────┐                   │
│         │        Using Configuration $\phi$             │                   │
│         │           For n = 1 to 8                      │                   │
│         │   ADC measures $(\overline{V_{B,m}})_{\phi,n}$ │                  │
│         │        Calculate $(\alpha_s)_{\phi,n}$        │                   │
│         └──────────────────────────────────────────────┘                   │
│                            │                                               │
│                            ▼                                               │
│         ┌──────────────────────────────────────────────┐                   │
│         │ Display the chosen function selected configurations $\phi$ (where │
│         │    $\phi$ =I,II or III)  and rotational positions n              │
│         └──────────────────────────────────────────────┘                   │
└──────────────────────────────────────────────────────────────────────────┘
```

Figure 5.5 Flow chart for VM-1 microcontroller software

5.4 PC Based Measurement System

In the present investigation, a cross correlation technique was used to measure the solids velocity in solids–in-water flow. For a cross correlation system, the axial separation of the two array sensors (L) and the sampling period (τ_s) have a great effect on the accuracy of the velocity measurement. Equation 5-4 shows the relationship between the actual velocity v_{act} and the measured velocity v_{est} obtained using cross correlation and the flowmeter parameters as described above. This relationship is explained in detail in [56]

$$v_{est} = \frac{v_{act}}{1 \pm \frac{\tau_s v_{act}}{L}}$$
Equation 5-4

where $\tau_s = 1/f$ and f is the sampling frequency.

Equation 5-4 shows that, in order to make v_{est} as close as possible to v_{act}, the term $\frac{\tau_s v_{act}}{L}$ needs to be as small as possible. In fact τ_s was set to 5 x 10^{-4} seconds (frequency of 2000 Hz) so that for a separation of L = 50 mm, $\frac{\tau_s}{L}$ was equal to 0.01s/m and hence v_{est} will be within 1% of v_{act}. In Ideal conditions, this is the best accuracy that is achievable from the system.

The VM-1 microcontroller has a sampling rate limited to less than 250 samples/second for two channels(A & B), thus a PC based measurement system was used to collect the signals data from arrays A and B at 2000 samples/second using an NI USB-6343 DAQ board with a LABVIEW and MATLAB software platform, and the PC as host computer. This system was linked to the VM-1 microcontroller, which was used to select the desired Configuration ϕ and rotational position n, see the flow chart in Figure 5.7.

The schematic diagram, Figure 5.6, shows the PC based measurement system, including VM-1 microcontroller and ICC device.
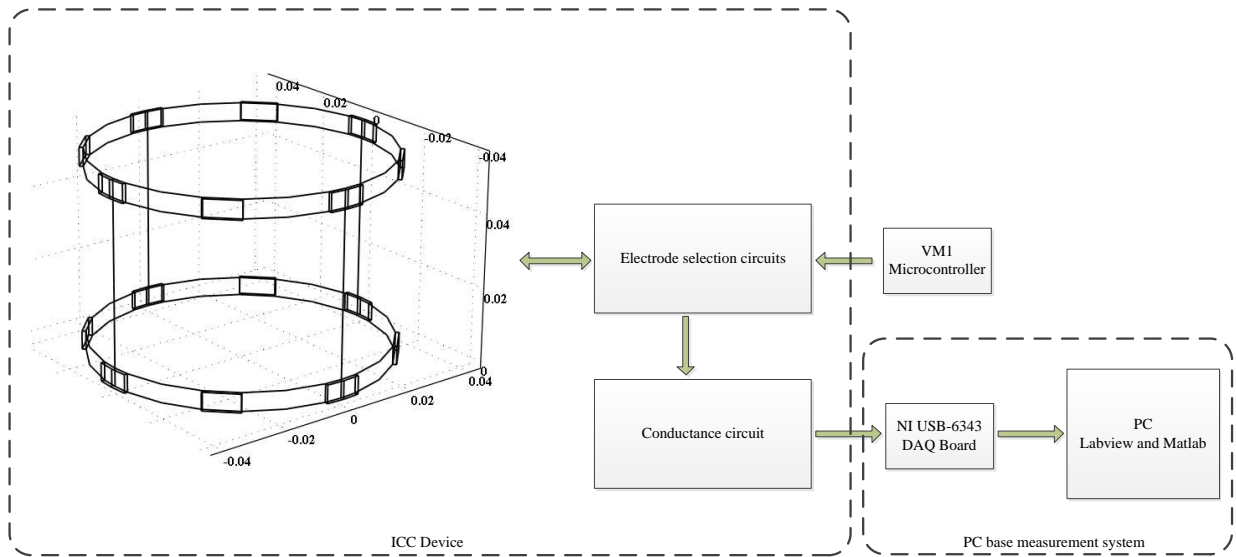
Figure 5.6 ICC device integrated with VM-1 and PC based measurement system

The NI USB-6343 DAQ data acquisition unit has thirty two 16-bit analogue inputs (AI) channels, forty eight digital I/O channels and four 32-bit counter/timers. The NI board could control the electrode selection circuits and simultaneously collect data from arrays A and B. Because the VM-1 was integrated with the electrode selection circuits in the earlier stages of this investigation, Therefore, the electrode selection circuits were controlled by the VM-1 microcontroller and NI board was used to collect the measured data from the two arrays.

```
┌─────────────────────────┐
│   Set the sampling rate  │
│  2000 samples per second │
└─────────────────────────┘
             │
             ▼
┌─────────────────────────┐        ┌──────────────────────────┐
│     Set the sampling     │        │   VM-1 microcontroller    │
│    duration T of each    │        │  used to set the desired  │
│  rotation (e.g. 60 second)│       │   configuration φ and     │
└─────────────────────────┘        │   rotational position n   │
                                    └──────────────────────────┘
```

Set the number of cycles
C

Collect V_A and V_B using NI USB-6343
DAQ Board and save as text files

Calculate the cross correlation
function using MATALB
command:
C.F= xcorr (V_B,V_A)

Determine the the delay
time τ_p

Determine the solids
velocity

$$(v_s)_{\phi,n} = \frac{L}{(\tau_p)_{\phi,n}}$$

Display the results

Figure 5.7 The flow chart diagram for PC based measurement system

Using LABVIEW and the NI board, the data from arrays A and B were collected for a one minute sampling duration T at sampling rate 2000 samples/second. Using the MATLAB program, V_A and V_B were processed and analysed to determine the cross correlation function and provide the delay time τ_p , see Section 4.3.2, and information concerning the solids passing between the two arrays. Using τ_p, the solids velocity for a given configuration and rotational position was found.

The LABVIEW program allows the measurements to be processed in either online or off-line mode. The offline mode can be used if the data needs further analysis.

5.5 Summary

- A stand-alone microcontroller for the ICC has been designed and constructed.

- Online analysis software has been written for a VM-1 microcontroller using the Venom-SC programing language with a predetermined electrode status (refer to Section 5.3).

- The ICC stand-alone system consists of a VM-1 microcontroller, an application board, an LCD graphics panel with a resistive touch screen (QVGA module) and a data acquisition module.

- The routine in Appendix (B) was downloaded onto the VM-1 memory. The VM-1 microcontroller controls electrode selection and collects output signal data from the conductance circuit (V_B).

- Using the output signal V_B from channel B, the solids volume fraction $(\alpha_s)_{\phi,n}$ was determined for each Configuration ϕ and rotational position n, refer Section 5.3.3.1. The results are presented on the LCD graphic panel. The QVGA module is used to display the calculated $(\alpha_s)_{\phi,n}$.

- Due to VM-1 sampling limitations, a PC measurement system was used to calculate the solids velocity distributions.

- The PC measurement system consists of a data acquisition unit (NI USB-6343 DAQ Board) and a host computer. The programming routine was written in LABVIEW programming language using MATLAB sub-routines.

- A VM-1 microcontroller was used to select the desire Configuration ϕ and rotational position n.

- The program processed the voltages V_A and V_B obtained via the NI acquisition unit and performed all the necessary calculations to determine the solids velocity (refer to 5.4).

- For enhanced accuracy, the data was collected at a sampling frequency of 2000 Hz. (refer to Section 5.4)

- The LABVIEW program allowed for offline analysis by saving the data in text files and process the saved data using a MATLAB program.

6. CHAPTER 6: Multiphase Flow Loop Facility and Experimental Procedure

6.1 Introduction:

In order to test the performance of the proposed flow meter with an actual multiphase flow through it, a flow loop was used. This chapter presents the experimental apparatus used in the investigations, including the multiphase flow loop facility and the reference measurement instruments used in this study.

This chapter is divided into four main sections:

Section 6.2 shows the flow loop facility. This facility is capable of carrying solids-in-water flows at different solids and water flow rates and different solids volume fractions. In addition, the working section of the flow loop could be positioned at different inclination angles to the vertical.

Section 6.3 shows the reference measurement instruments used in this study. It also describes: i) the pressure gradient method which is used to measure the mean reference solids volume fraction $\overline{\alpha}_{s,dp}$ and its calibration, (refer to section 6.3.2) and ii) the gravimetric flow measurement system which is used to measure the reference solids volumetric flow rate $Q_{s,ref}$ and the reference water volumetric flow rate $Q_{w,ref}$ and its calibration, (refer to section 6.3.3).

In the current investigation, an Electromagnetic Velocity Profiler (EVP) system was used to measure the local axial velocity distribution of the water in solids-in-water flow. Section 6.4 describes the background theory of the Electromagnetic Velocity Profiler (EVP) flow meter

(section 6.4.1) together with an explanation of the integration of the ICC device and EVP flow meter (section 6.4.2).

Section 6.5 presents the flow conditions which were used in the experiments and experimental data acquisition and analysis.

6.2 Flow Loop Facility

The University of Huddersfield flow loop is shown in Figure 6.1 and Figure 6.2 and can be arranged to produce single-phase "water only flows" or solids-in-water multiphase flows by operating the relevant pumps. The working-section of the pipe is 80 mm internal diameter and approximately 3 m long and can be inclined at an angle θ to the vertical (where $0° \leq \theta \leq 60°$). See Figure 6.1.

The flow loop is capable of generating solids-in-water flows via two methods:

1. Method I: Operating the solids pump only and opening valve 2 only, refer to Figure 6.1.

2. Method II: Operating both the solids and water pumps and opening both valves 1 and 2, refer to Figure 6.1.

The flow rates of solids and water can be varied by adjusting valve 1 and adjusting the speed of solids pump, refer to Figure 6.1. In solids-in-water flow, non-conducting spherical solid beads of 4 mm diameter with density of 1340.8 kgm^{-3} were used. These solids were mixed homogenously using a stirrer mounted above the solids and water reservoir before being pumped to the working-section (see Figure 6.1).
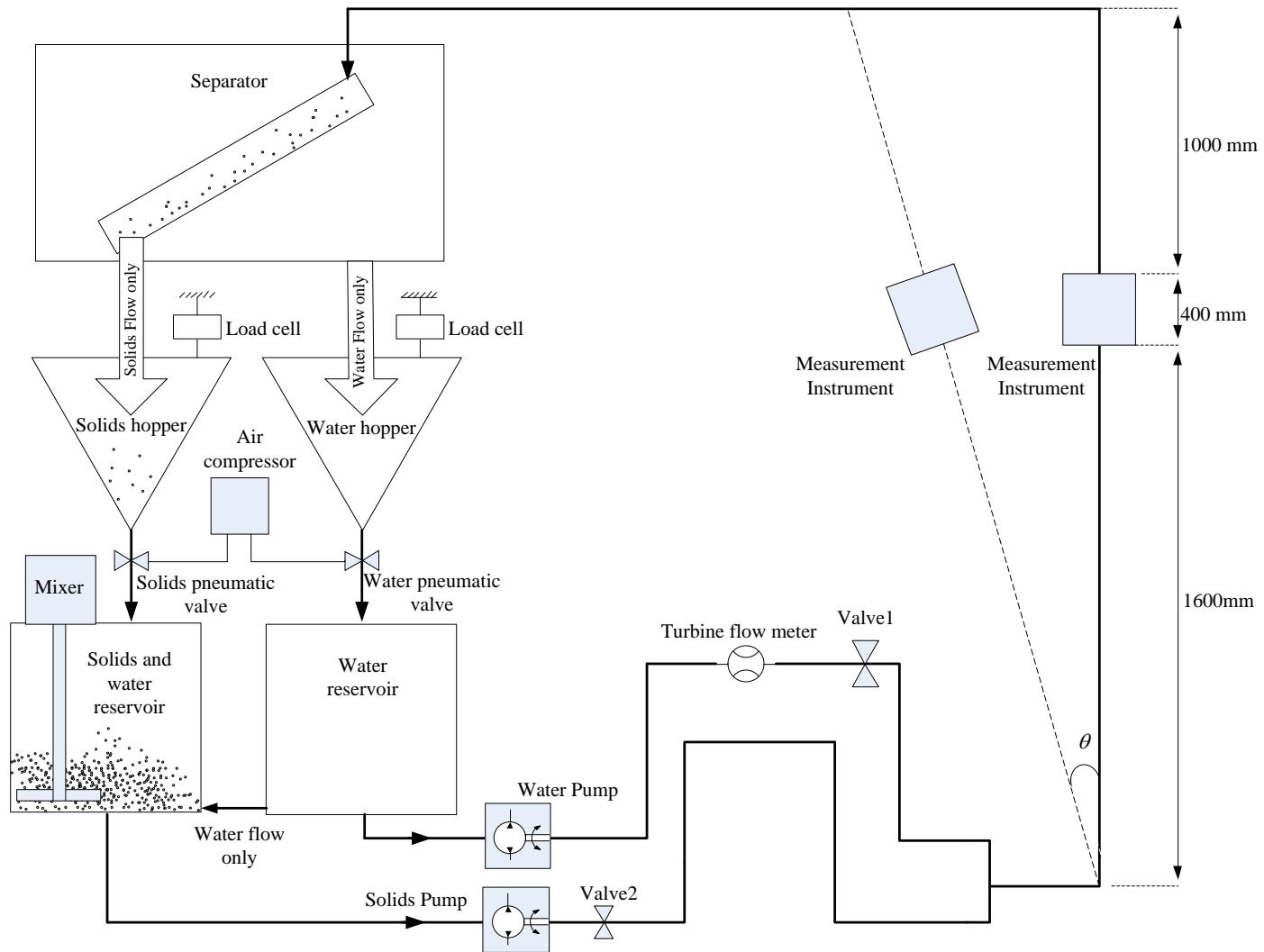
Figure 6.1 Schematic of University of Huddersfield multiphase flow loop

145
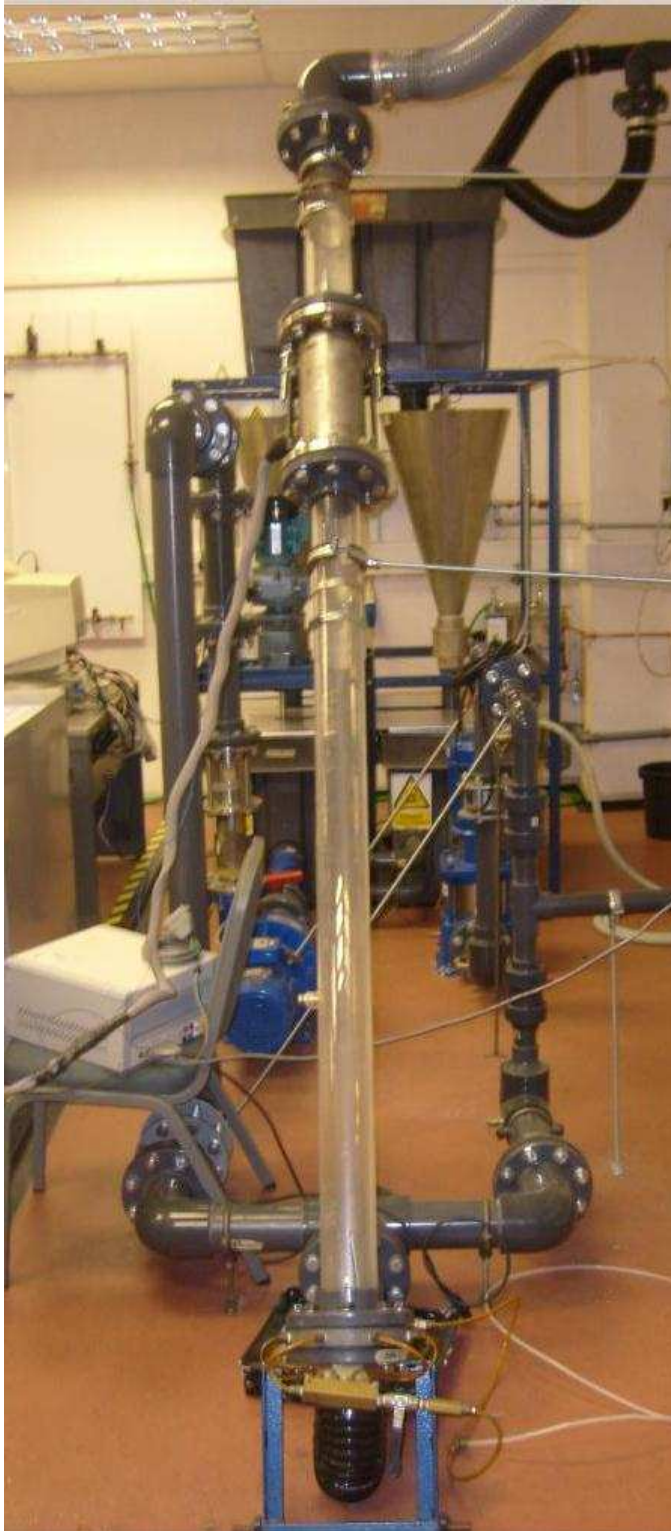
a)   ICC inclined at 30° to vertical

b) EVP System at vertical position

c) Gravimetric flow measurement system

Figure 6.2 Photographs of the University of Huddersfield multiphase flow loop

146

The solids-in-water flow passes through the working-section into a separator. The separator consists of a tank containing a rectangular cross-section chute of stainless steel mesh which separates the phases. The phases then pass into two individual conical stainless steel hoppers. Baffles are positioned along the separator to slow down the mixture flow velocity and so improve the efficiency of the separation (Figure 6.3).
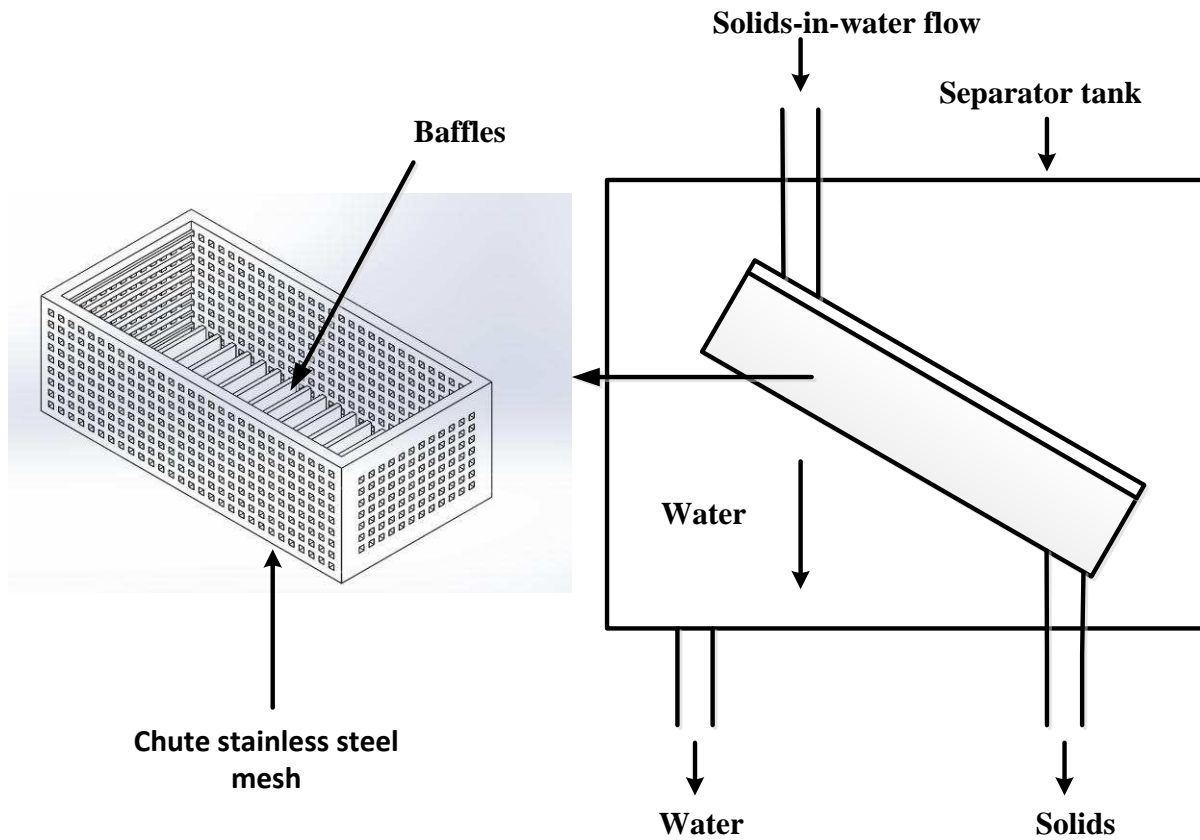
Figure 6.3 schematic diagram for the stainless steel mesh separator

Each of the two hoppers is suspended on a load cell allowing the total mass of each separated phases to be measured. Pneumatically actuated ball valves are installed in-line at the outlet of each hopper. By closing the ball valves and measuring the rate of mass increase in each hopper, the solids and water mass and volumetric flow rates ($Q_{s,ref}$ and $Q_{w,ref}$) can be obtained as described in (Section 6.3.3).

A Differential Pressure (DP) sensor mounted across one metre length of the working section provides a reference measurement of the solids volume fraction $\overline{\alpha}_{s,dp}$ (see Section6.3.2). A flushing system ensures that no air is trapped in the transducer or measurement lines. This helps to eliminate errors in the measured mean reference solids volume fraction $\overline{\alpha}_{s,dp}$ and to protect the transducer from being damaged due to the water hammer effect. Filling the measurement lines with water helped to eliminate the chance of obtaining a hydraulic shock which is known as the water hammer effect.

For the current investigation, working section inclinations of 0° and 30° degrees from the vertical were used and the 400 mm long tube in which the ICC and the EVP were installed was placed 1.6 m from the inlet of the working section.

6.3 Reference Measurement Devices

The flow loop was instrumented to provide reference measurements of solids-in-water flow parameters, these reference measurements were, (i) the mean solids volume fraction, $\overline{\alpha}_{s,dp}$, (ii) the solids volumetric flow rate $Q_{s,ref}$ and (iii) and the water volumetric flow rate, $Q_{w,ref}$, in the working section.

This section describes the reference measurement devices that were used for this purpose.

6.3.1 Turbine Meter

The turbine meter is installed in the water line as shown Figure 6.1. By operating the water pump and opening valve 1 (valve 2 closed) water is pumped through the turbine meter into the work-section. The turbine meter was used to measure the volumetric flow rate of the single-phase

"water only" flow by counting the rotation frequency f_r of the turbine rotor. The water volumetric flow rate Q_w is given by:

$$Q_w = Kf_r \qquad\qquad\qquad \text{Equation 6-1}$$

Where K is the calibration factor of the turbine meter and is equal to 0.0462 $m^3h^{-1}Hz^{-1}$ (according to the manufacturer's calibration certificate). The turbine meter was used to help calculate the pipe friction factor, f_P, which is used to measure the reference mean solids volume fraction $\overline{\alpha}_{s,dp}$ as described in Section 6.3.2.

6.3.2 Differential Pressure Sensor

In the current investigation, a Differential Pressure (DP) cell, Yokogawa EJA 110A, was used to measure the mean reference solids volume fraction $\overline{\alpha}_{s,dp}$ in the flow cross-section. The DP cell was installed on the flow loop as shown in Figure 6.4 to measure the differential pressure along a one metre length of the working-section.
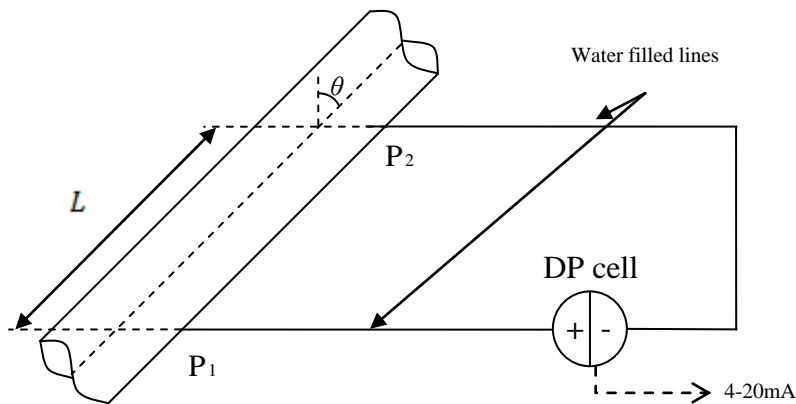
Yokogawa EJA 110A
differential pressure sensor

Figure 6.4 Schematic of the differential pressure connection

For two phase flow solids-in-water flow:

$$P_1 = \rho_m gL\cos\theta + F + P_2 \qquad\qquad \text{Equation 6-2}$$

where P_1 and P_2 are the upstream and downstream static pressures at points 1 and 2 respectively, ρ_m is the mean density of the fluid, g is the acceleration of gravity (9.81 m/s^2), L is the distance between the upstream and downstream pressure tapping 1 and 2, θ is the inclination angle and F is the frictional pressure loss along L.

The differential pressure ΔP measured by DP cell when it is connected to the flow tube via water filled lines is given by:

$$\Delta P = P_1 - (P_2 + \rho_w gL\cos\theta) \qquad\qquad \text{Equation 6-3}$$

$$\Delta P = (P_1 - P_2) - \rho_w gL\cos\theta \qquad\qquad \text{Equation 6-4}$$

where ρ_w is the water density.

Substituting Equation 6-2 into Equation 6-4:

$$\Delta P = \rho_m gL\cos\theta + F - \rho_w gL\cos\theta \qquad\qquad \text{Equation 6-5}$$

Equation 6-5 can be written as:

$$\frac{\Delta P - F}{gL\cos\theta} + \rho_w = \rho_m \qquad\qquad \text{Equation 6-6}$$

The density of the mixture can be expressed as:

$$\rho_m = \alpha_s \, \rho_s + (1 - \alpha_s)\rho_w \qquad\qquad \text{Equation 6-7}$$

Where α_s is the mean solids volume fraction, ρ_s is the solid density.

Substituting Equation 6-7 into Equation 6-6 gives:

$$\frac{\Delta P - F}{gL\cos\theta} + \rho_w = \alpha_s\,\rho_s + (1-\alpha_s)\rho_w \qquad \text{Equation 6-8}$$

$$\frac{\Delta P - F}{gL\cos\theta} + \rho_w = \alpha_s\,(\rho_s - \rho_w) + \rho_w \qquad \text{Equation 6-9}$$

$$\frac{\Delta P - F}{gL\cos\theta} = \alpha_s\,(\rho_s - \rho_w) \qquad \text{Equation 6-10}$$

Re-arrange Equation 6-10

$$\alpha_s = \frac{\Delta P - F}{gL\cos\theta(\rho_s - \rho_w)} \qquad \text{Equation 6-11}$$

where ΔP is the differential pressure measured by the dp cell.

On the basis of work by Cory [56] and Al-Hinai [49], it is acceptable to a first approximation to assume that a single-phase friction factor could be used to represent the frictional pressure loss F in the present investigation. Cory [56] and Al-Hinai [49] found that the Darcy-Weisbach equation is the best empirical relation for pipe-flow resistance. The Darcy-Weisbach equation applied to a circular pipe gives the frictional pressure loss as:

$$F = \frac{2\rho_w\, L\cos\theta\, f_P\, U_h^2}{D} \qquad \text{Equation 6-12}$$

where the pipe friction factor, f_P depends solely on the pipe Reynolds Number ,U_h is the mean or "homogeneous" flow velocity and D is the working-section diameter (80 mm). According to

Cory [56] and Al-Hinai [49] the single-phase pipe friction factor f_P for the flow loop at the University of Huddersfield is 0.007. In solids-in-water flow, the mean flow velocity U_h in Equation 6-12 (the "homogeneous velocity" or mixture superficial velocity) is given by:

$$U_h = \frac{Q_{s,ref} + Q_{w,ref}}{A} \qquad \text{Equation 6-13}$$

where $Q_{s,ref}$ and $Q_{w,ref}$ are obtained using the gravimetric hopper system described in Section 6.3.3 and A is the working-section cross-sectional area. The mean reference solids volume fraction $\overline{\alpha}_{s,dp}$ in the flow cross-section is obtained from Equation 6-11 , Equation 6-12 and Equation 6-13 .

A current-to-voltage converter circuit (refer to Figure 6.5) was used to convert the Yokogawa DP cell output signal (4 mA – 20 mA) to 1 V – 5 V for the differential pressure range 0 – 40 inches water gauge. In this circuit, R_{ref1} is a 250 Ω ±1% high precision resistor. The voltage drops across this resistor is fed into two buffer amplifiers. The outputs from the two buffers are connected to the input of a unity gain differential amplifier as shown Figure 6.5. The output voltage v_h of the differential amplifier was connected to the NI USB-6343 DAQ Board.
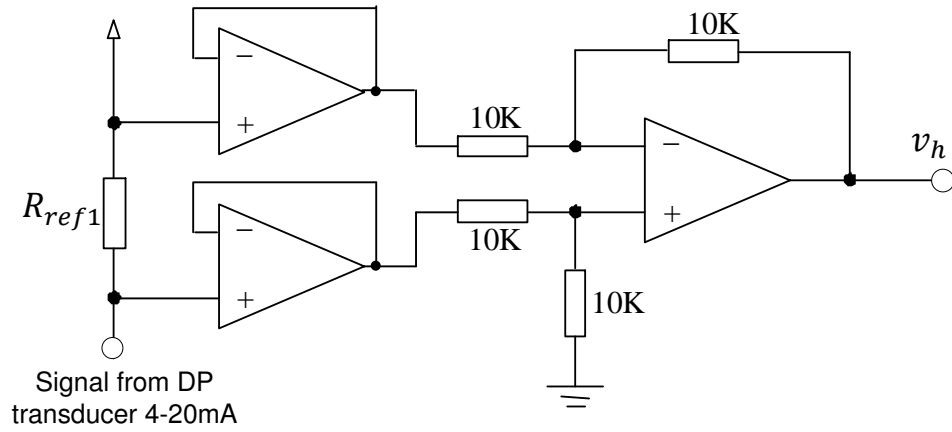
Figure 6.5 Schematic of current-to-voltage converter circuit

Figure 6.6 shows the results for voltage output from the current-to-voltage converter circuit for

differential pressures in the range 0 to 40 inches water gauge .
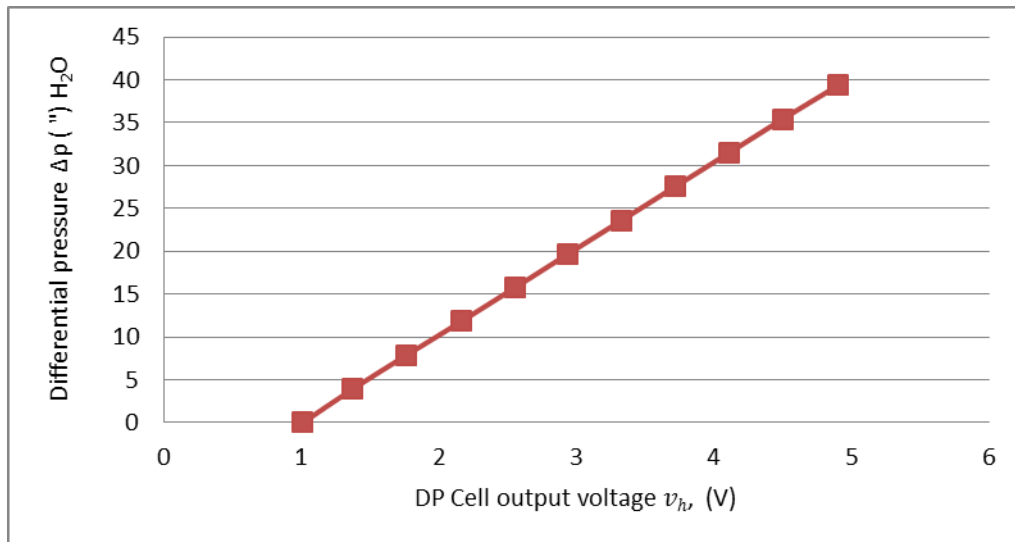
Figure 6.6 Calibration plot for Yokogawa DP cell

From Figure 6.6, the differential pressure ,ΔP, (Pascal) is obtained using:

$$\Delta P = (10.1v_h - 10.04)(\frac{2.54}{100}) * 9.81 * 1000$$

<div align="right">Equation 6-14</div>

where v_h is the output voltage from the current-to-voltage converter circuit

The differential pressure ΔP from Equation 6-14 is used in Equation 6-11 to obtain the mean volume fraction $\overline{\alpha}_{s,dp}$ of the solid phase in multiphase flow.

6.3.3 Gravimetric Flow Measurement System

In a solids-in-water flow, the reference solids volumetric flow rate $Q_{s,ref}$ and the reference water volumetric flow rate $Q_{w,ref}$ can be obtained using gravimetric methods. As shown in Figure 6.1, the solids-in-water flow passes through a separator which separates the different phases into stainless steel hoppers. Each hopper has a pneumatic ball valve at its base and is suspended from a load cell. Both the load cells and the valve control system are interfaced to a PC. By closing the valve and recording the time taken to fill the hopper with a given phase, the mean mass flow rate for a given phase $\dot{M}$ can be calculated immediately. Using the measured mean mass flow rate $\dot{M}$ and the density of the phase, ρ_w or ρ_s, the volumetric flow for the phase can be calculated as:

$$Q = \frac{\dot{M}}{\rho}$$

<div align="right">Equation 6-15</div>

A correction to compensate for the effect of water adhering to the surface of the beads is presented in Section 6.2.3.3.

6.3.3.1 Hopper Load Cell Calibration

The load cell for each hopper was calibrated by incrementally adding known masses of water to the hopper and recording the output voltage signal from the hopper load cell. For each hopper the mass was added in equal increments for the full range of the load cells, i.e. 0kg to 45kg. To ensure the repeatability and accuracy, the calibration was carried out twice for each hopper during this project.

The hopper calibration curves show a good linear relationship between the added masses and the load cell output voltages for each hopper, see Figure 6.7.
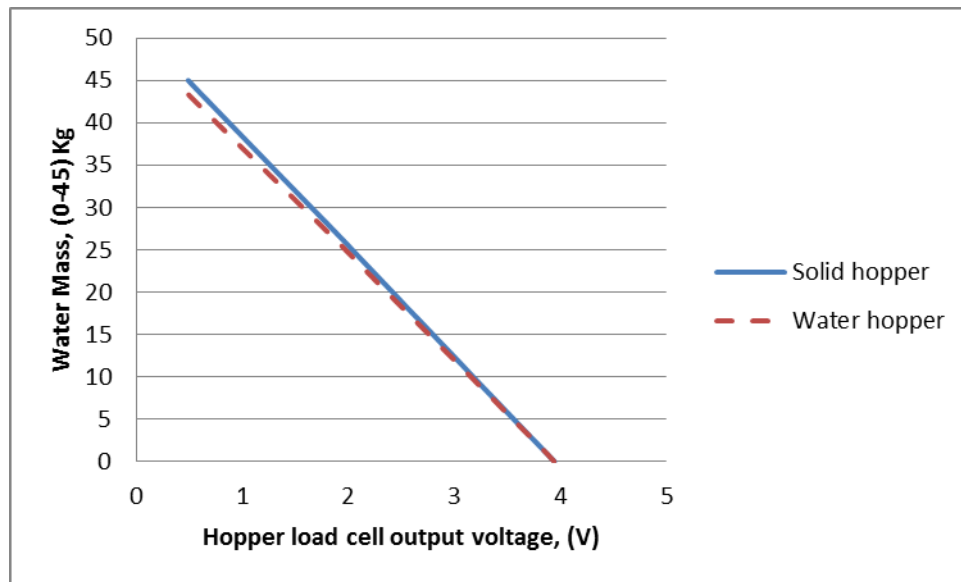
Figure 6.7 Hoppers load cell calibration curve

Using linear regression, the relationship between the masses (M_s and M_w for solids and water respectively) and the hopper load cell output voltages (V_s and V_w for solids and water respectively) were:

$$M_s = 51.491 - 13.055V_s$$

Equation 6-16

$$M_w = 49.653 - 12.563 V_w \qquad \text{Equation 6-17}$$

6.3.3.2 Operation of the Gravimetric Flow System

Both load cells and the pneumatic ball valves were interfaced with a PC to measure V_s and V_w. The valve at the base of the hopper was closed and the time taken for a given mass of material to collect in the hopper was measured, from which the mass flow rates of the solids and water were obtained. The program determined the mass flow rates according to the following steps:

- The pneumatic ball valves are closed and the control program starts to sample each load cell continuously. As the mass in the water hopper reaches a set lower limit, $M_{w,l}$, the program starts a timer. Similarly for the solids hopper, as the mass of the solid reaches its set lower limit, $M_{s,l}$ second timer starts.

- When the mass in the water hopper reaches an upper set limit, $M_{w,u}$, the program halts the first timer and measures the time taken, ΔT_w. The same process occurs for the solids hopper giving the time taken ΔT_s.

- The pneumatic ball valves are then opened ready for a new measurement to be made.

Using the measured time intervals and the corresponding measured masses, the solids reference volumetric flow rate $Q_{s,ref}$ and water reference volumetric flow rate $Q_{w,ref}$ can be obtained as:

$$Q_{s,ref} = \frac{M_{s,u} - M_{s,l}}{\Delta T_s \rho_s} \qquad \text{Equation 6-18}$$

Where ρ_s is the solid density which is 1340.8 kgm^{-3}.

$$Q_{w,ref} = \frac{M_{w,u} - M_{w,l}}{\Delta T_w \rho_w}$$

Equation 6-19

Where ρ_w is the water density which is 1000 kgm^{-3}.

For each flow condition, thirty values of $Q_{s,ref}$ and $Q_{w,ref}$ were taken to eliminate random errors which could occur during testing , the flow loop was left for 1 minute after each reading and 5 minutes after any change in flow conditions to make sure that the flow profile had stabilised. More detailed explanations can be found in Cory [56].

6.3.3.3 Correction Methodology for the Solids Reference Volumetric Flow Rate $Q_{s,ref}$

The separation method used in the current investigation cannot separate the solids from the water with complete efficiency. This happens because some water will always adhere to the surface of the solid particles and so will be carried into the solids hopper. The volumetric flow rate of excess water into the solids hopper is $Q_{w,exc}$. As such, the solids volumetric flow rate needs to be corrected using a correction factor. For the current investigation, $Q_{w,ref}$ was much higher than $Q_{s,ref}$ and this made ΔT_w much lower than ΔT_s. Which means that even with water excess in the solids hopper, the ratio of $Q_{w,exc} / Q_{w,ref}$ through the ΔT_w period is very small and can be negated. The excess mean volume fraction γ of the water inside the solids hopper and mixture flow density $\rho_{s,w}$ can be defined as

$$\gamma = \frac{U_{w,exc}}{U_{w,exc} + U_{s,corr}}$$

Equation 6-20

The mean density of the solids-in-water mixture inside the solids hopper can be defined as:

$$\rho_{s,w} = \frac{\rho_s U_{s,corr} + \rho_w U_{w,exc}}{U_{w,exc} + U_{s,corr}}$$

Equation 6-21

where $U_{w,exc}$ is the final excess volume of the water attached to the solid particles and $U_{s,corr}$ is the final correct volume of the solid particles. Combining Equation 6-18 and Equation 6-19, the mean mixture density in the hopper can be written as:

$$\rho_{s,w} = \rho_s (1 - \gamma) + \rho_w \gamma$$

Equation 6-22

The total volume of the mixture U_{ToT} in the hopper during the time ΔT_s can be defined as:

$$U_{ToT} = U_{s,Corr} + U_{w,exc}$$

Equation 6-23

Using Equation 6-20, $U_{w,exc}$ can be written as

$$U_{w,exc} = \frac{\gamma U_{s,Corr}}{1 - \gamma}$$

Equation 6-24

Substituting Equation 6-24 into Equation 6-21 gives:

$$U_{ToT} = U_{s,Corr}\left(1 + \frac{\gamma}{(1 - \gamma)}\right)$$

Equation 6-25

$$U_{s,Corr} = U_{ToT}(1 - \gamma)$$

Equation 6-26

By multiplying the both side of Equation 6-26 with time ΔT_s, Equation 6-26 can be written in terms of volumetric flow rates as:

$$Q_{s,Corr} = Q_{ToT}(1-\gamma)$$ Equation 6-27

where $Q_{s,Corr}$ is the correct solids volumetric flow rate, and Q_{ToT} is total volumetric flow rate of the mixture flow into the solids hopper, furthermore Q_{ToT} can be defined as:

$$Q_{ToT} = \frac{\dot{M}_{s,ref}}{\rho_{s,w}}$$ Equation 6-28

where $\dot{M}_{s,ref}$ is the mean measured mixture mass flow rate and $\rho_{s,w}$ is the mean mixture density, moreover $\dot{M}_{s,ref}$ can be defined as:

$$\dot{M}_{s,ref} = Q_{s,ref}\rho_s$$ Equation 6-29

where $Q_{s,ref}$ is the solid reference volumetric flow rate obtained by the hopper measurement (see section 6.3.3.2). Substituting Equation 6-29 into Equation 6-28 gives Equation 6-30:

$$Q_{ToT} = \frac{\rho_s Q_{s,ref}}{\rho_{s,w}}$$ Equation 6-30

Using Equation 6-30 , $Q_{s,Corr}$ in Equation 6-27 can be written as following

$$Q_{s,Corr} = \frac{\rho_s Q_{s,ref}}{\rho_{s,w}}(1-\gamma)$$ Equation 6-31

$$Q_{s,Corr} = \frac{\rho_s Q_{s,ref}}{(\rho_s(1-\gamma)+\rho_w\gamma)}(1-\gamma)$$ Equation 6-32

$Q_{s,Corr}$ in Equation 6-32 can be re-arranged as following

159

$$Q_{s,Corr} = Q_{s,ref} \left[\frac{1}{1 + (\frac{\gamma}{1-\gamma})(\frac{\rho_w}{\rho_s})} \right]$$

Equation 6-33

where $\left[\dfrac{1}{1 + (\frac{\gamma}{1-\gamma})(\frac{\rho_w}{\rho_s})} \right]$ represents the correction factor for the hopper measurements.

J. Cory [50] carried out an investigation to measure the amount of the water carried into the solids hopper and found γ to be 0.05. Knowing the solids and water densities, the correction factor was calculated to be equal to 0.962.

6.4 Electromagnetic Velocity Profiler (EVP)

In the work described in this section solids-in-water flows were investigated, the local axial velocity distribution of the water being measured using a novel instrument known as an Electromagnetic Velocity Profiler (EVP). The EVP was designed, constructed and used by Lucas and Leeungculsatien [87, 95, 107] based on existing electromagnetic flow meter theory. The EVP was used to obtain the local axial velocity distribution of electrically conducting continuous phase (water) in the flow cross-section.

The local axial velocity distribution of the solids and the local volume fraction distribution of both phases were measured using the ICC flow meter. Experimental results were obtained for the water and solids velocity and volume fraction profiles in upward vertical flow and upward flow inclined at 30 degrees to the vertical, in which non-uniform velocity and volume fraction profiles occur.

6.4.1 Background Theory of the Electromagnetic Velocity Profiler

The fundamental basis of electromagnetic flow meters is that charged particles in a conducting medium, which moves in a magnetic field, experience a Lorentz force acting in a direction perpendicular to both the material's motion and the applied magnetic field. Shercliff [108] showed that the local current density $\mathbf{j}$ in the fluid is governed by Ohm's law in the form

$$\mathbf{j} = \sigma(\mathbf{E} + \mathbf{v} \times \mathbf{B}) \qquad\qquad \text{Equation 6-34}$$

where σ is the local fluid conductivity, $\mathbf{v}$ is the local fluid velocity, and $\mathbf{B}$ is the local magnetic flux density. The expression $(\mathbf{v} \times \mathbf{B})$ represents the local electric field induced by the fluid motion, whereas $\mathbf{E}$ is the electric field due to charges distributed in and around the fluid. For fluids where the local conductivity variations are relatively minor i.e. of the order of about 10:1 (the multiphase flows under consideration in this study) Shercliff simplified Equation 6-34 and showed that the local potential U in the flow can be obtained by solving

$$\nabla^2 U = \nabla \cdot (\mathbf{v} \times \mathbf{B}) \qquad\qquad \text{Equation 6-35}$$

For a circular cross section flow channel bounded by a number of electrodes, with a uniform magnetic field of flux density $\overline{\mathrm{B}}$ normal to the axial flow direction, it can be shown with reference to Shercliff that, in a steady flow, the potential difference U_j between the jth pair of electrodes is given by an expression of the form

$$U_j = \frac{2\overline{\mathrm{B}}}{\pi a} \iint v(x, y) W(x, y)_j \, dx dy \qquad\qquad \text{Equation 6-36}$$

where $v(x, y)$ is the steady local axial flow velocity at the point (x, y) in the flow cross section, $W(x, y)_j$ is the so-called 'weight value' relating the contribution of $v(x, y)$ to U_j and a is the internal radius of the flow channel. It is shown in [95, 107] that Equation 6-36 can be discretised to give:

$$U_j = \frac{2\bar{B}}{\pi a} \sum_{i=1}^{N} v_i w_{ij} A_i \qquad\qquad \text{Equation 6-37}$$

where v_i is the mean axial velocity in the ith of N regions (or 'pixels') into which the flow cross section is divided, A_i is the cross-sectional area of the ith region and w_{ij} is a weight value relating U_j to v_i. Provided that the number of potential difference measurements U_j and the number of regions are both equal to N, Equation 6-37 can be inverted using matrix theory to enable estimates of the local axial flow velocity v_i in each of the N pixels to be determined from the N potential difference measurements U_j made on the boundary of the flow:

$$\mathbf{V} = \frac{\pi a}{2\bar{B}} [\mathbf{WA}]^{-1} \mathbf{U} \qquad\qquad \text{Equation 6-38}$$

where $\mathbf{V}$ is a single column matrix containing the pixel velocities v_i, $\mathbf{W}$ is a square matrix containing the relevant weight values w_{ij}, A is a diagonal matrix containing information on the pixel areas A_i, and $\mathbf{U}$ is a single column matrix containing the measured potential differences U_j for a given imposed velocity profile.

The EVP device (see Figure 6.9a) was used to investigate the solids-in-water two phase flow when the flow cross-section was divided into seven pixels, see Figure 6.9b. Pixel 1 was at the top

of the flow cross-section and pixel 7 was at the bottom. This pixel arrangement was chosen because, for many stratified flows of interest, variations in the axial velocity tend to occur in a single direction (i.e. in the y direction in Figure 6.9b). For measurements in horizontal or inclined solids-in-water flows the line joining e5 to e13 would be in the direction from the uppermost side of the included pipe to the lowermost side.

A Helmholtz coil was used to generate a uniform magnetic field over the flow cross section. At the plane of the electrodes, where $z = 0$, the magnetic flux density vector was always perpendicular to both the fluid flow direction and to the chords joining the electrode pairs. The flow pipe was machined from Delrin and had an internal radius of 80 mm. Delrin is a non-conducting and non-magnetic material with a relative permeability of 1. Additionally, Delrin has a very low coefficient of friction so the internal surface of the flow pipe was smooth which helped to reduce friction and viscous drag at the interface of the water and internal pipe wall.

Each coil forming the Helmholtz coil was constructed from copper wire with a diameter of 0.776 mm and a current rating of 1.62A for normal operation [107]. A Helmholtz coil driver circuit was used to generate the periodic magnetic field, see Figure 6.8, from Helmholtz coil by switching a high voltage, high current power source using Solid-State Relays. Using the periodic magnetic field helped to eliminate the chemical reactions (electrochemical effects) between the measurement electrodes and the metered fluid. Additionally, in the case of using AC magnetic flux density, the flow creates potential differences which are proportional to the product of the instantaneous magnetic field and the instantaneous flow velocity. Furthermore, these potential difference are of different frequencies to the non-flow induced noise voltages measured by the detection circuitry. Therefore using the periodic magnetic field helps to avoid signal interference from these " noise potentials" [107].
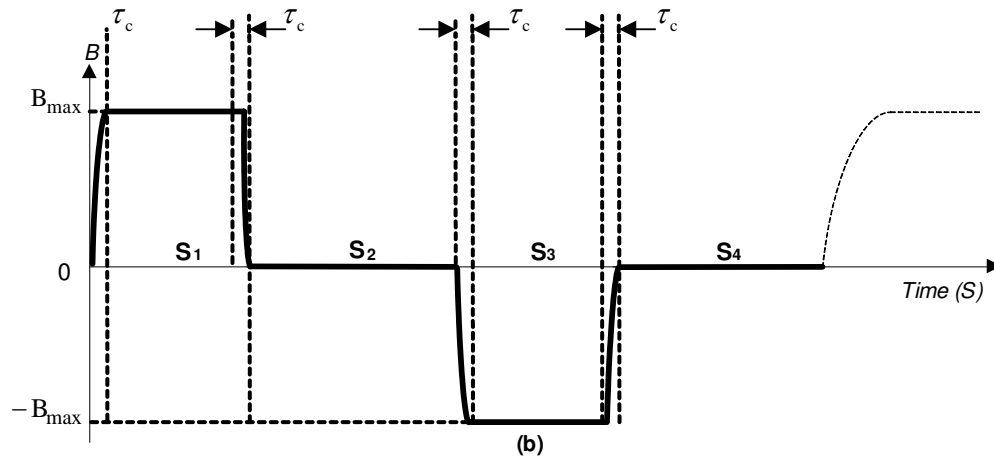
Figure 6.8 the magnetic flux density with time over one excitation cycle

The electrodes were made from low permeability stainless steel with high corrosion resistance. For the experiments described in Chapter Eight, the EVP device was used to measure the mean in-situ water velocity v_w in each of the seven pixels shown in Figure 6.9b.
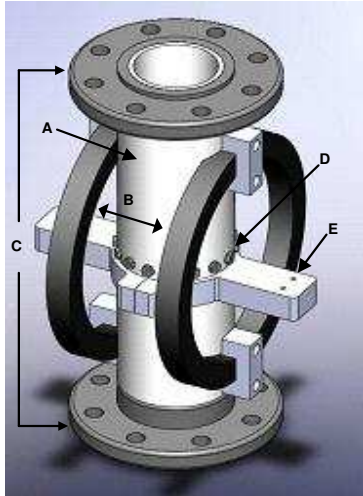
A: Meter Body   B: Helmholtz Coil

C: Flanges   D: Electrode Array

E: Cable Support
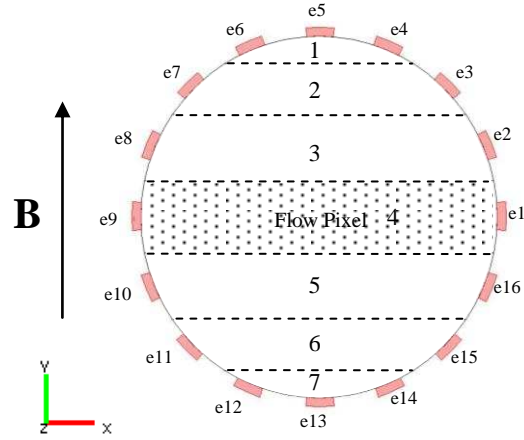
Figure 6.9 a) Electromagnetic Velocity Profiler ; (b) Schematic diagram of the flow pixels, the electrode arrangement and the direction of the magnetic field

Table 6-1 shows the areas and corresponding optimum electrode pairs for the seven geometrical regions (pixels) shown in Figure 6.9b.

Table 6-1 Appropriate electrode pairs for EVP geometry shown in Figure 6.7b

Area A_i (m^2)	
Region 1 (i=1)	$1.738e^{-4}$
Region 2 (i=2)	$6.267e^{-4}$
Region 3 (i=3)	$1.077e^{-3}$
Region 4 (i=4)	$1.264e^{-3}$
Region 5 (i=5)	$1.077e^{-3}$
Region 6 (i=6)	$6.267e^{-4}$
Region 7 (i=7)	$1.738e^{-4}$

(a) Region areas

Electrode pair Uj	
Pair 1 (j=1)	e4 – e6
Pair 2 (j=2)	e3 – e7
Pair 3 (j=3)	e2 – e8
Pair 4 (j=4)	e1 – e9
Pair 5 (j=5)	e16 – e10
Pair 6 (j=6)	e15 – e11
Pair 7 (j=7)	e14 – e12

(b) Electrode pair

The flow induced voltage U_{ref} between the jth electrode pair was measured using the circuit shown in Figure 6.10 which consisted of two voltage followers and a differential instrumentation amplifier with a gain of 996. Seven such circuits were required, one for each electrode pair. The measured induced voltage, after division by the circuit gain, was used in Equation 6-38 to determine the local water velocity in each pixel.
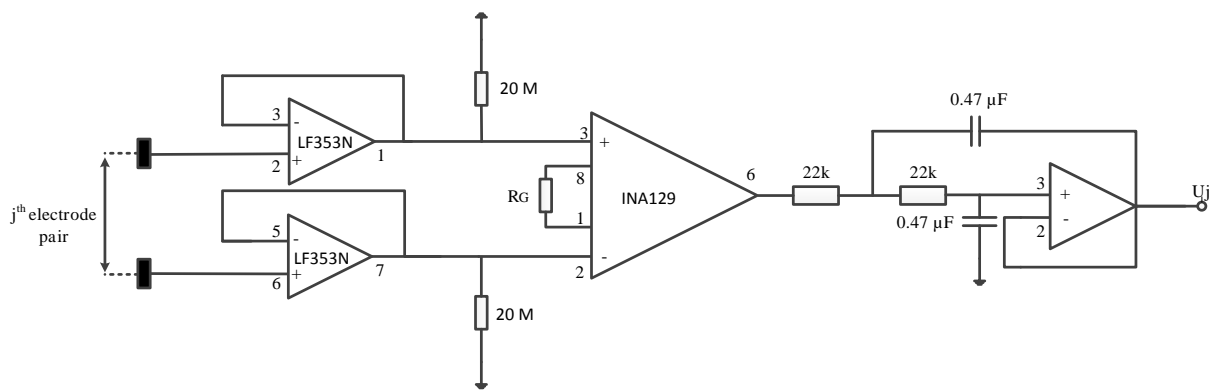
Figure 6.10 Electronic circuit used for measuring the flow induced voltage difference between each electrode pair

In normal operation a VM-1 microcontroller was used to control the EVP system and make measurements. A coil current monitoring circuit was also designed to continuously monitor the Helmholtz coil current i_c , so that compensation could be made in the coil current, and hence the magnetic flux density, arising from variations in the coil temperature.

The overall setup for the electromagnetic velocity profiler system is shown in Figure 6.11.
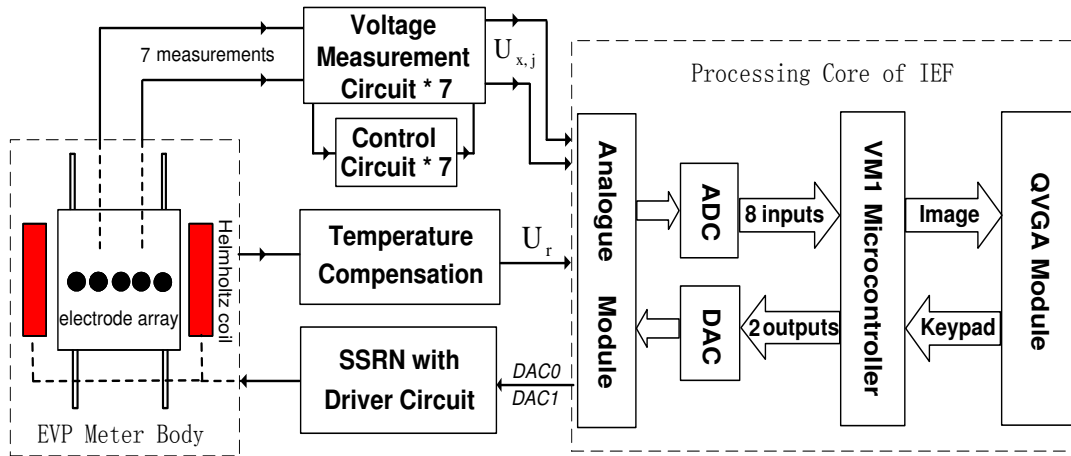
Figure 6.11 Online measurement electromagnetic velocity profiler

More detail for the EVP structure / signal measurement and analysis can be found in Lucas and Leeungculsatien [87, 95, 107].

6.4.2 Integration of ICC and EVP

Figure 6.12 shows the design of the two-phase flow meter for obtaining the individual volumetric flow rates of the solids and water phases. The two-phase flow meter system includes the EVP measurement instruments described above (see Section 6.4.1) and ICC (refer chapter 3). This system is limited to flows in which the continuous phase is electrically conducting and the discontinuous phase is an insulator.
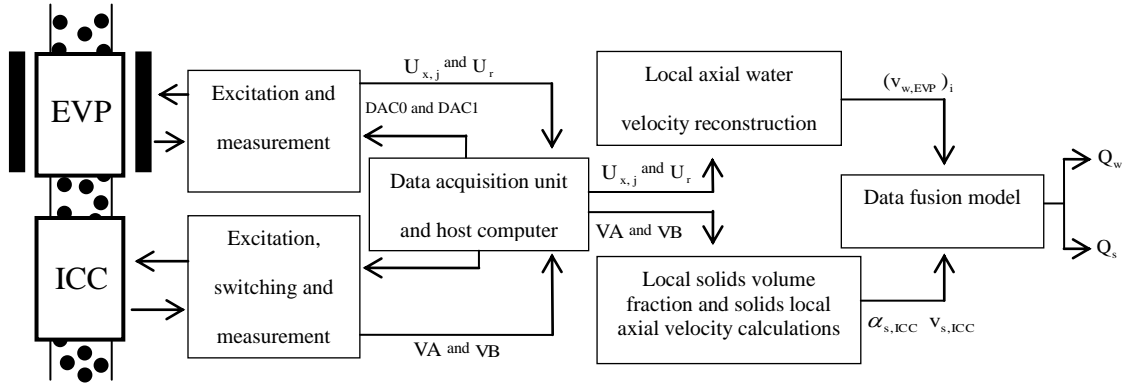
Figure 6.12 Two phase flow meter system

For two-phase solids-in-water flow, the ICC device is used to obtain the local volume fraction and the local flow velocity distribution of the dispersed phase. The volumetric flow rate of the dispersed phase can be expressed as:

$$Q_{s,ICC} = \int_A \alpha_{s,ICC} v_{s,ICC} \, dA \qquad \text{Equation 6-39}$$

where $\alpha_{s,ICC}$ and $v_{s,ICC}$ represent respectively the interpolation of the measured local solids volume fraction and the measured local solids velocity across the pipe section, see section 6.5.2.3.

The EVP is used to obtain the local axial velocity distribution of the electrically conducting continuous phase. The local volume fraction distribution of the dispersed phase obtained using the ICC device is used with the measured continuous phase velocity distribution to obtain the continuous phase volumetric flow rate as:

$$Q_{w,EVP} = \int_A (1 - \alpha_{s,ICC})_i (v_{w,EVP})_i \, dA \qquad \text{Equation 6-40}$$

It should be noted that the EVP device uses a seven pixel Configuration denoted from region 1 to region 7, see Figure 6.9b. For the purpose of integration, the local volume fraction distribution

168

of the dispersed phase obtained using the ICC device (refer to Figure 7-2 to 7-4 and 7-6 to 7-8) is integrated in each of the seven regions in order to determine the mean in-situ solids volume fraction in each of the regions 1 to 7. Based on the above, Equation 6-38 can be written in the term of the seven regions as:

$$Q_{w,EVP} = \sum_{i=1}^{7} (1 - \alpha_{s,ICC})_i (v_{w,EVP})_i (A)_i \qquad \text{Equation 6-41}$$

where $(v_{w,EVP})_i$ is the mean in-situ water velocity for the ith region and $(A)_i$ is the area for the ith region (where i= 1 to 7), see Table 6-1.

6.5 Experimental Procedure

The experimental procedure used in the present investigation can be divided into two sections: (i) defining the solids-in-water flow conditions which were used through the experimental procedures and (ii) experimental data acquisition and analysis.

6.5.1 Solids-in-Water Flow Conditions

The ICC and EVP flow meters were installed in the working section of the flow loop at a distance of 1.6 m from the inlet. The DP cell was mounted to measure the differential pressure along a one meter length as shown in Figure 6.1.

For inclinations of 0° and 30° degrees to the vertical, different flow conditions were selected using Arrangements I and II (see Section 6.1). The choice of the conditions depended on the stability of the flow inside the working section and the range of variation of the solids and water volumetric flow rates. For each of the conditions, the reference solids and water volumetric flow

169

rates were measured using the gravimetric flow measurement system (see Section 6.3.3). Table 6-2 shows the solids and water volumetric flow rates for each flow condition.

Table 6-2 Flow conditions used in the current investigation

Flow Condition	Angle of inclination θ to the Vertical	Solid Volumetric flow rate $Q_{s,ref}$ (m^3h^{-1})	Water volumetric flow rate $Q_{w,ref}$ (m^3h^{-1})
fm1	0	0.494	7.307
fm2	0	0.63	10.574
fm3	0	0.698	10.311
fm4	0	0.828	11.534
fm5	0	0.944	11.975
fm6	0	0.935	13.817
fm7	0	0.788	11.977
fm8	0	1.023	11.788
fm9	30	0.467	8.666
fm10	30	0.623	10.196
fm11	30	0.706	12.01
fm12	30	0.723	13.718
fm13	30	0.939	11.072
fm14	30	1.116	11.431

(0 Hz means the water pump was switched off)

6.5.2 Data Acquisition and Analysis

As described in Section 4.2.3, the ICC flow meter is controlled by electrode switching circuits which allow selection of each Configuration ϕ and rotational position n.

6.5.2.1 The Solids Velocity Measurement

The ICC device was configured as a dual-plane system to measure the solids velocity measurements which were simultaneously acquired from the two electrode arrays (A and B) as shown in Section 5.4. For both Centre of Action (CoA) and Area Methodology (AM) techniques,

the output signals from the channel A (array A) and channel B (array B) were cross correlated to provide the local solids velocity of the flow at the 'interrogated' flow cross-sections.

Both the local solids velocity $(v_s)_{\phi,n}$ obtained by CoA and the local solids velocity $(v_{s,AM})_i$ (i=1 to 32) obtained by Area Methodology were interpolated into 80x80 elements (side of 1 mm) in order to obtain the solids velocity distributions through the pipe cross section, see the MATLAB program at Appendix C. For the current study, the interpolation method was MATLAB 4 griddata method V4 which is based on the Green function of the biharmonic operator.

For each flow condition, a set of data from channels A and B was collected at 2000 samples / second and saved to be analyzed offline using a MATLAB program. The program code is shown in Appendix C code_1.

6.5.2.2 The Solid Volume Fraction Measurement

In inclined solids-in-water flow, channel B in the conductance measurement circuit is used to measure the local mixture conductivity $(\sigma_m)_{\phi,n}$ and this value of local mixture conductivity is assigned to the corresponding CoA, at positions $(Cx)_{\phi,n}$ and $(Cy)_{\phi,n}$, for a given Configuration ϕ and rotational position n. This local mixture conductivity can be used to estimate the local solids volume fraction $(\alpha_s)_{\phi,n}$ by invoking the simplified form of Maxwell's equation for the conductivity of a mixture [55]:

$$\left(\alpha_s\right)_{\phi,n} = \frac{2(\sigma_w)_{\phi,n} - 2(\sigma_m)_{\phi,n}}{2(\sigma_w)_{\phi,n} + (\sigma_m)_{\phi,n}} \qquad\qquad \text{Equation 6-42}$$

where σ_w is the electrical conductivity of the water.

The Area Methodology method (AM), refer to section 3.4.3, was used to measure the local solids volume fraction distribution in solids-in-water vertical flow. The obtained solids volume fraction $(\alpha_{s,AM})_i$ (i=1 to 32) were assigned to the corresponding 32 positions inside the pipe cross section, see Figure 3.26.

Similarly as for the solids velocity measurement, the local solids volume fraction $(\alpha_s)_{\phi,n}$ obtained using the CoA method and the local solids volume fraction $(\alpha_{s,AM})_i$ obtained by AM were interpolated into 80x80 elements (side of 1 mm) in order to obtain the solids volume fraction distributions throughout the pipe cross section.

Both the VM-1 and the NI card were used to collect data and analyse it. The data was collected for 60 seconds for each Configuration ϕ and rotational position n using 500 samples / second for VM-1 and 2000 samples /second for NI card. It was found that there was a good agreement between the VM-1 solids volume fraction results and the solids volume fraction results obtained by NI card.

6.5.2.3 Measurement of the Solids Volumetric Flow Rate

The ICC solids volumetric flow rate $Q_{s,ICC}$ for each flow condition was obtained by integrating the local solids volume fraction and local solids velocity data in the flow cross-section according to the following equation:

$$Q_{s,ICC} = \int_A \alpha_{s,ICC} \, v_{s,ICC} \, dA \qquad\qquad \text{Equation 6-43}$$

where

172

- For the solids-in-water inclined flow, $\alpha_{s,ICC}$ and $v_{s,ICC}$ represent respectively the interpolation of the local solids volume fraction $(\alpha_s)_{\phi,n}$ and the local solids velocity $(v_s)_{\phi,n}$ across the pipe section. Where $(\alpha_s)_{\phi,n}$ and $(v_s)_{\phi,n}$ where obtained by the Centre of Action CoA technique.

- For the solids-in-water vertical flow, $\alpha_{s,ICC}$ and $v_{s,ICC}$ represent respectively the interpolation of the local solids volume fraction $(\alpha_{s,AM})_i$ (i=1 to 32) and the local solids velocity $(v_{s,AM})_i$ across the pipe section. Where $(\alpha_{s,AM})_i$ and $(v_{s,AM})_i$ where obtained by the Area Methodology technique.

6.5.2.4 Reference Measurements for Solid Velocity

The reference solids volume fraction $\overline{\alpha}_{s,dp}$ and the volumetric flow rates ($Q_{s,ref}$ and $Q_{w,ref}$) were obtained using the measurement technique as described in Sections 6.3.2 and 6.3.3. It is possible to calculate a reference solids axial $\overline{v}_{s,ref}$ using $\overline{\alpha}_{s,dp}$ and $Q_{s,ref}$ as shown below:

$$\overline{v}_{s,ref} = \frac{Q_{s,ref}}{A\overline{\alpha}_{s,dp}}$$

Equation 6-44

where A is the pipe cross-section area.

It should be noted that $\overline{\alpha}_{s,dp}$, $\overline{v}_{s,ref}$, $Q_{s,ref}$ and $Q_{w,ref}$ are global measurements, so comparison of the measurements made by the ICC and EVP systems will require integration of the relevant quantities within the pipe cross-section area as shown in the following equations:

$$\overline{\alpha}_{s,ICC} = \frac{1}{A}\int_A \alpha_{s,ICC}\ dA$$

Equation 6-45

$$\overline{v_{s,ICC}} = \frac{\int_A \alpha_{s,ICC}\ v_{s,ICC}\ dA}{\int_A \alpha_{s,ICC}\ dA}$$

Equation 6-46

$$Q_{s,ICC} = \int_A \alpha_{s,ICC}\ v_{s,ICC}\ dA$$

Equation 6-47

$$Q_{w,EVP} = \int_A (1-\alpha_{s,ICC})\,v_{w,EVP}\ dA$$

Equation 6-48

where A is the pipe cross-section area.

6.6 Summary

In this chapter, the capabilities of the Huddersfield University multiphase flow loop have been described. As shown in Section 6.1, the flow loop can deliver single- phase or multiphase flows to the working-section at different solids-water flow rates. In solids-in-water flow, several reference instruments have been introduced to validate the results obtained from the EVP and ICC systems. In brief summary:

- A turbine meter is used to measure the volume flow rate from which pipe friction factor f_P is derived in order to measure the reference mean solids volume fraction $\overline{\alpha}_{s,dp}$ see Sections 6.3.1 and 6.3.2.

- A differential pressure sensor is used to measure the mean reference solids volume fraction $\overline{\alpha}_{s,dp}$ in the flow cross-section (Section 6.3.2).

- Gravimetric flow measurements are used to measure the reference solids volumetric flow rate $Q_{s,ref}$ and the reference water volumetric flow rate $Q_{w,ref}$ (Section 6.3.3).

- An Electromagnetic Velocity Profiler (EVP) based on the fundamental electromagnetic theory that charged particles in a conducting material which moves in a magnetic field, experience a

Lorentz force acting in a direction perpendicular to both the material's motion and the applied magnetic field is described.

- The EVP device was used to measure the mean in-situ water velocity v_w in each of the seven pixels shown in Figure 6.9b.

- The Impedance Cross Correlation (ICC) device was used to determine the distribution of the local solids velocity v_s and the distributions of the local solids volume fraction α_s and the local water volume fraction α_w (where $\alpha_w = 1 - \alpha_s$).

- A combined ICC/EVP two phase flow meter has been designed and built which can be used in solids-in-water two phase pipe flows to measure the volume fraction distributions of both phases, the velocity profiles of both phases and the volumetric flow rates of both phases.

- The reference solids axial $\overline{v_{s,ref}}$ is calculated using the measured reference mean solids volume fraction $\overline{\alpha}_{s,dp}$ and the measured reference solids volumetric flow rate $Q_{s,ref}$ (Section 6.5.2.4).

- Finally, the ICC and EVP measurements were integrated over the pipe cross-section area in order to compare with the global results obtained from reference devices as shown in Section 6.5.2.4.

7. CHAPTER 7: Results and Discussion

7.1 Introduction

This chapter presents the experimental results for the solids-in-water flow parameters obtained using the ICC and EVP systems. The experimental methodology is described in Section 6.5. The results cover the range of solid-in-water flow conditions fm1-fm14 listed in Table 6-2 and described in Section 6.5.1.

7.2 Solids Volume Fraction Measurement

7.2.1   Solids-in-Water Upward Flow in Vertical Pipe

Al-Hinai [49] used the ICC flow meter to measure the solids volume fraction distributions in solids-in-water upwards flow in a vertical pipe. In vertical solids-in-water flow, the mean reference solids volume fraction for his flow conditions was between 0.15 and 0.30 and Al-Hinai's results shows that the solids volume fraction α_s has small variations across the pipe cross-section, see Figure (7-1).
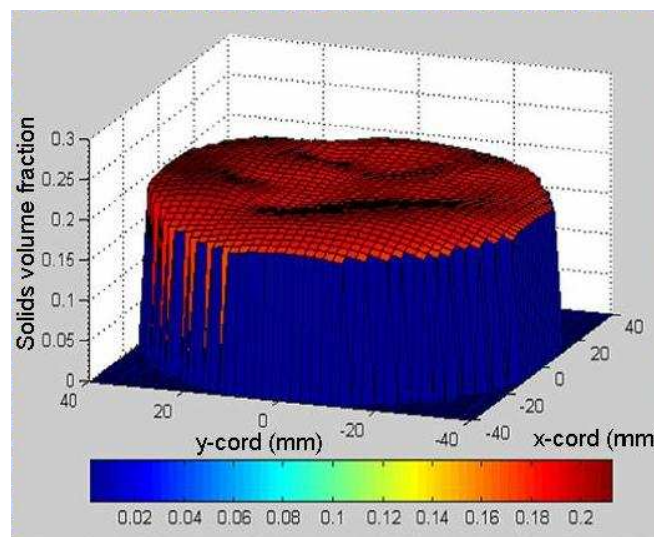
Figure 7.1Local solids volume fraction profiles for flow in a vertical pipe obtained by Al-Hinai[49] ,$\overline{\alpha_s}$ = 0.21

For the current investigation the mean reference solids volume fraction was between 6 and 8 %, therefore it is expected there will be a differences in solids distribution between the two investigations.

A number of experiments were carried out in this investigation to measure the local solids volume fraction distribution using the Centre of Action method, but this method produced unacceptable errors which reached 70%. The reasons for this are explained in Section 3.4.2. Thus a new methodology (Area Methodology) was used to measure the local solids volume fraction distribution inside the pipe cross-section for vertical flow. The Area Method and measurement procedure are described in Section 3.4.3. There are a total of 32 local solids volume fraction $(\alpha_{s,AM})_i$ measurements, each assigned to the corresponding x and y coordinates, see Figure 3.26. By interpolating these 32 measured solids volume fractions over the pipe cross-section, 3D solids volume fraction distribution profiles were obtained for flow conditions fm1-fm8 as shown in Figure 7.2 to 7.5.

 Figure 7.2 to 7.5 present the solids volume fraction distributions for vertical flow using the Area Methodology technique.
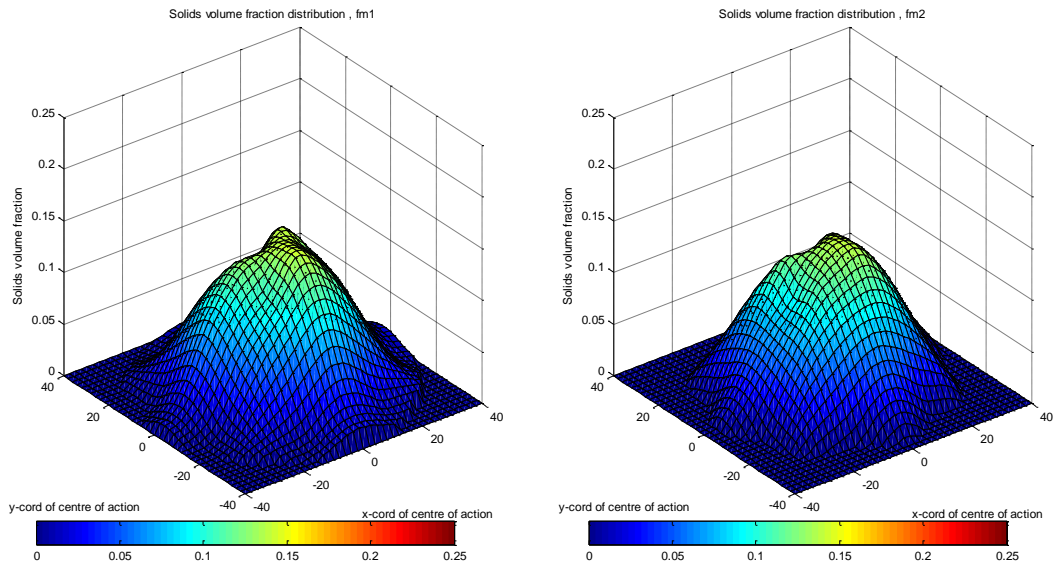
Figure 7.2 Solids volume fraction distributions for upward flow in vertical pipe, flow conditions fm1 and fm2 (Table 6-2)
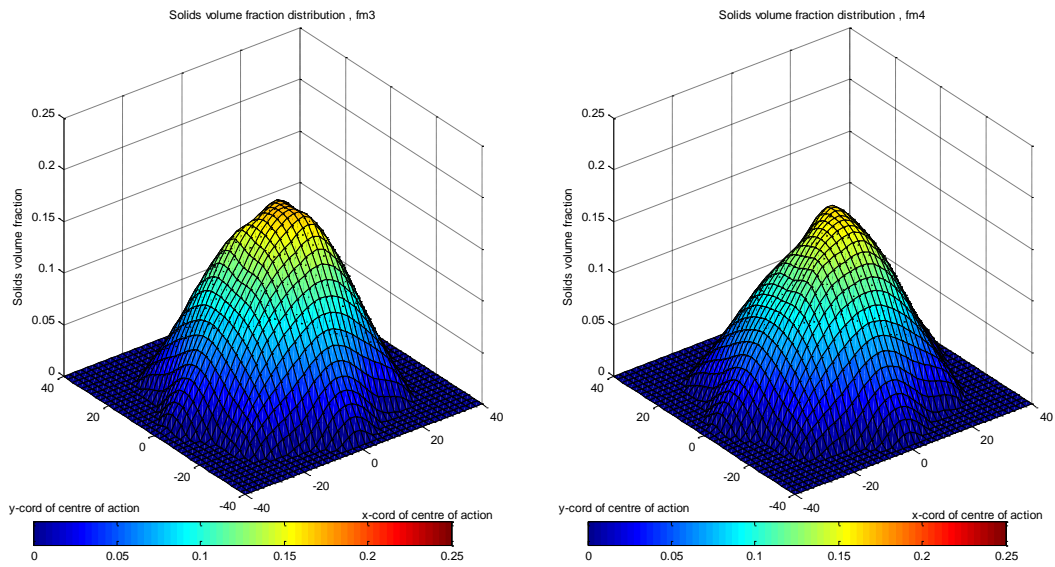
Figure 7.3 Solids volume fraction distributions for upward flow in vertical pipe, flow conditions fm3 and fm4 (Table 6-2)
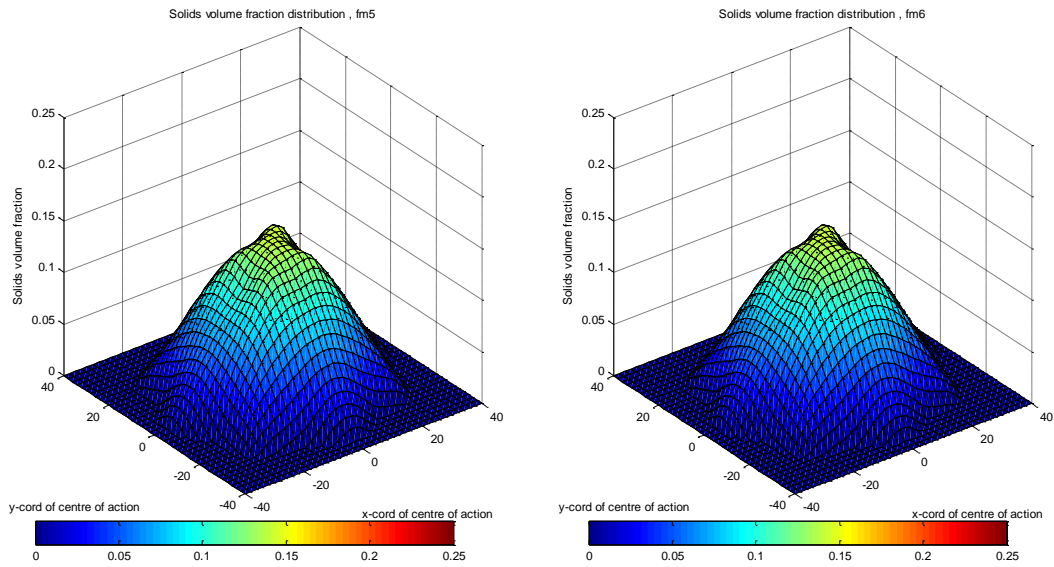
Figure 7.4 Solids volume fraction distributions for upward flow in vertical pipe, flow conditions fm5 and fm6 (Table 6-2)
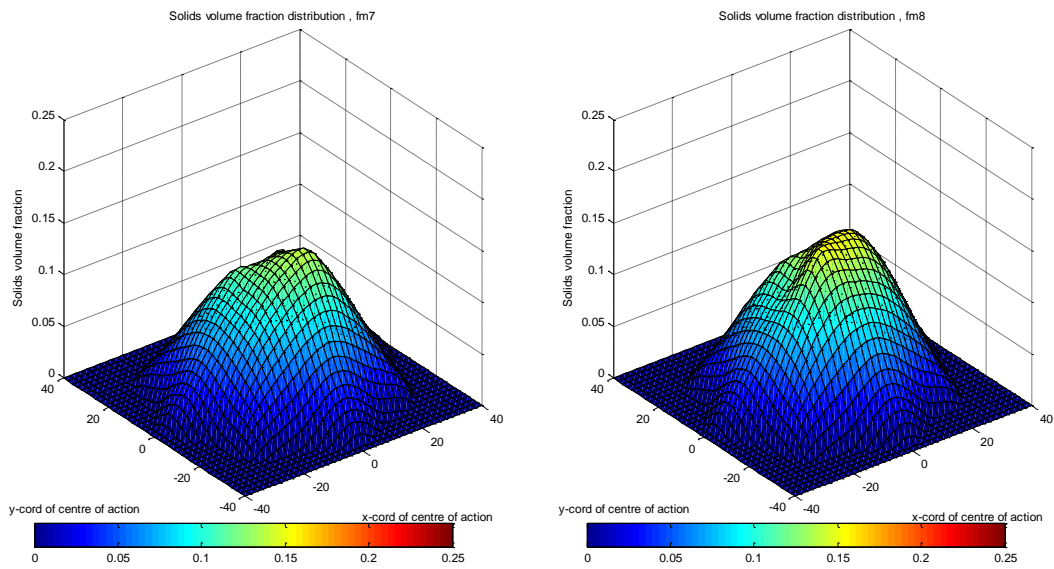
Figure 7.5 Solids volume fraction distributions for upward flow in vertical pipe, flow conditions fm7 and fm8 (Table 6-2)

The profiles of the solids volume fraction distributions for the eight flow conditions fm1-fm8 presented in Table 6-2 show a bell shape with a marked decrease in solids volume fraction $\alpha_{s,ICC}$ close to the pipe wall due to the "wall effect". This wall effect was reported by Cory [56],

179

Asakura et. al., [109] and Alajbegovic et. al., [13] for vertical solids-in-water flow. Complete cross-sectional profiles for low solids volume fractions in vertical upward flow could not be found in the literature, although, Cory (1999)[56] and Al-Hinai [49] have presented solids volume fraction distributions with a mean value α_s up to 30 % which showed only small variations of α_s across the central area of the flow cross-section.

Using the solids volume fraction distribution profiles shown in Figure 7.2 to Figure 7.5, the mean solids volume fraction in each of the regions 1 to 7 (see Figure 6.9b) were found and are plotted in Figure 7.6.
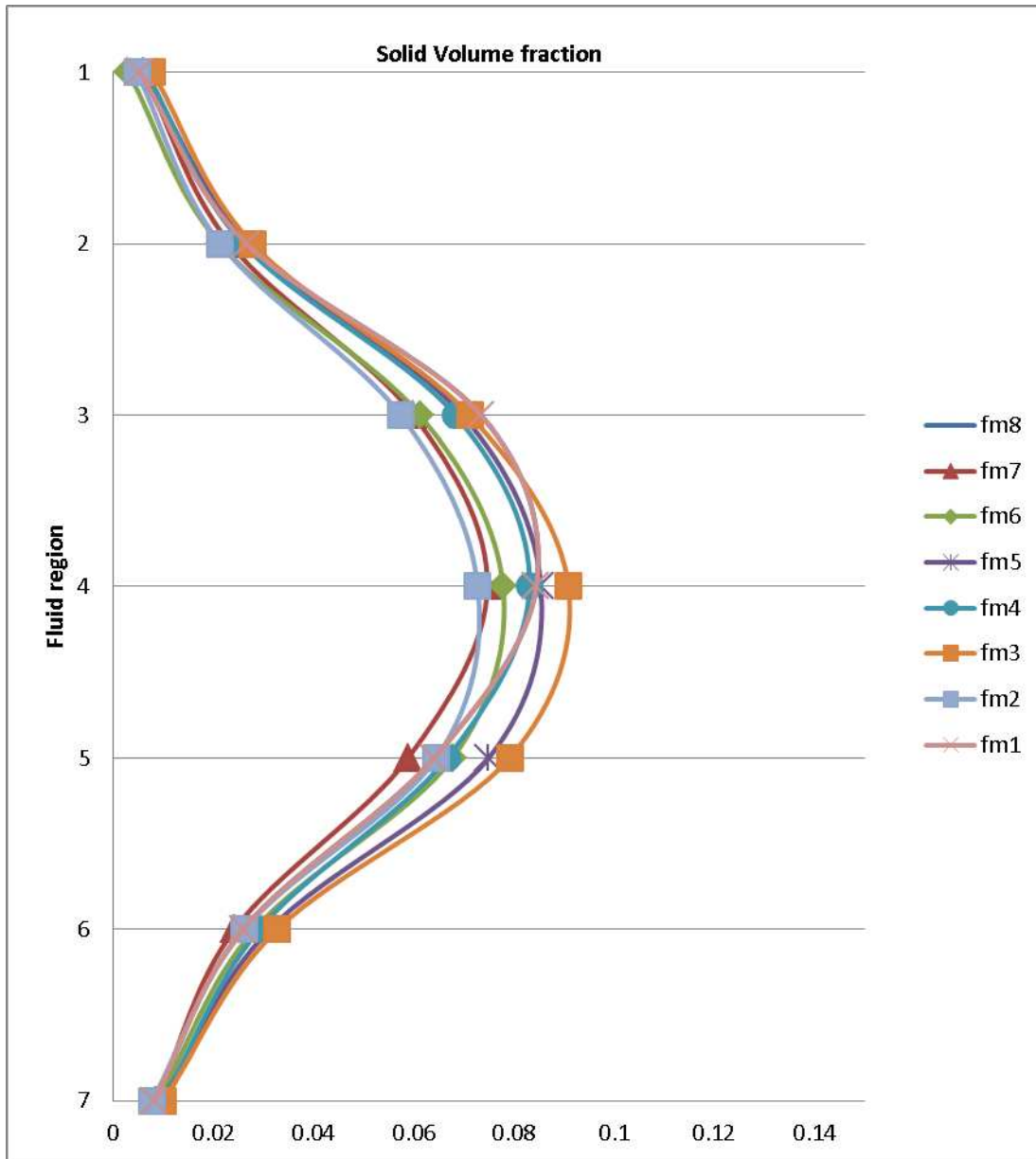
Figure 7.6 Solid volume fraction profiles for upward vertical flow in each of the seven flow regions shown in Figure 6-7b

Figure 7.6 shows that the local solids volume fraction profiles follow a symmetrical bell shape or 'power law' curve. These profiles match previous studies by Alajbegovic et. al., [13] and Sakaguchi et. al., [14] for solids-in-water vertically upward flows, see Figure 7.7, and Lucas and Panagiotopulos [110] for bubbly oil-in-water vertically upward flow.

181
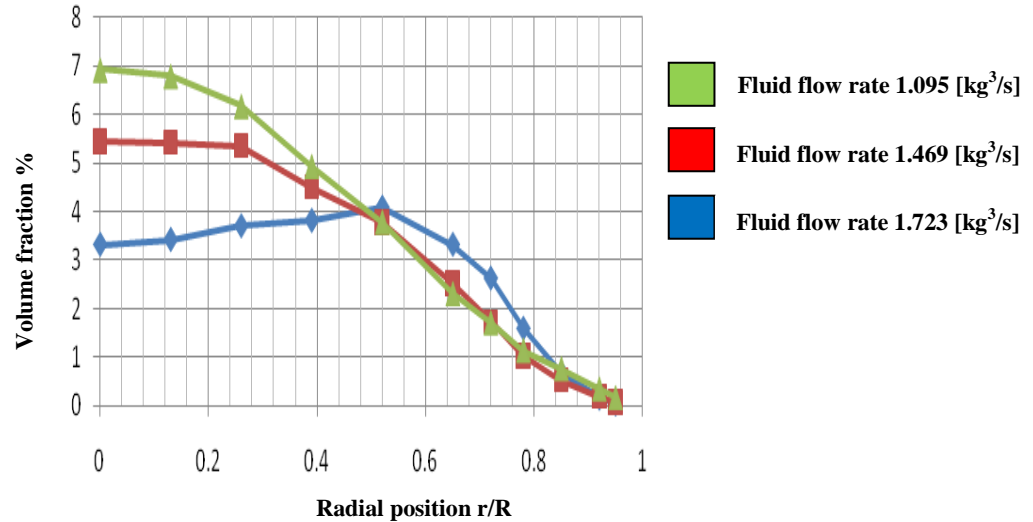
Figure 7.7 Volume fraction profiles of the ceramic beads in water in solids-in-water vertical flow using three different flow rate values, Alajbegovic et. al., [13]

Both results in Figures 7.6 and 7.7 show that the solids volume fraction has low values near the pipe wall and tends to increase toward the pipe centre. However, there is a different in solids volume fraction profiles shape between the two experiments, and this could be due to the difference in solids type and density and fluid flow rate.

For the current experiment, the non-conducting spherical solid beads of 4 mm diameter with density of 1340.8 kg/m^{-3} were used and the minimum water flow rate was 2 kg^3 /s (7.3 m^3/h). Whilst, Alajbegovic et. al., [13] used 2 mm ceramic practices with a density of 2.45 kg/m^{-3} .

The experiments performed in oil-in-water flows by Panagiotopuolos et. al, [111, 112] showed that for low dispersed phase volume fractions (α_d < 0.08 which is the same as the current flow conditions), the oil tends to migrate toward the pipe centre which may represent an equilibrium position for the dispersed phase in very low volume fraction flows.

In 2009 Panagiotopuolos et. al, [111, 112] used a dual-sensor conductance probe to measure the local axial oil velocity distribution and the local oil volume fraction distribution in vertical, oil-in-water bubbly flows in an 80 mm diameter vertical pipe. A simple DC amplifier circuit was used to measure the fluid conductance between the tip of the relevant needle and the probe body.

Panagiotopoulos showed that when the mean oil volume fraction $\overline{B} < 0.08$, the oil volume fraction distribution is approximately a `power law' in shape as show in Figure 7.8.
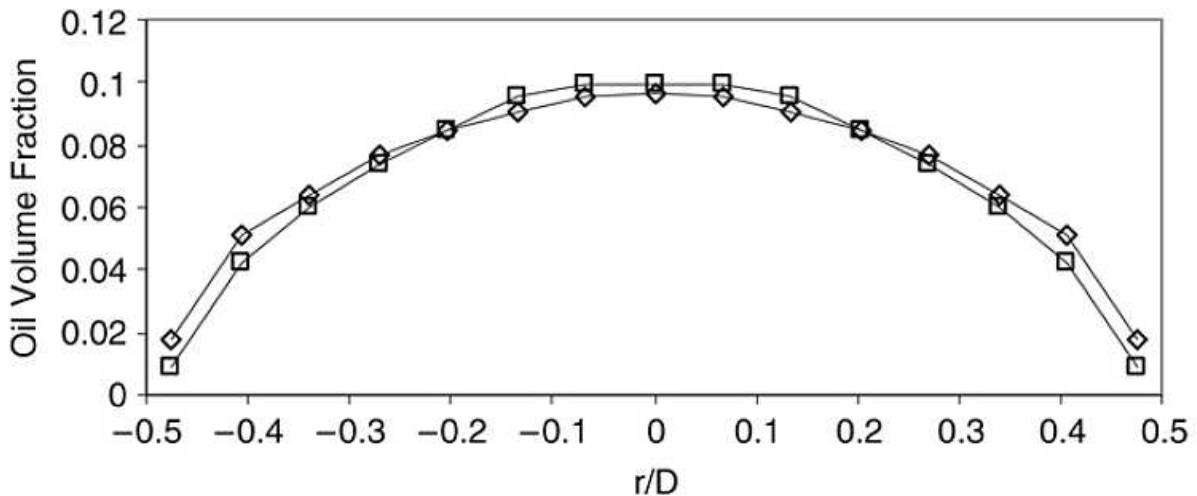
Figure 7.8 Local oil volume fraction B versus r/D for values of mean oil volume fraction less than 0.08,

B (diamonds)= 0.068, B (squares)= 0.056 [111]

Using results obtained by Beyerlein et al., [31], Panagiotopoulos et al showed that for very low dispersed phase volume fraction flow in co-current, upward, bubbly two phase flows where the superficial velocity of the continuous phase is greater than zero, it is possible to have a radial hydrodynamic force on particles of the dispersed phase. They concluded that the particles will tend to move toward the pipe centre, which may represent an equilibrium position for dispersed phase particles in very low volume fraction flows. This produces a low pressure region in their wakes and hence additional oil droplets will be drawn towards the pipe centre.

183

This behaviour is also reported in [9, 113]. This may be an explanation of the shape for the solids volume fraction profiles shown in Figure 7.6.

The solids volume fraction profiles in Figure 7.6 were used to calculate the water volume fraction distribution in the seven regions as shown in Section 7.4.4.

7.2.2 Solids-in-Water Upward Flow in Pipe Inclined at 30° to the Vertical

For the $30°$ degree inclined flow, the Centre of Action method was used to measure the solids parameter for the solids-in-water flow, see section 3.4.2. The Centre of Action method was chosen based on the experimental results for the solids volume fraction as shown later through this section.

Configuration I, II and III were used to obtain the solids volume fraction distributions profiles for flow conditions, fm9-fm14, see Table 6-2. For each flow condition, using a given Configuration ϕ and a given rotational position, n, the solids volume fraction $\alpha_{s,ICC}$ was obtained using Maxwell's equation for the conductivity of a mixture[55]:

$$\left(\alpha_{s},_{ICC}\right)_{\phi,n} = \frac{2(\sigma_{w})_{\phi,n} - 2(\sigma_{m})_{\phi,n}}{2(\sigma_{w})_{\phi,n} + (\sigma_{m})_{\phi,n}}$$

Equation 7-1

For the ϕth electrode Configuration ($\phi = I, II \text{ or } III$) and the nth rotational position ($n = 1 \text{ to } 8$), there are a total of 24 local solids volume fraction $\left(\alpha_{s}\right)_{\varphi,n}$ measurements, each assigned to the corresponding CoA position $(Cx)_{\phi,n}$, $(Cy)_{\phi,n}$ see Section 3.4.1. By interpolating these 24 measured solids volume fractions over the pipe cross-section, 3D solids volume fraction distribution profiles were obtained for flow conditions fm9-fm14 as shown in Figure 7.9 to Figure 7.11.
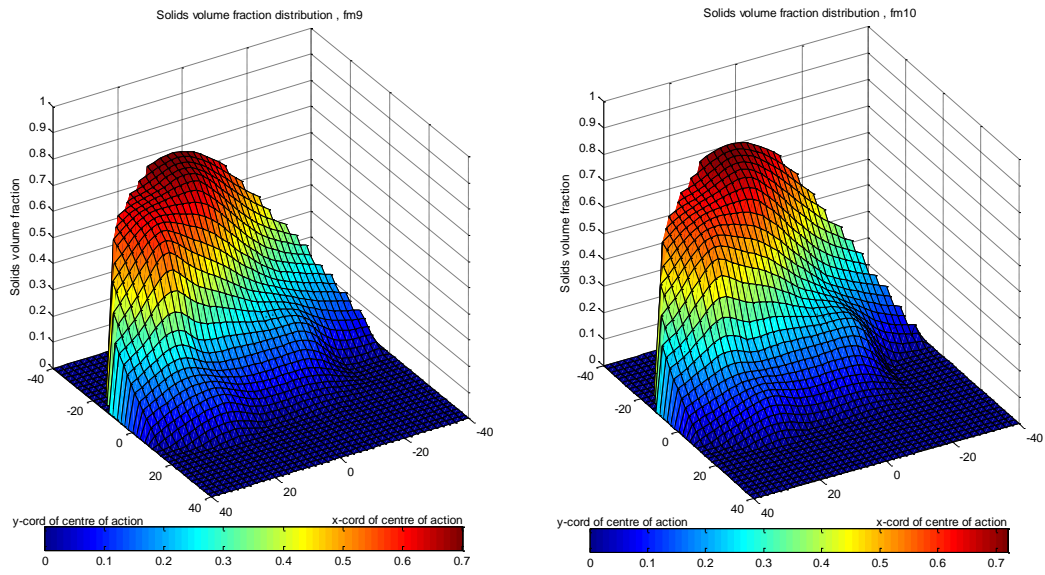
Figure 7.9 Solids volume fraction distributions for upward flow in pipe inclined at 30° to the vertical, for flow conditions fm9 and fm10 (Table 6-2)
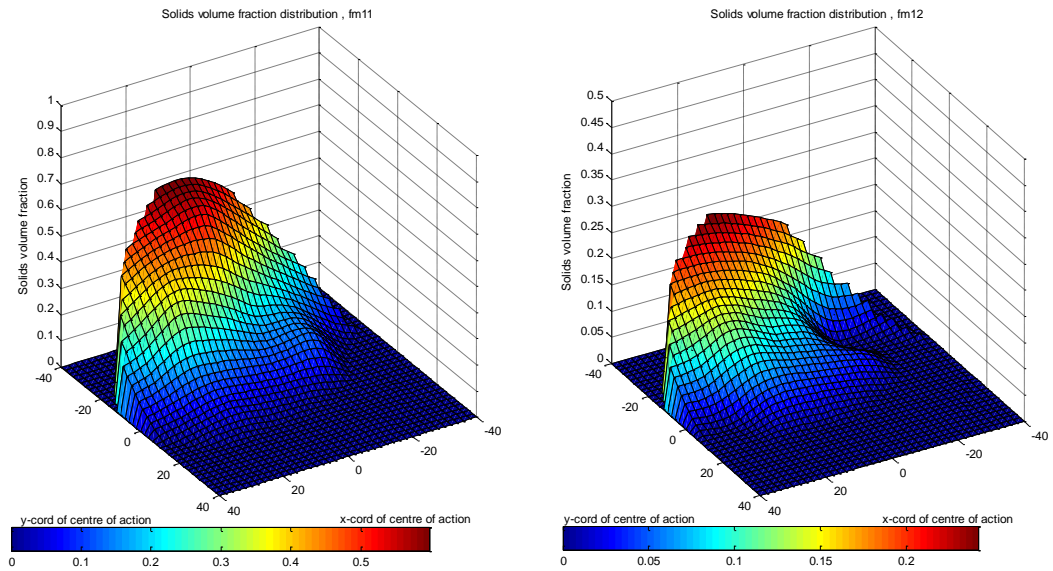
Figure 7.10 Solids volume fraction distributions for upward flow in pipe inclined at 30° to the vertical, for flow conditions fm11 and fm12 (Table 6-2)
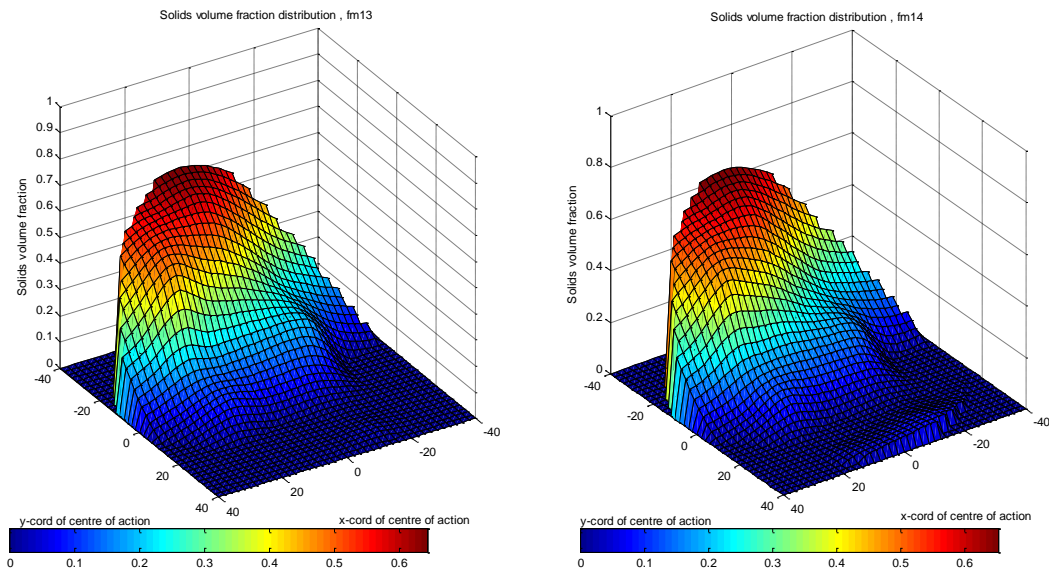
Figure 7.11 Solids volume fraction distributions for upward flow in pipe inclined at 30° to the vertical, for flow conditions fm13 and fm14 (Table 6-2)

As expected, Figures 7.9 to 7.11 show that the solids volume fraction $\alpha_{s,\text{ICC}}$ is a function of the y co-ordinate, where α_s at the lowest side of the inclined pipe is much greater than at the upper side due to the fact that solids particles are more dense than water. These measured profiles agree with visual observation of the solids-in-water flow through the Perspex working section of the flow loop, see Figure 7.12 and Figure 7.13. The measured solids volume fraction profiles show qualitative agreement with previous experimental profiles obtained by Cory [56] and Al-Hinai [49].
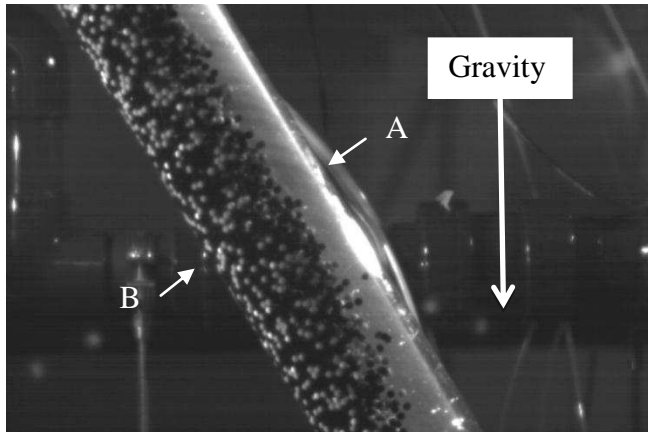
Figure 7.12 Photo of solids-in-water flow in pipe inclined at 30° to the vertical obtained using high speed camera
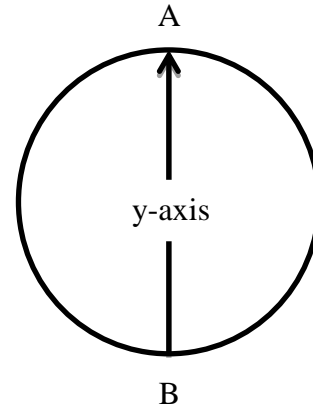
Figure 7.13 The y axis relative to the pipe cross-section from upper side of pipe (A) to lower side of pipe (B)

Figure 7.14 presents the mean solids volume fraction in the regions 1 to 7 (see Figure 6.7b) for flow conditions fm9 to fm14. The mean solid volume fraction of each region was found using the solids volume fraction distribution profiles in Figure 7.9 to Figure 7.11.
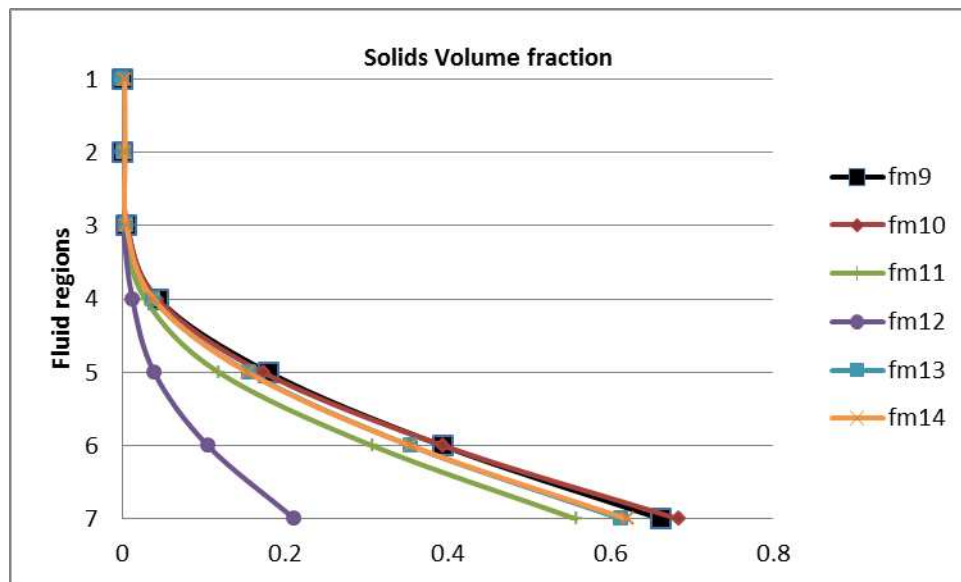
Figure 7.14 Solid volume fraction profiles for upward flows in pipes inclined at 30° to the vertical

187

The solids volume fraction profiles shown in Figure 7.14 demonstrate that for upward flow in pipes inclined at 30° degrees to the vertical, the upper regions of the flow cross-section (regions 1, 2 and 3 in Figure 6.7b) contain only a very small proportion of the solid particles present, i.e. these regions were mostly occupied by water. However, the solids volume fraction increased towards the lower regions in the pipe, reaching a maximum in region 7. The maximum measured value of the solids volume fraction in region 7 was 0.68 for flow condition fm10 ($0.623\,Q_{s,ref}$, $10.196\,Q_{w,ref}$ and $0.19\,\overline{\alpha}_{s,dp}$) while the minimum value was 0.21 for flow condition fm12 ($0.723\,Q_{s,ref}$, and $13.718\,Q_{w,ref}$ and $0.08\,\overline{\alpha}_{s,dp}$) .

7.3 Solids-in-Water Velocity Measurements

This section shows the results for solids and water velocity profiles obtained by the ICC flow meter and the EVP system in upward vertical and inclined solids-in-water flow.

7.3.1   Solids-in-Water Profile for Upward Flow in Vertical Pipe

7.3.1.1 Solids velocity profiles using ICC flow meter

The local solids velocity was obtained by cross correlation between the two electrode arrays. In vertical flow, the Area Methodology (refer to Section 3.4.3) was used in order to find the local solids velocity $(v_{s,AM})_i$ at 32 measurement points inside the pipe cross section, see Section 3.4.3.3. The local solids velocity $(v_{s,AM})_i$ was interpolated through the pipe section using MATLAB 4griddata method.

The solids velocity distribution for a given flow condition fm1 to fm8 in vertical solids-in-water flow, see Table 6-2, is presented in the following figures.
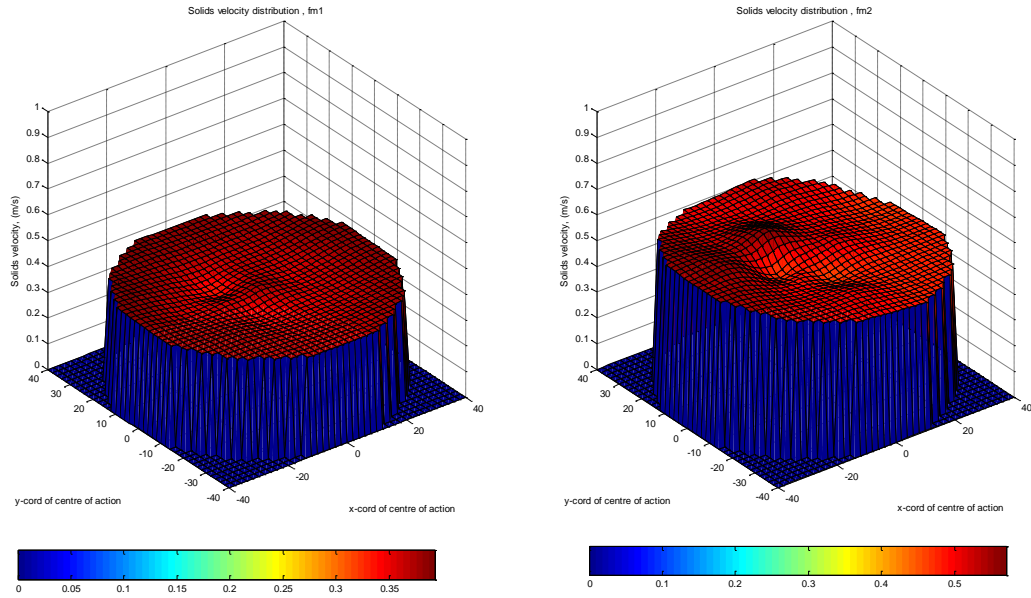
Figure 7.15 Solids velocity distributions for upward flow in vertical pipe for flow conditions fm1 and fm2
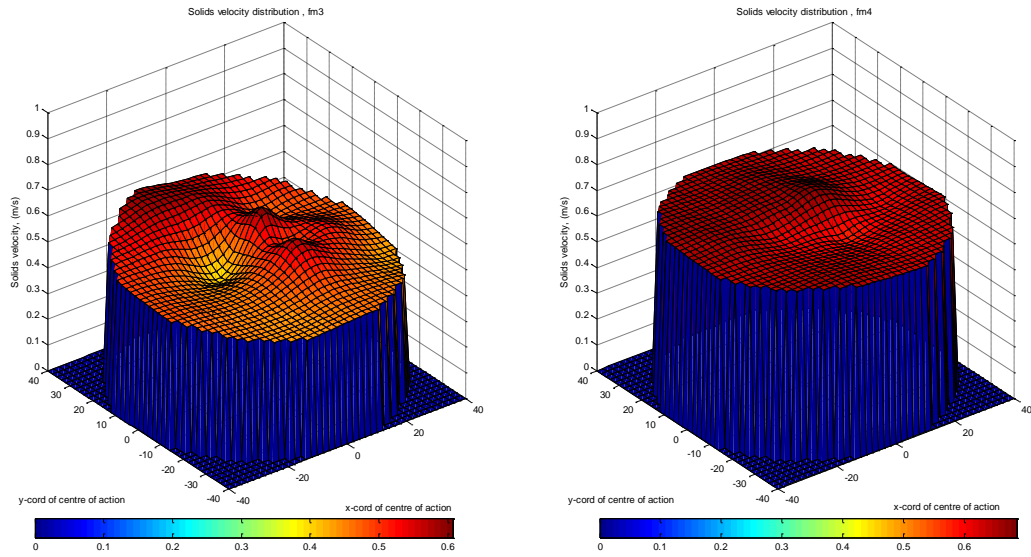
Figure 7.16 Solids velocity distributions for upward flow in vertical pipe for flow conditions fm3 and fm4
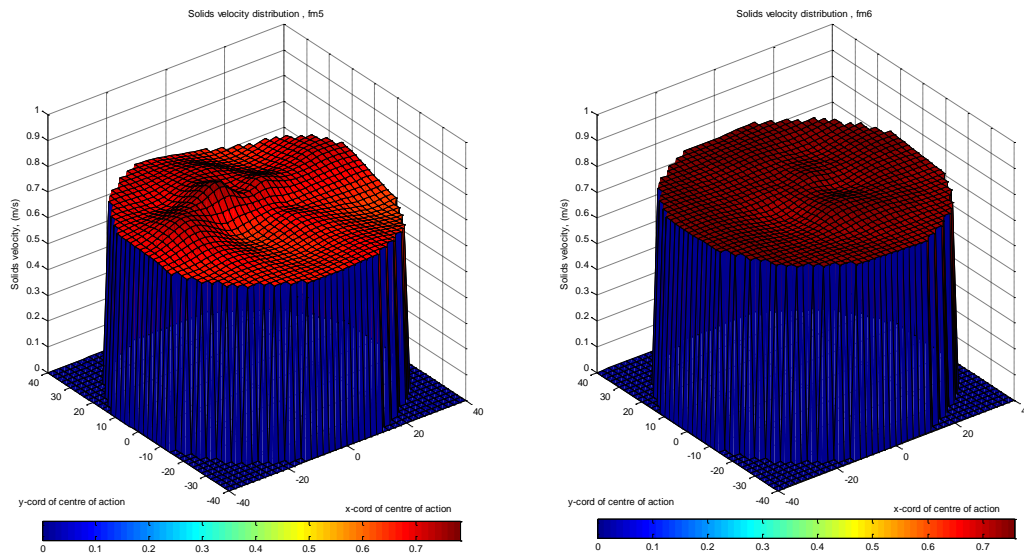
Figure 7.17 Solids velocity distributions for upward flow in vertical pipe for flow conditions fm5 and fm6
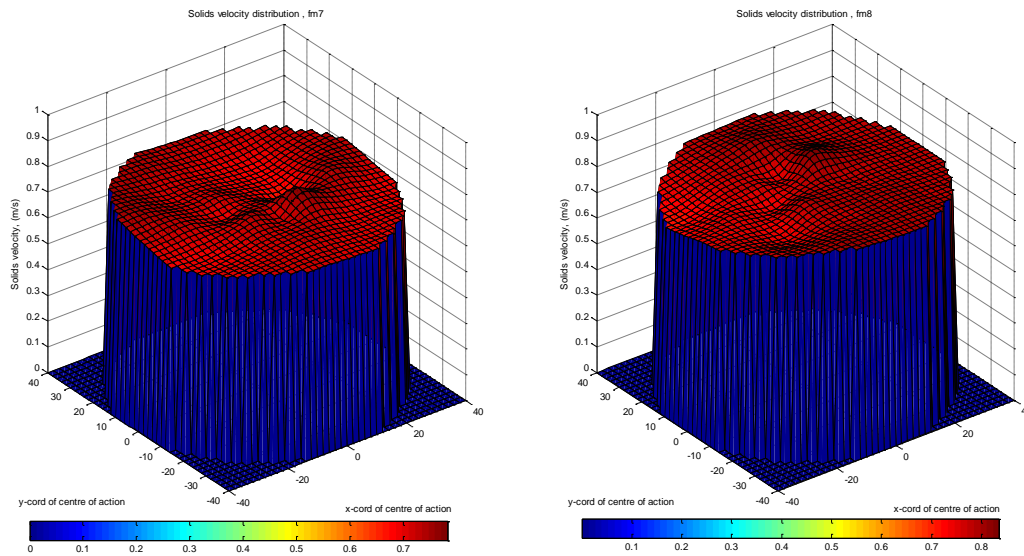
Figure 7.18 Solids velocity distributions for upward flow in vertical pipe for flow conditions fm7 and fm8

The solids velocity profiles shown in Figure 7.15 to Figure 7.18 indicate only small variations of $v_{s,ICC}$ over the cross-section. These profiles are flatter than those of the volume fraction $\alpha_{s,ICC}$ and show no drop in velocity at the wall pipe.

The velocity profiles show good agreement with the experimental profiles reported by Cory [56] and Al-Hinai [49], see Figure 2.8.

Cory reported previous research which showed a drop in solids velocity near the pipe wall due to the "wall effect", and this drop become more pronounced as the mean solids axial velocity v_s is increased. However, these trends are not noticeable either in the current investigation's velocity profiles or in the Cory (1999)[56] and Al-Hinai(2010)[49] velocity profiles.

Additionally, the profiles mentioned above are flatter than the solids velocity profiles obtained by Alajbegovic et. al., [13] for solids-in-water vertical flow, Figure 7.19 and the oil velocity profile obtained by Panagiotopuolos et. al, [111, 112] for oil-in-water vertical flow, Figure 7.20.
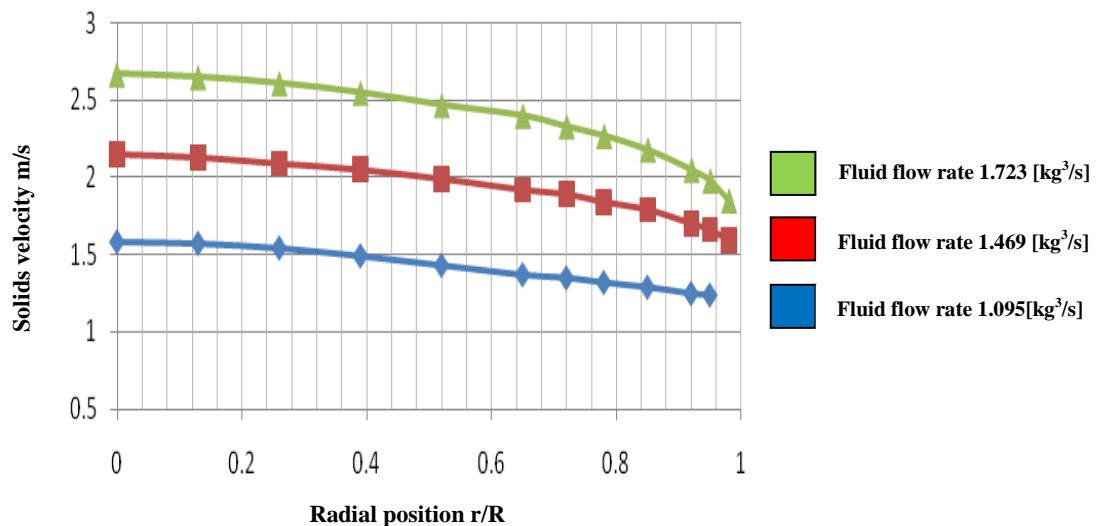
Figure 7.19 Velocity profiles of ceramic beads in water in solids-in-water vertical flow, Alajbegovic et. al., [13] for different fluid flow rate
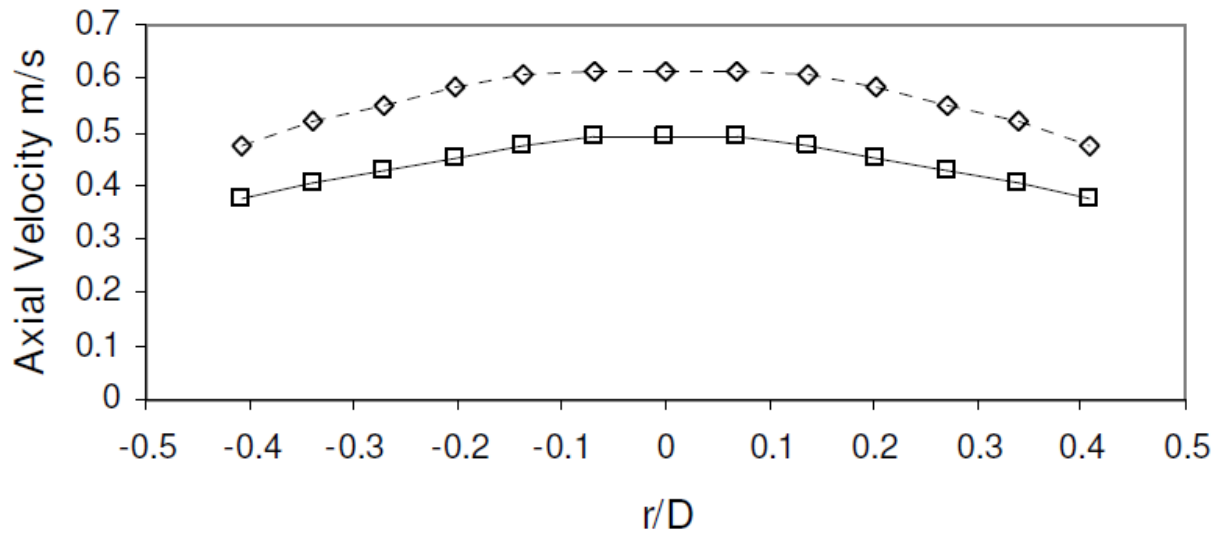
Figure 7.20 Local oil velocity versus r/D for values of mean oil volume fraction less than 0.08, B (diamonds)= 0.068, B (squares)= 0.056 [111]

7.3.1.2 Water Velocity Profiles for Vertical Upward Flow Using the Electromagnetic Velocity Profiler

This section describes the experimental tests carried out using the EVP system to obtain the water velocity profile for solids-in-water flow (see Section 6.4). The EVP and ICC flow meter used the same flow loop experimental arrangement and flow conditions. With the working-section vertical, the EVP system was placed 1.6 m from the inlet so that the measurement plane of the EVP was the same as for the ICC flow meter. The operating procedure and the velocity calculations associated with the EVP system instrument are explained in Section 6.4.

The reconstructed local axial velocity profiles of the water in vertical solids-in-water flow are shown in Figure 7.21(b).

(a) The Solids velocity profiles in 7 pixels

(b) The water velocity profiles in 7 pixels
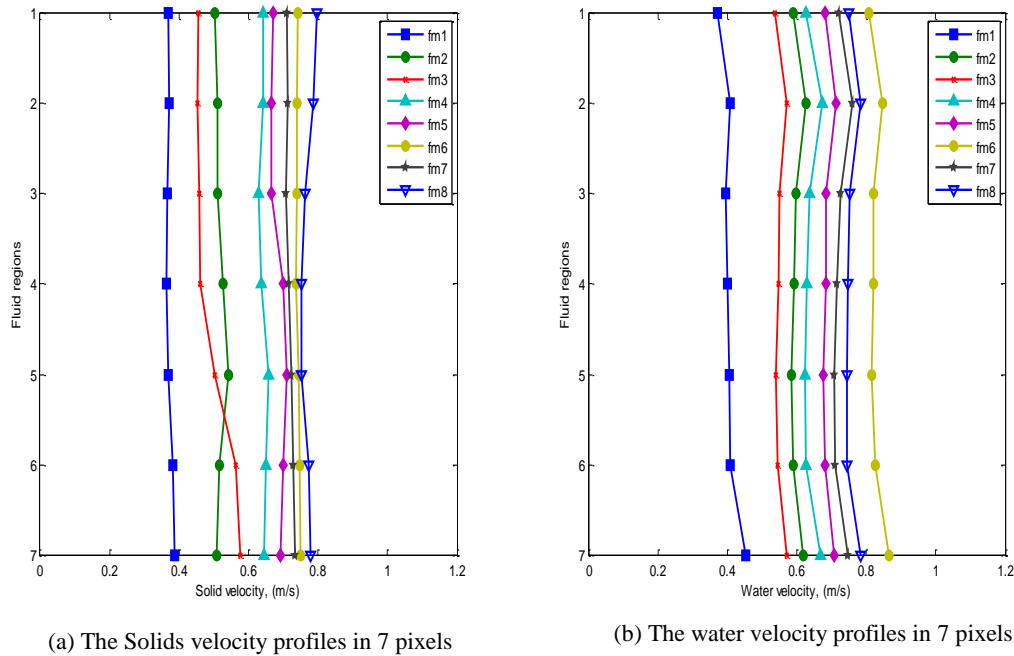
Figure 7.21 Reconstructed water velocity and solids velocity in solids-in-water upward flow in vertical pipe for the 7 flow regions shown in Figure 6.7(b) and flow conditions fm1 – fm8

A MATLAB program was used to divide the solids velocity distribution, Figure 7.15 to Figure 7.18, into 7 regions shown in Figure 6.9b and determine the mean solids velocities in each of these regions.

Figure 7.21(a) shows similar behaviour for the different axial solids velocity profiles when the solids have a uniform velocity across the pipe.

In all of the vertical upward flows, the water velocity profiles (refer to Figure 7.21b) showed relatively small variation over the pipe cross-section. The reconstructed water velocities, $v_{w,EVP}$, shown in Figure 7.21(b) are relatively uniform across the pipe for the different flow conditions.

193

The comparison between the solids velocity $v_{s,ICC}$ and water velocity $v_{w,EVP}$ for each of solids-in-water conditions can be seen in Figure 7.22 to 7.25.
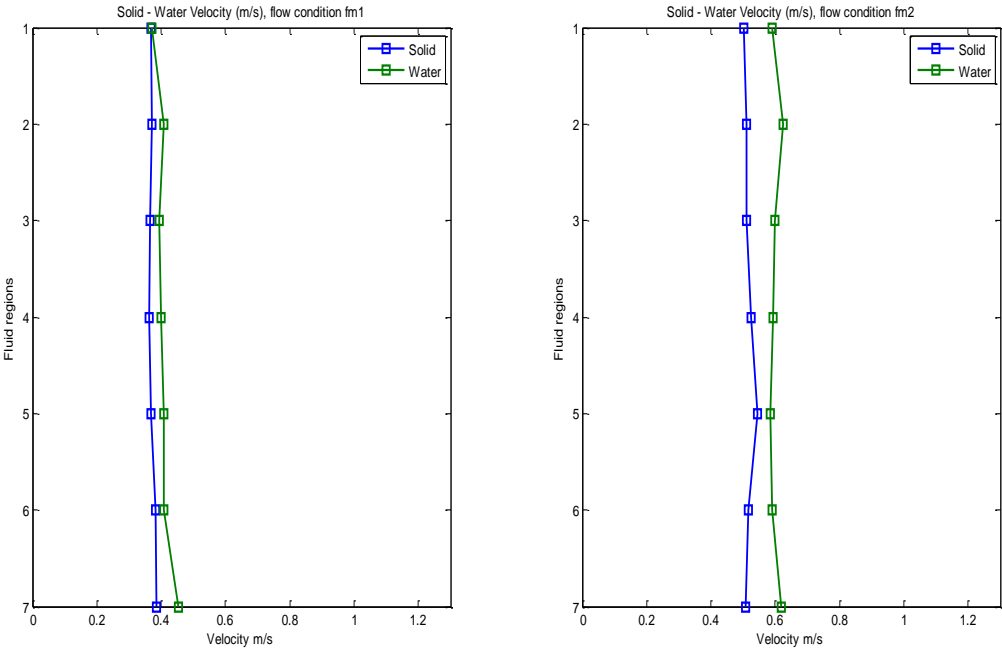
Figure 7.22 Reconstructed water and solids velocities for upward flow in vertical pipe for flow conditions fm1 and fm2
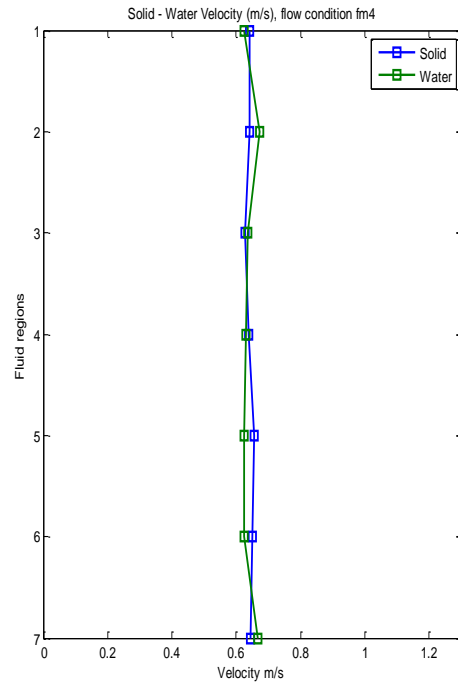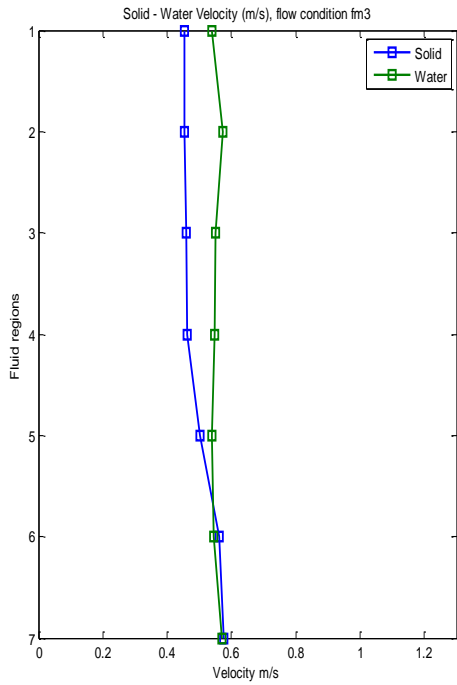
Figure 7.23 Reconstructed water and solids velocities for upward flow in vertical pipe for flow conditions fm3 and fm4
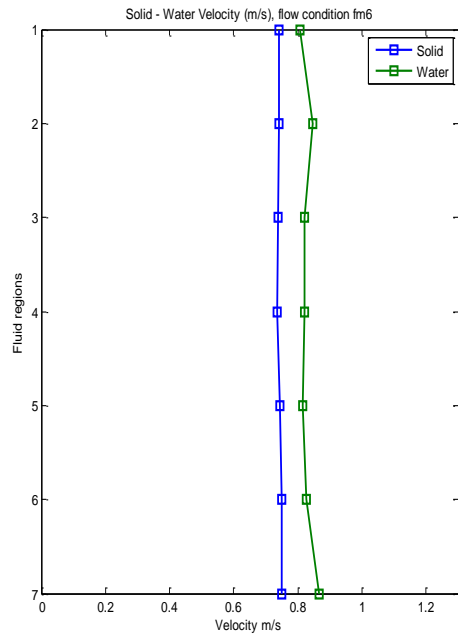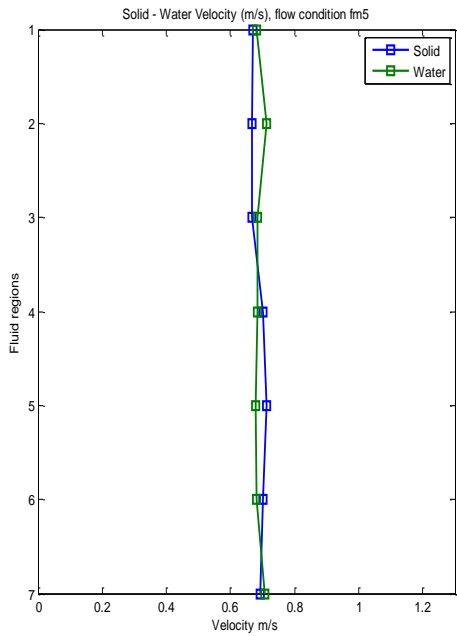
Figure 7.24 Reconstructed water and solids velocities for upward flow in vertical pipe for flow conditions fm5and fm6
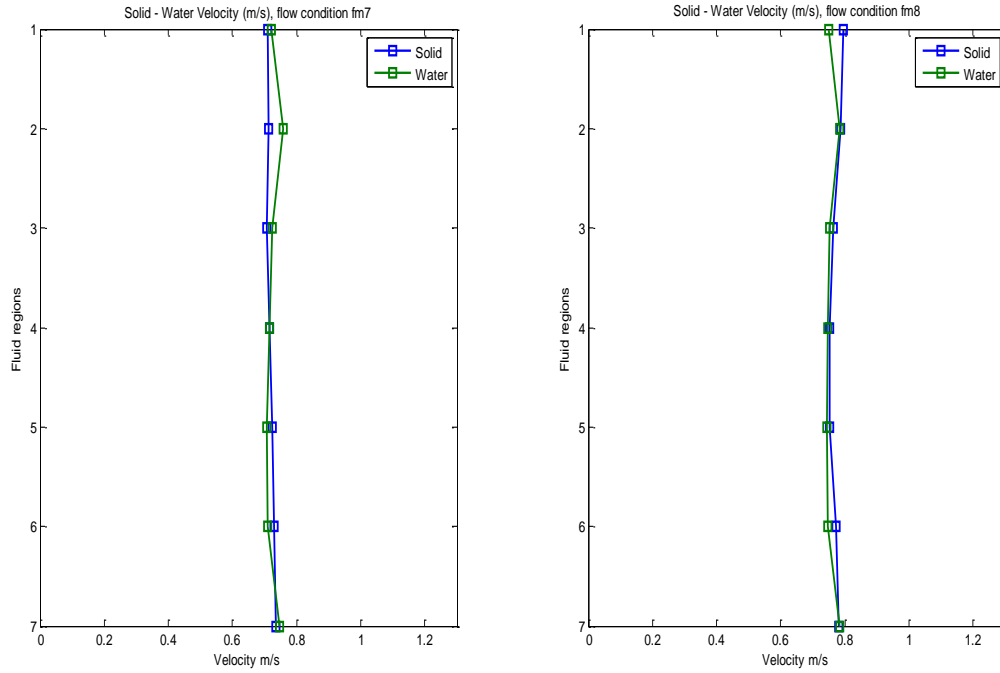
Figure 7.25 Reconstructed water and solids velocities for upward flow in vertical pipe for flow conditions fm7 and fm8

The slip velocity between the solid phase and water phase can be clearly noticed in flow conditions fm1, fm2, fm3 and fm6 where the water is travelling faster than the solids. Though in conditions fm4, fm5, fm7 and fm8 the profiles show that the solids phase and water phase are travelling with relatively similar velocities. The reason behind the similarity in solids and water velocities in these cases could be that the EVP system gives underestimated values for the water velocity. As shown in Section 6.4.1, the measured induced voltage is divided by the circuit gain before using it in Equation 6-38. Therefore, the water velocity results are highly dependent upon the calculated circuit gains which may vary due to the effects of temperature on passive component in the amplifier in circuits.

The underestimated values could be seen clearly in the comparison between the EVP water volumetric flow rate $Q_{w,EVP}$ and the reference water volumetric rate $Q_{w,ref}$ for the fm1 to fm5 flow conditions (see section 7.4.4).

7.3.2 Solids-In-Water Upward Flow Inclined 30° to the Vertical

7.3.2.1 Solids Velocity for Upward Flow in Pipe Inclined At 30° to the Vertical Using ICC Flow Meter

The ICC flow meter for measuring solids-in-water flow was mounted in the working section of the flow loop with the working section inclined at 30° to the vertical. Configurations I, II and III were used to find the solids velocity profiles over the pipe cross-section. The six flow conditions were fm9-fm14 (see Table 6-2). Figures 7.21 to 7.23 show the interpolated local axial solids velocity profiles obtained from the ICC flow meter (note the reversal of the x and y axes compared with Figure 7.9 to Figure 7.11).
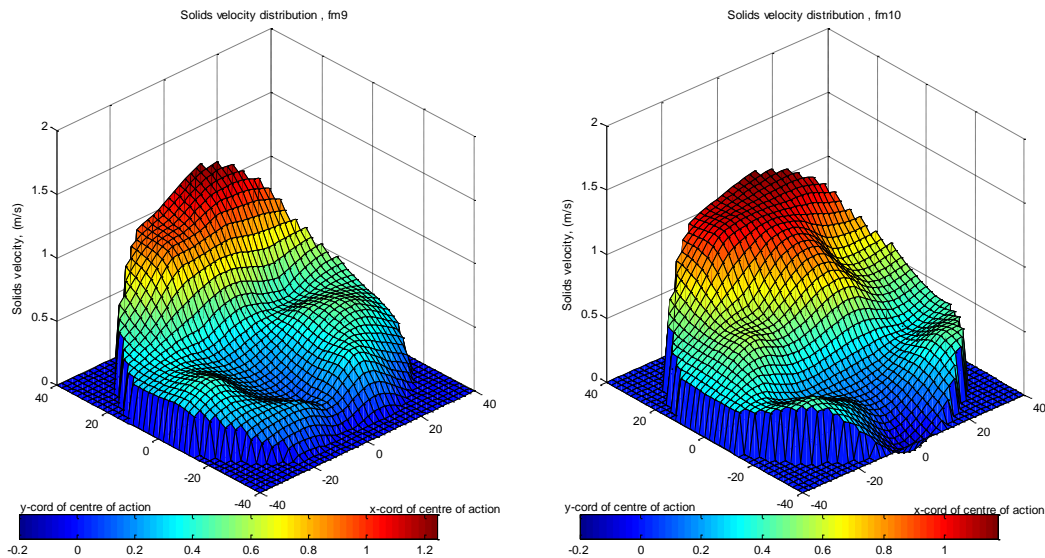
Figure 7.26 Solids velocity distributions for upward flow in pipe inclined at 30° to the vertical. Flow conditions fm9 and fm10
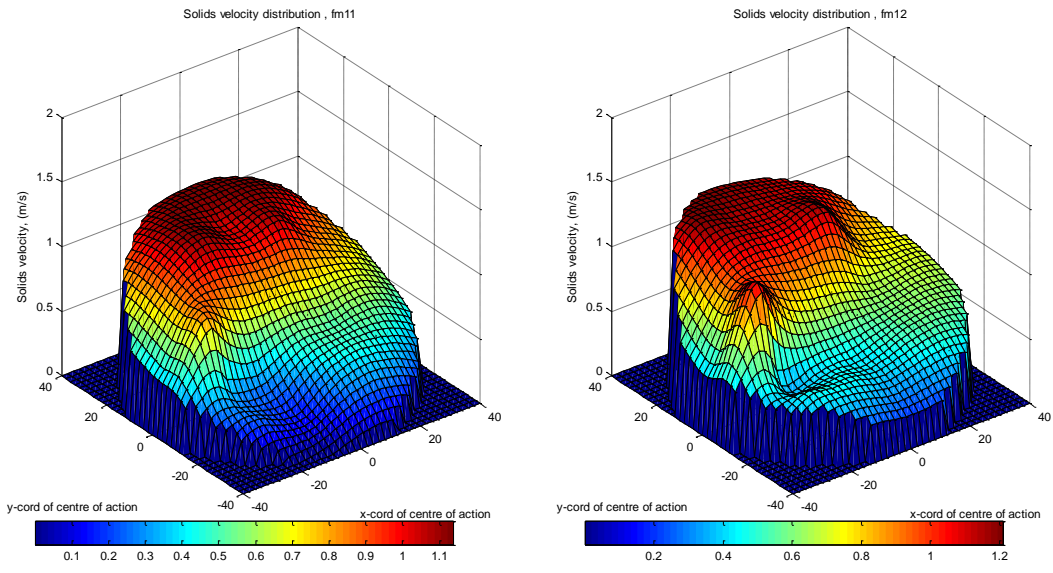
Figure 7.27 Solids velocity distributions for upward flow in pipe inclined at 30° to the vertical. Flow conditions fm11 and fm12
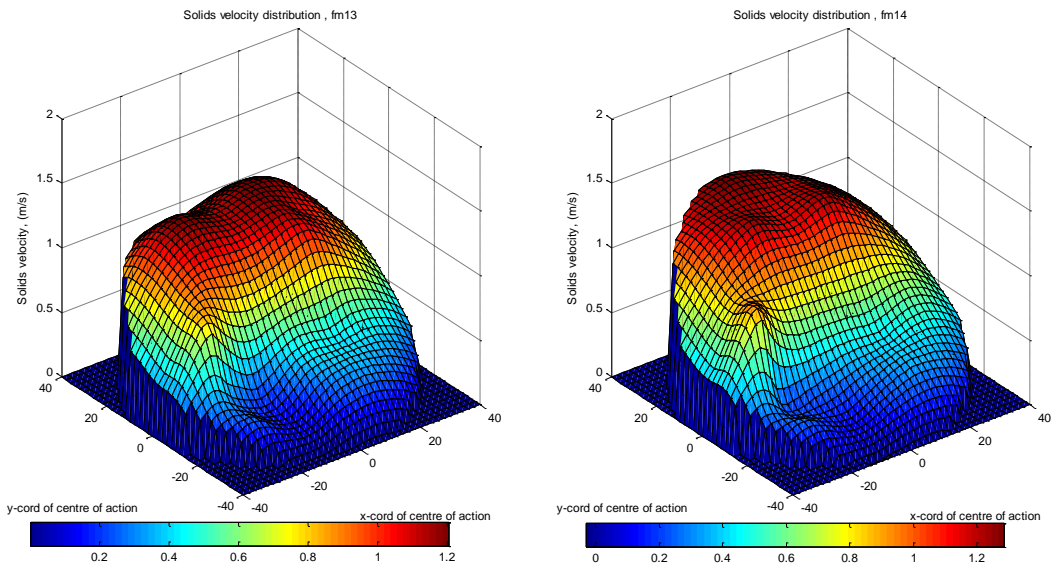
Figure 7.28 Solids velocity distributions for upward flow in pipe inclined at 30° to the vertical. Flow conditions fm13 and fm14

198

The profiles of v_s for upward flows inclined at $30°$ to the vertical show that $v_{s,ICC}$ varies as a function of the y coordinate (see Figure 7.12 and Figure 7.13). For inclined upward flow, the measured local axial solids velocity v_s is a minimum at the lower side of the inclined pipe (where the mean density of the solids–water mixture was a maximum due to the high local solids volume fraction, see Figure 7.14) and is a maximum value at the upper side. Figure 7.26, for flow conditions fm9 and fm10, shows a negative axial solids velocity at the bottom of the pipe due to solid particles flowing backwards down the pipe. These results agree with visual observations of the flow and previous experimental profiles obtained by Cory [56] and Al-Hinai [49].

Using the data shown in Figure 7.26 to Figure 7.28, the mean solids velocity in each of the seven regions was calculated and the results are presented in Figure 7.29(a).

7.3.2.2 Water Velocity Profiles for Upward Flow in Pipe Inclined At $30°$ to the Vertical Using the Electromagnetic Velocity Profiler (EVP)

Using the same experimental setup described in Section 7.3.1.2, the EVP was used to measure the water velocity for upwards solids-in-water flow with the pipe inclined at $30°$ to the vertical. Figure 7.29b shows the results obtained for the seven regions of flow cross-section.

(a) Solids velocity profiles in the 7 regions

(b) Water velocity profiles in the 7 regions
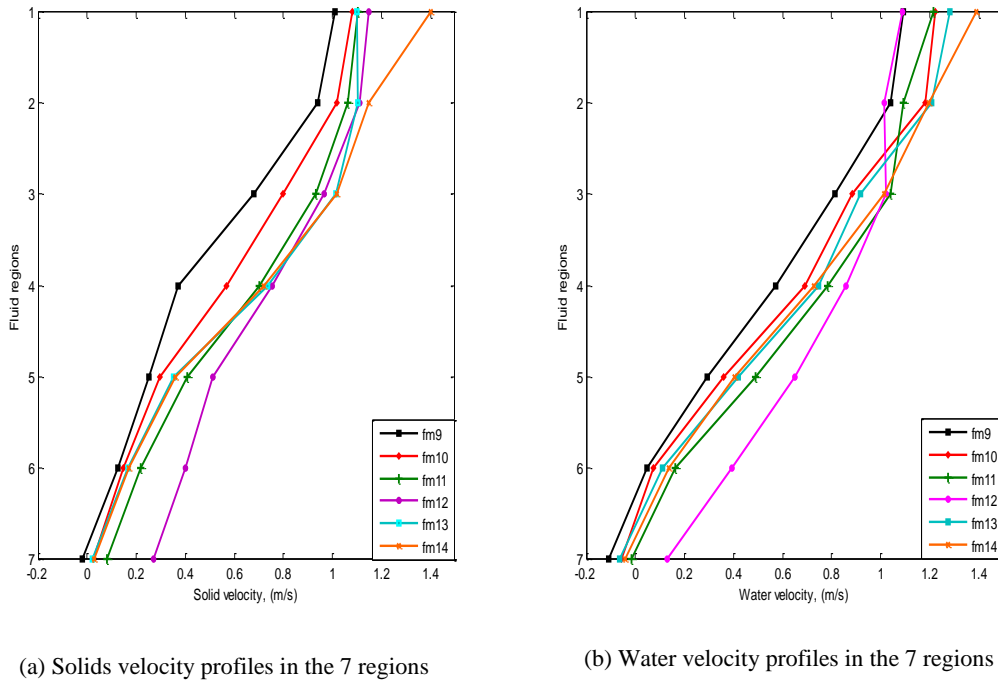
Figure 7.29 Reconstructed water and solids velocities for upwards solids-in-water flow with pipe at 30° to the vertical

Figure 7.29(a) shows that the local axial solids velocity decreases as moving from the upper side of the pipe (region 1) to the lower side (region 7) - the solids have a much lower velocity in region 7 than they do in region 1. The water velocity profile, Figure 7.24(b), shows a similar behaviour. For all flow conditions from fm9 to fm14 (except fm12 where $\overline{\alpha}_s$ is small) it is seen that at the lower side of the inclined pipe, in fluid region 7, the water velocity is negative (reverse flow occurs). As we move towards the upper side of the pipe the velocity becomes positive.

Figure 7.30 to Figure 7.32 show the comparison between solids and water velocity in the seven regions for each flow condition.
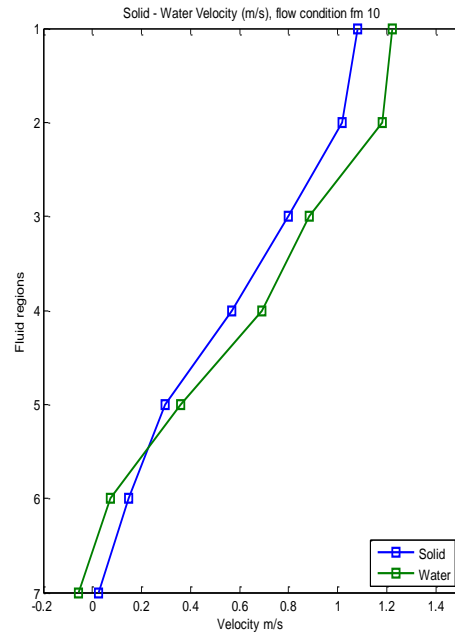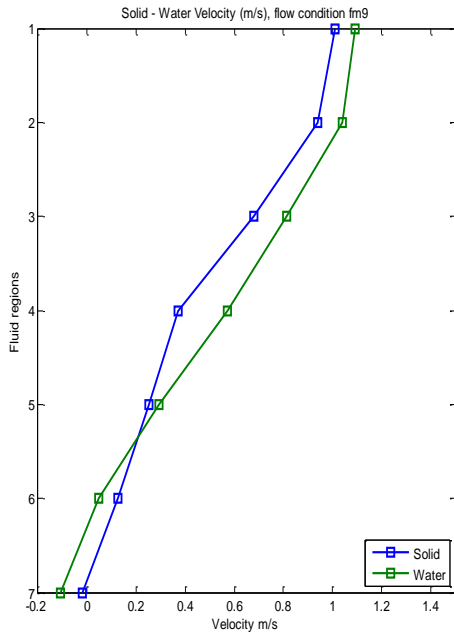
Figure 7.30 Reconstructed water and solids velocities for upward vertical flow, flow conditions fm9 and fm10
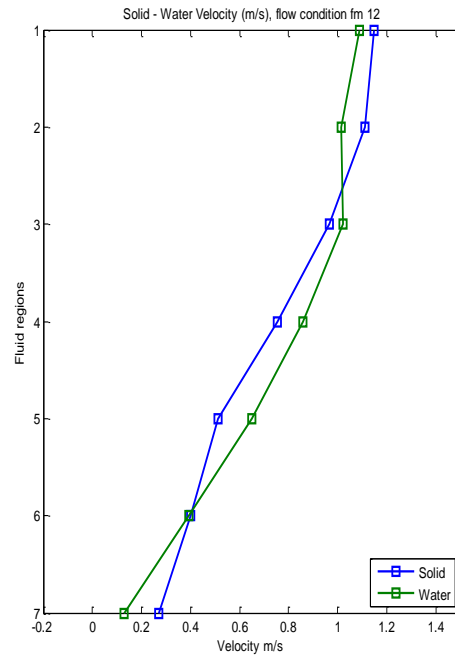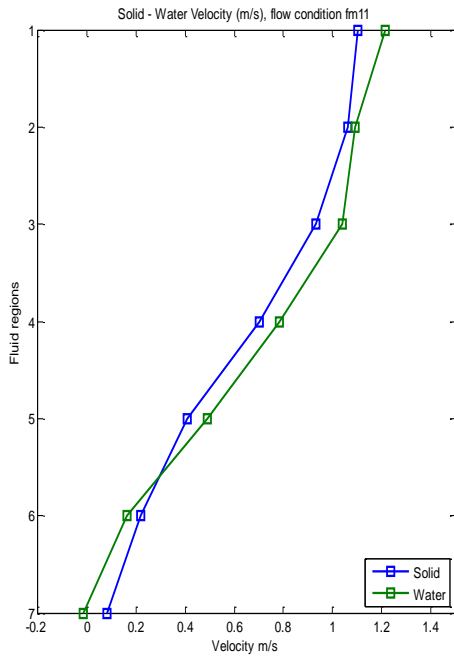

Figure 7.31 Reconstructed water and solids velocities for upward vertical flow, flow conditions fm11 and fm12

201
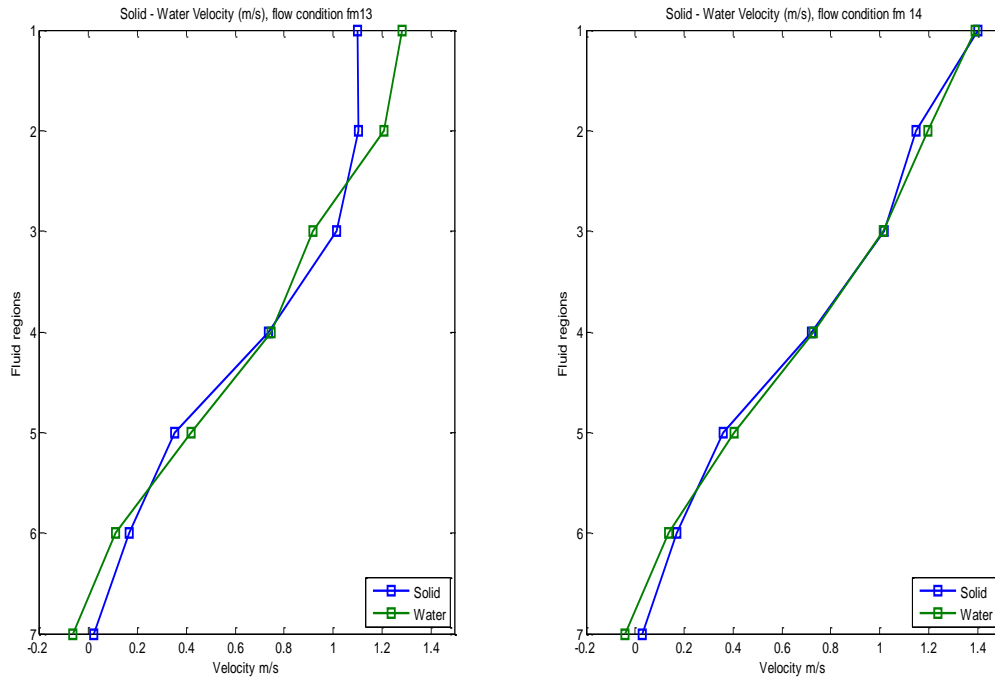
Figure 7.32 Reconstructed water and solids velocities for upward vertical flow, flow conditions fm13 and fm14

At the lower side of the inclined pipe v_s is negative or close to zero - the solids particles are flowing down the pipe - but the total solids volumetric flow rate is upward. Thus the solids which flow down the pipe must at some stage be re-circulated into the upward flow. This was noticed through the cross correlation analysis in region 6 and region 7 where the data from channel A and B was taken for 60 seconds, then the data was divided and cross correlated for every 2 seconds. The results show that v_s has both negative and positive values. The positive values represent the velocity of the re-circulated solids flow upwards in the working section. The re-circulation phenomenon was also observed by high speed camera and previously reported by Cory [56] and Al-Hinai [49].

The water velocity near the lower side of the pipe is also affected by the re-circulation phenomenon. As the solids re-circulate, the local water velocity is close to zero and this was observed in region 7 in Figure 7.30 to Figure 7.32.

It is clear from Figure 7.30 to Figure 7.32 that at region 6 and region 7, the solids velocity was higher than water velocity, which is considered to be an unexpected occurrence. This could have happened because these two regions were highly subject to re- circulation phenomena which affected the cross correlation results for at least region 7 which in turn gave $v_{s,ICC}$ results in those regions higher than the reality.

At the upper side of the pipe the solids velocity v_s and water velocity v_w were at a maximum and almost reached 1.4 ms^{-1} (see Figure 7.32, flow condition fm14, region 1).

The similarities in behaviour of the solids and water velocities suggest that the water velocity profiles and solids velocity profiles obtained from the EVP and ICC instruments during the current investigation are realistic.

7.4 Comparison of Experimental Results Acquired By the ICC and EVP Systems with Reference Measurements

To evaluate the performance of the ICC and EVP systems for solids-in-water flow, the integrated values of α_s, v_s and v_w were calculated and compared with reference measurements.

For the purposes of the quantitative comparison, the errors could be defined as following:

percentage error:

$$\varepsilon_x^{per} = \frac{X_{meas.} - X_{ref}}{X_{ref}}$$

Equation 7-2

where ε_x^{per} is the percentage error in x. $x_{meas.}$ is the integrated measured parameter obtained using the ICC or EVP system, x_{ref} is the corresponding relevant reference measurement.

absolute error:

$$\varepsilon_x^{abs} = x_{meas.} - x_{ref}$$ Equation 7-3

where ε_x^{abs} is the absolute error in x.

standard deviation of the percentage error:

$$\sigma_x^{per} = \sqrt{\frac{\sum_{i=0}^{i=n}(\varepsilon_{x,i}^{per} - \overline{\varepsilon}_x^{per})^2}{n}}$$ Equation 7-4

where n is the number of flow conditions for which the error was calculated, $\overline{\varepsilon}_x^{per}$ is the mean percentage error.

standard deviation of the absolute error

$$\sigma_x^{ABS} = \sqrt{\frac{\sum_{i=0}^{i=n}(\varepsilon_{x,i}^{abs} - \overline{\varepsilon}_x^{abs})^2}{n}}$$ Equation 7-5

where n is the number of flow conditions for which the error was calculated, $\overline{\varepsilon}_x^{abs}$ is the mean absolute error.

7.4.1   Solids Volume Fraction Results

The aim of this section is to evaluate the accuracy of the results of the ICC measured solids volume fraction α_s. This evaluation can be done by comparing the measured ICC mean solids volume fraction $\overline{\alpha}_{s,ICC}$ with the the reference mean solids volume fraction $\overline{\alpha}_{s,dp}$ measured using

the DP cell. This was done for flow conditions fm1 to fm14. The solids volume fraction distributions profiles shown in Sections 7.2.1 and 7.2.2 were used to find $\overline{\alpha}_{s,ICC}$ using Equation 7-6.

$$\overline{\alpha}_{s,ICC} = \frac{1}{A}\int_{A} \alpha_{s,ICC}\ dA \qquad\qquad \text{Equation 7-6}$$

7.4.1.1 The Error of the Solids Volume Fraction Results in Vertical Flow

The integrated solids volume fraction $\overline{\alpha}_{s,ICC}$ data obtained from the ICC device for each vertical upward flow condition, and the relevant values for $\overline{\alpha}_{s,dp}$, are presented in Table 7-1.

Table 7-1 Integrated solids volume fraction data from ICC and reference devices for vertical upward flow

Flow condition (see Table 6-2)	Solid volumetric flow rate $Q_{s,ref}$ (m³h⁻¹)	Water volumetric flow rate $Q_{w,ref}$ (m³h⁻¹)	Mean solids volume fraction $\overline{\alpha}_{s,ICC}$ obtained Using ICC	Mean solids volume fraction $\overline{\alpha}_{s,dp}$ obtained Using DP cell	The solids volume fraction % error $\varepsilon_{\alpha}^{per}$	The solids volume fraction absolute error $\varepsilon_{\alpha}^{abs}$
fm1	0.422	7.3070	0.063	0.080	-21.3%	-0.017
fm2	0.532	10.574	0.058	0.065	-10.8%	-0.007
fm3	0.638	10.311	0.072	0.074	-2.7%	-0.002
fm4	0.762	11.534	0.066	0.071	-7.0%	-0.005
fm5	0.872	11.975	0.071	0.065	8.7%	0.006
fm6	0.807	13.817	0.061	0.058	3.8%	0.002
fm7	0.717	11.977	0.055	0.065	-15.3%	-0.010
fm8	0.882	11.788	0.063	0.068	-7.3%	-0.005
Standard deviation for the percentage error σ_{α}^{per}					9.14%	
Standard deviation for the absolute error σ_{α}^{abs}					0.006	

7.4.1.2 The Error of the Solids Volume Fraction for Upward Flow in a Pipe Inclined At $30^{°}$ to the Vertical

The integrated solids volume fraction values obtained from the ICC device for each upward flow condition for the pipe inclined at 30° to the vertical, and the relevant DP cell reference measurements, are presented in Table 7-2

Table 7-2 Integrated solids volume fraction data from ICC and reference devices for upward flow in pipe inclined at $30^{°}$ to the vertical.

Flow condition (see Table 6-2)	Solid volumetric flow rate $Q_{s,ref}$ (m^3h^{-1})	Water volumetric flow rate $Q_{w,ref}$ (m^3h^{-1})	Mean solids volume fraction $\overline{\alpha}_{s,ICC}$ obtained Using ICC	Mean solids volume fraction $\overline{\alpha}_{s,dp}$ obtained Using dp cell	The solids volume fraction % error $\varepsilon_{\alpha}^{per}$	The solids volume fraction absolute error $\varepsilon_{\alpha}^{abs}$
fm9	0.467	8.666	0.193	0.220	-12.2%	-0.027
fm10	0.623	10.196	0.189	0.190	-0.5%	-0.001
fm11	0.706	12.010	0.133	0.118	12.7%	0.015
fm12	0.723	13.718	0.068	0.080	-15.0%	-0.012
fm13	0.939	11.072	0.170	0.178	-4.5%	-0.008
fm14	1.116	11.431	0.172	0.187	-8.0%	-0.015
Standard deviation for the percentage error σ_{α}^{per}					9.08 %	
Standard deviation for the Absolute error σ_{α}^{abs}					0.012	

7.4.1.3 Discussion of the Solids Volume Fraction Error, ε_{α}

Figure 7.28 shows the percentage error $\varepsilon_{\alpha}^{per}$ for the ICC measurements of solids volume fraction plotted against the reference value $\overline{\alpha}_{s,dp}$ measured using the DP cell, for both vertical and inclined pipes.
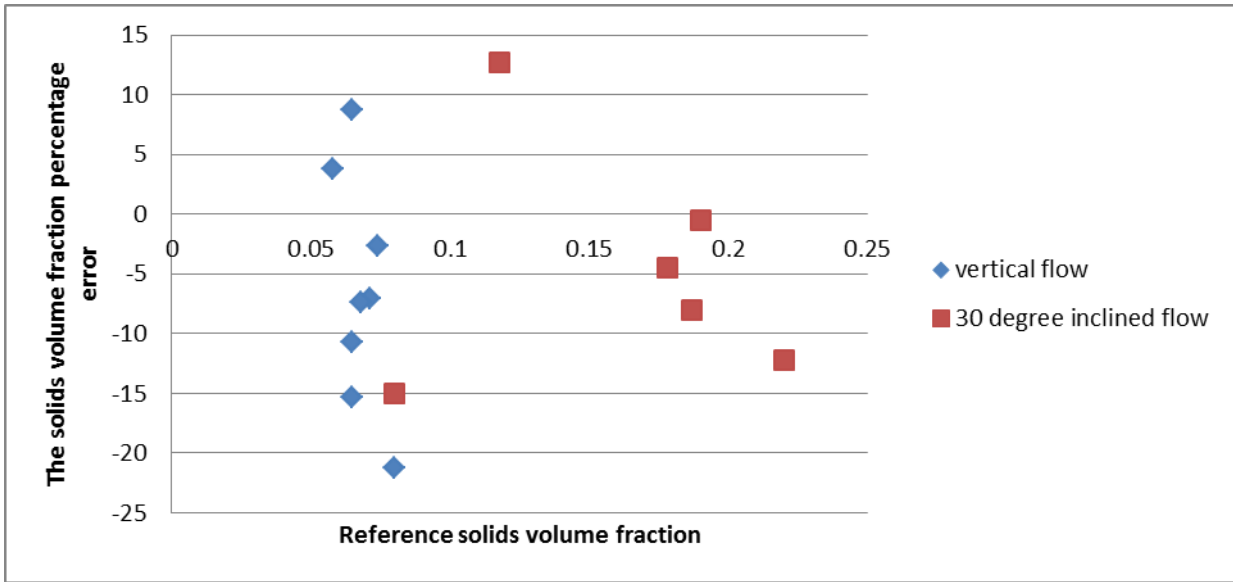
Figure 7.33 Percentage error $\varepsilon_{\alpha}^{\text{per}}$ plotted against the reference solids volume fraction $\overline{\alpha}_{\text{s,dp}}$ measured using the DP cell

Inspection of Figure 7.33 shows that the error $\varepsilon_{\alpha}^{\text{per}}$ in $\overline{\alpha}_{\text{s,ICC}}$, as compared with $\overline{\alpha}_{\text{s,dp}}$ in vertical flow, varied from 8.7% to -21.2% with a mean value of $\overline{\varepsilon}_{\alpha}^{\text{per}}$ equal to $-$ 6.4% and a standard deviation $\varepsilon_{\alpha}^{\text{std}}$ equal to 9.14% . It should be noted that the reference solids volume fraction was more or less constant at approximately 0.06.

For inclined flow, the error $\varepsilon_{\alpha}^{\text{per}}$ varied from 12 % to -15% with a mean value of $\overline{\varepsilon}_{\alpha}^{\text{per}}$ -4.6 % and standard deviation $\sigma_{\alpha}^{\text{per}}$ of 9.08%. The reference solids volume fraction for inclined flow varied from about 0.08 to about 0.22.

The results show the largest percentage error $\varepsilon_{\alpha}^{\text{per}}$ occurred for vertical flow when the mean volume fraction $\overline{\alpha}_{\text{s,dp}}$ was 0.08.

Figure 7.34 shows the absolute error $\varepsilon_{\alpha}^{\text{abs}}$ for ICC measurements of solids volume fraction plotted against the reference value $\overline{\alpha}_{\text{s,dp}}$ measured using the DP cell, for both vertical and inclined

207

flows. For vertical flow, $\varepsilon_\alpha^{\mathrm{abs}}$ varied from 0.0056 to -0.017 with a mean value for $\overline{\varepsilon_\alpha}^{\mathrm{abs}}$ of -0.004,

and for flow at 30° to the vertical, $\varepsilon_\alpha^{\mathrm{abs}}$ varied from 0.015 to -0.027 with a mean value for $\overline{\varepsilon_\alpha}^{\mathrm{abs}}$ of

-0.008.
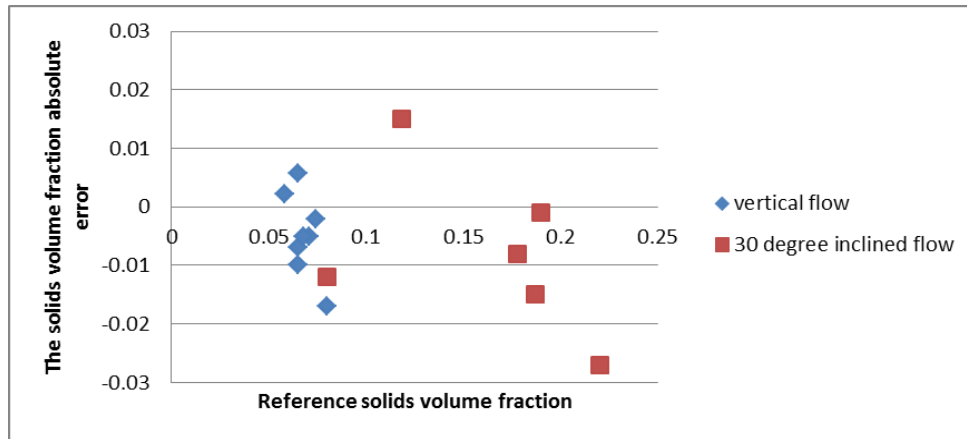
Figure 7.34 **absolute error** $\varepsilon_\alpha^{\mathrm{abs}}$ **plotted against the reference solids volume fraction** $\overline{\alpha}_{\mathrm{s,dp}}$ **measured using the DP cell**

For the majority of flow conditions (except fm5, fm6 and fm11), the results obtained for $\overline{\alpha}_{\mathrm{s,ICC}}$

were underestimated relative to the reference volume fractions $\overline{\alpha}_{\mathrm{s,dp}}$. This could simply be due to

the accuracy of the reference measurements. From the survey of previous work [55], the

accuracy of the reference dp cell measurements depends upen the superficial velocity U_h shown

in Equation 6-10. From a visual inspection, at some flow conditions such as fm1,fm2 and fm9,

there was constant water flow into the water hopper but a pulsing of the solids flow into the

solids hopper. Additionally, as shown in Section 6.3.3.3, the separation in not entirely efficient

for all flow conditions. The above reasons suggest that the assumption of constant U_h may be

incorrect and hence this may have produced an error in the dp cell measurements. The very low

values of the absolute error $\varepsilon_\alpha^{\mathrm{abs}}$ show that the in general the value of solids volume fraction

obtained from ICC device were quite accurate, despite the percentage error being large.

7.4.2 Solids-in-Water Velocity Results

The mean solid velocity $\overline{v_{s,ICC}}$ and mean reference solids velocity $\overline{v_{s,ref}}$ are obtained using Equations 7-5 and 7-6:

$$\overline{v_{s,ICC}} = \frac{\int_A \alpha_{s,ICC} \, v_{s,ICC} \, dA}{\int_A \alpha_{s,ICC} \, dA} \qquad\qquad \text{Equation 7-7}$$

$$\overline{v_{s,ref}} = \frac{Q_{s,corr}}{A \, \overline{\alpha}_{s,dp}} \qquad\qquad \text{Equation 7-8}$$

7.4.2.1 The Percentage Error of Solids Velocity for Vertical Upward Flow

Table 7-3 Integrated solids velocity from ICC measurements and reference velocity measurements for vertical upward flow of solids-in-water in vertical pipe

Flow condition (see Table 6-2)	Solid volumetric flow rate $Q_{s,ref}$ (m^{3}h^{-1})	Water volumetric flow rate $Q_{w,ref}$ (m^{3}h^{-1})	Mean solids velocity $\overline{v_{s,ICC}}$ obtained Using ICC	Mean solids velocity $\overline{v_{s,ref}}$ obtained using $Q_{s,corr}$ and $\overline{\alpha}_{s,dp}$	The solids velocity % error ε_v^{per}	The solids velocity absolute error ε_v^{abs} m/s
fm1	0.494	7.307	0.367	0.331	10.8%	0.035
fm2	0.630	10.574	0.525	0.518	1.3%	0.007
fm3	0.698	10.311	0.478	0.504	-5.1%	-0.025
fm4	0.828	11.534	0.640	0.623	2.7%	0.017
fm5	0.944	11.975	0.692	0.776	-10.7%	-0.080
fm6	0.935	13.817	0.74	0.861	-14.0%	-0.120
fm7	0.788	11.977	0.716	0.648	10.4%	0.067
fm8	1.023	11.788	0.758	0.804	-5.7%	-0.040
Standard deviation for the percentage error				σ_v^{per}	8.6 %	
Standard deviation for the Absolute error				σ_v^{abs}	0.059	

7.4.2.2 Absolute Error in Solids Velocity for Upward Flow in Pipe Inclined At 30° to the Vertical

Table 7-4 Integrated solids velocity from ICC measurements and reference velocity measurements for upward flow of solids-in-water in pipe inclined at 30° to the vertical

Flow condition (see Table 6-2)	Solid volumetric flow rate $Q_{s,ref}$ (m^{3}h^{-1})	Water volumetric flow rate $Q_{w,ref}$ (m^{3}h^{-1})	Mean solids velocity $\overline{V_{s,ICC}}$ obtained Using ICC	Mean solids velocity $\overline{V_{s,ref}}$ obtained using $Q_{s,corr}$ and $\overline{\alpha_{s,dp}}$	The solids velocity % error ε_v^{per}	The solids velocity absolute error ε_v^{abs} m/s
fm9	0.467	8.666	0.16	0.11	45.4 %	0.05
fm10	0.623	10.196	0.21	0.175	21.73 %	0.038
fm11	0.706	12.01	0.28	0.31	-11.08%	-0.035
fm12	0.723	13.718	0.43	0.48	-9.33%	-0.045
fm13	0.939	11.072	0.25	0.28	-10.22%	-0.028
fm14	1.116	11.431	0.26	0.31	-18.43%	-0.058
Standard deviation for the percentage error				σ_v^{per}	22.86 %	
Standard deviation for the Absolute error m/s				σ_v^{abs}	0.04	

7.4.2.3 Discussion of the Solids Velocity Error, ε_v
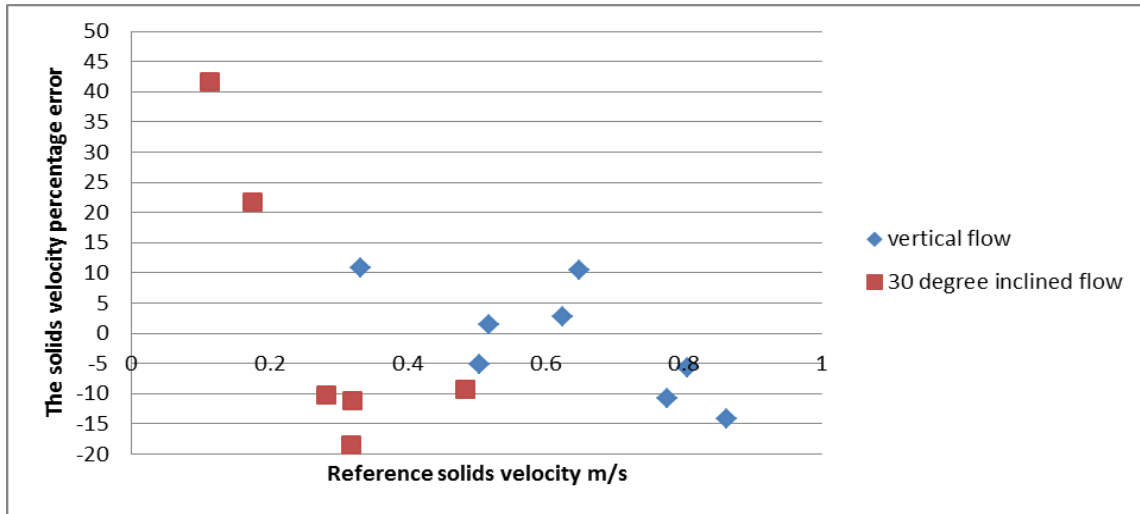
**Figure 7.35 Percentage error $\varepsilon_v^{\text{per}}$ plotted against the reference solids velocity $\overline{v_{s,ref}}$ measured using ICC device**

Figure 7.35 shows that the percentage error $\varepsilon_v^{\text{per}}$ for vertical upward solids-in-water flow varied

from 10.4% to -14.1 % with a mean value of $\overline{\varepsilon_v}^{\text{per}}$ equal to -1.2 % and the percentage error

standard deviation σ_v^{per} was 8.6%. As shown in Equation 7-8 , the estimation of $\overline{v_{s,ref}}$ depends

on $Q_{s,corr}$ and $\overline{\alpha}_{s,dp}$, however these reference measurements have their own sources of errors

(see, for example Section 7.4.1.3) which will feed into the reference solids velocity calculations.

For inclined flow, the percentage error $\varepsilon_v^{\text{per}}$ in fm9 and fm10 is high, possibly because either i)

the errors in the reference measurements as shown in $\varepsilon_v^{\text{per}}$ results for the vertical flow, or ii)

because these two flow conditions were subject to re-circulation which affected the cross

correlation results for at least region 7 (see Section 7.3.2.2) which gave $v_{s,ICC}$ results in those

regions higher than the reality. Additionally, the reference solids velocity $\overline{v_{s,ref}}$ in fm9 and fm10

is low which means that any tiny changes between the measured velocity values and reference

velocity values will produce a high percentage error.

211

Note that $\alpha_{s,ICC}$ in these regions is high and was used to calculate the $\overline{v_{s,ICC}}$. However the effect of

the re-circulation reduces as the mean flow is faster for the remainder of the flow conditions.

The relation between ε_v^{abs} and $\overline{v_{s,ref}}$ can be seen in Figure 7.36
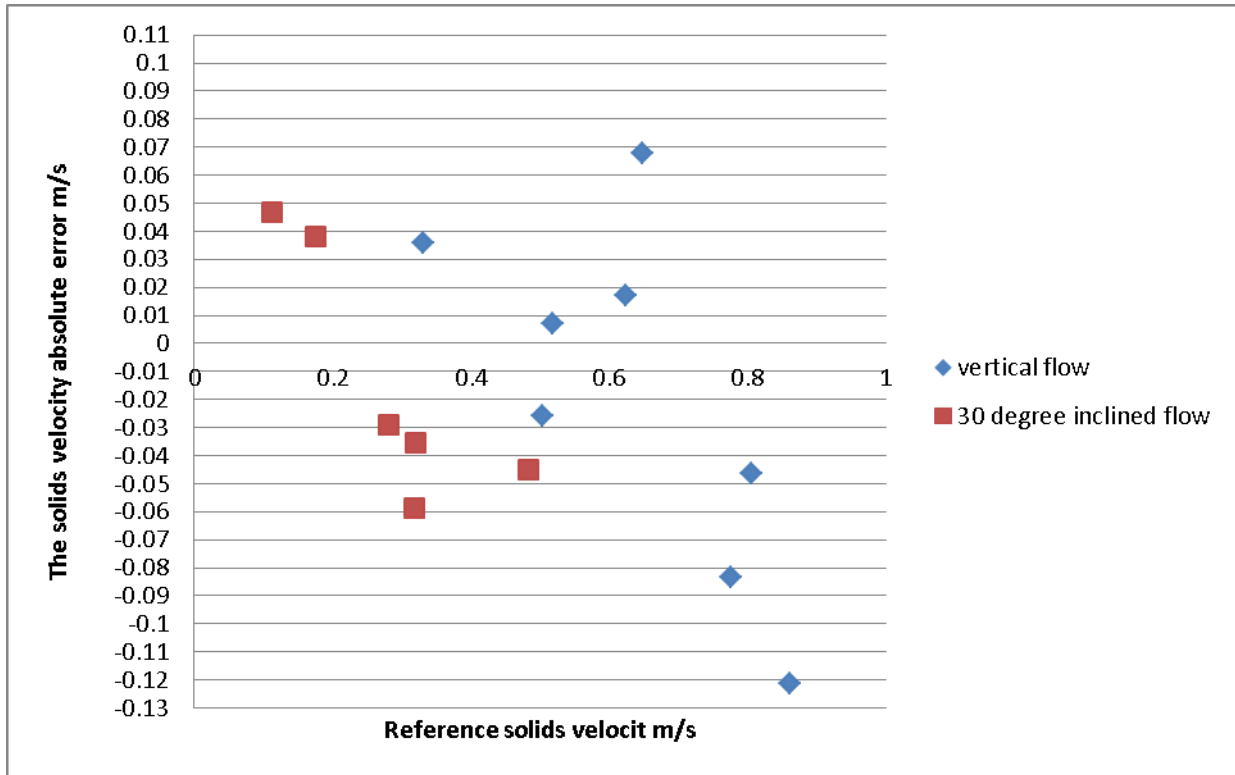
**Figure 7.36 Absolute error ε_v^{abs} plotted against the reference solids velocity $\overline{v_{s,ref}}$ measured using $Q_{s,corr}$ and $\overline{\alpha}_{s,dp}$**

Figure 7.36 shows the absolute error ε_v^{abs} for ICC measurements of solids velocity plotted against

the reference solids velocity $\overline{v_{s,ref}}$ measured using Equation 7-8, for both vertical and inclined

flows. For vertical flow, ε_v^{abs} varied from 0.067 to -0.12 with a mean value for $\overline{\varepsilon_v}^{abs}$ of -0.018, and

for flow at 30° to the vertical, ε_v^{abs} varied from 0.05 to -0.058 with a mean value for $\overline{\varepsilon}_v^{abs}$ of -0.013. These results show that the solids velocity obtained by the ICC device is quite good.

7.4.3   Solids Volumetric Flow Rate Results Obtained Using the ICC Flow Meter

In this section, the ICC solids volumetric flow rate $Q_{s,ICC}$ was compared with the $Q_{s,corr}$ to evaluate the system performance.

Section (6.3.3.1) shows how the solids reference volumetric flow rates were obtained, and Section (6.3.3.3) shows how the correction factor was estimated. The reference solids volumetric flow rate $Q_{s,ref}$ was corrected as:

$$Q_{s,corr} = 0.962 * Q_{s,ref} \qquad\qquad \text{Equation 7-9}$$

7.4.3.1 Solids Volumetric Flow Rate Error ε_{Qs} for Upward Flow in Vertical Pipe

The integrated solids volumetric flow rate values from the ICC device for the different flow conditions for a vertical pipe, and the relevant reference data, are presented in Table 7-5

213

Table 7-5 Comparison of the ε_{Qs} between corrected solids volumetric flow rate $Q_{s,corr}$ and ICC solids volumetric flow rate $Q_{s,ICC}$ for upward vertical flow

Flow condition (see Table 6-2)	Solid volumetric flow rate $Q_{s,ref}$ (m^3h^{-1})	Water volumetric flow rate $Q_{w,ref}$ (m^3h^{-1})	Solid volumetric flow rate $Q_{s,ICC}$ obtained Using ICC	Corrected Solids volumetric flow rate $Q_{s,corr}$	The solids volume-tric flow rate % error ε_{Qs}^{per}	The solids volume-tric flow rate absolute error ε_{Qs}^{abs} m^3/h
fm1	0.494	7.307	0.422	0.475	-11.0%	-0.052
fm2	0.630	10.574	0.532	0.606	-12.1%	-0.073
fm3	0.698	10.311	0.638	0.671	-4.9%	-0.032
fm4	0.828	11.534	0.762	0.796	-4.3%	-0.034
fm5	0.944	11.975	0.872	0.908	-3.9%	-0.035
fm6	0.935	13.817	0.807	0.899	-10.2%	-0.091
fm7	0.788	11.977	0.717	0.758	-5.3%	-0.040
fm8	1.023	11.788	0.882	0.984	-10.3%	-0.101
Standard deviation for the percentage error σ_{Qs}^{per}					3.2 %	
Standard deviation for the absolute error m^3/h σ_{Qs}^{abs}					0.025	

7.4.3.2 Solids Volumetric Flow Rate Error ε_{Qs} for Upward Flow in Pipe Inclined At $30^{°}$ to the Vertical

The integrated solids volumetric flow rate values from the ICC device for upward flow in a pipe inclined at $30^{°}$ to the vertical, and the relevant reference data, are presented in Table 7-6

Table 7-6 Comparison of the ε_{Qs} between corrected solids volumetric flow rate $Q_{s,corr}$ and ICC solids volumetric flow rate $Q_{s,ICC}$ for upward flow in pipe inclined at 30° to vertical

Flow condition (see Table 6-2)	Solid volumetric flow rate $Q_{s,ref}$ (m³h⁻¹)	Water volumetric flow rate $Q_{w,ref}$ (m³h⁻¹)	Solid volumetric flow rate $Q_{s,ICC}$ obtained Using ICC	Corrected Solid volumetric flow rate $Q_{s,corr}$	The solids volumetric flow rate % error ε_{Qs}^{pre}	The solids volumetric flow rate absolute error ε_{Qs}^{abs} m³/h
fm9	0.467	8.666	0.508	0.449	13.1%	0.050
fm10	0.623	10.196	0.695	0.599	16.0%	0.090
fm11	0.706	12.01	0.687	0.679	1.2%	0.008
fm12	0.723	13.718	0.66	0.695	-5.1%	-0.035
fm13	0.939	11.072	0.856	0.903	-5.2%	-0.047
fm14	1.116	11.431	1.07	1.073	-0.3%	-0.003
Standard deviation for the percentage error σ_{Qs}^{per}					8.7 %	
Standard deviation for the Absolute error m³/h σ_{Qs}^{abs}					0.05	

7.4.3.3 Discussion of the Solids Volumetric Flow Rate Error ε_{Qs}

The ICC solids volumetric flow rate $Q_{s,ICC}$ was calculated using values for $\alpha_{s,ICC}$ and $v_{s,ICC}$ found by integrating across the pipe cross-section:

$$Q_{s,ICC} = \int_A \alpha_{s,ICC} \, v_{s,ICC} \, dA \qquad \text{Equation 7-10}$$

It should be noted that any errors in $\alpha_{s,ICC}$ and $v_{s,ICC}$ will influence $Q_{s,ICC}$. Figure 7.37 shows the solids volumetric flow percentage errors ε_{Qs}^{pre} compared with the corrected solids volumetric flow rates for all 14 flow conditions.
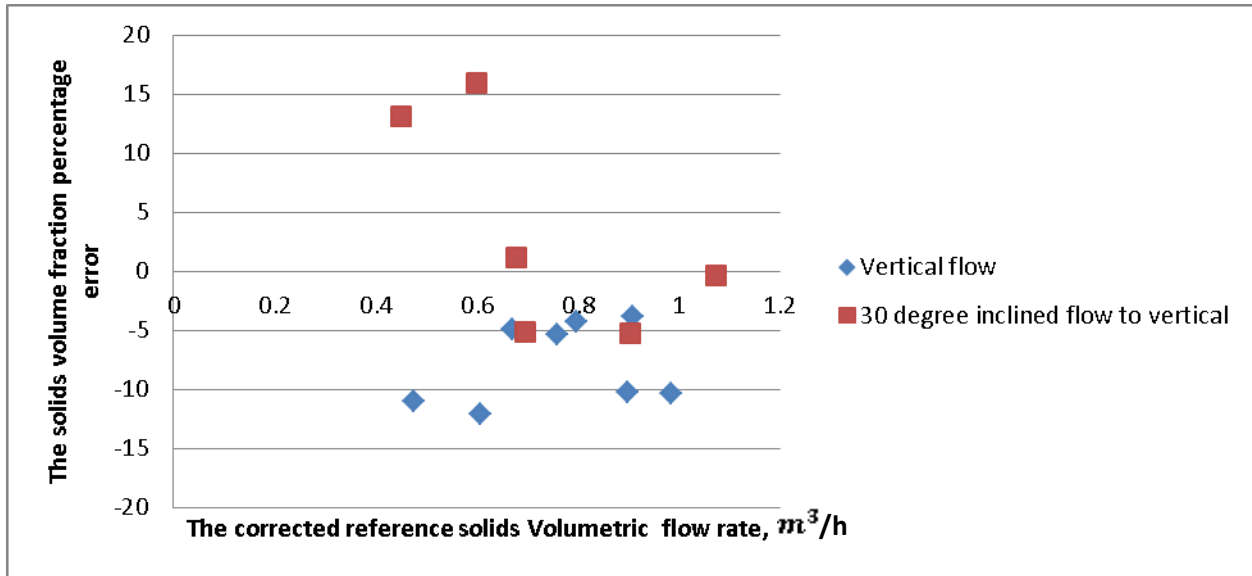
Figure 7.37 Percentage error ε_{Qs}^{per} plotted against the corrected reference solids volume fraction $Q_{s,corr}$

For vertical flows, ε_{Qs}^{per} varied between -3.87% to -12.1%, indicating that $Q_{s,ICC}$ is always less than the reference measurements possibly due to errors occurring in the separation process. It is shown in Section 6.2.3 that the separation is not entirely efficient because solid particles will always carry an amount of water on their outer surface into the solids hopper. From a visual inspection of the separator there was constant water flow into the solids hopper even when there was no solids flow. These results indicate that the assumed water volume fraction γ (Section 6.2.3.3) used to correct the reference solids volumetric flow rate could be higher than 0.05 .

For the pipe inclined at 30° to the vertical ε_{Qs}^{pre} varied between -5.2 % to 15.9 %. For flow conditions fm9 and fm10 the errors were largest probably due to the velocity in regions 6 and 7 being overestimated. As mentioned in Sections 7.3.2.2 and 7.4.2.3, re-circulation phenomena produced an error in velocity measurements for regions 6 and 7, which affected the volumetric flow rate measurements. However, for the remainder of the flow conditions, the re-circulation

effects were reduced due to the increased flow velocity, and that reduced the errors for flow conditions fm11 to fm14.

The relation between ε_{Qs}^{abs} and $Q_{s,corr}$ can be seen in Figure **7.38**
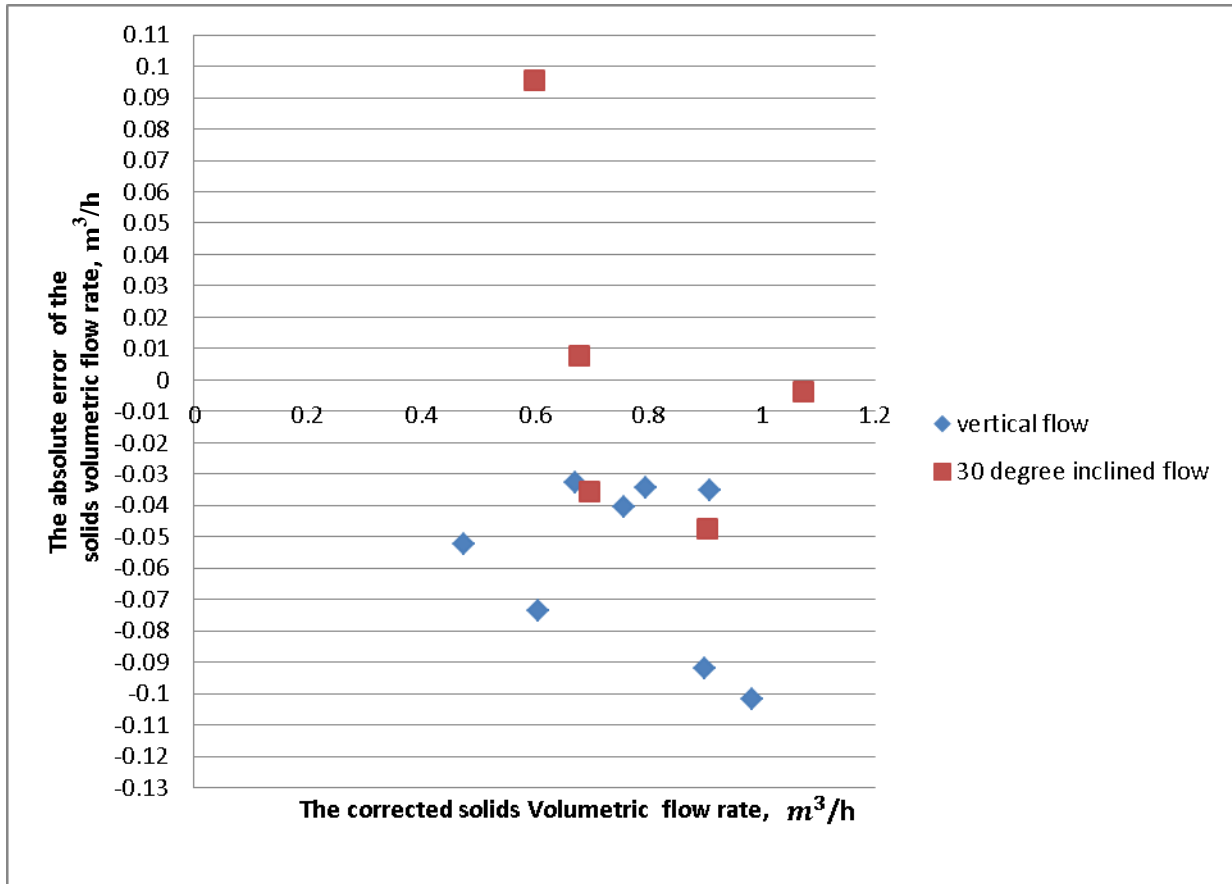
Figure 7.38 Absolute error ε_{Qs}^{abs} plotted against the corrected solids volumetric flow rate $Q_{s,corr}$

7.4.4   Water Volumetric Flow Rate Results

The EVP was used to measure the water velocity $v_{w,EVP}$ in solids-in-water flow, using the technique of dividing the pipe cross-section into 7 regions as shown in Figure 6.7b. The measurement methodology is explained in Section 6.4.2. The EVP used the ICC solids volume fraction profiles (see Figure 7.6 and Figure 7.14) to determine the water volume

fraction $\alpha_{w,EVP}$ in each of the 7 regions, note that $\alpha_{w,EVP} = 1 - \alpha_{s,ICC}$. The water volumetric flow rate can be estimated using:

$$Q_{w,EVP} = \sum_{n=1}^{7} (1 - \alpha_{s,ICC})_n (v_{w,EVP})_n A_n$$

Equation 7-11

where A_n is the cross section area of each of the 7 regions (see Table 6-1)

7.4.4.1 Water Volumetric Flow Rate Error ε_{Qw} for Vertical Flow

The integrated water volumetric flow rate values from the EVP device for each of the upward vertical flow condition, and the relevant reference data, are presented in Table 7-7

Table 7-7 Comparison of ε_{Qw} with reference water volumetric flow rate $Q_{w,ref}$ and EVP water volumetric flow rate $Q_{w,EVP}$ for upward flow in vertical pipe

Flow condition (see Table 6-2)	Solid volumetric flow rate $Q_{s,ref}$ (m³h⁻¹)	Water volumetric flow rate $Q_{w,ref}$ (m³h⁻¹)	Water volumetric flow rate $Q_{w,EVP}$ (m³h⁻¹) Obtained using EVP	Water volumetric flow rate % error ε_{Qw}^{per}	Water volumetric flow rate absolute error ε_{Qw}^{abs} m3/h
fm1	0.494	7.307	6.867	-6.0%	-0.439
fm2	0.63	10.574	10.23	-3.2%	-0.343
fm3	0.698	10.311	9.300	-9.8%	-1.010
fm4	0.828	11.534	10.831	-6.1%	-0.702
fm5	0.944	11.975	11.660	-2.6%	-0.310
fm6	0.935	13.817	14.100	2.1%	0.283
fm7	0.788	11.977	12.388	3.4%	0.411
fm8	1.023	11.788	12.820	8.8%	1.038
Standard deviation for the percentage error m³/h σ_{Qw}^{per}				5.6 %	
Standard deviation for the Absolute error m³/h σ_{Qw}^{abs}				0.623	

7.4.4.2 Water Volumetric Flow Rate Error ε_{Qw} for Upward Flow in Pipe Inclined At $30°$ to the Vertical

The integrated solids volumetric flow rate values from the EVP device for upward flow in pipe inclined at $30°$ to the vertical, and the relevant reference data, are presented in Table 7-8

Table 7-8 Comparison of ε_{Qw} with reference water volumetric flow rate $Q_{w,ref}$ and EVP water volumetric flow rate $Q_{w,EVP}$ in pipe inclined at $30°$ to the vertical

Flow condition (see Table 6-2)	Solid volumetric flow rate $Q_{s,ref}$ (m^3h^{-1})	Water volumetric flow rate $Q_{w,ref}$ (m^3h^{-1})	Water volumetric flow rate $Q_{w,EVP}$ (m^3h^{-1}) Obtained using EVP	Water volumetric flow rate % error ε_{Qw}^{per}	Water volume- tric flow rate absolute error ε_{Qw}^{abs} m3/h
fm9	0.467	8.666	9.638	11.2%	0.972
fm10	0.623	10.196	11.087	8.7%	0.891
fm11	0.706	12.010	12.661	5.4%	0.651
fm12	0.723	13.718	14.064	2.5%	0.346
fm13	0.939	11.072	11.860	7.1%	0.788
fm14	1.116	11.431	12.158	6.4%	0.727
Standard deviation for the percentage error σ_{Qw}^{per}				2.69 %	
Standard deviation for the Absolute error m^3/h σ_{Qw}^{abs}				0.2	

7.4.4.3 Discussion of the Water Volumetric Flow Rate Error, ε_{Qw}

The EVP water volumetric flow rate $Q_{w,EVP}$ was calculated using the water volume fraction $(1-\alpha_{s,ICC})$ and water velocity $v_{w,EVP}$ integrated through the pipe cross-section as shown in Section 6.4.2. The same condition applied here as for the solids volumetric flow rate calculations that is, any errors in water volume fraction $(1-\alpha_{s,ICC})$ or water velocity $v_{w,EVP}$ will

affect the $Q_{w,EVP}$ calculations. Values for ε_{Qw}^{per} listed in Table 7-7 and Table 7-8 are presented Figure 7.39
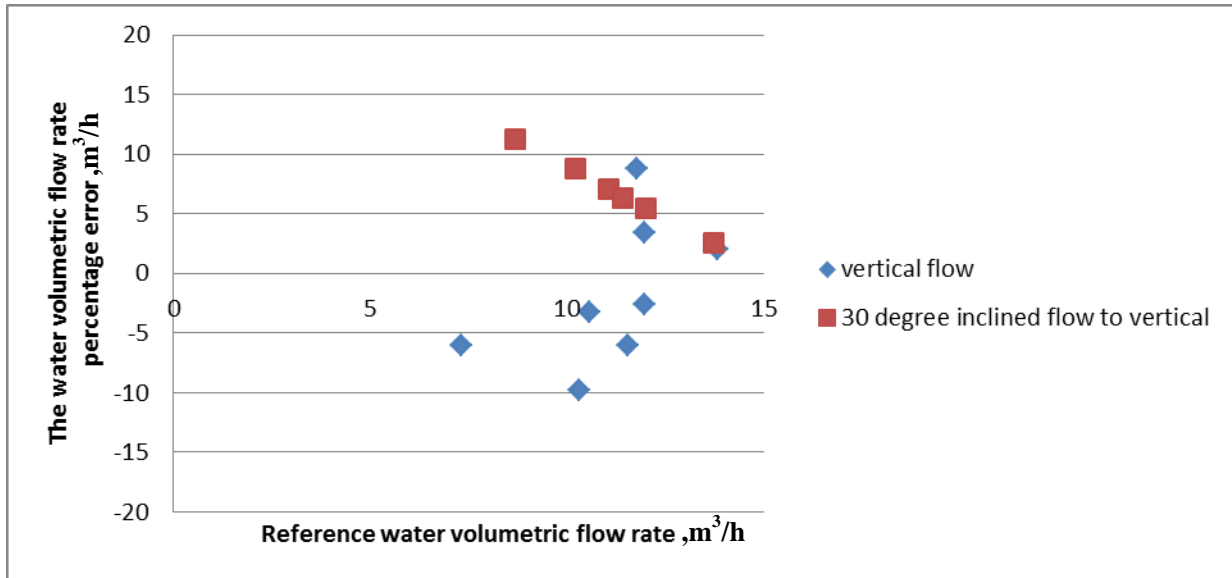
Figure 7.39 Percentage error ε_{Qw}^{pre} plotted against the reference water volumetric flow rate $Q_{w,ref}$ measured using the hopper system

The percentage errors presented in Figure 7.39 are heavily reliant on the accuracy of the local volume fraction distribution obtained by the ICC instrument and the reference water volumetric flow rate obtained from the gravimetric flow measurement system. However, the $\alpha_{s,ICC}$ for vertical flow was less than 0.080, which meant ε_{Qw}^{per} could be highly reliant on the reference water volumetric flow rate and the accuracy of water velocity $v_{w,EVP}$. The $Q_{w,EVP}$ for conditions fm1 to fm5 were underestimated, but as the flow increased the $Q_{w,EVP}$ started to be overestimated. This could mean that use of an EVP system leads to an underestimation of $v_{w,EVP}$. This behaviour was also observed in Leeungculsatien's experiments [83] for single phase flow using the EVP

system. Leeungculsatien used 6 different flow conditions and 5 of them indicated that that $v_{w,EVP}$ is underestimated. Additionally, in the present investigation, the reconstructed water and solids velocity profiles show that the EVP system underestimated $v_{w,EVP}$ for flow conditions fm4, fm5, fm7 and fm8, see Figure 7.22 to Figure 7.25.

For inclined flow, due to the high values of $\alpha_{s,ICC}$ in the flow conditions investigated, the percentage errors are likely to be very reliant on the accuracy of the local volume fraction distribution and the reference water volumetric flow rate. The mean solids volume fraction percentage error $\bar{\varepsilon}_\alpha^{per}$ for the flow in the pipe at 30° to the vertical was -4.6 %. Flow condition fm9 showed the maximum error of 11.2 % where ε_α^{per} in the same condition was 12.2 %.

In this investigation, the reference water volumetric flow rate was assumed to be accurate and did not need correcting. However, as shown above some of the water emerging from the flow loop outlet section entered the solids hopper which would result in a small underestimation of the reference water volumetric flow rate obtained from the gravimetric flow measurement.

The relation between ε_{Qw}^{abs} and $Q_{w,ref}$ can be seen in Figure 7.40.
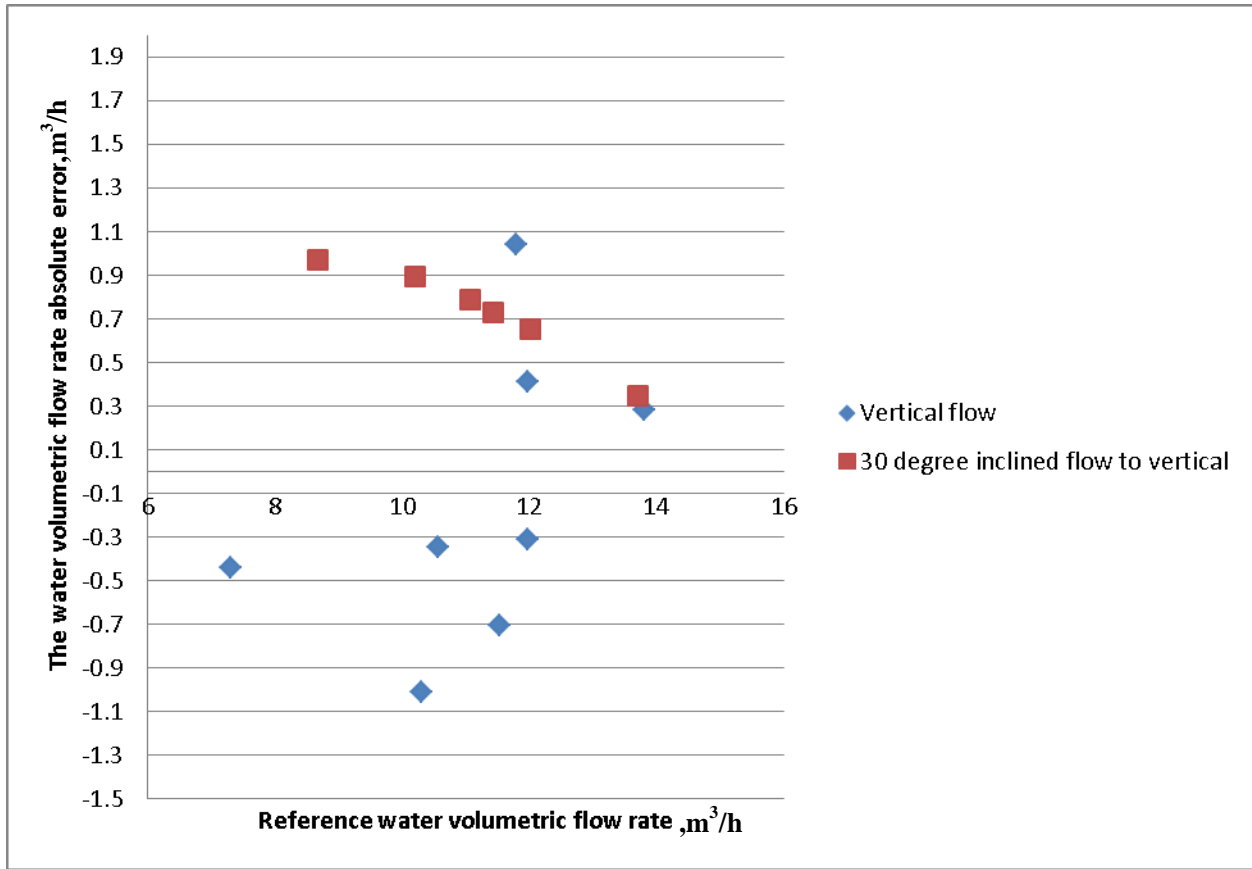
Figure 7.40 Absolute error ε_{Qw}^{abs} **plotted against the reference water volume fraction** $Q_{w,ref}$ **measured using the hopper system**

Multiphase flow meters are commercially available but expensive and the error could be as high as 10% (which was the accuracy achieved by the techniques described in this thesis). For example, the typical relative error of the Roxar subsea multiphase meter [99] were $+/- 4\%$ for the liquid flow rate and $+/- 8\%$ for the gas flow rate.

7.5 Summary

The ICC flow meter and the EVP system can be used for in-situ measurements of volume fraction distribution, velocity profiles and volumetric flow rates for both phases of solids-in-water two phase pipe flows.

The solids volume fraction distributions in vertical flow had the shape of a power law distribution, where the solids particles tended preferentially to be located towards the centre of the pipe. However, in a pipe inclined at 30° to the vertical, the solids volume fraction at the lower side of the inclined pipe is much greater than at the upper side.

In vertical solids-in-water two-phase-flows, the local solids velocity and water velocity are uniformly distributed over the flow cross-section. However, in a 30° inclined working-section, the local solids velocity and water velocity distributions are highly non-uniform.

To obtain an accurate value for the solids volumetric flow rate it is necessary to integrate the local solids velocity distributions and the local solids volume fraction distributions over the flow cross-section.

In vertical flow the maximum error in the solids volumetric flow rate was -12.1%, while in a 30° inclined working-section, the maximum error in the solids volumetric flow rate was 15.9%.

The local water volume fraction was obtained using the local ICC solids volume fraction given by $\alpha_{w,EVP} = 1 - \alpha_{s,ICC}$. The water volumetric flow rate was determined by integrating the local water volume and local water axial velocity over the 7 flow regions shown in Figure6.7b.

The maximum error in the water volumetric flow rate estimates was -9.8% in vertical flow and 11.2% in flows inclined at 30° to the vertical.

It should to be noticed that a large component of the errors in solids and water volumetric flow rates were almost certainly due to the inaccuracies in measurements made with the gravimetric reference system.

The mean error in the solids volumetric flow rate at 0° and 30° inclination is -7.7% (refer to Table 7-5) and +3.2% (refer to Table 7-6) respectively.

The mean error in the water volumetric flow rate at 0° and 30° inclination is -1.6% (refer to Table 7-7) and +6.8% (refer to Table 7-8) respectively.

In vertical solids-in-water flow, the Area Methodology AM shows more accurate results than the Centre of Action CoA method. In vertical low mean solids volume fraction flow, i.e. $\overline{\alpha} < 0.08$, the CoA method produced an error in the solids volume fractions results which reached 70%.

Yet in inclined solids-in-water flow, the Area Methodology methods shows unrealistic value for the solids volume which fraction reached $\alpha < 1.6$. Unlike Area Methodology, the Centre of Action method shows more accurate results for the solids volume fraction measurement. The reason for the differences between the two methods is explained in Sections 3.4.2 and 3.4.4.

The magnitude of the mean errors in solids and water volumetric flow rates using the ICC instrument in conjunction with EVP instrument were relatively small, the combined technique is believed to be helpful in improving the accuracy of current two-phase flow metering technology.

8. CHAPTER 8: Conclusions and Future Work

8.1 Conclusions

This thesis has presented a study of the development of a novel non-intrusive multiphase flow meter for measuring flow parameters for two-phase, highly non-uniform solids-in-water flow in vertical and inclined pipes. The flow meter that has been developed is based on the integration of two measurement techniques: Impedance Cross Correlation and an Electromagnetic Velocity Profiler.

The impedance cross correlation flow meter is a novel and non-intrusive device and able to measure the solids and water local volume fraction distributions, the solids local velocity distribution and the solids volumetric flow rate in highly non-uniform solids-in-water flow. The ICC device consists of two electrode arrays separated by an axial distance of 50mm. each array has eight electrodes equi-spaced around the pipe wall.

The ICC device has two electrode selection circuits which were designed to allow selection of any electrodes from a given array (A or B) and connect them to the excitation signal (V^+), measurement circuit (ve) or earth (E) in the corresponding channel (A or B) of the conductance measurement circuit, refer to Section 4.2.2. Based on the truth Tables 4.1 and 4.2, the electrode m in each array was connected to one of three potentials (V^+, ve and E). The ICC device has a conductance circuit to measure the conductance of the multiphase mixture between the V^+ and ve electrodes, sequentially for each of the eight rotational positions, for a given configuration.

Using the measured conductance for a given configuration and rotational position, the local solids volume fraction α_s is measured using Maxwell's relationship, see Equation 4-9.

For a given configuration and rotational position, the DC output voltages $VA_{\phi,n}(t)$ and $VB_{\phi,n}(t)$ were cross correlated to provide information on the local solids velocity of a two phase flow, refer to Section 4.3.2

Standalone and computer based ICC systems have been developed. The standalone ICC system can be operated without any computer interaction after all the programming routines had been download onto the microcontroller memory. The standalone ICC system can be used to measure the solids volume fraction for a given configuration and rotational positions (n=1 to 8) and display the results on a LCD screen. This is extremely useful as an industrial unit where space is limited. Due to limitations in the sampling frequency of the microcontroller, a computer based system was used to cross correlate the DC output voltages $VA_{\phi,n}(t)$ and $VB_{\phi,n}(t)$ and provide information on the local solids velocity of a two phase flow.

Two measurements approaches were used with the ICC: the Area Method and Centre of Action Method. Both techniques depend on finding the sensitivity distribution for each electrode configuration and determining the measured solids and water parameters for those distributions.

A successful COMSOL computational model of the ICC flow meter was achieved to investigate which electrode configurations interrogated deepest into the flow cross-section. The model was used to calculate the sensitivity distribution for different electrode configurations:

- **Configuration I** (see Table 3-1)**:** in this configuration, only one electrode is excited with an adjacent electrode selected as the virtual earth measurement (ve) electrode. The remaining six electrodes are earthed (E). For example, in rotational position-1, electrode 1 is the excitation electrode and electrode 2 is the measurement electrode (ve), with electrodes 3, 4, 5, 6, 7 and 8

connected to ground (E). Seven similar arrangements are possible by simple rotation of the arrangement.

- **Configuration II** (see Table 3-2): in this configuration, only one electrode is excited and the two adjacent electrodes are used for virtual earth measurements. The remaining five electrodes are earthed (E). For example, in rotational position-1, electrode 1 is the excitation electrode, electrodes 2 and 8 are the measurement electrodes and electrodes 3, 4, 5, 6 and 7 are connected to ground. Again seven similar arrangements are possible by simple rotation of the first arrangement.

- **Configuration III** (see Table 3-3): in this configuration, two adjacent electrodes are excited and the two adjacent electrodes are used for virtual earth measurements (ve). The remaining four electrodes are earthed (E). For example, in rotational position-1 electrodes 1 and 2 are the excited, electrodes 3 and 8 are the measurement electrodes and electrodes 4, 5, 6 and 7 earthed (E). Again seven similar arrangements are possible by simple rotation of the first arrangement.

The boundary of the effective sensing region in each Configuration ($\phi = \text{I, II or III}$) and the nth rotational position ($n = 1\,\text{to}\,8$) was arbitrarily defined as 10% of the maximum sensitivity. Each effective sensing region has a Centre of Action which can be taken as a measure of how far the sensing field extends into the fluid. The x and y coordinates for each Centre of Action in the three configurations for each of the eight rotational positions can be calculated using Equations 3-5 and 3-6 in Section 3.4.1.

Centre of Action CoA was used to measure the solids parameters in solids-in-water stratified flow inclined at 30˚ to the vertical. However, The Centre of Action method was found to have limited capability with low solids volume fraction in vertical flow, though it worked effectively

227

for inclined flows, see Section 3.4.2. An obvious reason for this is the lack of precision in measuring the solids parameters at the centre of the pipe. Thus a new measurement technique (Area Method) was developed to measure the solids-in-water parameters for vertical flow.

The **Area Method (AM)** is based on dividing the pipe cross-section into defined sub-areas. The boundary outline of these regions depends on the sensitivity distributions of the configurations (A new configuration, Configuration IV, was used to obtained an effective sensing region extending deeper toward the centre of the pipe, see Section 3.4.3.1). This technique will depend on a sensitivity parameter ψ obtained from the sensitivity distribution for Configuration IV, see Section 3.4.3.2.

- **Configuration IV** (see Table 3-4): is similar to Configuration I, but while Configuration IV has only one excitation electrode and only one virtual earth (ve), the virtual earth is not the adjacent electrode but the next one along. Thus if the excitation electrode is electrode 1 the virtual earth is electrode 3. As previously the remaining electrodes, 2, 4, 5, 6, 7 and 8 are earthed (E). Obviously seven similar arrangements are possible by simple circular rotation.

The Area Method has a limitation when measuring the solids volume fraction in inclined flow, see Section 3.4.4. In solids-in-water flow inclined at 30° to the vertical, the solids volume fraction α_s is much greater at the lower side of the pipe than the upper side. This happened due to the fact that α_s is effected by the gravity and varies as a function of the y co-ordinate. This failure of the AM could be due to the large variation in solids volume fraction between the lower and upper sides of the pipe. The relationship in Equation 3-12 is used to measure the solids volume fraction $\alpha_{n,0}$ at position $B_{n,0}$ and it is highly dependent on a symmetric solids' distribution in X and Y co-ordinates. Additionally, the relationship in Equation 3-12 is also

highly dependent on the mean sensitivity parameter $\overline{\psi}$. Any small error in $\overline{\psi}$ will effect α_s especially if α_s is relatively high, e.g. if it reaches 0.65-0.70 at the lower side of the pipe.

Based on the above it was decided to use the CoA to determine the solids' parameters in solid-in-water inclined flow only and to use the Area Method to determine the solids' parameters in solid-in-water vertical flow.

This thesis has also presented a novel non-intrusive multiphase flow meter for measuring highly non-uniform velocity profiles in single-phase flows in vertical and inclined two-phase flows. The developed flow meter is a multi-electrode electromagnetic device called the **Electromagnetic Velocity Profiler (EVP).** The EVP consists of a non-conducting flow tube of 80 mm ID, with sixteen stainless steel electrodes mounted flush and equi-spaced around the pipe wall, a Helmholtz coil, and the associated electronic and electrical circuitries, see Section 6.3.

Using the multiphase flow loop at the University of Huddersfield an experimental investigation was carried out of the performance of the combined ICC/EVP instruments for solids-in-water multiphase flows. Reference measurements of the mean reference solids volume fraction $\overline{\alpha}_{s,dp}$ in the flow cross-section (Section 6.3.2), the reference solids volumetric flow rate, $Q_{s,ref}$, and the reference water volumetric flow rate, $Q_{w,ref}$ (Section 6.3.3) were obtained.

By combining the ICC/EVP techniques into a two-phase flow meter the volume fraction distributions of both phases, the velocity profiles of both phases and the volumetric flow rates for both phases were measured for solids-in-water two-phase pipe flows.

In solids-in-water 30°inclined flow to the vertical, the solids volume fraction profiles show that a very small proportion of solids particles are present at the upper regions of the flow cross –

section (region 1, 2 and 3 in Figure 6.9). The solids volume fraction increased towards the lower side of the pipe reaching a maximum in region 7. The reference solids volume fraction for inclined flow varied from about 0.08 to about 0.22. The comparison between the mean measurement results $\overline{\alpha}_{s,ICC}$ and the reference results $\overline{\alpha}_{s,dp}$ for the solids volume fraction shows that the percentage error $\varepsilon_{\alpha}^{per}$ varied from 12 % to -15% with a mean value of $\overline{\varepsilon}_{\alpha}^{per}$ -4.6 % and standard deviation σ_{α}^{per} of 9.08%.

Additionally, the experimental results show that the local axial solids and water velocity both decrease as moving from the upper side of the pipe to the lower.

For inclined flow, the mean percentage solids velocity error $\overline{\varepsilon}_{v}^{per}$ was 3.01% with percentage standard deviation σ_{v}^{per} of 22.86%.While the mean absolute solids velocity error $\overline{\varepsilon}_{v}^{abs}$ was 0.013 m/s with absolute standard deviation σ_{v}^{abs} of 0.04 m/s.

The solids velocity percentage error in fm9 and fm10 is high, possibly because either i) the errors in the reference measurements ($\overline{\alpha}_{s,dp}$ and $Q_{s,ref}$) which were used to determine the mean reference solids velocity $\overline{v_{s,ref}}$ or ii) because these two flow conditions were subject to re-circulation which effected the cross correlation results for at least region 7 (see Section 7.3.2.2) which gave $v_{s,ICC}$ results in those regions higher than the reality.

The local solids volume fraction distributions and the local solids axial velocity distributions show qualitative agreement with previous experimental profiles obtained by Cory [56] and Al-Hinai [49].

In solid-in-water vertical flow, the solids volume fraction profiles show a bell shape with a marked increase in solids volume fraction $\alpha_{s,ICC}$ close to the pipe centre and decreases toward the pipe wall due to the "wall effect". However, the solids velocity profiles and the water velocity profiles have only small variation of $v_{s,ICC}$ over the pipe cross-section.

The solids volume fraction percentage error ε_α^{per} in $\overline{\alpha}_{s,ICC}$, as compared with $\overline{\alpha}_{s,dp}$ in vertical flow, varied from 8.7% to -21.2% with a mean value of $\overline{\varepsilon_\alpha^{per}} - 6.4\%$ and standard deviation ε_α^{std} of 9.4%. While the solids volume fraction absolute error ε_α^{abs} is varied from 0.005 to -0.017 with a mean value of $\overline{\varepsilon_\alpha^{per}}$ -0.004 and absolute standard deviation σ_α^{abs} of 0.006.

The local solids volume fraction profiles in vertical flow match previous profiles obtained by Alajbegovic et. al., [13] and Bartosik and Shook [15].

Additionally ε_v^{per} for vertical upward solids-in-water flow varied from 10.4% to -14.1 % with a mean value of $\overline{\varepsilon_v^{per}}$ -1.2 % and percentage error standard deviation σ_v^{per} 8.6%. The mean absolute solids velocity error $\overline{\varepsilon_v^{abs}}$ was 0.013 m/s with absolute standard deviation σ_v^{abs} of 0.04 m/s.

Again, the local solids axial velocity distributions for the current study show qualitative agreement with previous experimental profiles obtained by Cory [56] and Al-Hinai [49].

Using the ICC device, the solids volumetric flow rate can be estimated by integrating the local solids velocity profiles and local solids volume fraction profiles through the pipe cross section.

The EVP was used to measure the water velocity $v_{w,EVP}$ in solids-in-water flow. Additionally, the EVP used the ICC local solids volume fraction profiles (see Figure 7.6 and Figure 7.14) to

determine the local water volume fraction $\alpha_{w,EVP}$, note that $\alpha_{w,EVP} = 1 - \alpha_{s,ICC}$. The water volumetric flow rate can be estimated by integrating the local water velocity profiles and the local water volume profiles through the pipe cross section.

For solids-in-water vertical flows, the solids volumetric flow rate $Q_{s,ICC}$ results obtained by the ICC device were always less than the reference measurements. The percentage error for the solids volumetric flow rate ε_{Qs}^{pre} varied between -3.87% to -12.1%, with a mean solids volumetric flow rate percentage error $\overline{\varepsilon}_{Qs}^{per}$ -7.7%.

The percentage error for the water volumetric flow rate ε_{Qw}^{per} varied between -9.8% to 8.8%, with a mean water volumetric flow rate percentage error $\overline{\varepsilon}_{Qw}^{per}$ -1.68%.

For the pipe inclined at $30^{°}$ to the vertical ε_{Qs}^{pre} varied between -5.2 % to 15.9 % with a mean value 3.2%. While the ε_{Qw}^{per} varied between 2.5 % to 11.2 % with a mean value 6.8%.

For solids-in-water pipe flows the solids and water velocity profiles and the solids and water local volume fraction distributions are all highly non-uniform, especially when the flow pipe is inclined at $30^{°}$ to the vertical. Nevertheless the two phase flow meter was able to measure solids and water volumetric flow rate to about +/-10 % of references reading. It is expected that the magnitude of these errors will be substantially reduced when better reference measurements of the solids and water volumetric flow rates can be made.

The achieved results show that the performance of the techniques described in this thesis can be matched with the existing commercial multiphase flow meter for vertical and inclined (stratified) solids-in-water flows.

8.2 Future Work

The results of the current investigation and the conclusions reached, suggest a number of avenues for further work:

- The **Area Method** needs to be investigated using solids-in-water vertical flow with high mean solids volume fraction to evaluate its performance. Additionally, more investigation is needed for find other suitable configurations which can interrogate deeper into the flow cross-section.

- Using the Centre of Action CoA method, the **ICC** device shows a good performance in stratified upward flow with a moving bed in pipes inclined at $30^{°}$ to the vertical; it is recommended that the ICC be applied to the investigation of horizontal stratified solids-in-water flows.

- The **ICC** device is used to measure the dispersed phase parameters in two-phase solids-in-water flow and it is recommended to investigate the performance of the ICC in liquid-liquid oil-water flows, since oil-in-water flow is one of the most common and important multiphase flow types in the oil industry.

- In inclined non-uniform solids-in-liquid flow, the flow structure is changing through different pipe work sections depending on the mixture flow rates. Therefore, it is recommended that the use of more than 2 electrode arrays be investigated. For example 4 arrays as shown in Figure 8-1 would be expected to provide a better indication of any wave structures in the flow that occur while measurements are being made.

  It could also be better to use 3 earthed electrode rings to achieve symmetric electrical distributions and eliminate the interface between the electrode arrays.

233
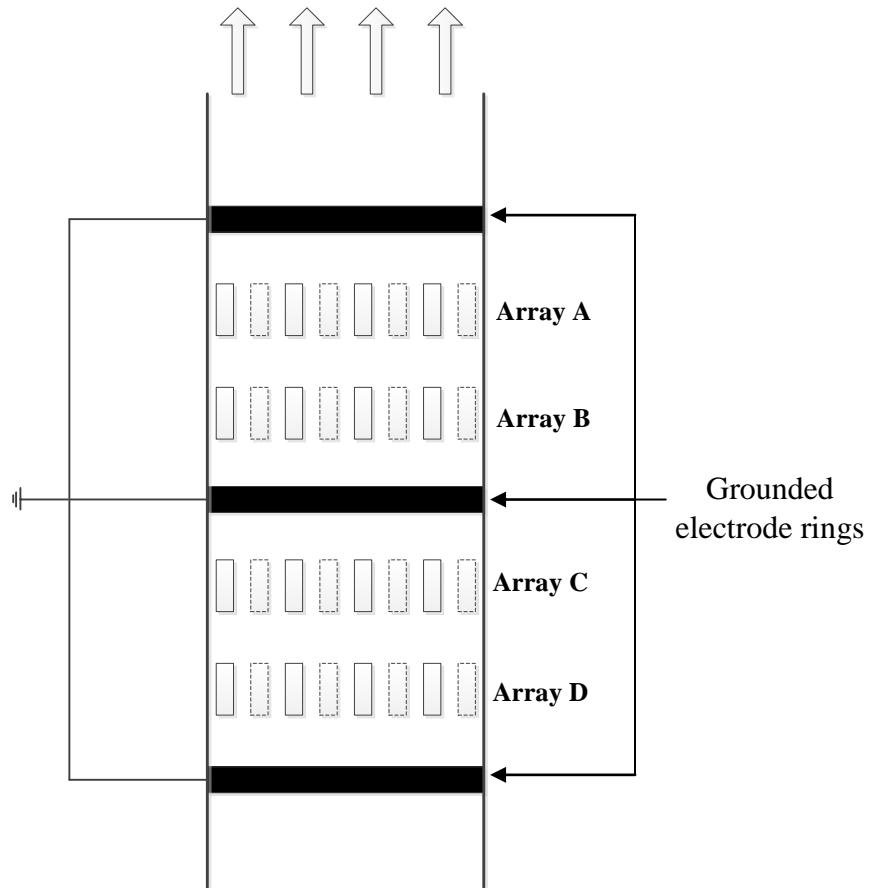
Figure 8.1 Suggested four electrode array flow meter.

Additionally, Using more than 8 electrodes (i.e 16) would increase the number of measurements and give greater precision to the calculated flow pattern and its parameters.

- The electrodes geometry was rectangular with dimensions of 10 mm long x 5 mm wide x 1.5 mm thick. Investigations are needed to examine the effects of electrode size and shape on measurement accuracy.

- The reference measurements devices used on the University of Huddersfield flow loop need to be improved: a better separation method or a sensor in the solids hopper to measure the volumetric flow rate of the water emerging with the solids, refer to Figure 8.2.
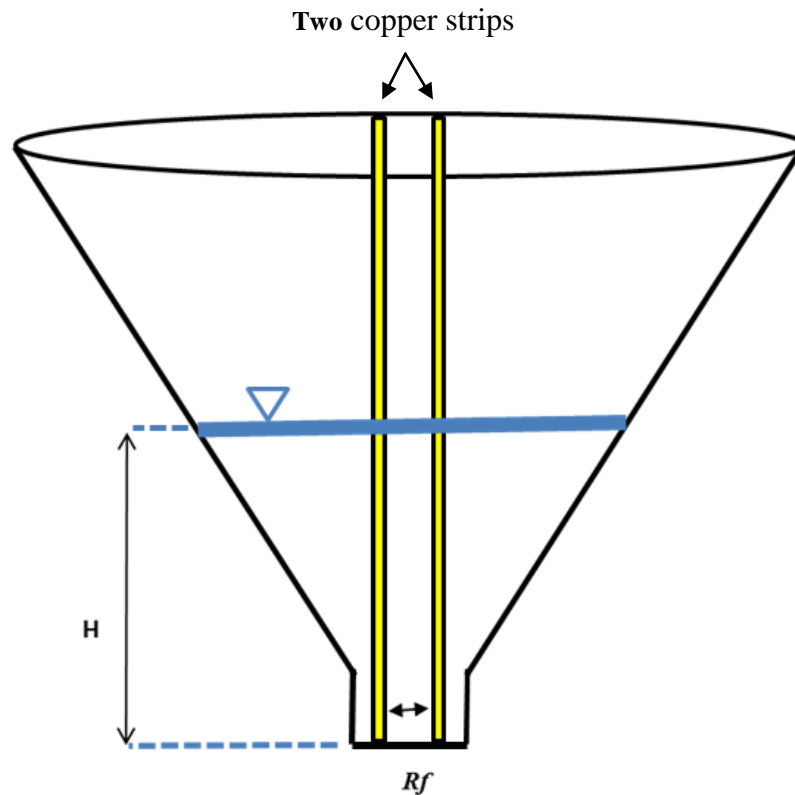
Figure 8.2 Schematic diagram of the water level sensor inside the solids hopper

Figure 8.2 shows the level sensor inside the solids hopper. The system consists of two parallel copper strips mounted on a layer of insulating material and fixed over the wall of the hopper. An electrical connection between the strips will form as water start filling the solids hopper. The fluid electrical resistance R_f between the strips will be related to the level of water in the hopper, H. By using the same circuit conductance shown in Figure 4.9, the relation between the output voltage V_{out} from the conductance circuit and the water level can be found.

For the current investigation, the level of water in the solids hopper is always less than the level of the solids because the mixture has already been partially separated. Therefore the

exact relationship between the water volumes emerged inside the solids hopper and the output voltage V_{out} from the conductance circuit can be determined using experimental calibration. The calibration can be carried out by adding dry solids to the hopper and then adding measured volumes of water whilst recording the value of V_{out} given by the conductance circuit.

- The ICC /EVP system could be combined with a density flowmeter to measure the parameters of the multiphase flow i.e. oil-gas-water flow. The density flowmeter, refer to Figure 8.3 , is used to measure the fluid mixture density.
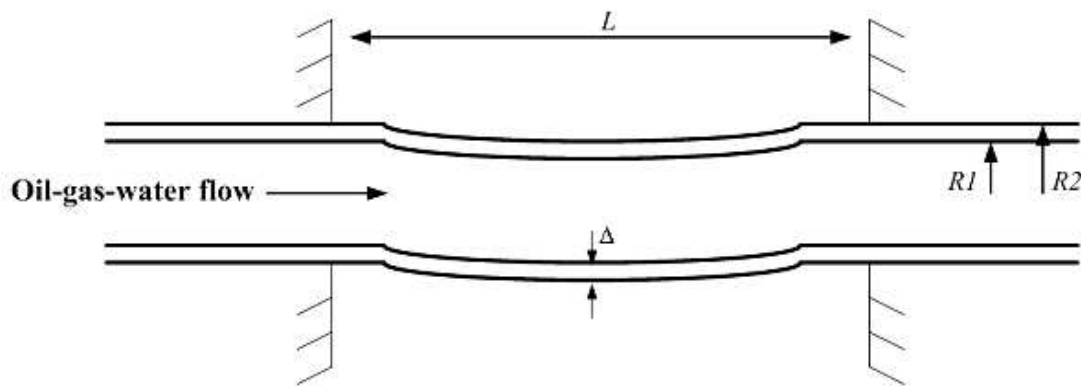
Figure 8.3 schematic diagram of the density flowmeter

The **density flowmeter** in Figure 8.3 shows a horizontal pipe of radii R1 and R2 of length L supported rigidly at both ends. By measuring the deflection of the pipe Δ, the fluid mixture density ρ_f is determined. The deflection at the centre of the span is given by[]:

$$\Delta = \frac{1}{384} \frac{\left\{ \pi (R_2^2 - R_1^2) \rho_p g + \pi R_1^2 \rho_f g \right\} L^4}{1/2 E (R_2^4 - R_1^4)}$$

Equation 8-1

where ρ_p is the density of the pipe material, kg/m^3, ρ_f is the density of the fluid mixture, kg/m^3, g is the gravity m/s^2 and E is the modulus of elasticity of the pipe material.

The mixture fluid density ρ_f in oil-gas-water flow is defined as:

$$\rho_f = \alpha_o \rho_o + \alpha_w \rho_w + \alpha_g \rho_g$$

Equation 8-2

where α_o, α_w and α_g represent respectively the volume fraction of the oil, water and gas. ρ_o, ρ_w and ρ_g represent respectively the density of the oil, water and gas.

Since ρ_g is very small compared with water and oil density, therefore, the term $\alpha_g \rho_g$ in Equation 8-2 can be neglected. Hence Equation 8-2 can be re-written as:

$$\rho_f = \alpha_o \rho_o + \alpha_w \rho_w$$

Equation 8-3

In three phase flow condition, it is only needed to measure the volume fraction for two phases in order to find the third one as shown below:

$$1 = \alpha_o + \alpha_g + \alpha_w$$

Equation 8-4

Equation 8-4 can be re-written in term of the water volume fraction as:

$$\alpha_w = 1 - \alpha_o - \alpha_g$$

Equation 8-5

The **ICC device** can be used to measure the dispersed volume fraction in oil-gas-water multiphase flow. The measured volume fraction for the dispersed phase represents the gas and oil volume fractions. Therefore, the measured volume fraction from the ICC device can be written as:

$$\alpha_{ICC} = \alpha_o + \alpha_g$$

Equation 8-6

By solving Equation 8-6, Equation 8-5 and Equation 8-3, the volume fraction of the three phases can be determined.

The **ICC device** can be also used to measure the dispersed velocity in oil-gas-water multiphase flow using cross correlation technique. The signal obtained by the ICC represents the oil and gas signals. By filtering these signals, the velocity of both oil and gas can be found.

Additionally, the **EVP system** can be used to measure the water velocity in oil-gas-water multiphase flow. By integrated the velocity and volume fraction for all phases through the pipe across section, the volumetric flow rate can be easily determined.

9. References

1. Martyn, J., Tomographic multiphase flow measurement. 1999, University of Surrey.
2. Salman, W., A. Gavriilidis, and P. Angeli, On the formation of Taylor bubbles in small tubes. Chemical Engineering Science, 2006. **61**(20): p. 6653-6666.
3. Falcone, G., G.F. Hewitt, and C. Alimonti, Multiphase Flow Metering, ed. D.i.P. science. Vol. 54. 2010, Oxford,UK: Elsevier.
4. Klyuev, N.I. and E.A. Solov'eva, Method for the annular gas-liquid mixture flow regime in a vertical cylindrical channel. Russian Aeronautics (Iz VUZ), 2009. **52**(1): p. 68-71.
5. Rahim, R.A., M.H. Fazalul Rahiman, and M.N.M. Taib. Non-invasive ultrasonic tomography: Liquid/gas flow visualization. in Computers, Communications, & Signal Processing with Special Track on Biomedical Engineering, 2005. CCSP 2005. 1st International Conference on. 2005.
6. Rahiman, M.H.F., R.A. Rahim, and M. Tajjudin, Ultrasonic Transmission-Mode Tomography Imaging for Liquid/Gas Two-Phase Flow. Sensors Journal, IEEE, 2006. **6**(6): p. 1706-1715.
7. Shao, N., A. Gavriilidis, and P. Angeli, Flow regimes for adiabatic gas–liquid flow in microchannels. Chemical Engineering Science, 2009. **64**(11): p. 2749-2761.
8. Tan, C., F. Dong, and M. Wu, Identification of gas/liquid two-phase flow regime through ERT-based measurement and feature extraction. Flow Measurement and Instrumentation, 2007. **18**(5–6): p. 255-261.
9. Wang, M., et al., Visualisation of Bubbly Velocity Distribution in a Swirling Flow Using Electrical Resistance Tomography. Particle & Particle Systems Characterization, 2006. **23**(3-4): p. 321-329.
10. Xu, L.J. and L.A. Xu, Gas/liquid two-phase flow regime identification by ultrasonic tomography. Flow Measurement and Instrumentation, 1998. **8**(3–4): p. 145-155.
11. Henthorn, K.H., K. Park, and J.S. Curtis, Measurement and Prediction of Pressure Drop *in Pneumatic Conveying: Effect of Particle Characteristics, Mass Loading, and Reynolds* Number. INDUSTRIAL & ENGINEERING CHEMISTRY RESEARCH, 2004. **44**(14): p. 5090-5098.
12. Lee, S.L. and F. Durst, On the motion of particles in turbulent duct flows. International Journal of Multiphase Flow, 1982. **8**(2): p. 125-146.
13. Alajbegović, A., et al., Phase distribution and turbulence structure for solid/fluid upflow in a pipe. International Journal of Multiphase Flow, 1994. **20**(3): p. 453-479.
14. Sakaguchi, T., et al., Microscopic characteristics of multiphses flow using digital image processing, in Proc. Int. Conference on Multiphase Flows. 1991: Tsukuba, Japan. p. 375-360.
15. Bartosik, A.S. and C.A. Shook, Prediction of vertical liquid-solid pipe flow usingmeasured concentration distribution, in Particulate Science & Technology. 1995. p. 85-104.
16. Doron, P. and D. Barnea, Flow pattern maps for solid-liquid flow in pipes. International Journal of Multiphase Flow, 1996. **22**(2): p. 273-283.

17.   Ramadan, A., P. Skalle, and A. Saasen, Application of a three-layer modeling approach for solids transport in horizontal and inclined channels. Chemical Engineering Science, 2005. **60**(10): p. 2557-2570.

18.   limited, D.-W., The World Deepwater Report,2000-2004. 2004.

19.   Scheers, A.M. and B.R. Noordhuis, Multi-phase and Wet Gas Flow Measurement, in 5th Annual Multi-Phase Metering Conference. 1999: Aberdeen, Scotland.

20.   Danielson, T.J., Transient Multiphase Flow: Past, Present, and Future with Flow Assurance Perspective. Energy & Fuels, 2012. **26**(7): p. 4137-4144.

21.   de Oliveira, M.C.K., et al., Flow Assurance Study for Waxy Crude Oils. Energy & Fuels, 2012. **26**(5): p. 2688-2695.

22.   Jamaluddin, A.K.M. and C.S. Kabir, Flow assurance: Managing flow dynamics and production chemistry. JOURNAL OF PETROLEUM SCIENCE AND ENGINEERING, 2012. **100**: p. 106-116.

23.   Wang, W., et al., A model for estimating flow assurance of hydrate slurry in pipelines. Journal of Natural Gas Chemistry, 2010. **19**(4): p. 380-384.

24.   Zerpa, L.E., et al., Surface Chemistry and Gas Hydrates in Flow Assurance. Industrial & Engineering Chemistry Research, 2011. **50**(1): p. 188-197.

25.   Zhang, J., et al., Advances in rheology and flow assurance studies of waxy crude. Petroleum Science, 2013. **10**(4): p. 538-547.

26.   Engineering, I.o.P. Why are Gas Hydrates Important? 2013 [cited 2013 31/10/2013]; Available from: http://www.pet.hw.ac.uk/research/hydrate/hydrates_why.cfm.

27.   Congress, G.C. Researchers Seeking Better Understanding of Asphaltenes; Potential for Improving Oil Recovery. 2009 [cited 2013 6/8/2013]; Available from: http://www.greencarcongress.com/2009/09/asphaltenes-20090925.html.

28.   Azar, J.J., Drilling Engineering. 2007: PennWell Corporation.

29.   Mankad, S. and P.J. Fryer, A heterogeneous flow model for the effect of slip and flow velocities on food steriliser design. Chemical Engineering Science, 1997. **52**(12): p. 1835-1843.

30.   Mankad, S., C.A. Branch, and P.J. Fryer, The effect of particle slip on the sterilisation of solid-liquid food mixtures. Chemical Engineering Science, 1995. **50**(8): p. 1323-1336.

31.   Benabderrahmane, Y. and J.P. Pain, Thermal behaviour of a solid/liquid mixture in an ohmic heating sterilizer - slip phase model. Chemical Engineering Science, 2000. **55**(8): p. 1371-1384.

32.   Lareo, C., R.M. Nedderman, and P.J. Fryer, Particle velocity profiles for solid-liquid food flows in vertical pipes part II. Multiple particles. Powder Technology, 1997. **93**(1): p. 35-45.

33.   Siegen, U.o. Workshop on Proposed Technologies for Deep Seabed Mining of Polymetallic Nodules. 2006 [cited 2013 04/09/2013]; Available from: http://www.mb.uni-siegen.de/inko_schwarz/workshop/vortrag1.html?lang=e.

34.   Wang, Z., Q.-h. Rao, and S.-j. Liu, Fluid-solid interaction of resistance loss of flexible hose in deep ocean mining. Journal of Central South University, 2012. **19**(11): p. 3188-3193.

35.   Wang, Z., Q. Rao, and S. Liu. Dynamic Analysis of Seabed-Mining Machine-Flexible Hose Coupling in Deep Sea Mining. in Proceedings of the Ninth (2011) ISOPE Ocean Mining Symposium. 2011. Maui, Hawaii, USA: The International Society of Offshore and Polar Engineers (ISOPE).

36.   Wakeman, R.J. Liquid-Solid Separation. 2011 [cited 2013 9/5/2013]; Available from: http://www.thermopedia.com/content/928/.

37.   Chu, C.P. and D.J. Lee, Moisture Distribution in Sludge: Effects of Polymer Conditioning. Journal of Environmental Engineering, 1999. **125**(4): p. 340-345.

38.   M. Abu-Orf M. and S.K. Dentel, Polymer dose assessment using the streaming current detector. Water Environment Research, 1997. **69**(6): p. 1075-1085.

39.   Baker, R.C., Flow measurement handbook: industrial designs, operating principles, performance, and applications. 2000, Cambridge, [England]: Cambridge University Press.

40.   Chao, T. and D. Feng. Gas-water two-phase flow regime identification with feature fusion from an ERT system and a V-cone meter. in Imaging Systems and Techniques, 2009. IST '09. IEEE International Workshop on 2009.

41.   Chisholm, D., Flow of Incompressible Two-Phase Mixtures through Sharp-Edged Orifices. Journal of Mechanical Engineering Science, 1967. **9**(1): p. 72-78.

42.   Chisholm, D., Research Note: Two-Phase Flow through Sharp-Edged Orifices. Journal of Mechanical Engineering Science, 1977. **19**(3): p. 128-130.

43.   Hasan, A. and G. Lucas. Modelling and Measurement of the Gas Flow Rate in Vertical Annular Gas-*Water Flow Using a 'Conductance Multiphase Venturi meter'*. in Multi-dimensional Advances for Industrial Process Monitoring International Symposium,Leeds, UK. . 2009.

44.   Hasan, A. and G. Lucas, Simulation and static measurement of the gas volume fraction in a separated flow model using a Conductance Multiphase Venturi Meter (CMVM). 2008, University of Huddersfield.

45.   Hasan, A. and G. Lucas, Experimental and theoretical study of the gas–water two phase flow through a conductance multiphase Venturi meter in vertical annular (wet gas) flow. 2011.

46.   Hong-jian, Z., Y. Wei-ting, and H. Zhi-yao, Investigation of oil-air two-phase mass flow rate measurement using Venturi and void fraction sensor. Journal of Zhejiang University Science A, 2005. **6**(6): p. 601-606.

47.   Murdock, J.W., Two-Phase Flow Measurement With Orifices. Journal of Basic Engineering, 1962. **84**(4): p. 419-432.

48.   Chao, T. and D. Feng. Gas-water two-phase flow regime identification with feature fusion from an ERT system and a V-cone meter. in Imaging Systems and Techniques, 2009. IST '09. IEEE International Workshop on. 2009.

49.   Al-Hinai, S., Non-invasive velocity and volume fraction profile measurement in multiphase flows. 2010.

50.   Al-Hinai, S. and G. Lucas. An Impedance Cross Correlation (ICC) device for measuring solids velocity and volume fraction profiles in solids-water flows.

51.   Al-Hinai, S. and G. Lucas. A flowmeter for measuring the dispersed phase velocity in multiphase flow with non-uniform velocity profiles.

52.   Al-Yarubi, Q. and G. Lucas, Measurement of the film thickness, film velocity and entrainment fraction in a liquid-air annular flow using a conductance flowmeter. 2008, University of Huddersfield.

53.   A-Yarubi, Q. and G. Lucas. Measurement of the Film Thickness, Film Velocity and Entrainment Fraction in a Liquid-Air Annular Flow Using a Conductance Flowmeter.

54. Lucas, G., J. Cory, and R.C. Waterfall, A six-electrode local probe for measuring solids velocity and volume fraction profiles in solids-water flows. 2000(Journal Article).
55. Maxwell, J.C., A treatise on electricity and magnetism. 1954, United States.
56. Cory, J., The measurement of volume fraction and velocity profiles in vertical and inclined multiphase flows. 1999, The University of Huddersfield.
57. Devia, F. and M. Fossa, Design and optimisation of impedance probes for void fraction measurements. Flow Measurement and Instrumentation, 2003. 14(4–5): p. 139-149.
58. Li-pin, L., et al. The analysis and study on electromagnetic field of conductance water fraction sensor. in Image and Signal Processing (CISP), 2010 3rd International Congress on. 2010.
59. Yanyan, S., D. Feng, and T. Chao. Conductance probe for the measurement of liquid volume fraction and axial velocity in gas-liquid two phase flow. in Electronic Measurement & Instruments, 2009. ICEMI '09. 9th International Conference on. 2009.
60. Yu, L. and Y. Li. On Conductance Probe Measurement Model for Measuring Oil-Water Annular Flow. in Information Science and Engineering (ICISE), 2009 1st International Conference on. 2009.
61. Matousekh, V., Internal structure of slurry flow in inclined pipe. Experiments and mechanistic modelling, in Proceedings of the 13th International Conference on Slurry Handling and Pipeline Transport,: Johannesburg,South Africa. p. 187-210.
62. Chen, R.C., Experimental and numerical studies of solid-liquid multiphase flow in pipes. 1991, Case Western Reserve University.
63. Chao, T. and D. Feng. Cross correlation velocity of oil-water two-phase flow by a Dual-plane Electrical Resistance Tomography system: IEEE.
64. Hua, L., et al. Research on electrical resistance tomography and cross-correlation technique to measure the two-phase flows.
65. Wang, M., T.F. Jones, and R.A. Williams, Visualization of Asymmetric Solids Distribution in Horizontal Swirling Flows Using Electrical Resistance Tomography. Chemical Engineering Research and Design, 2003. 81(8): p. 854-861.
66. Lucas, G. and N.D. Jin, Measurement of the homogeneous velocity of inclined oil-in-water flows using a resistance cross correlation flow meter. 2001(Journal Article).
67. Lucas, G. and N.D. Jin, A new kinematic wave model for interpreting cross correlation velocity measurements in vertically upward, bubbly oil-in-water flows. 2001(Journal Article).
68. Ismail, I., et al., Tomography for multi-phase flow measurement in the oil industry. Flow Measurement and Instrumentation, 2005. 16(2–3): p. 145-155.
69. Azzopardi, B.J., et al., Comparison between Electrical Capacitance Tomography and Wire Mesh Sensor Output for Air/Silicone Oil Flow in a Vertical Pipe. Industrial & Engineering Chemistry Research, 2010. 49(18): p. 8805-8811.
70. Datta, U., T. Dyakowski, and S. Mylvaganam, Estimation of particulate velocity components in pneumatic transport using pixel based correlation with dual plane ECT. Chemical Engineering Journal, 2007. 130(2): p. 87-99.
71. Deyun, C., et al. An Image Data Capture System for Electrical Capacitance Tomography of Oil/Water Two-Phase Flow: IEEE.
72. Li, Y., et al., Image Reconstruction Algorithm for Electrical Capacitance Tomography. Information Technology Journal, 2011. 10(8): p. 1614-1619.

73.   Liu, S., et al., Electrical capacitance tomography for gas–solids flow measurement for circulating fluidized beds. Flow Measurement and Instrumentation, 2005. **16**(2): p. 135-144.

74.   Mohamad, E.J., et al. Multiphase flow reconstruction in oil pipelines by portable capacitance tomography: IEEE.

75.   Ostrowski, K.L., et al., Application of capacitance electrical tomography for on-line and off-line analysis of flow pattern in horizontal pipeline of pneumatic conveyer. Chemical Engineering Journal, 2000. **77**(1): p. 43-50.

76.   Pradeep, C., et al. Electrical Capacitance Tomography (ECT) and gamma radiation meter for comparison with and validation and tuning of CFD modeling of multiphase flow: IEEE.

77.   Wuqiang, Y., et al. Multiphase flow measurement by electrical capacitance tomography: IEEE.

78.   Yang, W.Q. and L. Peng, Image reconstruction algorithms for electrical capacitance tomography. Measurement Science and Technology, 2003. **14**(1): p. R1-R13.

79.   Yi, L., et al. Gas/oil/water flow measurement by electrical capacitance tomography: IEEE.

80.   Zhang, J. and J. Coulthard, Theoretical and experimental studies of the spatial sensitivity of an electrostatic pulverised fuel meter. Journal of Electrostatics, 2005. **63**(12): p. 1133-1149.

81.   Limited, P.T. Electrical Capacitance Tomography and Tomographic Flow Measurement. 28/8/2013]; Available from: http://www.tomography.com/.

82.   Dyakowski, T., L.F.C. Jeanmeure, and A.J. Jaworski, Applications of electrical tomography for gas–solids and liquid–solids flows — a review. Powder Technology, 2000. **112**(3): p. 174-192.

83.   Leeungculsatien, T. Novel Multi-Electrode Electromagnetic Flow Meter.

84.   Bernier, R.N. and C.E. Brennen, Use of the electromagnetic flowmeter in a two-phase flow. International Journal of Multiphase Flow, 1983. **9**(3): p. 251-257.

85.   Wyatt, D.G., Electromagnetic flowmeter sensitivity with two-phase flow. International Journal of Multiphase Flow, 1986. **12**(6): p. 1009-1017.

86.   Cha, J.-E., Y.-C. Ahn, and M.-H. Kim, Flow measurement with an electromagnetic flowmeter in two-phase bubbly and slug flow regimes. Flow Measurement and Instrumentation, 2002. **12**(5–6): p. 329-339.

87.   Leeungculsatien, T., G. Lucas, and X. Zhao, A numerical approach to determine the magnetic field distribution of an electromagnetic flow meter. 2009, University of Huddersfield.

88.   Bates, C.J. and B. Franklin, The performance characteristics of a novel multi-electrode electromagnetic flowmeter. Measurement, 2004. **35**(4): p. 399-408.

89.   Horner, B., A novel profile-insensitive multi-electrode induction flowmeter suitable for industrial use. Measurement, 1998. **24**(3): p. 131-137.

90.   Horner, B., F. Mesch, and A. Trächtler, A multi-sensor induction flowmeter reducing errors due to non-axisymmetric flow profiles. Measurement Science and Technology, 1996. **7**(3): p. 354-360.

91.   Jingzhuo, W. and G. Chenglong. Sensing Induced Voltage of Electromagnetic Flow Meter with Multi-electrodes: IEEE.

92. Liang, H., et al. Reconstruction of the magnetic field in the measuring volume of an electromagnetic flow sensor.

93. Liang, H., L. Kok-Meng, and F. Xin. A Method Based on Measured Boundary Conditions for Reconstructing the Magnetic Field Distribution of an Electromagnetic Mechatronic System. PISCATAWAY: IEEE.

94. Xu, L.J., et al., Optimum estimation of the mean flow velocity for the multi-electrode inductance flowmeter. Measurement Science and Technology, 2001. **12**(8): p. 1139-1146.

95. Leeungculsatien, T. and G. Lucas, Measurement of velocity profiles in multiphase flow using a multi-electrode electromagnetic flow meter. 2013(Journal Article).

96. Wang, J., et al. Simulation of magnetic field distribution of excitation coil for EM flow meter and its validation using magnetic camera. in 17th World Conference on Nondestructive Testing. 2008.

97. Lucas, G. and T. Leeungculsatien. A New Method of Measuring Velocity Profiles using a MultiElectrode Electromagnetic Flow Meter.

98. Busaidi, K., H. Bhaskaran, and P.D.O. (PDO), Multiphase Flow Meters: Experience and Assessment in PDO, in SPE Annual Technical Conference and Exhibition. 2003, Society of Petroleum Engineers Denver, Colorado.

99. Management, E.P. The Roxar Multiphase Meter 2600. [cited 2013 24/9/2012]; Available from: http://www2.emersonprocess.com/siteadmincenter/PM%20Roxar%20Documents/Flow%20Metering/Roxar%20Multiphase%20meter%202600%20Brochure.pdf.

100. Offshere. Multiphase specialist looking to build on East Spar subsea breakthrough. 1995 [cited 2012 12/10/2012]; Available from: http://www.offshore-mag.com/articles/print/volume-55/issue-11/news/general-interest/multiphase-specialist-looking-to-build-on-east-spar-subsea-breakthrough.html.

101. Limited, S. Vx Multiphase Well Testing Technology. 12/10/2012]; Available from: http://www.slb.com/services/characterization/testing/multiphase/vx_technology.aspx.

102. COMSOL. Product Suite. 2013 [cited 9/9/2013; Available from: http://www.uk.comsol.com/products.

103. Facility, N.N. MATLAB Function Reference. [cited 2014 10/2/2014]; Available from: http://nf.nci.org.au/facilities/software/Matlab/techdoc/ref/griddata.html#998812.

104. Sandwell, D.T., Biharmonic Spline Interpolation of GEOS-3 and SEASAT Altimeter Data. Geophysical Research Letters, 1987. **2**: p. 139-142.

105. X. Deng, et al., The design of a dual-plane ERT system for cross correlation measurement of bubbly gas/liquid pipe flow Measurement Science and Technology 2001. **12**(2001): p. 1024-1031.

106. Micro-Robotics. The Venom Language. 2013 [cited 2013 9/5/2013]; Available from: http://www.microrobotics.co.uk/company/contactus.html.

107. Leeungculsatien, T., Measurement of velocity profiles in single-phase and multiphase flows using a multi-electrode electromagnetic flow meter in Ph.D thesis. 2012, University of Huddersfield.

108. J. A. Shercliff, the Theory of Electromagnetic Flow-Measurement. 1987, New Ed: Cambridge University Press,.

109. Asakura, K., M. Ito, and I. Nakajima, Local mean profiles of velocity, concentration and concentration fluctuations of solid phase in a vertical pipe, in Proceedings of the

International Conference on Bulk Materials Storage, Handling & Transportation:Symposium on Freight Pipelines. 1992: Wollongong, Australia.

110. Panagiotopoulos, N. and G. Lucas, Simulation of a local four-sensor conductance probe using a rotating dual-sensor probe. 2007(Journal Article).

111. Lucas, G.P. and N. Panagiotopoulos, Oil volume fraction and velocity profiles in vertical, bubbly oil-in-water flows. Flow Measurement and Instrumentation, 2009. **20**(3): p. 127-135.

112. Lucas, G. and N. Panagiotopoulos. Measurement and modelling of oil volume fraction and velocity profiles in vertical bubbly oil water flows.

113. Lucas, G., Gas volume fraction and velocity profiles: vertical and inclined bubbly air-water flows. 2006(Journal Article).

10. Appendix A

10.1 CoA Coordinates for Configuration I, II and III
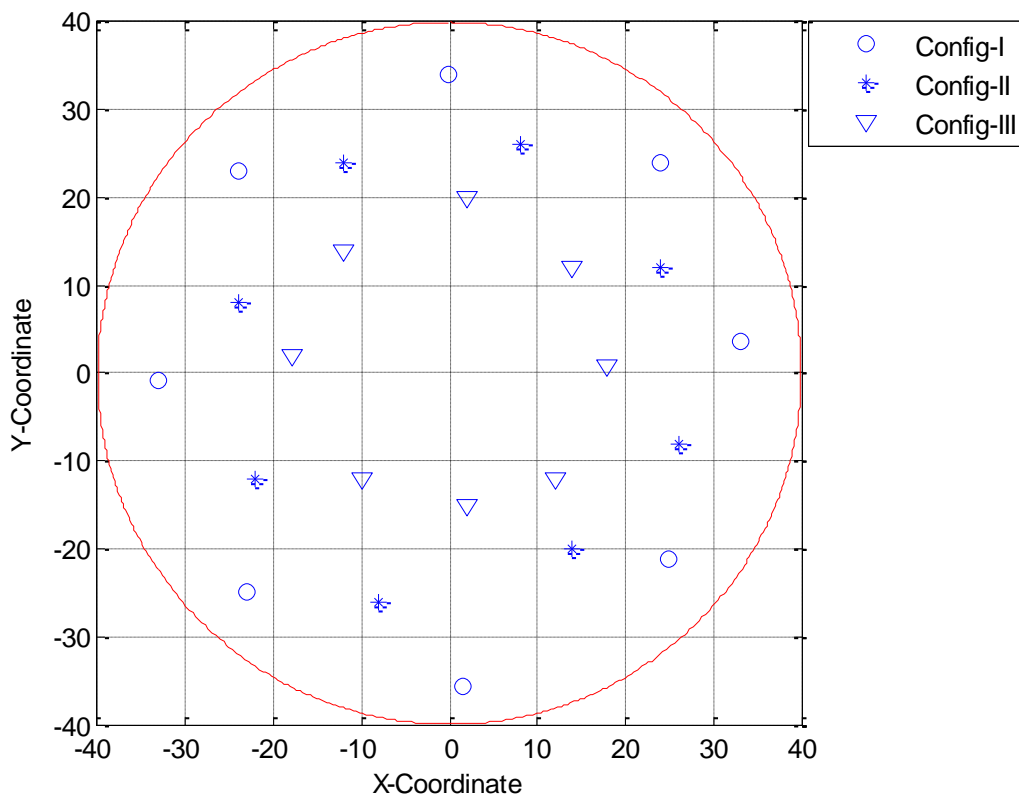
Figure 10.1 Location of CoA for Config-I, II and III for each of the eight possible electrode rotational positions

Table 10-1 CoA coordinates for Configuration I, II and III for each of the eight possible electrode rotational positions per configuration.

Configuration _I	X - coordinate	Y - coordinate
Rotational position 1	-23	-24.9
Rotational position 2	1.5	-35.6
Rotational position 3	25	-21.1
Rotational position 4	33	3.7
Rotational position 5	24	24

Rotational position 6	-0.1	34.1
Rotational position 7	-24	23
Rotational position 8	-33	-0.8
Configuration _II	**X - coordinate**	**Y - coordinate**
Rotational position 1	-22	-12
Rotational position 2	-8	-26
Rotational position 3	14	-20
Rotational position 4	26	-8
Rotational position 5	24	12
Rotational position 6	8	26
Rotational position 7	-12	24
Rotational position 8	-24	8
Configuration _III	**X - coordinate**	**Y - coordinate**
Rotational position 1	-10	-12
Rotational position 2	2	-15
Rotational position 3	12	-12
Rotational position 4	18	0.8
Rotational position 5	14	12
Rotational position 6	2	20
Rotational position 7	-12.1	14
Rotational position 8	-18	2

10.2 The Coordinates of the 32 Measurements Points (Area Methodology)
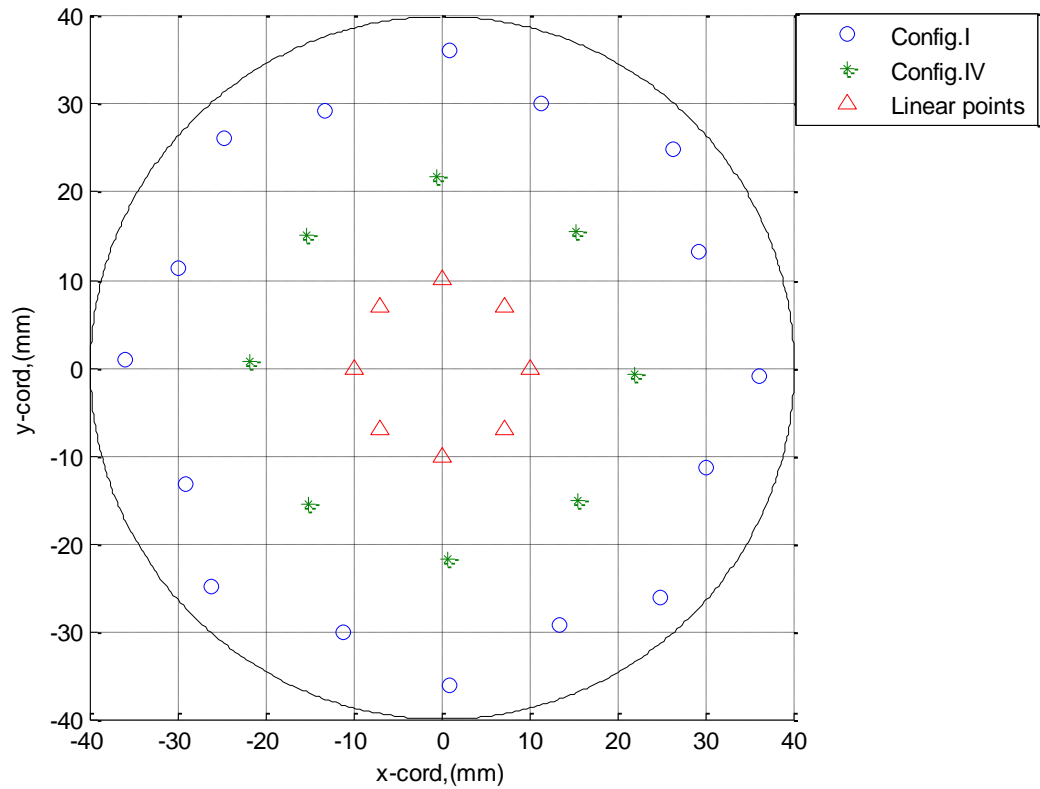
Figure 10.2 X and Y coordinates of the 32 measurements points

Table 10-2 X and Y coordinate shown in Figure 9-2

32 Points	X - coordinate	Y - coordinate
A_1	-29.22	-13.24
A_2	-11.30	-30.02
A_3	13.24	-29.22
A_4	30.024	-11.30
A_5	29.22	13.24
A_6	11.30	30.02
A_7	-13.24	29.22
A_8	-30.02	11.30
$A_{8,1}$	-36.07	0.93
$A_{1,2}$	-26.16	-24.85

$A_{2,3}$	0.93	-36.07
$A_{3,4}$	24.85	-26.16
$A_{4,5}$	36.07	-0.93
$A_{5,6}$	26.16	24.85
$A_{6,7}$	0.93	36.07
$A_{7,8}$	-24.85	26.16
$B_{1,0}$	-17.6	-15.1
$B_{2,0}$	-1	-23
$B_{3,0}$	15.1	-17.6
$B_{4,0}$	23	-1
$B_{5,0}$	15.1	17.6
$B_{6,0}$	1	23
$B_{7,0}$	-17.6	15.1
$B_{8,0}$	-23	1
LP_1	-10	0
LP_2	-7	-7
LP_3	0	-10
LP_4	7	-7
LP_5	10	0
LP_6	7	7
LP_7	0	10
LP_8	-7	7

11. Appendix B

1.   Code-1: this code is used to determine the solids velocity. The Labview program used to collect the data from channels A and B at1 min sampling time and 2000 samples/second. the program save the collected data as lvm file into two columns.

```
clc;
clear all;
close all;

load('D:\yousif2012\yousif\t4-3-configur1-rot8-34hz-test.lvm'); loading the the lvm file

N=2*2048; %Number of samples
T=N/2000;  %Sampling time

cha= t4-3-configur1-rot8-34hz-test (1:N,2);% define the data for channel A
chb= t4-3-configur1-rot8-34hz-test (1:N,1);% define the data for channel B

tempcha = mean(cha);
tempchb = mean(chb);


cha = cha(1:N)-tempcha;  % Linear the data in order to remove the DC offset
chb = chb(1:N)-tempchb; % Linear the data in order to remove the DC offset
c1 = xcorr(chb,cha);        % cross correlated channel A and channel B
figure(2);
t=linspace(-T,T,2*N-1);
plot(t,c1)
xlabel('Time (s)');
ylabel('C.C. Function');
TITLE('34 Solid Pump + 0 Water Pump');
[m I] = max(c1);
m
t(I)
V(1)=(0.05/t(I)); % Calculate the velocity V=L/t(I), where t(I) is the delay time.
time_d(1)=t(I);
figure(1);
t=linspace(0,T,N);
plot (t,cha,'green')
hold on
plot (t,chb,'red')
xlabel('Time (s)');
ylabel('Vout');
TITLE('34 Solid Pump + 0 Water Pump');
legend('cha','chb');

for i=1:28 % loop to determine the velocity every 2 seconds

cha= t4-3-configur1-rot8-34hz-test (i*N:(i+1)*N,2);
chb= t4-3-configur1-rot8-34hz-test (i*N:(i+1)*N,1);

tempcha = mean(cha);
```

```matlab
tempchb = mean(chb);

cha = cha(1:N)-tempcha;
chb = chb(1:N)-tempchb;
c1=xcorr(chb,cha);
figure(i+2);
t=linspace(-T,T,2*N-1);
plot(t,c1);
xlabel('Time (s)');
ylabel('C.C. Function');
TITLE('34 Solid Pump + 0 Water Pump');
[m I] = max(c1);
m
t(I)
V(1+i)=(0.05/t(I));
time_d(i+1)=t(I);
figure(i+30);
t=linspace(0,T,N);
plot (t,cha,'green')
hold on
plot (t,chb,'red')
xlabel('Time (s)');
ylabel('Vout');
TITLE('34 Solid Pump + 0 Water Pump');
legend('cha','chb');

end
```

2.   Code-2: This code is used to draw the solids velocity and volume fraction distributions in 3-D figure,

```matlab
close all;
clear all;
clc;

load('C:\Documents and Settings\sengymm\Desktop\ICC \36\wyz.txt')% loading wxz file where the first column in the x coordinates for the CoA, second column is the Y coordinates for the CoA, and the third column represent the volume fraction values.

[xx,yy]=meshgrid(min(-40):2:max(40),min(-40):2:max(40));
 x=wyz(:,1);
 y=wyz(:,2);
  z=wyz(:,3);
zz=griddata(x,y,z,xx,yy,'V4');
zz(xx.^2 + yy.^2>= 1600) = 0; ;% define the pipe cross-section x^2+y^2=r^2
figure(1)
surf(xx,yy,zz)
axis square;
xlabel('x-cord of centre of action');
ylabel('y-cord of centre of action');
zlabel('Solids Volumr fraction');
TITLE('38Hz Solid Pump + 50Hz Water Pump');
 COLORBAR('vert')
```

%%%

```matlab
load('C:\Documents and Settings\sengymm\Desktop\ICC\36\wyzv.txt') % loading wxzv file
where the first column in the x coordinates for the CoA, second column is the Y coordinates for
the CoA, and the third column represent the Velocity values.
[xxv,yyv]=meshgrid(min(-40):2:max(40),min(-40):2:max(40));
 xv=wyzv(:,1);
 yv=wyzv(:,2);
 zv=wyzv(:,3);
zzv=griddata(xv,yv,zv,xxv,yyv,'v4');
zzv(xxv.^2 + yyv.^2>= 1600) = 0;% define the pipe cross-section x^2+y^2=r^2
surf(xxv,yyv,zzv)

end
```